Development of aluminum-phosphate hybrid materials via sol-gel route for additive manufacturing of photonic materials

Thèse en cotutelle
Doctorat en Physique

Gabriel Toshiaki Tayama

Sous la direction de :

Prof. Tigran Galstian, directeur de recherche

Prof. Younes Messaddeq, directeur de cotutelle

Ph.D. Silvia Helena Santageneli, codirectrice de cotutelle

GABRIEL TOSHIAKI TAYAMA

Development of aluminum-phosphate hybrid materials via sol-gel route for additive manufacturing of photonic materials

Thesis in cotutelle with Université Laval – Quebec – Canada presented to the Institute of Chemistry, Universidade Estadual Paulista, to obtain the degree of Doctor in Chemistry

Brazilian advisor: Younes Messaddeq
Brazilian co-advisor: Silvia Helena Santagneli
Canadian advisor: Prof. Tigran Galstian

Araraquara
2023

Tayama, Gabriel Toshiaki
T236d Development of aluminum-phosphate hybrid materials via sol-gel route for additive manufacturing of photonic materials / Gabriel Toshiaki Tayama – Araraquara: [s.n.], 2023
265 p.: il.

Thesis (doctor) – Universidade Estadual Paulista, Instituto de Química
Advisor: Younes Messaddeq
Co-advisor: Silvia Helena Santagneli

1. Three-dimensional printing. 2. Photonics. 3. Phosphates. 4. Lanthanides. 5. Optical properties. I. Title.

Sistema de geração automática de fichas catalográficas da Unesp. Biblioteca do Instituto de Química, Araraquara. Dados fornecidos pelo autor(a).

Essa ficha não pode ser modificada

IMPACTO POTENCIAL DESTA PESQUISA

Os potenciais impactos decorrentes deste projeto de doutorado compreendem o aprofundamento e nacionalização do conhecimento em manufatura aditiva aplicada a síntese de materiais obtidos a partir da rota sol-gel, que tem ganhado destaque nos últimos anos, dada sua aplicação na manufatura de vidros inorgânicos e materiais híbridos. Dessa maneira, espera-se que essa tese possa contribuir no desenvolvimento desse setor industrial estratégico, com a geração de empregos e propriedade intelectual, fornecendo infraestrutura para uma miríade de aplicações de alta tecnologia.

POTENTIAL IMPACT OF THIS RESEARCH

The potential impacts arising from this doctoral project include the deepening and nationalization of knowledge in additive manufacturing applied to the synthesis of materials obtained from the sol-gel route, which has gained prominence in recent years, given its application in the manufacture of inorganic glasses and hybrid materials. In this way, it is expected that this thesis can contribute to the development of this strategic industrial sector, with the generation of jobs and intellectual property, providing infrastructure for a myriad of high-tech applications.

IMPACT POTENTIEL DE CETTE RECHERCHE

Les impacts potentiels découlant de ce projet de doctorat comprennent l'approfondissement et la nationalisation des connaissances en fabrication additive appliquées à la synthèse de matériaux obtenus à partir de la route sol-gel, qui a pris de l'importance ces dernières années, compte tenu de son application dans la fabrication de verres inorganiques et de matériaux hybrides. De cette façon, on s'attend à ce que cette thèse puisse contribuer au développement de ce secteur industriel stratégique, avec la création d'emplois et la propriété intellectuelle, fournissant une infrastructure pour une myriade d'applications de haute technologie.

UNIVERSIDADE ESTADUAL PAULISTA

Câmpus de Araraquara

CERTIFICADO DE APROVAÇÃO

TÍTULO DA TESE: "Development of aluminum-phosphate hybrid materials via sol-gel route for additive manufacturing of photonic materials"

AUTOR: GABRIEL TOSHIAKI TAYAMA

ORIENTADOR: YOUNES MESSADDEQ

COORIENTADORA: SILVIA HELENA SANTAGNELI

Aprovado como parte das exigências para obtenção do Título de , pela Comissão Examinadora:

Prof. Dr. YOUNES MESSADDEQ (Participaçao Virtual)
Departamento de Química Analítica, Físico-Química e Inorgânica / Instituto de Química - UNESP - Araraquara

Prof. Dr. TIGRAN GALSTIAN (Participaçao Virtual)
Centre d`Optique Photonique et Laser -
Université Laval

Prof. Dr. MARCELO NALIN (Participaçao Virtual)
Departamento de Quimica Analitica, Fisico-Quimica e Inorganica / Instituto de Quimica - UNESP - Araraquara

Prof. Dr. PETER MCBREEN (Participaçao Virtual)
Université Laval - Quebec

Prof. Dr. THIERRY CARDINAL (Participaçao Virtual)
Institut de Chimie de la Matière Condensée de Bordeaux - UB - França

Araraquara, 12 de outubro de 2023

gov.br Documento assinado digitalmente
YOUNES MESSADDEQ
Data: 26/10/2023 18:20:59-0300
Verifique em https://validar.iti.gov.br

CURRICULUM

Personal Data

Name: Gabriel Toshiaki Tayama

Name in bibliographic citations: Tayama, G.T.

Address: Universidade Estadual Paulista "Júlio de Mesquita Filho"

Instituto de Quimica

Departamento de Química Geral e Inorgânica

Rua Francisco Degni 55

Quitandinha – Araraquara – SP

CEP: 14800-900

Phone Number: (581) 849-3450

E-mail Address: gabrieltayama@gmail.com, gabriel.tayama.1@ulaval.ca, gabriel.tayama@unesp.br

Academic Education

2013-2017: Bachelor in Materials Engineering

Universidade Federal de São Carlos (UFSCar)

Bibliographic Production

Journal Publications:

G. T. Tayama, S. H. Messaddeq, S. H. Santagneli, and Y. Messaddeq, "Correlation Between Critical Energy, Penetration Depth, and Photopolymerization Kinetics in Aluminum-Phosphate-Silicate Hybrid Materials for Vat-Photopolymerization," Macromolecules, XXXX, XXX, XXX-XXX, Mai. 2023, doi 10.1021/acs.macromol.3c00363.

G. T. Tayama, S. H. Santagneli, M. de Oliveira Junior, and Y. Messaddeq, "Understanding the Microstructure Connectivity in Photopolymerizable Aluminum-Phosphate-Silicate Sol–Gel Hybrid

Materials for Additive Manufacturing," J. Phys. Chem. C, p. acs.jpcc.2c08027, Jan. 2023, doi: 10.1021/acs.jpcc.2c08027.

M. Posternak, G. T. Tayama, S. H. Messaddeq, and Y. Messaddeq, "Process modeling of laser scanning vat-photopolymerization operating under intermittent exposure conditions," *Addit. Manuf.*, vol. 60, p. 103234, Dec. 2022, doi: 10.1016/j.addma.2022.103234.

G. T. Tayama, S. H. Santagneli, H. Eckert, S. Pawsey, and Y. Messaddeq, "Preparation and Structural Characterization of New Photopolymerizable Transparent Aluminum-Phosphate Hybrid Materials as Resins for 3D Printing," *J. Phys. Chem. C*, vol. 124, no. 46, pp. 25621–25631, Nov. 2020, doi: 10.1021/acs.jpcc.0c08289.

Conference Presentations:

G. Tayama, S. Santagnelli, S. H. Messaddeq, T. Galstian, and Y. Messaddeq "Compositional dependency of 3D printing parameters in silica-aluminum-phosphate hybrid materials" Oral session presented at: Solgel 2022, July 24-29th, Lyon, France

G. Tayama, S. Santagnelli, M. O. Junior, and Y. Messaddeq "Deep understanding on the formation of silica-aluminum-phosphate hybrid materials using solid-state NMR". Poster session presented at: Sol-gel 2022, July 24-29th, Lyon, France

G. Tayama, S. Santagnelli, and Y. Messaddeq "Hybrid sol-gel as precursors towards additive manufacturing of photonic". Poster session presented at: 2nd Photonics National Institute for Science and Technology, February 12-15th, Araraquara, Brazil

G. Tayama, S. Santagnelli, and Y. Messaddeq "Hybrid sol-gel inks for stereolitography of aluminum-phosphate hybrids". Poster session presented at: 25th International Conference on Glasses 2019, June 9-14th, Boston, USA

G. Tayama, L. S. Gallo, and E. D. Zanotto "Glass-ceramics of high mechanical strength". Poster session presented at: X BraSGlass – Brazilian Symposium on Glass and Related Materials, October 26-30th, São Carlos, Brazil

ABSTRACT

Additive manufacturing (AM) is a technology with great potential for use in photonic applications because it overcomes the limitations of traditional manufacturing methods. Among the various AM techniques available, the vat-photopolymerization (VPP) is one of the few that meets the requirements for photonics manufacturing. However, one of the main challenges hindering the widespread adoption of VPP in optical device manufacturing is the limited availability of materials compatible with VPP techniques.

The aim of this thesis was to develop, elucidate the structure of, fabricate via additive manufacturing, and study the optical properties of 3D printed parts of aluminum-phosphate hybrid materials. These materials were developed using the sol-gel route as candidates for the fabrication of active and passive photonic devices. These materials were additive manufactured via VPP using a custom-made AM system operating under intermittent exposure conditions. We developed a mathematical model describing the exposure profile output by this custom-made VPP setup, since its operating principle greatly differs from commercial platforms. Then, these new materials were 3D printed after characterizing their VPP parameters and photopolymerization kinetics. Lastly, we examined the optical homogeneity and anisotropy of additive manufactured elements from these materials. These goals were explored throughout five scientific publications, composing the five chapters of this thesis.

In our first contribution, we synthesized photopolymerizable aluminum-phosphate sols, that were polymerized to result in organic-inorganic hybrid (OIH) materials composed by poly (2-hydroxyethyl methacrylate) chains with aluminum-phosphate groups covalently bonded to the polymeric backbone. These inorganic units provide numerous crosslinkers, resulting in a highly interconnected and interlocked inorganic/organic structure. The OIH materials were optically transparent between the 420 nm - 1100 nm, however, these materials showed low transmittance in the near-infrared region (NIR) due to the high organic content of these matrices.

In a second contribution, we modified the synthesis route to achieve aluminum-phosphate-silicate OIH materials with higher inorganic mass concentration and improved transmittance in the NIR. We investigated in-depth the structure of these materials by means of solid-state NMR and observed that the inorganic network is formed by aluminum-phosphate units interconnected by silicate chains.

The chemical environment of the phosphate and aluminate sites could be tuned based on the aluminum to phosphorus ratio, allowing the structure to be tailored in order to enhance the lanthanide ions hosting ability of these materials. These structural features present these materials as potential candidates to immobilize lanthanide ions for developing active optical components.

In a third contribution, we developed and tested a mathematical model describing the exposure profile outputted by the custom-built printer employed in this work, allowing us to model the laser-resin interaction in this equipment, and to correlate the printing parameters measured for our materials with those of commercial AM setups. Furthermore, we identified that this printing system can, theoretically, print faster compared to commercial platforms under specific conditions of beam diameter and overlap between pulses.

In a fourth contribution, we explored the additive manufacturing of the aluminum-phosphate-silicate resins. The evolution of the 3D printing parameters of these materials (critical energy and penetration depth), and of the photopolymerization kinetics with light intensity and silicate concentration was studied. These results indicate the shift of critical conversion towards higher polymerization degree as the concentration of silicate increases, which was associated to a higher tendency towards cyclization. These results were employed to validate a photochemical model published in the literature describing the laser-resin interaction in VPP systems, elucidating the link between critical energy and photopolymerization kinetics.

In our last contribution, we studied the refractive index distribution and the presence of optical anisotropies in 3D printed lines. We identified that the 3D printed parts are optically homogenous, despite the presence of a gradient of polymerization degree associated to the penetration of the laser into the resin and the beam profile. Optical anisotropies were identified, and polarized micro-Raman measurements indicate that the birefringence arises from the shear stress perpendicular to the scan direction due to the inflow of monomer towards the polymerization spot.

RESUMO

A manufatura aditiva (MA) é uma tecnologia com grande potencial para aplicações em fotônica, pois contorna as limitações impostas por métodos tradicionais de manufatura. Entre as várias técnicas de MA disponíveis, a fotopolimerização em cuba (VPP) é uma das poucas que atende os requisitos de tolerância presente na fabricação de dispositivos fotônicos. No entanto, um dos principais desafios que impedem ampla adoção da VPP na fabricação de dispositivos ópticos é a baixa disponibilidade de materiais processáveis com as técnicas de VPP.

O objetivo desta tese foi desenvolver, elucidar a estrutura, fabricar via manufatura aditiva e estudar as propriedades ópticas de peças impressas 3D de materiais híbridos de alumínio-fosfato. Esses materiais foram desenvolvidos utilizando a rota sol-gel como candidatos para a fabricação de dispositivos fotônicos ativos e passivos via impressão 3D. Esses materiais foram processados via VPP usando um sistema MA customizado, operando sob condições de exposição intermitente. Foi desenvolvido e testado um modelo matemático descrevendo o perfil de exposição produzido por esse sistema VPP customizado, uma vez que seu princípio operacional difere daquele de plataformas comerciais. Em seguida, os parâmetros de impressão 3D e a cinética de fotopolimerização desses novos materiais foram estudados, permitindo sua impressão 3D. Por fim, foi estudado a homogeneidade óptica e a presença de anisotropias ópticas em partes produzidas por MA desses materiais. Esses objetivos foram explorados ao longo de cinco publicações científicas, compondo os cinco capítulos desta tese.

Em nossa primeira contribuição, sintetizamos soluções fotopolimerizáveis de alumínio-fosfato, resultando em materiais híbridos orgânico-inorgânicos (HOI) compostos por cadeias de poli (2-hidroxietil metacrilato) com grupos alumínio-fosfato covalentemente ligados ao esqueleto polimérico. Essas unidades inorgânicas atuam como ligações cruzadas, resultando em uma estrutura inorgânica-orgânica altamente interconectada e interligada. Os materiais obtidos são totalmente transparentes entre 420 nm - 1100 nm, porem possuem baixa transmitância na região do infravermelho próximo (NIR) devido ao alto teor orgânico dessas matrizes.

Em uma segunda contribuição, modificamos a rota de síntese para obter materiais HOI de alumínio-fosfato-silicato com maior teor de massa inorgânica e melhor transmitância no NIR. Investigamos em detalhe a estrutura desses materiais por meio de RMN de estado sólido e

observamos que a rede inorgânica é formada por unidades de alumínio-fosfato interligadas por cadeias de silicato. O ambiente químico dos sítios de fosfatos e alumínio podem ser modificados por meio da razão alumínio para fosforo, permitindo que a estrutura seja otimizada para a introdução de íons lantanídeos. Essas características estruturais apresentam esses materiais como potenciais candidatos à imobilização de íons lantanídeos para o desenvolvimento de componentes ópticos ativos.

Em uma terceira contribuição, desenvolvemos e testamos um modelo matemático descrevendo o perfil de exposição produzido pela impressora personalizada empregada neste trabalho, permitindo-nos modelar a interação laser-resina e correlacionar os parâmetros de impressão medidos para nossos materiais com aqueles de plataformas comerciais de MA. Além disso, identificamos que este sistema de impressão pode, teoricamente, imprimir mais rápido comparado a plataformas comerciais, desde que condições específicas de diâmetro do feixe e sobreposição entre pulsos sejam atendidas.

Em uma quarta contribuição, exploramos a manufatura aditiva das resinas de alumínio-fosfato-silicato. Foi estudada a evolução dos parâmetros de impressão 3D desses materiais (energia crítica e profundidade de penetração) e da cinética de fotopolimerização com a intensidade de luz e a concentração de silicato. Os resultados obtidos indicaram um aumento da conversão critica das resinas com o aumento da concentração de silicato, o que estaria associado a uma maior contribuição da reação de ciclização. Esses resultados foram empregados para validar um modelo fotoquímico descrevendo a interação laser-resina em sistemas VPP publicados na literatura, elucidando a relação entre energia crítica e cinética de fotopolimerização.

Em nossa última contribuição, estudamos a distribuição do índice de refração e a presença de anisotropias ópticas em linhas impressas 3D. Foi verificado que as peças impressas em 3D são opticamente homogêneas, apesar da presença de um gradiente de grau de polimerização associado à penetração do laser na resina e do perfil do feixe. Anisotropias ópticas foram identificadas, e medidas de espalhamento micro-Raman polarizado indicaram que a birrefringência e oriunda da tensão de cisalhamento perpendicular à direção da varredura causada pelo influxo de monômero em direção ao centro da polimerização.

RESUME

La fabrication additive (FA) est une technologie à fort potentiel d'utilisation dans les applications photoniques car elle surmonte les limites des méthodes de fabrication traditionnelles. Parmi les différentes techniques de FA disponibles, la photopolymérisation en cuve (VPP) est l'une des rares à répondre aux exigences de la fabrication photonique. Cependant, l'un des principaux défis qui entravent l'adoption généralisée du VPP dans la fabrication de dispositifs optiques est la disponibilité limitée de matériaux compatibles avec les techniques VPP.

L'objectif de cette thèse était de développer, d'élucider la structure, de fabriquer via la fabrication additive et d'étudier les propriétés optiques de pièces imprimées en 3D de matériaux hybrides aluminium-phosphate. Ces matériaux ont été développés par voie sol-gel comme candidats pour la fabrication de dispositifs photoniques actifs et passifs. Ces matériaux ont été fabriqués via VPP en utilisant un système AM sur mesure fonctionnant dans des conditions d'exposition intermittentes. Nous avons développé un modèle mathématique décrivant le profil d'exposition produit par cette système VPP, car son principe de fonctionnement diffère grandement des plateformes commerciales. Ensuite, les paramètres VPP et la cinétique de photopolymérisation de ces nouveaux matériaux ont été caractérise, de façon a démontré leur impression 3D. Enfin, nous avons examiné l'homogénéité optique et l'anisotropie des éléments fabrique 3D à partir de ces matériaux. Ces objectifs ont été explorés à travers cinq publications scientifiques, composant les cinq chapitres de cette thèse.

Dans notre première contribution, nous avons synthétisé des sols de phosphate d'aluminium photopolymérisables, qui ont été polymérisés pour aboutir à des matériaux hybrides organiques-inorganiques (OIH) composés de chaînes de poly (méthacrylate de 2-hydroxyéthyle) avec des groupes de phosphate d'aluminium liés de manière covalente au squelette polymère. Ces unités inorganiques fournissent de nombreux agents de réticulation, résultant en une structure inorganique/organique hautement interconnectée et imbriquée. Les matériaux OIH étaient optiquement transparents entre 420 nm et 1100 nm, cependant, ces matériaux présentaient une faible transmission dans la région du proche infrarouge (NIR) en raison de la forte teneur en matières organiques de ces matrices.

Dans une deuxième contribution, nous avons modifié la voie de synthèse pour obtenir des matériaux OIH aluminium-phosphate-silicate avec une concentration en masse inorganique plus élevée et une transmittance améliorée dans le NIR. Nous avons étudié en profondeur la structure de

ces matériaux avec la RMN à l'état solide et observé que le réseau inorganique est formé d'unités d'aluminium-phosphate interconnectées par des chaînes de silicate. L'environnement chimique des sites de phosphate et d'aluminate pourrait être réglé en fonction du rapport aluminium sur phosphore, permettant à la structure d'être adaptée afin d'améliorer la capacité d'accueil des ions lanthanides de ces matériaux. Ces caractéristiques structurelles présentent ces matériaux comme des candidats potentiels pour immobiliser les ions lanthanides pour développer des composants optiques actifs.

Dans une troisième contribution, nous avons développé et testé un modèle mathématique décrivant le profil d'exposition produit par l'imprimante utilisée dans ce travail, nous permettant de modéliser l'interaction laser-résine dans cet équipement, et de corréler les paramètres d'impression mesurés pour notre matériau avec ceux des système FA commerciales. De plus, nous avons identifié que ce système d'impression peut, théoriquement, imprimer plus rapidement par rapport aux plateformes commerciales dans des conditions spécifiques de diamètre de faisceau et de chevauchement entre les impulsions.

Dans une quatrième contribution, nous avons exploré la fabrication additive des résines aluminium-phosphate-silicate. L'évolution des paramètres d'impression 3D de ces matériaux (énergie critique et profondeur de pénétration), et de la cinétique de photopolymérisation avec l'intensité lumineuse et la concentration en silicate a été étudiée. Ces résultats indiquent le déplacement de la conversion critique vers un degré de polymérisation plus élevé à mesure que la concentration de silicate augmente, ce qui était associé à une tendance plus élevée à la cyclisation. Ces résultats ont été utilisés pour valider un modèle photochimique publié dans la littérature décrivant l'interaction laser-résine dans les systèmes VPP, élucidant le lien entre l'énergie critique et la cinétique de photopolymérisation.

Dans notre dernière contribution, nous avons étudié la distribution de l'indice de réfraction et la présence d'anisotropies optiques dans les lignes imprimées en 3D. Nous avons identifié que les pièces imprimées en 3D sont optiquement homogènes, malgré la présence d'un gradient de degré de polymérisation associé à la pénétration du laser dans la résine et au profil du faisceau. Des anisotropies optiques ont été identifiées et des mesures micro-Raman polarisées indiquent que la biréfringence provient de la contrainte de cisaillement perpendiculaire à la direction de balayage due à l'afflux de monomère vers le point de polymérisation.

TABLE OF CONTENTS

TABLE OF FIGURES

LIST OF ABBREVIATIONS

ABS	*Acrylonitrile Butadiene Styrene*
ACAC	*Acetyl Acetonate*
AFM	*Atomic Force Microscopy*
AIBN	*Azobisisobutyronitrile*
AJ	*Adhesive Joining*
AM	*Additive Manufacturing*
ATR	*Attenuated Total Reflectance*
BAPO	*Phenylbis (2,4,6-trimethylbenzoyl)-phosphine oxide*
BJT	*Binder Jetting*
BSE	*Backscattered Electrons*
CAD	*Computer-Aided-Design*
CE	*Continuous Exposure*
CLIP	*Continuous Liquid Interface Production*
CN	*Coordination Number*
CP	*Cross-Polarization*
CPMAS	*Cross-Polarization Magical Angle Spinning*
CQ	*Quadrupolar coupling*
CRB	*Chemical Reaction Bonding*
CRC	*Chemical Reaction Consolidation*
CW	*Continuous Wave*
DDM	*Direct Digital Manufacturing*
DED	*Direct Energy Deposition*
DIW	*Direct Ink Writing*
DLP	*Digital Light Processing*
DMD	*Digital Micromirror Device*
3DP	*Three-Dimensional Printing*
DQ	*Double Quantum*
DTG	*Differential Thermogravimetric Analysis*
EB	*Electron Beam*
EOF	*Exposure Overlap Factor*

EPMA	*Electron Probe Microanalyzer*
EXSY	*Exchange Spectroscopy*
FA	*Fabrication Additif*
FDM	*Filament Deposition Modelling*
FM	*Formative Manufacturing*
FTIR	*Fourier Transform Infrared Spectroscopy*
HDA	*1, 6-hexanediol diacrylate*
HEMA	*2-hydroxyethyl methacrylate*
HETCOR	*Heteronuclear Correlation*
HOI	*Híbrido Organico-Inorganico*
HEMA-P	*hydroxyethyl methacrylate-phosphoric acid ester*
IE	*Intermittent Exposure*
IPN	*Interpenetrating Polymeric Network*
IR	*Infrared*
LAM	*Laser Additive Manufacturing*
LB	*Laser Beam*
LCD	*Liquid crystal display*
LED	*Light Emitting Diode*
MA	*Manufatura Aditiva*
MAEAA or MAEEA	*2-(Methacryloyloxy)ethyl acetoacetate*
MAS	*Magical Angle Spinning*
MEV	*Microscopia Eletrônica de Varredura*
MEX	*Material Extrusion*
MJT	*Material Jetting*
MOF	*Metal-Organic Framework*
MPP	*Multiphoton photopolymerization*
MPTMS or TMSPM or MTMS	*3-(trimethoxysilyl)propyl methacrylate*
ND	*Neutral Density*
NIR	*Near Infrared Region*
NMR	*Nuclear Magnetic Resonance*
OIH	*Organic Inorganic Hybrid*
ORMOCER	*Organically Modified Ceramic*

ORMOSIL	*Organically Modified Silane*
PBF	*Power Bed Fusion*
PC	*Polycarbonate*
PETA	*Pentaerythritol Tetra Acrylate*
PHEMA	*Poly Hydroxyethyl Methacrylate*
PLA	*Poly Lactic Acid*
PLC	*Poly Caprolactam*
PMMA	*Poly Methyl Methacrylate*
REDOR	*Rotational Echo Double Resonance*
RMN	*Ressonância Magnética Nuclear*
SEM	*Scanning Electron Microscopy*
SERS	*Surface Enhanced Raman Scattering*
SHL	*Sheet Lamination*
SLA	*Stereolithography*
SM	*Subtractive Manufacturing*
SOQE	*Second Order Quadrupolar Effect*
SQ	*Single Quantum*
TGA	*Thermogravimetric Analysis*
TMS	*Tetramethyl Silane*
TPO	*Diphenyl(2, 4, 6- trimethyl benzoyl)phosphine oxide*
TQMAS	*Triple Quantum Magic Angle Spinning*
TRB	*Thermal Reaction Bonding*
UC	*Ultrasonic Consolidation*
UV	*Ultraviolet*
UVL	*Ultraviolet Laser*
UVM	*Ultraviolet Mask*
VIS	*Visible*
VPP	*Vat Photopolymerization*
WAMM	*Wire and Arc Additive Manufacturing*
WDS	*Wavelength Dispersive Spectroscopy*

To my family, friends, and colleagues, with whom I shared, even for a brief moment, this tortuous and long path. I am grateful for their love and support.

ACKNOWLEDGEMENTS

The Ph.D. is quite a long path that is only possible, directly, or indirectly, by the people we meet on the way. I would like to use this space to remember and express my gratitude to all these people.

Normally I would start this section by thanking my supervisors, however I find it fitting to start by expressing my thanks to Julie Frechette. She is the only reason I managed to go to Canada as a cotutelle student. It was easily a more than one-year process of emails and correspondence going back and forth between the two universities that she had to manage. Thank you.

Now, I would like to thank Prof. Younes Messaddeq, and Prof. Tigran Galstian for their supervision, expertise, and enthusiasm. My Ph.D. was only possible because they gave me the opportunity to work, and most important, learn with them. Their guidance and support were essential. For similar reasons, I must also thank Prof. Marcelo Nalin, and Prof. Edgar Dutra Zanotto who were the pillars of my formation and gave me multiple opportunities that led me all the way here.

I have absolutely no way of expressing how grateful I am to Silvia Santagneli. She was the one who advised me during my stay in Brazil, and I can definitely say that Silvia's contribution towards this Ph.D. project could not be replaced. Her wide expertise in solid-state NMR, her patience to teach, and her supervision guided me through more than half of this thesis.

I must also express my gratitude towards my co-supervisor in Canada, Ph.D. Sandra Helena Messaddeq, for her insightful comments, constructive criticism, and helpful suggestions. Her feedback has greatly contributed to the quality of my research concerning the additive manufacturing.

I would like to thank the staff and faculty of Instituto de Quimica de Araraquara (UNESP) and COPL (Universite Laval), with special emphasis to the technicians Rafael Domeneguetti, Sergio Scarpari and Patrick Larochelle for their support and resources that have been instrumental in enabling me to carry out this research. Their assistance has been essential in navigating the various stages of the research process. Similarly, I must acknowledge the administrative staff at both universities, especially Wenia, Robson, Cintia, Michelle, Caroline, and David Helie for their support.

I am grateful as well to Prof Hellmut Eckert, Prof. Marcos de Oliveira Junior, and Ph.D. Shane Pawsey who collaborated in the publications integrating this thesis. Their insights, expertise, suggestions, and criticism were unvaluable for the quality of this thesis, as well my personal and professional development.

I would like to express my gratitude towards the whole Photonic Materials Group in Araraquara with special mention to Prof. Sidney Ribeiro, Prof. Willy Glen Santos, Prof. Elias Paiva Ferreira Neto, Prof. Danilo Manzani and Prof. Edson Percoraro for their scientific contributions. Similarly, I thank my friends from UNESP, Natalia Medeiros, Bruno Ekawa, Daniela Vassalo, Juliana Resges, Leonardo Albino, Leonardo Marchiori, Nina, Thais, Bia, Lia, Lais Galvao, Adriane Cherpinski and York for their support, encouragement, and great time together.

I would like to express my gratitude towards the whole Younes Messaddeq Lab in Universite Laval for their contribution, suggestions, and support for my thesis with special mention to Wagner Correr, and Prof. Ali Riaz. Similarly, I thank my friends from Universite Laval Hasnaa, Samar, Can, Alizee, Anees, Ishfaq, Rizan, Ismail, Nathaly, Iago, Rodrigo, Orisson, Victor, Alice, Mehran, Thomas, Brice, Simon, Theo, Antonin, and my friends from COPL, which is a pretty long list. In this regard, I must acknowledge all my Iranian friends and their fight for a better future in their country. Women, life, freedom.

I am also grateful to my family and friends for their unwavering support throughout my academic journey. Their love, support, and understanding have been crucial in helping me stay motivated and focused. Thank you Nkosi, Leleo, Gabi, Trop, Pita, Mari, my father, mother, and brother, and Halili, my love.

Lastly, this thesis was only possible thanks to the financial support of FAPESP (2018/06426-3, 2019/24367-7, 2015/ 22828-6, and 18/ 24735-3), and CNPQ (141186/2018-6).

Thank you all for your support, encouragement, and contributions. I could not have completed this thesis without your help and guidance.

FOREWORD

This thesis manuscript was based on four published manuscripts in peer-reviewed journals plus one unpublished work. Gabriel T. Tayama is the first author in three of them, and second author in the remaining one. A list of these articles is provided below, with details of submission and publication dates. Further information on the contribution of each co-author, and the alterations from the original manuscript to the version presented in this thesis manuscript are also provided.

Title: Understanding the Microstructure Connectivity in Photopolymerizable Aluminum-Phosphate-Silicate Sol–Gel Hybrid Materials for Additive Manufacturing

Authors: G. T. Tayama, S. H. Santagneli, M. de Oliveira Junior, and Y. Messaddeq,

Journal: Journal of Physical Chemistry C

DOI: 10.1021/acs.jpcc.2c08027.

Status: Submitted on November 15th, 2022. Published on January 19th, 2023.

Co-author Contributions: Synthesis of the materials, sample preparation, and all characterizations, except solid-state NMR, were executed by Gabriel Tayama. ^{29}Si, ^{27}Al, and ^{31}P uni- and bidimensional solid-state NMR experiments were performed by Ph.D. Silvia Santagneli. ^{1}H, and ^{13}C uni- and bidimensional solid-state NMR experiments were performed by Prof. Marcos Junior. Data interpretation was performed by Gabriel Tayama, Ph.D. Silvia Santagneli and Prof. Marcos Junior. The manuscript was prepared by Gabriel Tayama, and reviewed, edited, and completed by Ph.D. Silvia Santagneli and Prof. Marcos Junior. Prof. Younes Messaddeq supervised all the steps during the execution of this work.

Description of alterations: Formatting (font and line spacing) were adjusted to match the requirements of FESP. The figure numbering was adjusted to match the numbering of other figures presented along the thesis document. An abstract in French and in Portuguese was added.

Title: Preparation and Structural Characterization of New Photopolymerizable Transparent Aluminum-Phosphate Hybrid Materials as Resins for 3D Printing

Authors: G. T. Tayama, S. H. Santagneli, H. Eckert, S. Pawsey, and Y. Messaddeq

Journal: Journal of Physical Chemistry C

DOI: 10.1021/acs.jpcc.0c08289

Status: Submitted on September10th, 2020. Published on November 10th, 2020.

Co-author Contributions: Synthesis of the materials, sample preparation, and all characterizations, except solid-state NMR, were executed by Gabriel Tayama. ^{29}Si, ^{27}Al, and ^{31}P uni- and bidimensional solid-state NMR experiments were performed by Ph.D. Silvia Santagneli. ^{1}H, and ^{13}C uni- and bidimensional solid-state NMR experiments were performed by Ph.D. Shane Pawsey. Data interpretation was performed by Gabriel Tayama, Ph.D. Silvia Santagneli, Ph.D. Shane Pawsey, and Prof. Hellmut Eckert. The manuscript was prepared by Gabriel Tayama, and reviewed, edited, and completed by Ph.D. Silvia Santagneli, Ph.D. Shane Pawsey and Prof. Hellmut Eckert. Prof. Younes Messaddeq supervised all the steps during the execution of this work.

Description of alterations: Formatting (font and line spacing) were adjusted to match the requirements of FESP. The figure numbering was adjusted to match the numbering of other figures presented along the thesis document. An abstract in French and in Portuguese was added.

Title: Process modeling of laser scanning vat-photopolymerization operating under intermittent exposure conditions

Authors: M. Posternak, G. T. Tayama, S. H. Messaddeq, and Y. Messaddeq,

Journal: Additive Manufacturing

DOI: 10.1016/j.addma.2022.103234

Status: Submitted on April18th, 2022. Published on October 14th, 2022.

Co-author Contributions: Synthesis of the materials, sample preparation, and all characterizations were executed by Mykola Posternak. Data interpretation and the mathematical modelling was performed by Gabriel Tayama. The manuscript was prepared by Gabriel Tayama, and reviewed, edited, and completed by Ph.D. Sandra Messaddeq. Prof. Younes Messaddeq supervised all the steps during the execution of this work.

Description of alterations: Formatting (font and line spacing) were adjusted to match the requirements of FESP. The figure numbering was adjusted to match the numbering of other figures presented along the thesis document. An abstract in French and in Portuguese was added. Bibliographic references were adjusted to match the ACS (American Chemical Society) citation style.

Title: Correlation Between Critical Energy, Penetration Depth, and Photopolymerization Kinetics in Aluminum-Phosphate-Silicate Hybrid Materials for Vat-Photopolymerization

Authors: G. T. Tayama, S. H. Messaddeq, S. H. Santagneli, and Y. Messaddeq

Journal: Macromolecules

DOI: 10.1021/acs.macromol.3c00363

Status: Submitted on February 27th, 2023. Accepted on May 12th, 2023.

Co-author Contributions: Synthesis of the materials, sample preparation, and all characterizations were executed by Gabriel Tayama, except solid-state NMR (S. H. Santagneli). Data analysis, and interpretation was executed by Gabriel Tayama. The manuscript was prepared by Gabriel Tayama, and reviewed, edited, and completed by Ph.D. Sandra Messaddeq, Ph.D. Silvia Santagneli. Prof. Younes Messaddeq supervised all the steps during the execution of this work.

Description of alterations: Formatting (font and line spacing) were adjusted to match the requirements of FESP. The figure numbering was adjusted to match the numbering of other figures presented along the thesis document. An abstract in French and in Portuguese was added.

Title: Refractive Index Distribution and Optical Anisotropies in Additive Manufactured Materials

Authors: G. T. Tayama, S. H. Messaddeq, Tigran Galstian, and Y. Messaddeq

Status: Results to be published.

Co-author Contributions: Synthesis of the materials, sample preparation, and all characterizations were executed by Gabriel Tayama. Data analysis, and interpretation was executed by Gabriel Tayama. The manuscript was prepared by Gabriel Tayama, and reviewed, edited, and completed by Ph.D. Sandra Messaddeq, Prof. Tigran Galstian. Prof. Younes Messaddeq, and Prof. Tigran Galstian supervised all the steps during the execution of this work.

Description of alterations: Formatting (font and line spacing) were adjusted to match the requirements of FESP. The figure numbering was adjusted to match the numbering of other figures presented along the thesis document. An abstract in French and in Portuguese was added.

INTRODUCTION

Three-dimensional printing or additive manufacturing (AM) refers to a family of different techniques sharing a layer-by-layer manufacturing approach. Because of its features, AM allow the fabrication of complex structures with fixed processing time and costs, and simplified process planning, which is ideal for the small-scale production of high customizable products [1]. There are extensive reviews on literature on how additive manufacturing technologies are promising for a wide range of applications [2]–[4].

AM is a promising technology for photonic applications which has received great attention in the last decade as a method to circumvent the limitations of traditional manufacturing methods, which could enable a new generation of integrated optical devices. AM technologies for photonics requires high resolution (<10 um) and high surface finishing quality [5], which are conditions met by few AM technologies. The vat-photopolymerization (VPP) family of techniques is one of the few who meet such requirements, and although there are numerous examples in literature concerning the use of VPP in photonics, there are few fundamental investigations on the optical quality of produced parts, especially when it concerns optical homogeneity and anisotropies, since AM is a fundamentally anisotropic process.

The availability of materials compatible with VPP techniques is one of the main issues preventing more expressive application of VPP into the manufacturing of optical devices. VPP construct objects by inducing the selective photopolymerization of a resin to form each layer, therefore this technique is constrained to methacrylate and epoxy-based polymers. The organic nature of polymers restricts the optical applications of objects manufactured by AM to the visible and the terahertz regimes of the electromagnetic spectrum [6], [7]. In recent years, there has been intense research to enable the AM of inorganic glasses via VPP, which is a staple optical material for both active and passive optical devices. The main drawback, however, is that all approaches available require thermal treatment at high temperatures, hindering the construction of integrated electro-optical devices. In this context, the use of organic-inorganic hybrid (OIH) materials with VPP has arisen as an alternative to polymeric materials and inorganic glasses, since their optical properties can be tuned to meet the transmission requirements for active and passive optical devices operating from UV (ultraviolet) to NIR (near-infrared) spectrum [5], [8], [9]. They are not widely explored in photonics as glasses, however they are

excellent candidates for integrated active and passive photonic structures, since they do not require thermal treatments[5], [8], [10]–[12]

The hybrid sol-gel route has emerged in the last 3 years as a convenient chemical route to obtain transparent OIH materials processable through VPP. This chemical route employs chemical precursors capable of forming inorganic bonds through condensation reactions at mild processing conditions, with pendant photopolymerizable groups for the VPP process [13]. Alternative synthesis routes for OIH materials are not innately compatible for VPP as the hybrid sol-gel route, and often suffer from phase segregation, yielding opaque materials [14]–[16].Controlling the hydrolysis and condensation reactions are a fundamental step in this chemical route because it allows the organic and inorganic connectivity to be tailored and avoid phase segregation, resulting in a transparent material. So far, this chemical route has successfully allowed the printing of silicate-based OIHs with good optical quality, which have been explored in the fabrication of passive optical structures, such as waveguides [17], [18]. However, these matrices are bad candidates for the development of active optical devices, because of their poor solubility of lanthanide ions, requiring either thermal treatment at high temperature or additional strategies to introduce the lanthanide ions in the structure. Thus, there is the need for OIH materials which are inherently compatible with the chemistry of lanthanides for the fabrication of active optical devices via VPP.

In this regard, aluminum-phosphate (AlP) OIH materials are promising candidates for the fabrication of active optical devices. The chemistry of aluminum-phosphate shows a remarkable solubility for lanthanide ions , which prevents clustering and concentration quenching in photoluminescence[19], [20]. As a matter of fact, AlP inorganic glasses are widely used in telecommunications as signal amplifiers and fiber lasers. Despite these characteristics, little is reported in literature about AlP OIH materials obtained through the hybrid sol-gel route. The AlP sol-gel chemistry is challenging compared to the well-stablished silicate sol-gel chemistry. For instance, there is no convenient phosphate precursor for sol-gel chemistry, being either too reactive or unreactive [21]. Aluminum precursors in sol-gel chemistry are too reactive and require special complexing agents to reduce their reactivity [22], [23]. When aluminum and phosphate precursors are combined, their reaction results in precipitation or gelation, hindering the materials transparency. To date, there is little information on the synthesis of transparent and photopolymerizable AlP OIH materials.

In this work, we developed AIP OIH materials by the hybrid sol-bel approach. These materials are stable resins that can undergo photopolymerization, and be processed by VPP, to result in transparent hybrid materials. These materials' structure and properties were characterized in-depth using a different technique. Furthermore, we modelled the exposure profile of a custom-made VPP setup, which was further employed in the additive manufacturing of these materials. Lastly, we analyzed the optical properties of the additive manufactured elements to assess their optical homogeneity and the presence of anisotropies. A bibliography review concerning the main points related to this project, that is, additive manufacturing and its application in photonics, the technicalities of VPP process, and the hybrid sol-gel approach, are presented below.

Additive manufacturing (AM)

a. Definition and history

Additive manufacturing (AM), also known as three-dimensional printing (3DP), is an umbrella term encompassing different manufacturing techniques sharing the same layer-by-layer approach for fabrication based on a digital model, as shown in **Figure 1** [24]. Historically, the first AM technologies date back to 1800s, however it is widely recognized that the modern starting point of AM technologies was the patents filed in 1984s by Charles Hull, which started to be commercialized by the company 3D Systems stablished in 1986 [4]. In its early days, AM was better known as rapid prototyping (RP) because it was originally designed to allow the fast fabrication of prototypes and physical models required for product design. The evolution of AM as a proper manufacturing method was only possible due to the technological advances in printing, laser, and numerical control technologies, computer graphics, computer-aided design (CAD), and materials availability [4], [24]. AM platforms were able to print faster, cheaper, more accurate, and with a wider range of materials, leading AM to be slowly incorporated into the production chain of some industrial sectors. The field steadily grew with the application of new patents and foundation of new companies, stimulating research and development [4]. However, AM technologies were still expensive, because of intellectual property, and the low availability of personnel with know-how restricted widespread adoption of AM by the industry.

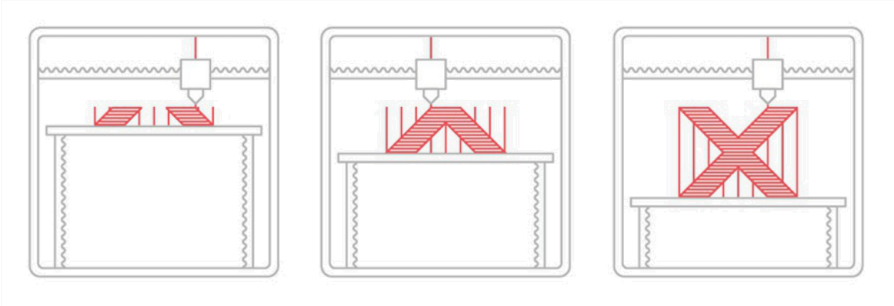

Figure 1. Layer-by-layer principle of a generic additive manufacturing method [25].

The boom of AM occurred in the 2000s, with 2007 being considered a milestone due to the expiration of many AM related patents. Numerous companies appeared and the domestic market became a hotspot, lowering the cost of AM platforms, resulting in a leap from 60 3D printers in 2007 to 23000 in 2011 marketed in the domestic market[4]. The easy access to AM platforms allowed different industrial sectors and research institutes to explore the applicability of AM in their fields. This is evident if we analyze the evolution of publications and patents in the last years as shown by the web of Science database and Espacenet ("additive manufact*" OR "3D print*" OR "rapid protot*"), and compiled in **Figure 2**. Today, the term DDM (*Direct digital manufacturing*) is already used, referring to the additive manufacturing process where the final product is entirely manufactured by AM techniques.

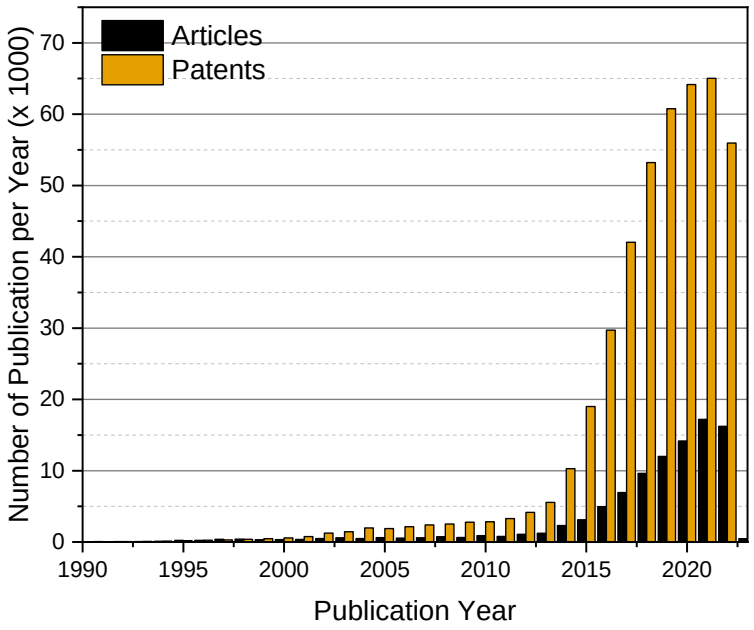

Figure 2. Research string ("additive manufact*" OR "3D print*" OR "rapid protot*") in Espacenet and Web of Science (Web of Science Core Collection database)

b. The AM process

A generic AM process is composed by four major steps, as illustrated in **Figure 3.** The first step consists in obtaining a digital tridimensional representation of the desired geometry`s or object`s surface. This is accomplished with CAD (*computer-aided design*) softwares, such as SketchUp®, and SolidWorks®, or though imaging techniques such as laser scanning and tomography. The design is saved as a STL file, which is the standard file format used by AM systems. This format describes the surface of an object as a collection of triangles in cartesian coordinates. The second step comprehends the manipulation of the STL file and slicing, which is done in a software provided by the own AM equipment manufacturer, or directly in the AM equipment. Adjustments such as position, orientation and size are made, and the object is sliced in numerous cross-section layers representing the printing instructions for each layer. The third step is the transference of the file to the equipment and the adjustments of the printing settings by the operator. The printing settings are related to the building parameters according to the type of AM equipment and it physical-chemical process responsible for the fabrication. The printing process starts, which is fully automated, and does not require any supervision. Once finished, the object is removed. The fourth step is post processing, which will depend on the application, which could include polishing, thermal treatment, rinsing and drying, depending on the AM technique.

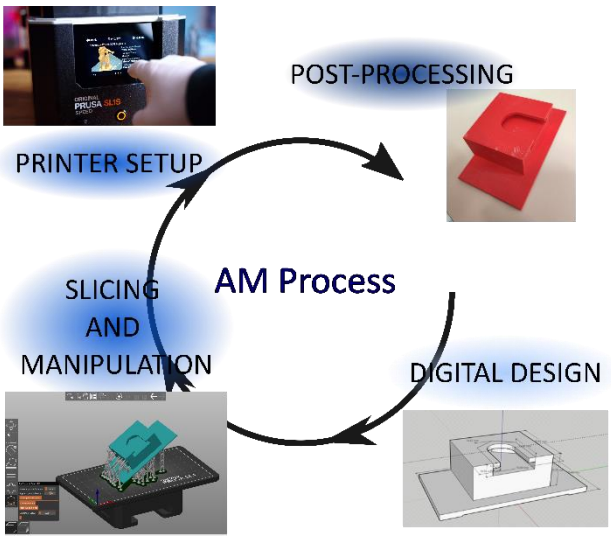

Figure 3. The main steps of a generic AM process.

c. AM and Industry

The importance of AM in the industry arises from the intrinsic limitations associated by traditional manufacturing, which encompasses formative (FM) and subtractive (SM) manufacturing methods. In FM methods, the final shape of the object is obtained by casting, blowing, or plastic deformation strategies, while in SM this is achieved by removing material from a raw workpiece[26]. A common problem with both methods is geometry constrains, making it challenging and requiring a large number of productive steps (and time) to achieve certain shapes. FM is an appropriate manufacturing method for mass produced goods, due to the high acquisition cost of the equipment and subsequent modifications. SM, on the other hand, is specially suited for small scale production of goods with high accuracy, however it suffers from low throughput, high material waste, and high cost. Ultimately, we lack a manufacturing method for fast and small-scale production of complex articles, at low cost and material consumption, which are the features of AM [27].

These limitations are a problem in face of Industry 4.0 concept, whose ultimate goal is to achieve a more efficient (material and energy consumption) fabrication process with real time feedback of custom-made products [28]–[30]. Industry 4.0 is centered in the real-time intercommunication between management and autonomous industrial equipment, so that production and decisions are decentralized. Many technologies such as artificial intelligence, robotics, and Internet of Things have been presented as enabler towards the concept. Not surprisingly, AM is also considered an enabler technology, because it solves the aforementioned problems, and has an innate integration with digital systems. Another advantage of AM is the fact that the final part is directly correlated to its digital drawing, allowing the part performance to be further analyzed using engineering softwares to assess the feasibility of the project, speeding up optimization interactions during fabrication process [24].

There is still a lot of research on the implementation of AM process in the context of Industry 4.0, since the concept is still under development. Nonetheless, AM already occupies a strategic position in the production chain of different industrial segments, especially for developed countries, since mass production lines have migrated to developing countries. [31]. Essentially, AM enables the fabrication of high aggregated value products, and is regarded as a disruptive technology regarding the design, production and marketing of new products. There is great enthusiasm around its potential, and it has been envisioned as the beginning of another industrial revolution [24]. It represented a USD 13.84

billion in 2021, with projections of a 20% per year growth, expecting to reach a USD 76.12 billion by 2030, forcing industry to rethink its processes, production chain and organizational structure [32].

The most successful case of AM application in industry is the fabrication of hearing aids. About 97% of hearing aids are fabricated by 3D printing, reducing from 40% to 10% the rate of return due to poor fitting at lower price [25]. Many industrial segments and companies are integrating AM into their production chain, such as aerospace, automotive [33], medical and dental, tooling, health and biosciences applications, education [34], drug release systems [35], food industry[36], [37] just to cite a few.

d. Families of AM techniques

There is a great variety of AM technologies available, which led to their grouping and categorizing based in different criteria, such as the type of material printed. The most adopted classification was initially introduced by the ASTM F2792-12a [38], later becoming ISO/ASTM 52900:2021 [39], based on the configuration of the equipment used and the physical-chemical process involved in the layer formation, grouping into seven process categories. A concise description of each category, its features, and additional information on the most representative techniques for each process category is presented below. The objective of this section is to brief the reader into the type of materials, printing resolution and surface finishing achievable by each process category in order to understand why some techniques are far more interesting for photonic applications compared to other. Reference literature is provided for additional information for each one of these techniques and categories.

- Binder jetting (BJT) typically works in a two-step process. First a layer of powdered material is spread in the build chamber, then, a liquid binding agent is selectively deposited on top of the powdered materials to form one of the layers. The process repeats multiple times until all layers are printed. **Figure 4** shows the typical scheme of a BJT AM system [40]. Sand, metals, and ceramics are the most common materials for BJT, with some limited work on plastics. BJT of sand is typically used for fabricating dies for metal casting. In the case of metals and ceramics BJT, additional thermal treatment eliminates the binder and allows sintering to consolidate the metallic or ceramic part [25]. The technique is low cost, with feasible layer thickness as low as 30 μm. The technique is also suitable for large objects (500 mm), however post processing is required to improve surface finishing and the high porosity. It displays high printing speeds (up to 200 $cm^3.min^{-1}$) [40].

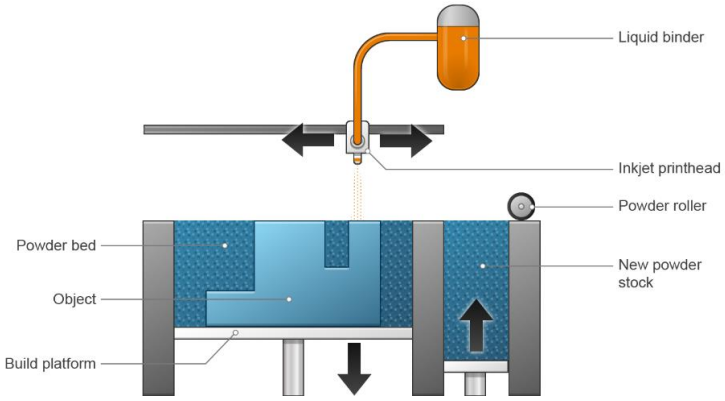

Figure 4. Typical scheme of a BJT additive manufacturing system. Extracted from https://make.3dexperience.3ds.com/processes/material-jetting on 10th of March 2023.

- Directed energy deposition (DED): a material (mostly metals), in the form of a filament or powder, is deposited and melted simultaneously by means of a concentrated source of thermal energy, such as a laser beam (-LB), electron beam (-EB) or electric arc (-Arc), following the ISO/ASTM 52900:2021 nomenclature [39]. DED techniques are grouped according to the type of feedstock employed (powder or filament) and the thermal source[41]. A typical DED AM system is presented in **Figure 5**. Resolution in the XY and in the Z axis depends on the specifications of each equipment, however the minimum values reported in literature are of 380 and 200 µm, respectively [41]. The technique suffers from poor surface finishing, with typical surface roughness higher than 25 µm.

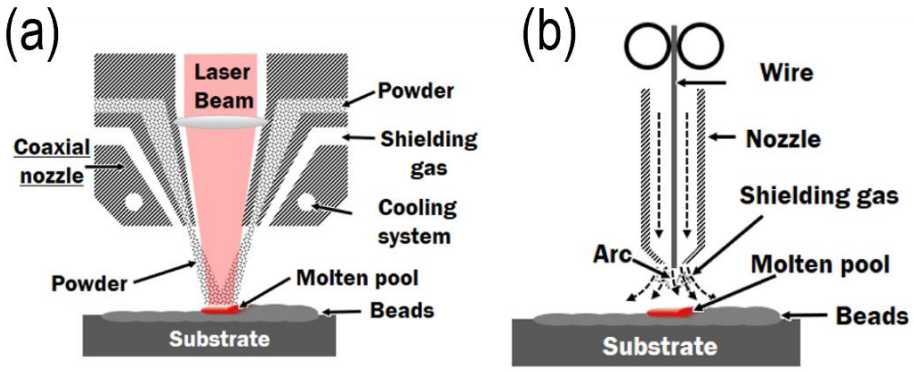

Figure 5. Typical schemes of a DED additive manufacturing system for a LAM (Laser Additive Manufacturing) in (a) and a WAMM (Wire and Arc Additive Manufacturing) in (b) [41].

- Material extrusion (MEX) is the most representative AM technology, being widely accessible for all commercial segments, ranging from a hobbyist to industrial production. These processes rely on continuously extruding the printing material through a nozzle, allowing the selective depositions of the

material on the building plate[24]. The main difference between the different AM techniques integrating MEX is the method for bonding the material after extrusion, which can be through a chemical reaction (-CRB) or a thermal reaction (-TRB), following the ISO/ASTM 52900:2021 nomenclature [39]. A typical MEX AM system is showed in **Figure 6**. The most well-known MEX technique is the fused deposition modelling (FDM), where a polymeric filaments is liquified and solidified by controlling the temperature. Direct Ink Writing (DIW) is another well-known method, where the feedstock material is either a liquid or gel, which solidifies upon light exposure, temperature control or low shear rate. MEX is typically used for printing polymers such as acrylonitrile-butadiene-styrene (ABS), poly caprolactone (PLC), polycarbonate (PC), and poly lactic acid (PLA) [24], [25]. Printing resolution is defined by the nozzle diameter, which is around 100 μm for most commercial equipment. MEX technologies are quite inexpensive, being able to print large volumes of material (1 m^3) but have limited dimensional accuracy and poor surface finish[42].

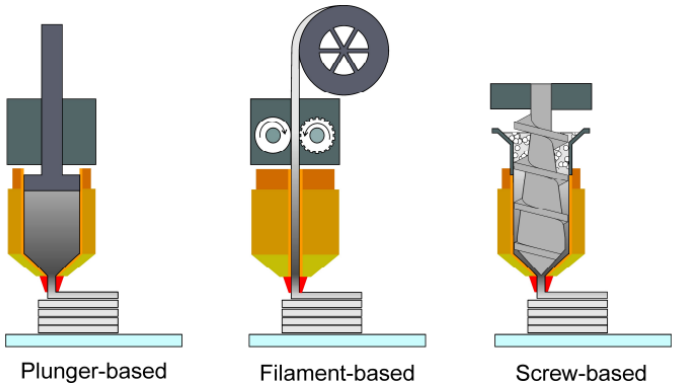

Figure 6. Typical scheme of a MEX additive manufacturing system employing different methods of extrusion. [43]

- Power bed fusion (PBF) is based on the selective fusion/sintering of particulate matter using a thermal source, typically a laser beam (-LB), electron beam (-EB), or infrared light (-IrL), following the ISO/ASTM 52900:2021 nomenclature [39]. In PBF, a layer of particulate raw material is deposited in the printing chamber, which is then scanned with the thermal source, forming that layer. A second layer of particulate material is then deposited, and the process repeats. A typical PBF AM system is presented in **Figure 7**. PBF is a widespread AM technology due to its low cost/part quality relationship compared to other AM process[24]. Furthermore, PBF is compatible with a wide range of materials, such as metals, ceramics, glasses, and polymers, and unused raw materials during one printing process can be easily reused [44]. The printing resolution of PBF process depends on the type of

material, the physical or chemical process associated, and the heat source. Typically, resolution on the order of 100 μm is easily achievable, however the printed parts have high porosity [24].

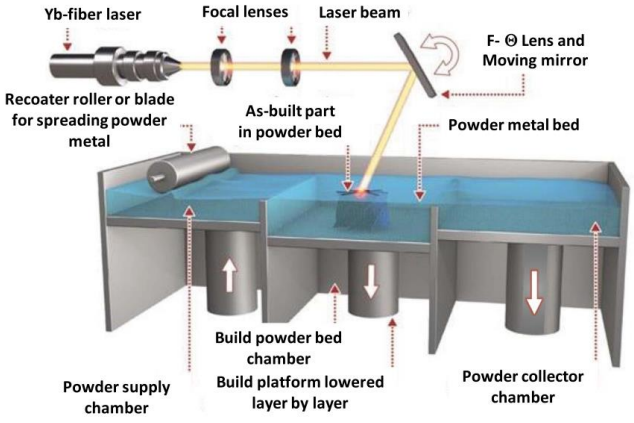

Figure 7. Typical scheme of a PBF additive manufacturing system. [45]

- Sheet lamination (SHL): process of building an object from the joining of plates of the desired material by means of an adhesive joining (-AJ) or ultrasonic consolidation (-UC), following the ISO/ASTM 52900:2021 nomenclature [39]. There is little literature on this AM category, and the technology is still in development. Most companies which were formed to commercialize SHL techniques have gone out of business or abandoned this technology. **Figure 8** shows a typical SHL AM system.

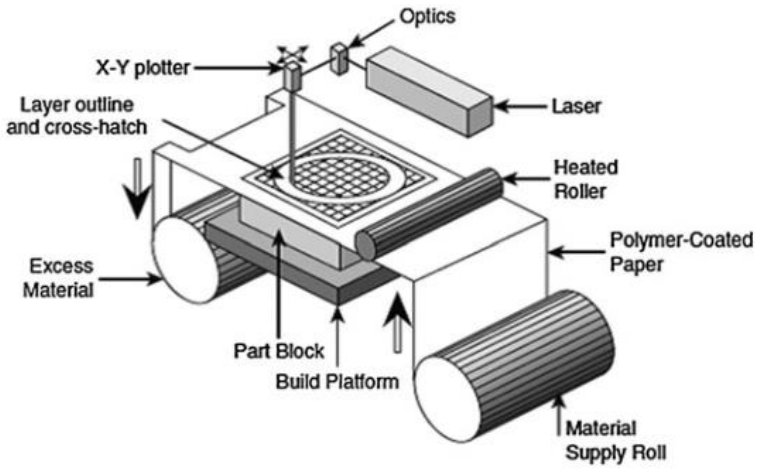

Figure 8. Typical scheme of a SHL-AJ additive manufacturing system. [24]

- Material jetting (MJT) works by selectively depositing droplets of raw material to form a layer, in a similar fashion as paper inkjet printer, followed by material consolidation, which can be achieved

by curing under ultraviolet light (-UV), by a chemical reaction (-CRC) or thermal reaction (-TRB), following the ISO/ASTM 52900:2021 nomenclature [39]. The materials employed are typically photopolymers, which are exposed to UV light once each layer is printed. A typical MJT AM system is presented in **Figure 9**. MJT is known for its high-quality printing, being able to print thin walls with very low staircase effect (visible layers). The technique allows resolution in Z axis as low as 16 µm [46]. In addition to polymers, developments for printing metals using this technique are already commercialized. This process has excellent surface finish, but its cost is high, and the materials development can be quite complicated due to strict rheological properties required for droplet formation [47].

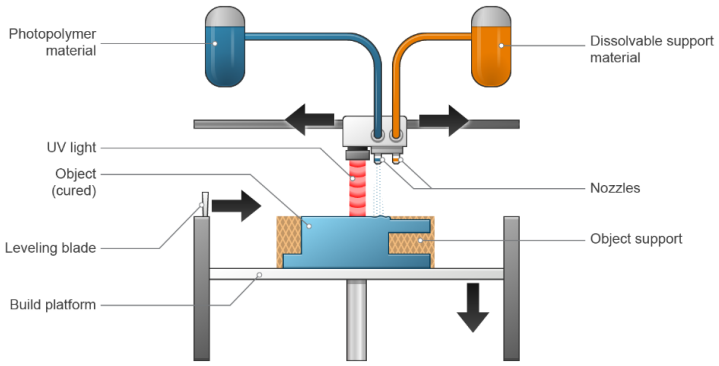

Figure 9. Typical scheme of a MJT-UV additive manufacturing system. Extracted from https://make.3dexperience.3ds.com/processes/material-jetting on 10th of March 2023.

- Vat photopolymerization (VPP) refers to a family of 3DP technologies based on the selective photopolymerization of a resin through localized light exposure (typically UV light) [48], [49]. The light exposure can be achieved by means of a guided ultraviolet laser (-UVL), ultraviolet light passing through a mask (-UVM) or by exposure to light emitting diodes (-LED), following the ISO/ASTM 52900:2021 nomenclature [39]. There a different VPP setups, however the most common is the stereolithography (SLA), which employs a UV laser as a light source. Examples of VPP AM systems are presented in **Figure 10**. These techniques excel in spatial resolution, printing time and surface finishing compared to other 3DP technologies, allowing the fabrication of objects with numerous fine features/structures[27], [50]. For instance, most commercial platforms are able to print features down to 25 µm, meanwhile high spec commercial printers and multiphoton polymerization setups can reach 10 µm and 200 nm resolution [24], [25], [27], respectively. Only methacrylate and epoxy-based polymers are compatible with VPP approach, however in the last years there has been considerable effort to print ceramics and glasses as well. It is one of the most dimensionally accurate AM techniques,

with great surface finish and ability to print highly detailed structures [24], [25]. Because of these characteristics, vat photopolymerization techniques are the most interesting for application in photonics, since surface quality and printing resolution are key parameters for such field[5].

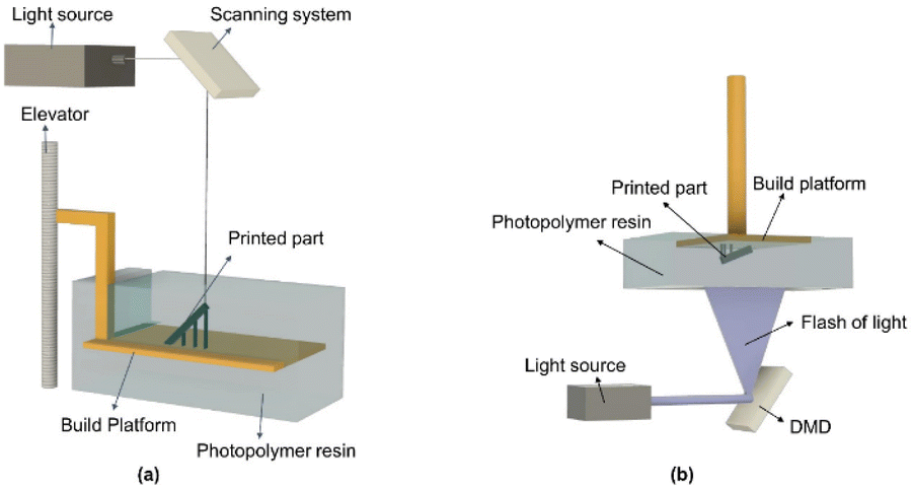

Figure 10. Typical scheme of VPP-UV and VPP-UVM additive manufacturing system in (a) and (b), respectively. [51]

e. AM for photonic applications

The fabrication of photonic devices by traditional manufacturing methods has a series of drawbacks, such as cost-intensive, low customizability, low reproducibility, bidimensional construction, lack integration and geometrical constrains [5], [52]. These factors are considered the major challenges to overcome concerning the fabrication of integrated photonic circuits [53], [54], as well three-dimensional lenses and waveguides at microscale/nanoscale [55], [56]. AM is considered a promising manufacturing technique for photonics[5], [57] because it theoretically addresses all the issues associated to traditional manufacturing methods. Similar to other fields, AM has experienced rapid growth in the fabrication of optical devices in the last 20 years.

To date, the most relevant AM technology families employed in optics manufacturing are the MEX, MJT and VPP [52], [58]. Fused deposition modelling (FDM) and Direct Ink Writing (DIW) are the most important concerning the MEX family. As previous mentioned, these techniques are inexpensive and can fabricate large volumes, however high surface roughness and low printing resolution are critical issues hindering their use in microscale optics, and so far, have been only used in the fabrication of THz optics [59]–[61], preforms for optical fibers [7], [62]–[64], and illumination and imaging applications at macroscopic dimensions[65]. Inkjet printing is the most relevant in the MJT

technologies, being adopted in the fabrication of lenses and micro-lenses array. Despite its good optical quality and precision, the technique is limited in printing volume and materials availability, since the development of new materials for Inkjet is challenging, having strict rheological requirements to achieve appropriate resolution. Lastly, VPP-MPP, VPP-UV and VPP-UVM are most important technologies from the VPP family, showing high resolution, and good surface quality. The field has expanded unevenly across VPP technologies, with VPP-MPP being considered matured, while VPP-UV and VPP-UVM are still on their infancy [58]. The main drawback of VPP-MPP has been the printing volume and speed, which has driven research to explore VPP-UV and VPP-UVM as alternatives for printing macroscopic volumes of material, with little compromise to surface quality.

AM has found successful commercial application in the manufacturing of lenses and lenses arrays by companies such as Luxexcel®, Nanoscribe®, and Multiphoton Optics®. Luxexcel® uses a patented MJT platform based on Drop-on-Demand (DoD) technologies to fabricate lenses for smart glasses [66]–[69]. The main advantage of using AM in their case is the easy integration of the lenses with electronics, projection screens, waveguides and LCD displays. Nanoscribe®, and Multiphoton Optics® have developed MPP platforms for microfabrication, with applications in micro-optics, microfluidics, micromechanical systems and integrated photonics, with on-fiber and on-chip printing. Academic research is very rich in terms of applications of AM in photonics[70], [71]. Overall, AM has been employed in the fabrication of waveguides [72] and fiber structures, lenses and lens arrays [73]–[75], grating and diffraction structures [76], photonic crystals, phase modulation elements, SERS (surface enhanced Raman scattering) sensors, metasurface fabrication, solar cells, LEDs [77], optical couplers [78], and many other applications Particularly, the additive manufacturing of optical fibers and preforms has been a topic of promising research in the last 10 years. As a few milestones, Pereira et al [79] directly printed optical fibers in 2014, Canning et al.[63] drew an optical fiber from a 3D printed preform in 2016, a step index 3D printed preforms has been reported in 2016[7] and non-circular core preforms in 2017 [62]. Furthermore, optical fiber with Bragg gratings[80], photonic crystals[61], [81], [82] and negative curvature cores[59] have been demonstrated.

Despite the promising results reported in the literature, keys problems have been identified in the last years. First, the fabrication of optical devices must have low tolerance concerning shape accuracy and surface roughness. Second, the range of materials available for AM is quite limited. Third, most techniques are currently incompatible with multi-material fabrication. Lastly, the fabrication of individual optical components has been widely reported, however its integration in optical devices must

be further explored [52], [58]. As prior mentioned, MPP technologies are the most advanced in terms of optical devices fabrication, since it can easily reach the surface roughness and shape accuracy requirements, allowing fabrication in arbitrary surfaces. However, this method can only manufacture small volumes, and using only one type of material. Conversely, larger scale manufacturing methods suffer from lower surface quality and shape tolerance. Addressing these issues would allow the one-step fabrication of dense multi-component optical devices, with arbitrary refractive and light guiding geometries combining imaging, detection, actuation and signaling in one single device [58].

f. New materials for AM of photonics

There are many challenges to allow widespread application of AM in the fabrication of photonic devices, and the lack of a variety of materials is one of the main issues. All the above-mentioned examples in the literature concerning AM in photonics are based on mature 3DP materials (polymers, metals and polycrystalline ceramics) [24]. New strategies to print photonic materials in the last 15 years have been studied with emphasis in glasses and most recently in organic-inorganics hybrid (OIH) materials.

Despite the intense use of glass in optical applications, this was one of the last materials to be explored in AM due to the lack of a convenient and inexpensive printing approach or technology [83]. The additive manufacturing of inorganic glasses can be divided in a direct approach, when the raw material is the glass itself, or an indirect, when composite material or glass precursor is printed, and then heat treated to yield final the glass [84]. Historically, the first attempts for AM of glasses were direct approaches, such as fused deposition modelling (FDM) using glass rods [85]–[87], and selective laser melting of glass powder [88] or glass filament [89], however these approaches did not achieve good optical quality and had low resolution. The first indirect approaches relied on the lithography of composites polymer/glass powder [90], [91], however the residual porosity hindered the materials transparency. The first successful approaches that could couple resolution and surface quality comprehended the use of a MPP process with a photocurable SiO_2 nanoparticles composite. In 2018, improvements were made by Nguyen et al. [92] using a DIW (direct ink writing) process with a silica-titania sol-gel. In both cases, post processing through thermal treatment yielded a transparent glass with resolution of hundreds of microns. The most recent strategy for AM of glasses was reported in 2018 by Cooperstein et al[17] using a photopolymerizable resin obtained from a hybrid sol-gel route employing alkoxysilane precursors, yielding a transparent OIH material which could be further heat

treated yielding a glass. To date, this approach have been the only one able to reach high printing accuracy and excellent surface quality [93], and is the foundation for all other publications in the area. Further application of these works in photonics encompasses the additive manufacturing of a silica preform [64].

The primary disadvantage of AM of glasses is thermal treatment at high temperature required, which is not compatible with electronics in order to achieve integrated electro-optical devices. As an alternative, organic-inorganic hybrid materials can be processed at low temperature, and have their optical properties tuned to meet the requirements of active and passive optical devices operating from UV (ultraviolet) to NIR (near-infrared) spectrum [5], [8], [9], making them excellent candidates for integrated active and passive photonic structures [5], [8], [10]–[12]. OIH materials have found numerous applications in photonics such as waveguiding, sensing, lenses, photonic crystals, LEDs and white light sources, random lasers, solar concentrators, luminescent thermometry, photochromic windows, photovoltaics, non-linear optics, plasmonic, electro-optical devices and many others [8], [94]. Despite the wide interest of OIH materials in photonics, the literature available on their AM for photonics is limited to the fabrication of lenses [95]–[114], waveguides [115] and photonic crystals [116]–[120] using alkoxysilane derived materials, with special emphasis on the commercial resin SZ2080 (zirconia-silica sol-gel). Other examples include the use of perovskite/PCL composites for additive manufacturing of LEDs [121], and polymer/VO_2 composites for solar cells [122].

There are different approaches for synthesizing OIH materials, however the hybrid sol-gel route is the most promising one concerning OIH materials for additive manufacturing of photonics. The main advantage of the sol-gel approach is the mixing at molecular level of organic and inorganic groups at room temperature, hindering phase segregation and being inherently compatible with photopolymerization [123]. However, the design of a transparent OIH requires deep understanding of the chemical reactions during synthesis conditions, since unproper control can results in opaque or translucid OIHs [124], [125]. Most works have been limited to silane chemistry since its chemistry and synthesis conditions are easy to control and is well established in literature[123]. Successful examples of OIH materials with good optical quality for photonic application using VPP-UV have been reported for at least 20 years as waveguides and lenses on ORMOCERs/ORMOSILs (i.e. silane hybrid sol-gel) [118], [126]–[129], but no other compositions have been demonstrated.

Vat-photopolymerization (VPP)

a. Fundaments

The VPP was patented by Charles Hull in the late 1980s and is considered to be the first AM technology. As briefly described, VPP is based on the selective exposure of a light-curing resin to UV or visible light radiation, resulting in localized photopolymerization. To date, VPP is represented by three main techniques, named stereolithography (SLA), digital light processing (DLP), and multiphoton polymerization (MPP), known as VPP-UV, VPP-UVM, and VPP-MPP according to ISO/ASTM 52900:2021 [39]. These techniques differentiate according to the light source employed, and the method to achieve selective exposure. VPP-UV, VPP-UVM, and VPP-MPP use a UV/VIS frequency multiplied laser, a UV/VIS lamp, and an infrared femtosecond laser, respectively, as light sources. The layer construction is accomplished by laser scanning in VPP-UV and VPP-MPP by either moving the object being printed or the laser spot by aid of galvanometer mirrors. VPP-UVM uses a digital micromirror device (DMD) or a liquid crystal display (LCD) to create a mask for each transversal section of the object, printing an entire layer in a single process [24], [25]. The typical setups for VPP-UV and VPP-MPP are illustrated in **Figure 11** (a). The main difference between the two setups is the polymerization volume, since the polymerization in VPP-UV occurs through a linear absorption and all the exposed volume undergoes polymerization. In opposition, the VPP-MPP is based on the multiphoton absorption, which is a non-linear process, with low efficiency, meaning that the polymerization is confined to the focal spot of the irradiation. These differences are illustrated in **Figure 11** (b). Lastly, a setup for VPP-UVM is illustrated in **Figure 11** (c).

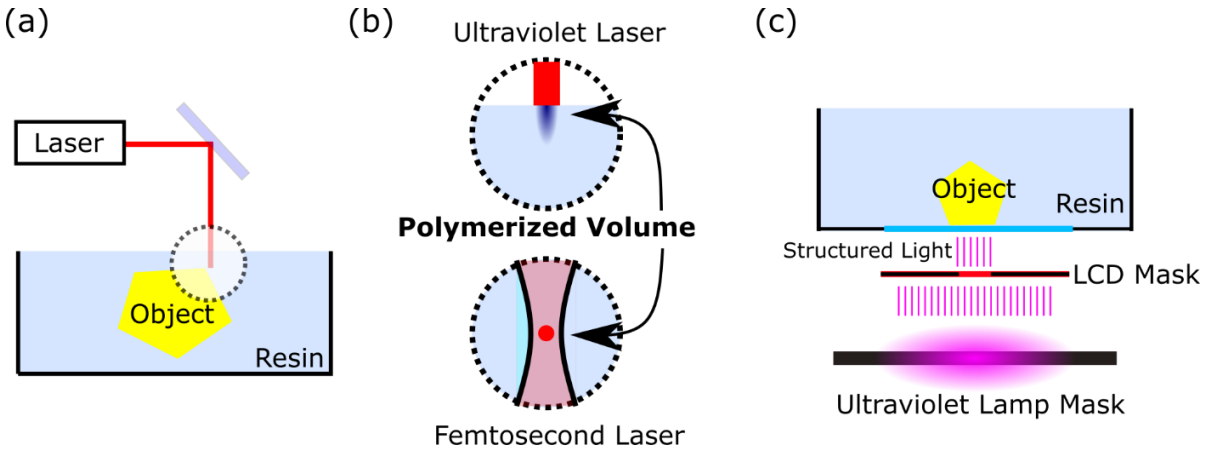

Figure 11. Typical setup for (a) VPP-UV and VPP-MPP, and the difference between their polymerization volumes in (c). A typical VPP-UVM setup is presented in (c).

In the VPP-UV and VPP-UVM process, the object is printed on top of a moving platform, called the build platform. The direction of the platform's movement defines if the equipment has a bottom-up or top-down approach, if the platform moves upwards or downwards during printing [24], as shown in **Figure 12** (a). These differences determine the layer construction direction, and the position of the optical elements in the equipment, which will introduce limitations in terms of build volume (maximum size of printable objects) and might require different printing strategies.

In the top-down configuration, the light source is positioned above the platform. The build platform stays submerged in the vat with a layer of resin between the build platform and the air. Once that layer is printed, the build platform submerges another one layer, allowing the next layer to be printed on top of the previous one. The layer of resin thickness is a user-defined parameter, and it correlates to the Z direction resolution. A delay time is introduced between each layer to homogenize the resins surface, which can be assisted by some type of recoating system, such as a blade or a vat stirrer. Surface homogenization is a key aspect since regions close to the exposed areas suffer from partial photopolymerization, causing variation of density and viscosity (evidenced by a tacky aspect). Thus, heterogeneities are carried to the next layer [130], which can lead to delamination (layer adhesion failures), voids, dimensional distortion, and poor surface quality [24]. Such defects are more prone to occur when printing hollow structures [131]. The need of recoating and surface homogenizing increases the printing time since the process must be slow, causing minimal disturbance on the resin's surface [132]. These steps (print-submerge-homogenize) repeats until the entire object is printed and sank in resin.

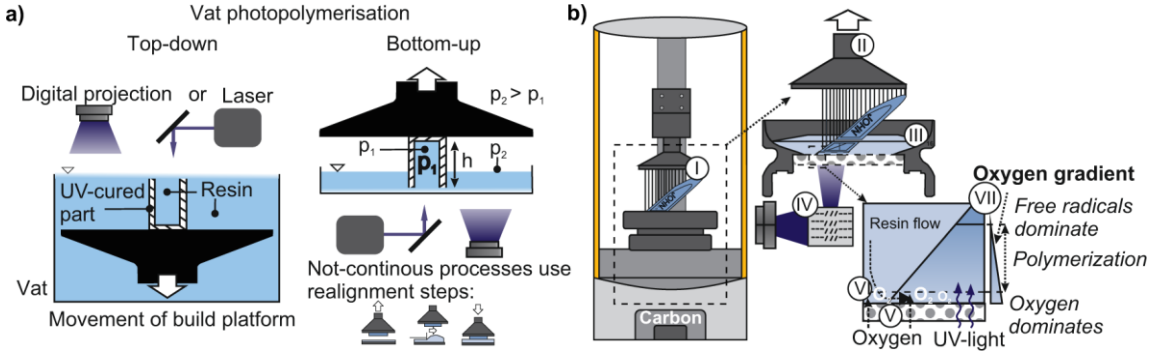

Figure 12. Bottom-up and top-down VPP setups in (a), and continuous liquid interface production (CLIP) setup in (b). [133]

Conversely, the optical setup is located below the vat in the bottom-up configuration, which requires the bottom of the vat to be transparent to the irradiation wavelength. In this setup, the polymerization takes place in the resin confined between the build platform and the bottom of the vat. Similar to the top-down setup, the space between the platform and the vat is a user-defined parameter which defines the Z resolution. Once the exposure occurs, the platform moves upwards, and a new layer is printed, with no need for the homogenization process. When the printing concludes, the object is entirely out of the resin tank. Most commercial equipment (both VPP-UV and DLP) employ the bottom-up approach because of its simplicity. Currently, there is a new generation of bottom-up VPP systems named continuous liquid interface production (CLIP), where the bottom of the vat is permeable to O_2, creating a dead zone where no polymerization occurs, as shown in **Figure 12** (b). In this process, the platform is constantly drawn instead of printing layer-by-layer, allowing faster printing and smother details. The bottom-up approach is very convenient for small objects, however printing larger parts can be challenging due to gravity and surface tension, which can cause detachment from the platform, leading to failure [24], [25]. Special strategies are also required for printing high surface area objects, such as tilting the object to reduce the surface area of each layer [25]. In these cases, a top-down approach is preferred, however the vat size limits the build volume and the homogenization process significantly increases the printing time [24].

Printing parts using DLP and VPP-UV require the use of supporting structures. These structures anchor the object to the platform and provide mechanical support for overhanging features. Furthermore, supporting structures reduce the warping caused by direct adhesion of the printed part to the platform. Most commercial platforms have an in-built function to add these supporting structures to the digital drawing, however the planning and positioning of support structures is also part of the design process, because they must be removed during post-processing. A build platform is not required in the case of VPP-MPP, because the part is printed directly inside the resin, however, it requires a support structure for fixing the part during the process [24].

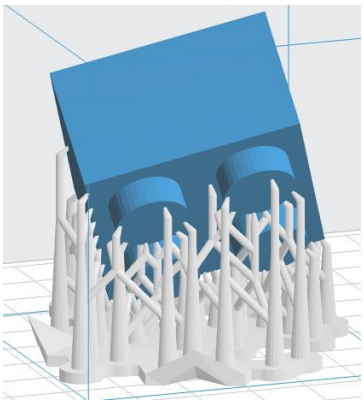

Figure 13. Drawing of support structures overlaid with the digital design of the object to be printed [133]

The absence of a scanning pattern was one of the main issues in the early days of the VPP technique [24]. The photopolymerization process is associated to shrinkage, creating localized stresses that can result in warping and cracking. The laser scan pattern is a fundamental aspect of VPP-UV and VPP-MPP, because it controls the distribution of these stresses and adhesion between layers. In the beginning, a trial-and-error approach was employed until acceptable results were achieved, which resulted in low success rate. The first scan pattern introduced into the market was the WEAVE, in 1990, where a mesh is created by fabricating one layer by scanning lines parallel to one axis, and the following layer by scanning lines in the perpendicular axis. The scan direction was kept constant between two layers, and it drastically improved the printing quality and success rate. Despite the improvements, deformation problems were still frequent, which originated the STAR-WEAVE pattern in 1991 [24], solving virtually all problems of the previous technique, by alternating the scanning direction from one layer to another and intertwining the layers, as illustrated in **Figure 14**. With the advent of epoxy-based resins, the ACES pattern was introduced to achieve better accuracy and higher polymerization given the slower kinetics associated to these new resins. The ACES pattern is actually a collection of different scan patterns, that give more control of the printing process to the user [24].

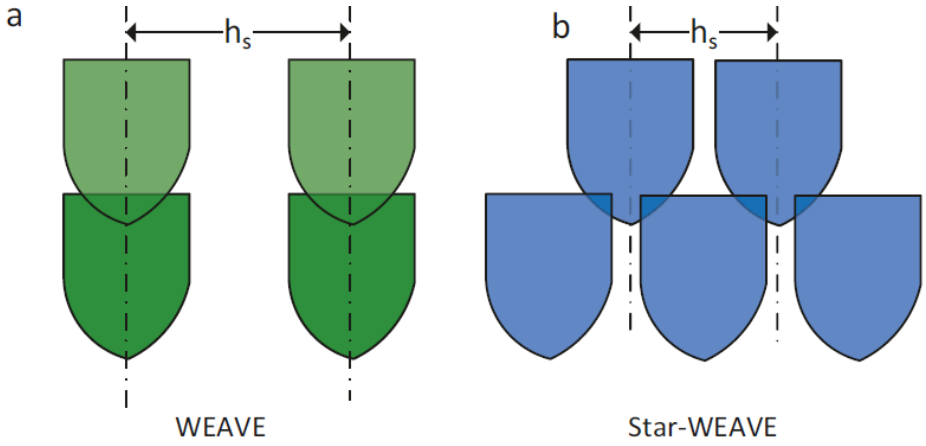

Figure 14. Positioning of each line scan for two layers using a WEAVE and Star-WEAVE laser scan pattern. [24]

b. The laser-resin interaction

Modeling the laser-resin interaction enables the selection of optimal exposure conditions to achieve the desired part/object, because the platform vertical movement must match the layer thickness. The Jacob`s work curve is a widely adopted mathematical model describing the relationship between energy dose (E_{max}) and the thickness of the cured layer, named cure depth (C_d), as shown in Equation 1 [24], [134], [135]. The model was derived in the earlies 60s by describing the light penetration using the Beer-Lambert law with a characteristic penetration depth (D_p) value, and a laser with gaussian profile scanning at constant speed. The model assumes the existence of a critical energy value (E_c) where the resin reaches a gel point [134], [135], and behaves like a solid.

$$C_d = D_p \ln \frac{E_{max}}{E_c} \tag{1}$$

E_{max} is the peak exposure and is calculated from Equation 2.

$$E_{max} = \sqrt{\frac{2}{\pi}} \frac{P_l}{W_o V_s} \tag{2}$$

where P_l is the laser power, V_s is the laser scanning speed and W_o is the beam diameter.

Experimentally, one measures E_{max} (laser intensity) and C_d, and fits the data to extract the D_p and E_c parameters, which are intrinsic to the resin, wavelength, and exposure conditions studied [24]. These parameters allow the resin in to be printed in any other VPP equipment operating with the same laser wavelength, power and exposure conditions employed. Most VPP-UV system manufacturers,

however, lock the exposure setting on their equipment so the printer can only fabricate with the manufacturer's resin. In addition, the Jacobs work curve parameters for most commercial resins are hardly available. Reference parameters for commercial resins were studied by Bennett in 2016 [136], showing a remarkable variation on E_c and D_p parameters from product to product, as shown in **Table 1**.

Table 1. Typical E_c and D_p values for commercial VPP resins measured at 365 and 405 nm. [136].

Resin	D_p (μm)		E_c (mJ/cm^2)	
	365 nm	405 nm	365 nm	405 nm
PR48®	42	53	18.3	6.3
VeroWhitePlus®	43	145	0.7	1.9
Formlabs Clear®	146	192	5.2	1.,6
TangoBlackPlus®	95	151	2.4	4.1
VeroClear®	186	568	2.1	6.9

The Jacob`s work curve model oversimplifies the photopolymerization reaction because its only assumption concerning the photochemical process is the existence of a critical energy parameter. This assumption implies that the photopolymerization is a time independent process, and that the gel point is a well-defined parameter. This is not true because the polymerization is a highly dynamic process with numerous parallel reactions [137], [138], and affected by many factors such as the dependence of kinetic constants on light intensity [139], presence of scattering centers [140]–[144], diffusion of active centers and monomers [145], [146], photobleaching of photoinitiator fragments [147], oxygen inhibition [146], [148], heat diffusion [149], self-focusing effects [150], polymerization shrinkage and cyclization reaction [151]–[153], and the gel effect [137], [138], [154], [155]. Consequently, the work curve model yields penetration depth and critical energy values which are valid only for the applied exposure conditions. Nonetheless, the model is widely adopted due to its simplicity.

The lack of chemical fundaments on the equation was addressed by Lee et al.[156], who derived a work curve based on steady-state models to describe the photopolymerization kinetics, obtaining Equation 3 and 4:

$$Ec = \frac{\alpha\beta}{\sqrt{[PI]}} \tag{4}$$

$$Dp \propto \frac{1}{\epsilon[PI]} \quad (5)$$

Where α and β are a combination of photochemical and processing parameters, respectively, and ε is the molar absorptivity. However, their model disregards polymerization inhibition effects before reaching steady state conditions and does not address how laser power affects the works curve, since the polymerization rate is dependent on the light intensity by a power law [157]. Further addressing such problem, Uzcategui et al [139] proposed a modification on the work curve in the form of Equation 6

$$C_d = \frac{Dp}{n} \ln \frac{t.I^n}{Ec} \quad (6)$$

where n is an exponential factor between 0 and 1. Thus, the authors proposed that both polymerization rate dependence on light intensity and the induction period can be expressed by a single exponential factor adjusting the intensity parameter, however we highlight that Wydra et al.[158] have demonstrated that the main hypothesis supporting their modified model is not accurate because of the bimolecular termination mechanism. Nonetheless, their model can still provide good fitting to experimental data.

c. Photopolymerization

Photopolymerization refers to a photoactivated polymerization process initiated by a photoinitiator, which are molecules that, when exposed to a proper range of wavelength, undergo an electronic transition, yielding an unstable excited singlet or triplet states [159]. The excited molecule undergoes scission, generating species that can start the polymerization process. Available photoinitiators can generate cationic species, which can initiate the polymerization of epoxy and vinyl-ether functional groups, or radical species, which can initiate the polymerization of methacrylate and thiol-ene groups [160].

The free-radical photopolymerization mechanism for acrylate-based monomers is presented in **Figure 15**. When irradiated, the photoinitiator undergoes photo-scission generating radical species, which are highly electrophilic and are promptly attacked by the electronic density of the C=C bond present in the acrylate. The electrophilic attack breaks the double bond and forms a new bond between the radical species and one of the carbons from the C=C bond [160]. The second carbon atom (which did not form new bonds upon scission) becomes a radical species susceptible to electrophilic attack

from a different acrylate group [159]. This new radical is defined as the propagating or active center. This chain of reaction from the irradiation to the formation of the active center is defined as the initiation step in the photopolymerization, which is then followed by either propagation, or termination steps. Propagation refers to the chain reaction of the active center with another monomer, adding a new monomer to the growing molecule and transferring the active center to the newly added monomer. This reaction repeats multiple times, resulting in a polymeric chain [161].

The free-radical polymerization process ends with the termination step, by deactivating the active center. There are multiple reaction pathways, but the most important ones are recombination, disproportionation, primary recombination, and oxygen inhibition [161], [161], [162]. The first three comprehend the reaction of two active centers, while the latter consists in the reaction of one active center with a radical-scavenging molecule (O_2). In recombination, the two active centers form a covalent bond between the two growing polymeric chains, annihilating the radical centers. In disproportionation, one of the active centers abstracts a hydrogen from the second active center, annihilating the first active center. Then, the second active center forms a double bond with carbon that had its hydrogen abstract, resulting in a polymeric chain with a unsaturation. Primary recombination is similar to the recombination mechanism, however one of the active centers is a free-radical generated from the photoinitiator instead.

Oxygen inhibition comprehends the reaction of a radical species (active center or primary radical), with molecular oxygen, resulting in active center that has very low reactivity [163]. Oxygen inhibition is a highly efficient reaction, which creates an induction time where no polymerization occurs, until molecular oxygen is depleted, which is typically represented by a decrease in concentration of three-orders of magnitude (from ~10^{-3} to ~10^{-6} mol.L^{-1} [164]). Oxygen inhibition plays a major role in VPP top-down approach since the resin`s surface is saturated with O_2, leading to incomplete and inefficient polymerization, which can cause printing defects. To overcome such problem, an excess of photoinitiator is employed, so that all molecular oxygen is quickly depleted.

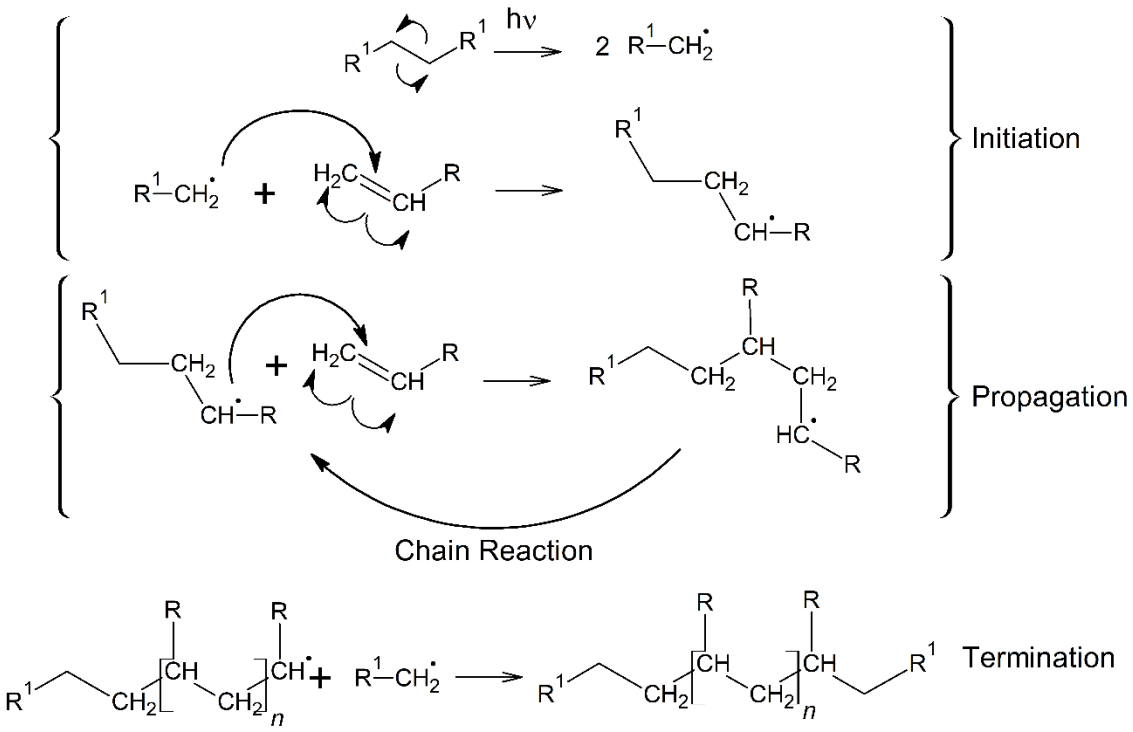

Figure 15. Typical radical polymerization reaction steps.

The cationic photopolymerization of epoxy and vinyl ether monomers is presented in **Figure 16**. Cationic photoinitiators are typically iodonium salts that undergo photo scission, releasing a non-nucleophilic anion [160]. There are many proposed reaction pathways following the formation of the anionic specie [159], [163], however the most common path is the hydrogen abstraction from monomer or solvent molecules, forming a super-Bronsted acid [165], that is a proton donating species. The proton is transferred to the heteroatom in the epoxy ring/vinyl-ether, linearizing the epoxy ring or promoting the scission of the double bond in the vinyl-ether, resulting in a carbocation species [159], which becomes the active center. The reactions from irradiation to the formation of the carbocation comprehends the initiation step. Similar to free-radical photopolymerization, initiation is followed by either propagation or termination steps. In propagation, the carbocation reacts with the heteroatom of other monomers, forming a covalent bond and transferring the active center to a new monomer [160]. The chemical pathways for termination are different compared to free-radical photopolymerization because it typically occurs by rearrangement with the counter anion. Other processes such as hydrogen abstraction, disproportionation, recombination or chain transfer reactions [160] do not effectively terminate the reaction, but only stop the growth of that polymeric chain, while generating a

new active center. A fundamental difference between cationic and radical polymerization is that inhibition of cationic polymerization occurs by nucleophilic attack of species such as water [159].

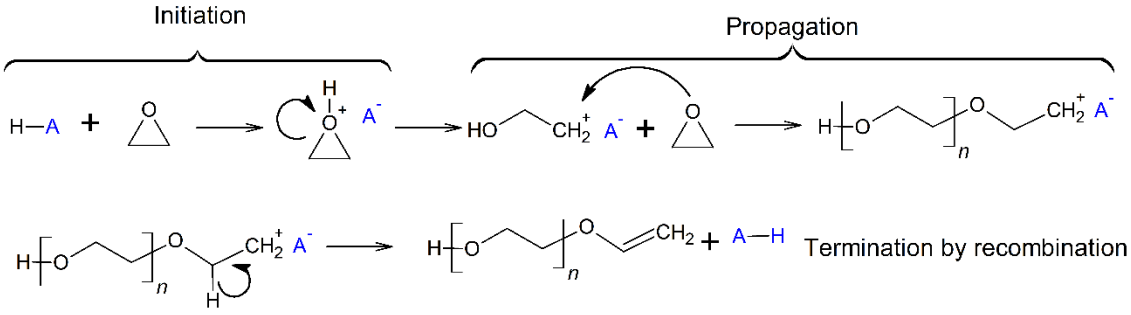

Figure 16. Typical photopolymerization mechanism for epoxy polymers.

The polymerization of resins for VPP is a very complex phenomenon, because the Trommsdorff–Norrish effect, also known as gel effect [137]. The gel effect refers to the autoacceleration and autodeacceleration of the polymerization reaction due to the formation of a three-dimensional polymeric network and entanglement of polymeric chains, restricting molecular mobility. Polymeric chains in solution tend to coil, forming primary gel particles, favoring intra-particle over inter-particle polymerization as the active centers are much closer to unreacted monomer species in the same chain [137], [155]. In this case, the propagation reaction is favored while the termination reaction is hindered, since the latter involves the reaction of two polymeric chains (which have far less mobility) while the first involves one polymeric chain and one monomer, which can easily diffuse through the medium. This leads to the autoacceleration behavior, that is, a remarkable increase in the polymerization rate. The second phase of the gel effect takes place when the network percolates through inter-particle polymerization, hindering segmental mobility and monomer diffusion, slowing down the propagation reaction. This is the autodeacceleration behavior, and results in incomplete polymerization [137], [138], [166].

Resins for VPP require a large concentration of multifunctional monomers, meaning that the formation of a three-dimensional network occurs at very early stages of polymerization. As a consequence, the gel effect manifests at very early stages during the polymerization process, and the polymerization kinetics change dramatically as the reaction progresses. Furthermore, the gel effect is based on the micro heterogenous nature of the polymerization reaction, which results in a polymeric micro-heterogenous structure as well. Thus, modelling the photopolymerization process is quite challenging, despite the simplicity of the polymerization reaction.

d. Resins for VPP

A resin for VPP is composed by multifunctional monomers and oligomers (monomers with molecular weight in the range of 1000 g/mol), photoinitiators, and additives. The development of resins for VPP is simple, requiring that the resin undergoes photopolymerization and is chemically stable during the printing process, which can take hours. Commercial resins are a combination of acrylate- and epoxy-based monomers with their respective photoinitiator system [24]. Acrylates have higher polymerization rates, higher linear retraction (20% while epoxies shows retraction of 10%), and no dark cure (photopolymerization once exposition is interrupted) compared to epoxy and vinyl ethers [48], [49]. The use of acrylate and epoxy based monomers has synergistic effects during the additive manufacturing process [24]. First, the polymerization of acrylates is very fast, allowing shape consolidation with minimal mechanical strength, which are further developed by the dark cure of epoxy monomers, giving the final mechanical properties [24]. The slower polymerization of epoxy allows low viscosity to be maintained for longer periods during the free-radical polymerization of acrylates, improving double bond conversion [167]. Also, the heat from acrylate polymerization accelerates epoxy polymerization, and inhibition effects due to water and oxygen are reduced [167]–[169]. These mixed systems also reduce the polymerization shrinkage, reducing residual stress and improving the mechanical properties. Residual stress is responsible for fractures, delamination, warping and other printing problems, and can result in birefringence[170], [171].

Monomers for VPP resins are multifunctional [48] [172]–[175], meaning that they possess more than one polymerizable group in the same molecule. They are a core aspect of a resin's formula since the polymers final structure plays a major role in the desired properties. The presence of multifunctional monomers forms a thermoset or highly crosslinked polymer [135] that is insoluble in the monomer. Furthermore, acrylates and epoxy undergo different polymerization mechanisms, forming two (or more) intertwined crosslinked polymeric networks [176]. This molecular structure avoids polymeric phase segregation, enhancing the mechanical properties and hindering swelling [177]. The final molecular structure is a special kind of polymeric blend namely interpenetrating polymeric networks (IPN)[176], [177] as shown in **Figure 17**.

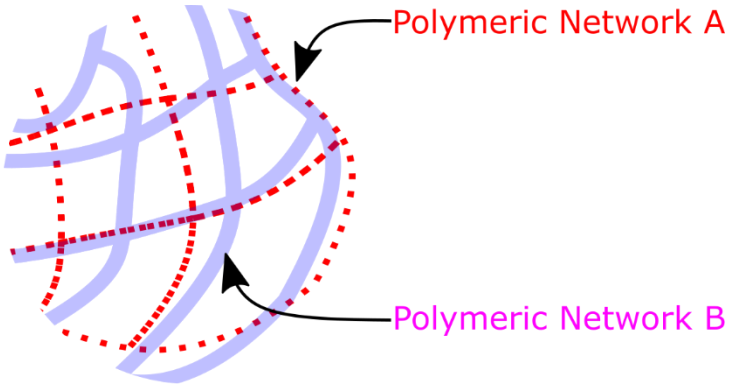

Figure 17. Representation of the structure of an interpenetrating polymeric network (IPN).

In addition to monomers, additive are used to control the absorption properties of the resins and viscosity. Opacifiers (UV absorbers) are commonly used to adjust the penetration depth of resin to match specific requirements by the manufactures, while solvent can be used to adjust the resins viscosity [24]. Typically, the viscosity of a commercial resin is between 200 and 8000 cP [135], however the rheological properties are not crucial, although high viscosity can slow the photopolymerization process. Lastly, appropriate photoinitiators are introduced in concentrations up to 10% w.t. [178], [179] to minimize oxygen inhibition [164]. The selection of photoinitiators is based on the irradiation wavelength and type of monomer employed. Because acrylates and epoxy monomers are used, at least two type of photoinitiators are present, which generate a photosensitizing effect, where the generated free-radical species can activate the cationic photoinitiator, providing comparable conversion rates between the epoxy and acrylate polymerization [180]. Although there is a diversity of formulations, one of the biggest problems related to 3D printing by VPP is stablishing the relationship between materials properties and the resin composition [48].

Sol-gel route

a. Fundaments on sol-gel

The sol-gel route is a soft-chemistry synthesis approach that started being explored in 1930s [181]. The chemistry of sol-gel is based on the reactions of hydrolysis, oxolation and olation (the latter two representing the condensation reactions) of chemical precursors, mostly metal alkoxides, as showed in reactions (1), (2) e (3), respectively [182]. The condensation reaction progressively forms M-O-M bonds (where M represent the metallic atom of the alkoxide source) resulting in a tree-dimensional network and in a colloidal suspension named sol, that further percolates to result in a gel

with a liquid phase trapped in the structure [182]. Post processing can include drying and calcination, allowing the elimination of organics and solvents. The microstructure can be controlled to yield xerogels, aerogels, or even dense monolithic parts depending on the drying process to meet the needs of a given application. The sol-gel route can synthesize inorganic materials under mild conditions of processing, such as low temperature (<200°C) and open atmosphere, which makes it compatible with organic chemistry [13]. Currently, the sol-gel route is employed in various applications such as drug distribution systems [183], [184], imaging and tissue engineering [184]–[190], development of fuel cells[191], ceramic lithography [192], synthesis and coating of nanoparticles [193], [194], 3D printing [195], functional coatings [196], [197] and a diversity of other applications [198].

$$M(OR)_n + m.H_2O \rightarrow M(OR)_{n-m}(OH)_m + m.ROH \quad (1)$$

$$MOR + MOH \rightarrow M - O - M + ROH \quad (2)$$

$$MOH + MOH \rightarrow M - O - M + H_2O \quad (3)$$

b. Controlling the kinetics of condensation

The main challenge of the sol-gel route is controlling the hydrolysis and condensation reaction. Ultimately, the main goal of controlling the hydrolysis and condensation kinetics is to achieve the higher hydrolysis and condensation degree before gel formation occurs. The sol-gel route is typically described using a bimolecular nucleophilic substitution mechanism (S_n2) [182], although there is evidence for the participation of unimolecular nucleophilic substitution (S_n1), and addition-elimination mechanisms [199]. Based on these mechanism, the key factors determining the kinetics of hydrolysis and condensation are the reactants choice (type of alkoxide), temperature, solvent, presence of complexing agents and the pH [182], [200].

The reactivity of each metal alkoxide will depend on the coordination number (CN) of the metal atom in the alkoxide, the electropositivity of the metallic atom, the size of the alkoxide groups, and the maximum CN that the metal atom can achieve [13], [15], [16]. For instance, the higher the electropositivity, the more susceptible the alkoxide is towards nucleophilic attack, meaning that hydrolysis and condensation are highly favored. The size of the alkoxide group is another important factor because it creates steric hindrance for hydrolysis and condensation, meaning that the reaction becomes slower as the alkoxide groups increase in size. Lastly, the greater the difference between the

CN of the metal in its alkoxide form and its maximum values, the higher the reactivity. The latter occurs because the metallic atom undergoes an expansion of its coordination sphere during the hydrolysis and condensation reactions, resulting in more sites available for reaction. The effect of CN is far more prevalent in transition metals alkoxides, such as zirconium, titanium, aluminum, and others. For these alkoxides, the addition of complexing agents to the reaction media can slow down the reaction, because they coordinate to the metallic atom, partly expand the coordination sphere, and create steric hindrance.

The solvent also plays an important role, because it can compete with the hydrolysis and condensation reactions. For instance, most sol-gel synthesis is performed using a combination of alcohol and water since the alcohol can compete with water during the hydrolysis, and with other alkoxide species during condensation, slowing down the reaction rate [182]. The pH is a very important factor that has a twofold effect. First, high pH and low pH increases the hydrolysis and condensation rates by promoting more nucleophilic species and more stable leaving groups during the substitution reaction, respectively. Second, the pH affects the charge balance on the surface of colloidal particles which have an isoelectric point around pH 5 for silica-based sol-gel. Thus, in acidic environments, the sol tends to be more stable compared to basic medium, since these colloidal particles are less favored to condense [182].

c. The hybrid sol-gel route

The hybrid sol-gel route is a special case of sol-gel chemistry employed in the synthesis of organic-inorganic hybrid (OIH) materials. It has received wide attention in the last 5 years because it is inherently compatible with VPP technologies, and has been the main approach to 3D print glasses with high resolution [84]. The hybrid sol-gel route employs chemical precursors with a non-labile functional organic group that can react through polymerization, such as acrylate and epoxy. Because of its mild conditions of processing, this chemical precursors can condense to form a tridimensional inorganic network, and polymerize to form a parallel polymeric network, resulting in OIH materials [13]. Typical examples of alkoxysilanes employed in this route are presented in **Figure 18**. This class of materials were widely explored in the synthesis of silicate-based OIH materials under the name of ORMOSILs (organically modified silane) and ORMOCERs (organic modified ceramics) [201]. By engineering the structure of these materials, their mechanical, optical and other physical-chemical properties can be tuned for different applications such as contact lenses, gas barriers and anti-scratch coatings[202],

synthesis of nano coated particles[203], production of functional coatings[204]–[207], photo catalysis[208], [209], protective coating for space instruments[210], light sensors [211], and the lithography of oxide ceramics[212]–[216]. Furthermore, the development of hybrid materials from the sol-gel route is of particular interest for the development of biomimetic, nano-structured, or multifunctional materials[181], [217]–[220].More recently, the hybrid sol-gel method has been applied in additive manufacturing of ceramics, glasses and OIH material [221].

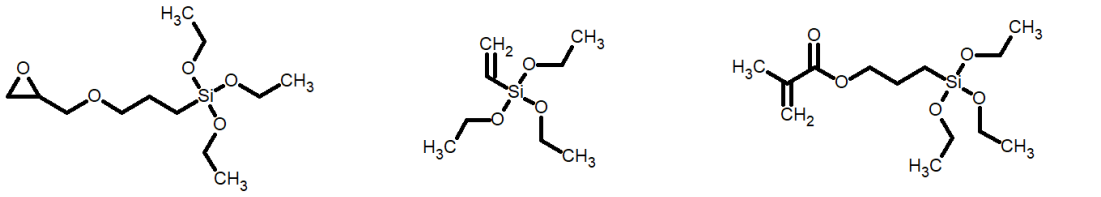

Figure 18. Examples of functional alkoxysilanes commonly used in the hybrid sol-gel route.

The selection of appropriate chemical precursors is of uttermost importance in the hybrid sol-gel route. The functional organic group must be stable against hydrolysis, that is, the chemical bond between the organic group and the moieties involved in the sol-gel chemistry must be strong, so that the organic groups responsible for the formation of the polymeric network are not eliminated during condensation [13]. In the case of silicon, tin, phosphor, lead or mercury alkoxides, the M-C bond is more stable against hydrolysis than M-O-C[222] due to the electronegative character of the central atom and the saturated coordinating sphere, making it less susceptible to the nucleophilic attack by water. Thus, in the case of these alkoxides, the polymerizable functional groups must have chemical bonds of type M-C.

Transition metals alkoxides such as zirconium, titanium, aluminum, cerium, among others, are far more challenging in the hybrid sol-gel route because both the M-C and M-O-C bond are very susceptible to hydrolysis due to the low electronegativity and CN [223]. One of the main strategies to use transition metal alkoxides in hybrid sol-gel route is to use complexing agents such as β-diketones, which show keto-enol tautomerism, as shown in **Figure 19** [184], [222]–[225], and bind to the metal **(Figure 20),** expanding their coordinating sphere and causing hysterical impediment against the nucleophilic water attack. These complexing agents are specially selected to have polymerizable groups, such as 2-methacryoloxyethylacetoaacetate (MAEAA) and acrylic and methacrylic acids [212]–[215], [223], [226]–[230].

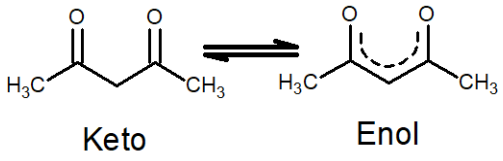

Figure 19. Keto-enol tautomerism of acetylacetonate.

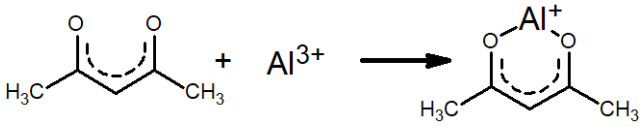

Figure 20.Chelating effect of acetylacetonate to aluminum ion.

d. Aluminum-phosphate hybrid sol-gel materials

Aluminum-phosphate (AlP) based materials have high solubility for lanthanide ions, preventing clustering and concentration quenching, making them ideal hosts for luminescence applications, [19], [20]. As a matter of fact, glasses based on AlP, such as silicate-aluminum-phosphate are staple materials for telecommunications as fiber lasers and signal amplifiers [231]. Thus, aluminum-phosphate OIH materials are a class of materials of great interest as matrices for dispersion of lanthanide ions for the fabrication of active optical devices. However, the literature available on AlP OIH materials is quite scarce because their synthesis is challenging. For instance, most reports in the literature are related to metal organic frameworks (MOFs) [232], which are opaque, and there are no reports of transparent AlP OIH materials. In this regard, the hybrid sol-gel route is one of the most promising approaches to achieve transparent AlP OIH materials compatible with VPP. However, obtaining AlP based materials via the sol-gel chemistry is quite challenging because its precursors are either too reactive or unreactive, not to mention the selection of aluminum and phosphate precursors with non-labile polymerizable pendant groups.

Phosphate are poor gel-formers, lacking self-condensation ability (formation of P-O-P) and their alkoxides are very stable towards hydrolysis [21]. Phosphorus high electronegativity hinders nucleophilic substitution (hydrolysis) [21], [233] and self-condensation in acid medium. The small positive charge on phosphorus also restricts homocondensation and hydrolysis in basic medium [21]. Consequently, phosphorus sol-gel chemistry is based on heterocondensation with other metals, often transition metals, since their small electronegativity favors the formation of P-O-M bonds[234], [235]. Phosphorus alkoxides are of limited use in sol-gel and preference is given to phosphoric and

phosphonic acids, phosphorus halides, phosphorus pentoxide or phosphites, which are very reactive in the presence of most metal alkoxides [13], [236], with uncontrolled condensation [234] leading to precipitation instead of gel formation[237]. Acidic phosphate group (P-O-H) are the main responsible for condensation reactions, meanwhile organic groups (P-O-R and P-C) reduces condensation rate, since the bond is unreactive and creates steric hindrance[233]. Conveniently, the stability of P-C and P-O-C bonds[21] allows us to select polymerizable organic groups to be used in the hybrid sol-gel synthesis as well. Thus, appropriate phosphate sources for sol-gel synthesis of AlP OIH materials, should present a good balance of P-O-H and P-O-C/P-C bonds, with the polymerizable organic function attached through either the P-O-C or the P-C bond.

Aluminum precursors for sol-gel, such as alkoxides (Al-O-C) and organometallics (Al-C), are highly unstable due to the unsaturated coordination sphere and high electropositivity of aluminum. In this case, aluminum alkoxides can be chemically modified with chelating agents to improve stability and adjust its reactivity towards condensation [13]. Chelating agents are molecules to bind using different sites to the metal atom, stabilizing it through steric hindrance and the chelating effect (multiple bonds have to broke in order to unbind the chelating agent to the metal) [13]. β-ketoester or carboxylic acids are common chelating agents for metal alkoxides. Furthermore, chelating agents with a polymerizable group, such as acrylic acid (AA), acetylacetone (ACAC) and 2-methacryoxyethylacetoacetate (MAEAA) can be selected to result in hybrid sol-gel materials[236], [238], [239]. To the best of our knowledge, there are not concise and broad studies regarding the stability of modified metal alkoxide for sol-gel synthesis.

OBJECTIVES

The main objective of this project was the development using the hybrid sol-gel route, and structural characterization of aluminum-phosphate-based hybrid materials. These materials must be compatible with additive manufacturing via vat-photopolymerization for potential application as new active and passive photonic devices. A custom-made vat-photopolymerization system operating under intermittent exposure conditions was used in this project, that required the development of a mathematical framework describing the printing process. To achieve this goal, the specific objects are presented below:

I. Development of long shelf-life photopolymerizable aluminum phosphate hybrid sol-gel matrices (Chapters 1 and 2).

II. Structural elucidation of the obtained materials (Chapters 1 and 2).

- **a.** Characterize microstructure.
- **b.** Elucidate inorganic connectivity via solid-state NMR.
- **c.** Elucidate organic structure.
- **d.** Understand the interactions between organic and inorganic networks.

III. Model the exposure profile of a new VPP setup (Chapter 3).

IV. Study the 3D printing parameters for VPP of these new materials (Chapter 4).

- **a.** Evaluate the kinetics of photopolymerization.
- **b.** Measure critical energy and penetration depth.
- **c.** Demonstrate de AM of these materials.

V. Characterization of optical properties in 3D printed parts using these new materials (Chapter 5).

- **a.** Identify the presence of anisotropies.
- **b.** Evaluate optical homogeneity.

CHAPTER 1. PREPARATION AND STRUCTURAL CHARACTERIZATION OF NEW PHOTOPOLYMERIZABLE TRANSPARENT ALUMINUM-PHOSPHATE HYBRID MATERIALS AS RESINS FOR 3D PRINTING

Gabriel Toshiaki Tayama[1], Silvia Helena Santagneli[1*], Hellmut Eckert[2], Shane Pawsey[3], Younes Messaddeq[1,4*]

1 - Chemistry Institute, São Paulo State University – UNESP, Rua Francisco Degni 55 Araraquara, SP 14800-900, Brazil

2- São Carlos Institute of Physics, University of São Carlos -USP, Avenida Trabalhardor Saocarlense 400, São Carlos, SP 13566-590, Brazil

3- Bruker BioSpin Corporation, 15 Fortune Drive, Billerica, MA, USA

4-Centre de Optique, Photonique et Laser – COPL – Universite Laval, 2375 rue de la Terrase, Quebec,G1V 0A6, Canada

KEYWORDS: Organic-inorganic Hybrid; Aluminum-phosphate; Solid state NMR;

Abstract

The use of a hybrid sol-gel route to prepare silicate hybrid materials and glasses through stereolithography and other photopolymerizable based additive manufacturing techniques has become a major topic. In this work, we present a new synthesis of 2-hydroxyethyl methacrylate/aluminum-phosphate hybrid materials with potential use on additive manufacturing through stereolithography (SLA). The unique sol-gel chemistry of phosphates and their strong reactivity towards metal alkoxide precursors pose special challenges towards stable sols with low solvent concentration. Here, we were able to control condensation reactions, avoiding precipitation, yielding clear and long shelf-life stable 2-hydroxyethyl methacrylate/aluminum-phosphate hybrid sols with different Al/(Al+P) ratios (from 0% up to 50%), which can be further photopolymerized, yielding transparent crack-free monolithic

materials. A detailed structural study through multinuclear solid-state NMR and infrared spectroscopies showed a high polymerization degree with inorganic $Al_y(PO_4)_x$ -like fragments acting as crosslinkers. These crosslinked structures are sensitive to the Al/(Al+P) ratio and increasing aluminum concentration results in a higher degree of inorganic condensation. The organic-inorganic structures are highly interconnected resulting in homogeneous materials.

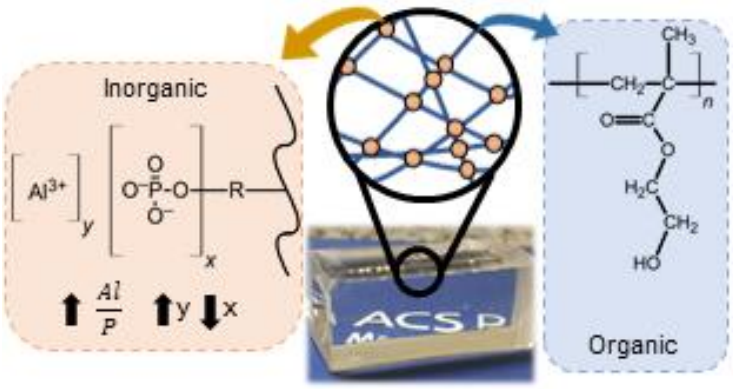

Resumo

O uso da rota sol-gel híbrida no processamento de materiais híbridos do tipo silicato, e vidros, através da estereolitografia e outras técnicas de manufatura aditiva baseadas na fotopolimerização recebeu grande destaque nos últimos anos. Neste trabalho, é apresentado a síntese de materiais híbridos baseados no 2-hidroxietil metacrilato/alumínio-fosfato com potencial de uso em manufatura aditiva através de estereolitografia (SLA). As particularidades da química sol-gel dos fosfatos e sua elevada reatividade com alcóxidos metálicos são grandes desafios para a obtenção de sóis estáveis com baixa concentração de solvente. Nesta contribuição, reportamos o controle da cinética de condensação de maneira a evitar a precipitação e obter sóis híbridos de 2-hidroxietuil metacrilato/alumínio-fosfato estáveis com longa vida útil e com diferentes proporções de Al/(Al+P) (de 0% até 50%), que podem ser fotopolimerizados e resultar em materiais monolíticos transparentes e sem trincas. Um estudo estrutural detalhado através de espectroscopias de RMN de estado sólido multinuclear e infravermelho mostrou um alto grau de polimerização com fragmentos inorgânicos Aly(PO4)x-like atuando como ligações cruzadas. Essas estruturas reticuladas são sensíveis à razão Al/(Al+P) e o aumento da concentração de alumínio resulta em um maior grau de condensação inorgânica. As estruturas orgânico-inorgânicas são altamente interligadas resultando em materiais homogêneos.

Résumé

L'utilisation d'une voie sol-gel hybride pour préparer des matériaux hybrides de silicate et des verres par stéréolithographie et d'autres techniques de fabrication additive à base de photopolymérisables est devenue un sujet majeur. Dans ce travail, nous présentons une nouvelle synthèse de matériaux hybrides méthacrylate de 2-hydroxyéthyle/phosphate d'aluminium avec une utilisation potentielle sur la fabrication additive par stéréolithographie (SLA). La chimie sol-gel unique des phosphates et leur forte réactivité vis-à-vis des précurseurs d'alcoolates métalliques posent des défis particuliers aux sols stables à faible concentration de solvant. Ici, nous avons pu contrôler les réactions de condensation, en évitant les précipitations, en obtenant des sols hybrides clairs et stables de longue durée de conservation méthacrylate de 2-hydroxyéthyle/phosphate d'aluminium avec différents rapports Al/(Al+P) (de 0% à 50%), qui peut ensuite être photopolymérisé, donnant des matériaux monolithiques transparents sans fissures. Une étude structurelle détaillée par RMN multi nucléaire à l'état solide et spectroscopies infrarouges a montré un degré de polymérisation élevé avec des fragments inorganiques de type $Al_y(PO4)_x$ agissant comme agents de réticulation. Ces structures réticulées sont sensibles au rapport Al/(Al+P) et l'augmentation de la concentration en aluminium entraîne un degré plus élevé de condensation inorganique. Les structures organiques-inorganiques sont fortement interconnectées, ce qui donne des matériaux homogènes.

Introduction

The hybrid sol-gel route has been known for at least 40 years as a facile way of producing organic-inorganic hybrid materials under mild processing conditions[1]. By utilizing alkoxides with a non-labile polymerizable group, it is possible to construct amorphous inorganic frameworks through hydrolysis and condensation reactions from a sol-gel route, leading to further reactions through a polymerization mechanism[2]. Furthermore, through a proper choice of reactants and control of hydrolysis and condensation kinetics, it is possible to tailor domain size, connectivity, and interface chemistry, or even eliminate domain or phase separation, achieving truly homogeneous hybrid materials[3]. A myriad of new applications and materials arises from such synthesis routes since intermediate or even emerging properties are possible depending on how the organic and inorganic counterparts are structured and inter-connected[4]. Furthermore, these hybrid materials are compatible with current industrial technologies and due to its inorganic-organic nature, can be easily employed in

multi-material integrated platforms for sensors, photonics, medicine and many other areas[5–7]. In the last years, the hybrid sol-gel route has also been explored by the additive-manufacturing (AM) community. Additive manufacturing refers to a family of different techniques used to fabricate objects in a layer-by-layer assembly method[8]. It has become a major topic in the last decade due to its capability of fabricating innovative and highly customized structures not accessible by traditional methods, on demand, with little time and material consumption[9]. Many areas are benefiting from these technologies, such as aerospace industry, pharmaceutics[10], medicine[11], photonics[12] and food industry[13] just to cite a few. Stereolithography (SLA) is one of the most promising AM technologies and fabricates objects by selectively polymerizing a photo-resin with a laser or lamp of appropriate emission wavelength/spectrum[14]. Such technique excels in printing speed and high dimensional resolution, achieving submicron scale depending on the setup[15]. Since SLA depends on photopolymerization and has been limited to organic polymers, the hybrid sol-gel route is an elegant way to print hybrid materials[16], ceramics[17] and even glasses[18]. By utilizing alkoxides with a non-labile polymerizable group, it is possible to incorporate and polymerize inorganic components through hydrolysis and condensation reactions from sol-gel route, which can further react through a polymerization mechanism[2]. Furthermore, by controlling hydrolysis and condensation kinetics, it is possible to slow gelation and form stable resins which is a crucial property towards its use in SLA.

So far, such routes have been explored mainly for silicate systems, using methacrylate or epoxy alkoxysilanes, and little effort has been dedicated to aluminum-phosphate hybrids, which are of special interest to photonics and biomaterials, due to the high solubility of rare-earth ions in them,[19] and due to their potential biocompatibility[20,21]. Aluminum-phosphate hybrids are particularly challenging to develop due to some unique features of phosphorus chemistry. Owing to its higher electronegativity, compared to silicon, phosphorus forms alkoxides that are very stable toward hydrolysis under normal conditions[22,23]. Therefore, acidic phosphates are usually preferred for phosphate sol-gel synthesis, however they are strong complexing agents towards metal ions, resulting in precipitation or quick gelation[24,25] when the metal alkoxide is added. Furthermore, the addition of metal alkoxides in sol-gel routes is already a complex task, since metal alkoxides are coordinatively unsaturated and possess highly electrophilic character, resulting in strong reactivity with atmospheric moisture[26] and requiring the use of appropriate complexing agents to reduce their reactivity[27]. These particularities are the main challenges towards the development of aluminum-phosphate hybrids for SLA, since stable resins are required and the obtention of transparent materials is highly desirable for optical applications.

In this work, we report the preparation of aluminum-phosphate hybrid resins with potential use in SLA. By employing a photopolymerizable β-diketone aluminum complex and acid phosphate, as well 2-hydroxyethyl methacrylate, we controlled condensation reactions, avoiding precipitation, yielding resins with different Al/(Al+P) ratio with long shelf life and high transparency upon photopolymerization. Control of the condensation reaction was achieved through reactants' selection, since its mechanism is normally a type 2 nucleophilic substitution (S_N2). By adding to the aluminum alkoxide a β-diketone, a more strongly-complexing (chelating) ligand we are reducing the aluminum alkoxide reactivity. On the other hand, the acid phosphate chosen has organic groups that increase steric hindrance and reduce the acidic character of the phosphate, further reducing its reactivity. The use of 2-hydroxyethyl methacrylate (HEMA) acts as a solvent and plays a key role in the condensation kinetics since it allows the ligand exchange with the aluminum alkoxide, competing with the P-O-Al bond formation. Thus, by careful tailoring steric hindrance, Lewis acidic/basicity character and use of a solvent, we were able to achieve extensive P-O-Al condensation without compromising homogeneity and transparency of the final material Initial 3D printing tests were conducted with a 405 nm laser and a moving platform, achieving lines approximately 2 mm thick and 5 mm in height. Structural study by FTIR and solid-state single- and, double- resonance NMR experiments allowed a comprehensive description of the inorganic-organic interaction for this hybrid system with different Al/(Al+P) ratios.

Experimental Section

Hybrid synthesis. All reactants were provided by Sigma Aldrich and were used without further purification. The hybrid materials were synthesized from Aluminum-tri-sec-butoxide, hydroxyethyl methacrylate-phosphoric acid ester (HEMA-P), 2-hydroxyethyl methacrylate (HEMA), 2-(Methacryloyloxy)ethyl acetoacetate (MAEAA) and diphenyl(2, 4, 6- trimethyl benzoyl)phosphine oxide (TPO) was used as the photoinitiator. The HEMA-P reactant is a mixture of phosphoric acid and phosphate esters with one or two ethoxy methacrylate pendant groups, as shown in **Figure 21**, with its respective molar proportions. Initially, the $Al(MAEAA)_2$ complex was prepared in a glovebox (N_2 atmosphere, H_2O levels < 100 ppm) by stirring a mixture of MAEAA and aluminum tri-sec-butoxide (2:1) for 12 h. After completion, the resulting material was removed from the glovebox environment and stored in closed vials. The complex formed has a good chemical stability under atmospheric conditions, and further procedures were followed in atmospheric conditions.

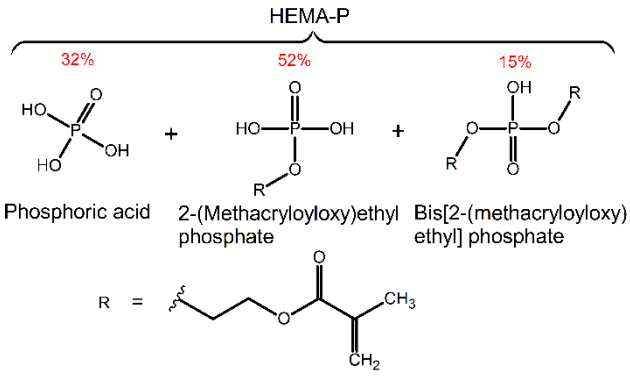

Figure 21. HEMA-P reactant components: structure and molar composition.

The resins were prepared by dissolving the required amount of HEMA-P in HEMA followed by addition of $Al(MAEAA)_2$ complex under intense stirring. The compositions were calculated with 50% wt. of HEMA and 50% wt. of a HEMA-P and $Al(MAEAA)_2$ mixture, with different Al/(P+Al) molar ratios (0%, 10%, 25%, 40% and 50%). The reactant compositions used for each sample are shown in Table S1 available in Supporting Information in Annex A. Upon $Al(MAEAA)_2$ addition, a clear gel readily formed for 50% and 40% Al/(P+Al) compositions, returning to a low viscosity liquid after 10 to 30 min of stirring, as shown in **Figure 22**. The 10% and 25% samples acquired an opaque aspect after 1 hour of aging. 1% wt. TPO was added, and the samples were photo-polymerized under a Hg lamp with emission lines at 402 nm and 362 nm (4 mW/cm^2) for 2 min inside disposable cuvettes in a cold-water bath. Once polymerized, the samples were sealed with parafilm and dried at 40°C for 1 week, yielding transparent samples as shown in **Figure 22** (a). 3D printability of such resins is demonstrated on Figure 22 (b), where the resin with composition Al/(Al+P) = 50% was polymerized on a glass slide by a 405 nm laser focused by a 20X objective coupled to a moving platform. As we can see in **Figure 22** (c), the polymerized material borders are smooth and the printed line width is about 1.5 mm.

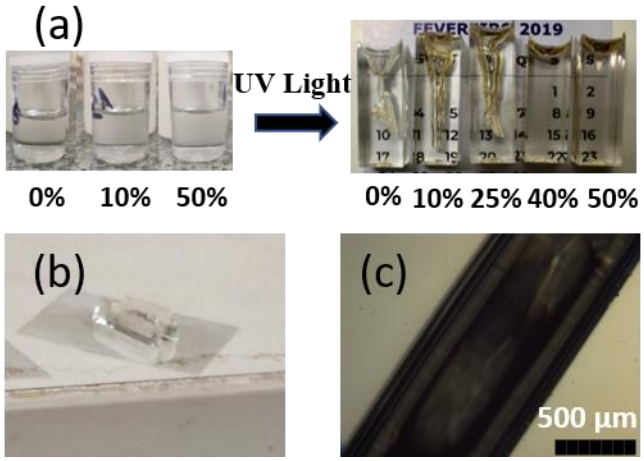

Figure 22. (a) Left: as prepared resins with 0%, 10% and 50% Al/(Al+P) ratio. Right: polymerized resins about 10mm thick. Void in the center due to volumetric retraction upon polymerization. (b), initial tests proving the printability of 50% Al/(P+Al) ink using a 405 nm laser coupled to a microscope and a moving platform with its top view micrograph shown in (c). Printed line has a 1.5 mm width.

Physicochemical properties. Refractive index was measured through M-Lines spectroscopy at 632.8 nm. Thermogravimetric analysis (TGA) was executed in an SDT Q600 (TA Instruments) system, from 30°C up to 800°C at 5°C/min with 100 mL/min air flow. Resin density was determined using a microscale and a transfer pipette. A fixed volume of resin was transferred by pipette and weighed. The operation was repeated at least 5 times and these values were fitted through a linear regression. Polymerized hybrid material density was measured by a helium pycnometer (averages over 10 measurements). Volumetric retraction upon polymerization and drying was determined using Archimedes's method[28].

$$\Delta V/V = \left(\frac{1}{\rho_{resin}} - \frac{1}{\rho_{polymer}}\right) \times \rho_{polymer} \times 100\%$$

UV-Vis spectroscopy. The absorbance spectra were collected from 400 nm up to 2000 nm in a Cary 5000 spectrometer using samples approximately 10 mm thick. Linear extinction coefficients were calculated by dividing absorbance by average sample thicknesses.

FTIR-ATR spectroscopy. Powder samples were analyzed in a VERTEX-70 (Bruker) spectrometer from 400 to 4000 cm^{-1}, with 64 scans and 1 cm^{-1} resolution.

Raman Scattering. The spectra were collected with a Lab RAM HR (Horiba Jobin Yvon) spectrometer equipped with a 632.8 nm laser. The measurement was performed from 400 to 4000 cm^{-1} with integration time of 40 s and 2 scans.

Solid-State NMR. ^{31}P and ^{13}C magic-angle spinning (MAS) NMR spectra were collected using a Bruker Avance III HD 400WB spectrometer equipped with a Triple Resonance probe. $^{13}C\{^{1}H\}$cross-polarization (CP)-MAS spectra were measured at a spinning a frequency of 10.00 kHz, using a CP contact time of 1.0 ms and relaxation delay of 5 s. All spectra were acquired with TPPM proton decoupling during the data acquisition. ^{31}P MAS NMR spectra were recorded on samples spinning at 14.00 kHz, using $\pi/2$ pulses of 3.3 µs length and a relaxation delay of 240 s (1800 s in the case of the *x*=10 sample). Chemical shifts were referenced against an external 85% H_3PO_4 standard. ^{27}Al MAS and TQMAS-NMR spectra were collected in a Bruker Avance Neo 600 MHz spectrometer at a spinning speed of 20.00 kHz, using short pulses of 1 µs length and a relaxation delay of 1 s. ^{27}Al TQMAS three-pulse z-filtered spectra were measured using pulse lengths of 2.75 and 0.85 µs for the hard excitation and reconversion pulses and a 10 µs soft detection pulse. The recycle delay was set to 1 s. Chemical shifts are reported relative to a 1M $Al(NO_3)_3$ aqueous solution. $^{27}Al\{^{31}P\}$ rotational echo double resonance (REDOR) measurements were conducted under the same conditions, using π recoupling pulses on the ^{31}P channel and acquisition of rotor-synchronized ^{27}Al spin echoes (the π pulse length was 4.5 µs in these experiments). The second moments $M_{2(Al\text{-}P)}$ characterizing the dipolar interaction between the ^{27}Al observation nuclei (I = 5/2) and the neighboring ^{31}P nuclei (I = ½), were obtained by applying a parabolic fit to the REDOR data within the range $S/S_0 \leq 0.2$, corresponding to the expression[29]:

$$\frac{\Delta S}{S_0} = \frac{4}{3\pi^2}(NT_R)^2 M_{2(Al-P)} \qquad (1)$$

An average number of Al−O−P linkages per Al unit, $\langle m_P(Al) \rangle$, can be estimated by comparison with M_2 values from REDOR data on the crystalline model compound $Al(PO_3)_3$ (six Al-O-P linkages with 3.207 pm bond length)[30]. ^{1}H and $^{13}C\{^{1}H\}$ CP-HETCOR experiments were collected on a 500 MHz Bruker AVANCE NEO spectrometer using a HX Bruker 1.3 mm very fast MAS probe. ^{1}H single pulse experiments were performed with an excitation pulse of 2.1 µs length. ^{1}H-^{1}H exchange spectroscopy (EXSY) experiments were performed at 60.00 kHz using a 1.4 s recycle delay for a range of mixing times from 0.01 to 100 ms. A total of 256 points were collected in the t_1 domain at 66.67 µs time delay corresponding to a 15 kHz spectral width in the indirect dimension. A 119 kHz nutation frequency was

used for all the pulses used in the above experiments corresponding to a 90° excitation pulse length of 2.1 μs. The $^{13}C\{^{1}H\}$ CP heteronuclear correlation (HETCOR) experiments were done using CP contact times of 500 and 150 μs. The experiments were carried out at a spinning speed at 60.00 kHz and recycle delay of 2 s. Chemical shifts are reported relative to TMS referencing standard for ^{1}H and ^{13}C nuclei.

Results

Physical-chemical properties. Thermogravimetric analysis is shown in **Figure 23** and a residue analysis for the studied materials is presented in Table **2**. From the TGA analysis, as the ratio x = [Al]/([Al] + [P]) increases, thermal events at T<400°C produce higher mass loss and are shifted to lower temperatures. These events are associated mainly with organic material degradation, with minor contributions from polyphosphoric acid formation and phosphate evaporation for poly(HEMA-P)[31–34]. From Table **2**, it is clear that this result arises from higher concentrations of organic groups in samples with higher [Al]/([Al] + [P]) ratios[33]. Between 400°C and 550°C, degradation from poly-Al$(MAEAA)_2$[35] and poly-(HEMA-P)[36] are the main thermal events, and poly(HEMA) has been completely degraded[34]. Weight losses at T>500°C are associated with phosphate evaporation[33]. The reduction in phosphate evaporation and the higher mass residues observed with increasing aluminum concentration is attributed to inorganic condensation, immobilizing phosphate units through P-O-Al bonds, in agreement with the ^{31}P NMR results presented within the structural characterization section.

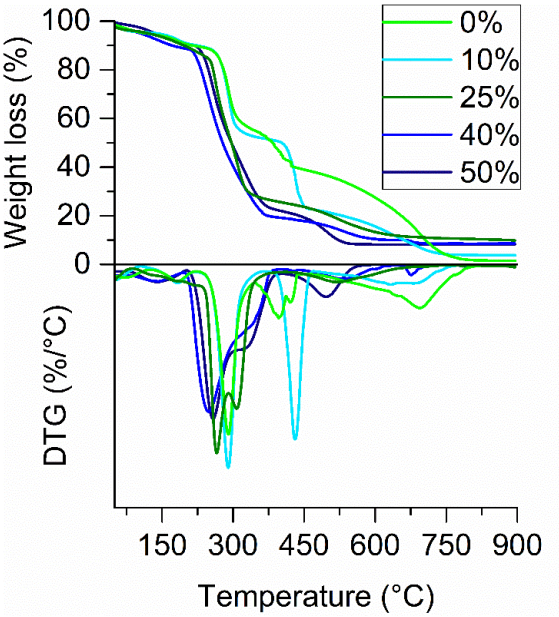

Figure 23. TGA curves of HEMA/Al(MAEAA)$_2$/HEMA-P samples with different concentration of Al ($0 \leq x \leq 50\%$)

The materials' volumetric retraction and refractive index associated with Al/(P+Al) ratio and Ethyl Methacrylate (EtM) molar concentration are shown in **Table 2**. A volumetric retraction within the lower limits displayed by acrylates (typically between 10% and 30%) was observed[14]. This is attributed to the inorganic components, which do not experience volumetric changes during photopolymerization, reducing the overall extent of volumetric retraction. Low volumetric retraction is especially interesting for SLA, since shrinkage can lead to printing defects such as delamination, bending and cracks[14]. The materials' refractive index values varied around 1.50, with no clear correlation with aluminum concentration.

Table 2. Refractive index (n), resin and polymer density (ρ), calculated volumetric retraction (ΔV), residue values from TGA and Ethyl Methacrylate (EtM) molar concentration relative to EtM+P+Al for 0%, 10%, 25%, 40% and 50% Al/(P+Al) samples. Standard deviation is presented in parenthesis. EtM Molar Concentration calculation is presented in Supporting Information in Annex A.

EtM Molar concentration	Al/(P+Al) molar ratio	n	$\rho_{(resin)}$ (g/cm^3)	$\rho_{(polymer)}$ (g/cm^3)	ΔV/V (%)	Residue (%)
73%	0%	1.5034 (0.0009)	1.162 (0.001)	1.35 (0.01)	14	2%
76%	10%	1.5027 (0.0007)	1.1305 (0.0007)	1.31 (0.01)	14	4%
80%	25%	1.5044 (0.0009)	1.1043 (0.0009)	1.32 (0.01)	16	10%
83%	40%	1.501 (0.004)	1.087 (0.005)	1.32 (0.01)	17	8%
85%	50%	1.499 (0.002)	1.0702 (0.0002)	1.303 (0.001)	17	8%

Linear extinction coefficient spectra, from 420 nm up to 2000 nm, of the hybrid materials are shown in **Figure 24**. A transmission window was observed from 420 nm up to 1100 nm, with a second window around 1300 nm. The observed absorption peaks are associated with characteristic vibrational motions arising from organic fragments containing C-H, C=O and O-H groups. These losses are observed at 1729 and 1176 nm for the second and third harmonic, respectively, of C-H vibrations, at 1836, 1382 and 1113 nm for the third, fourth and fifth harmonic, respectively, of C=O vibrations and at 1483 and 979 nm for the second and third harmonics of O-H vibrations[37,38]. The absorption band at 1550 nm results from a combination of C-H stretching and rocking overtones[38–40] and the second overtone from free phosphate hydroxyl groups[38]. The increase in light attenuation at 1550 nm as aluminum concentration decreases results from increasing amounts of free phosphate as shown by ^{31}P NMR results presented in **Figure 26** in the structural characterization section. Minor contributions from C-H groups are also expected since the concentration of ethyl methacrylate groups increases as aluminum concentration decreases, as shown by Table S2, in Supporting Information in Annex A.

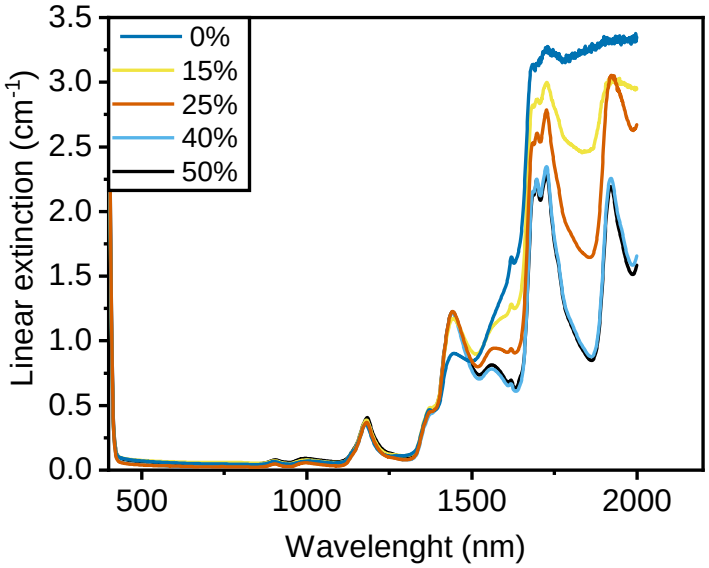

Figure 24. Linear extinction coefficient spectrum (from 2000 nm up to 400 nm) for samples with x = 0, 10, 25, 40 and 50 Al %.

Vibrational Spectroscopy. FTIR and Raman scattering spectra of the hybrid materials upon photopolymerization are shown in Figure 25. Band assignments are displayed in **Table 3** and are

compatible with those reported for poly(HEMA). The broad signal in the range 950 - 1180 cm^{-1} is an overlap of different vibrational bands characteristic of the P-O-C, C-C, O-C and P=O groups[41].

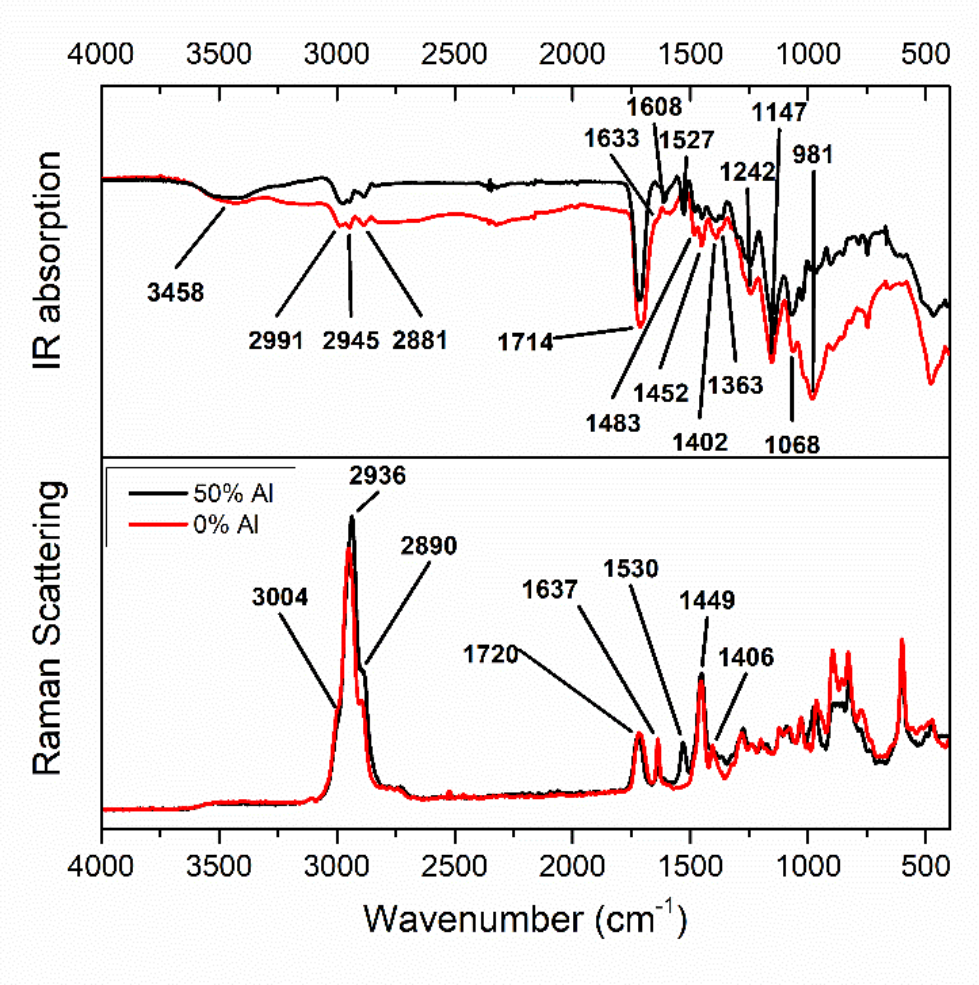

Figure 25. FTIR and Raman spectra of polymerized samples with Al/(Al+P) ratios of 0 and 0.5.

Table 3. Band positions and assignment of FTIR and Raman spectral components in the hybrid materials.

Raman and FTIR frequencies (cm^{-1})	Assignment	Reference
3458 (IR)	ν(O-H)	41,42
3200 (IR)	ν(PO-H)	41
2991 (IR), 2945 (IR), 2881 (IR), 3004 (R), 2936 (R) and 2890 (R)	ν(C-H)	41–43
1714 (IR) and 1720 (R)	ν(C=O)	42,43

1633 (IR) and 1637 (R)	v(C=C)	42–44
1608 (IR)	v(C-O) chelating ring	35
1527 (IR) and 1530 (R)	v(C-C) chelating ring	35
1483 (IR), 1452 (IR), 1402 (IR), 1363 (IR), 1449 (R) and 1406 (R)	δ(CH_2) and δ(CH_3)	41–43
1147(IR)	v(O=)C-O	41–43
1242(IR)	v(P=O)	33
1068(IR)	vO-C(H_2)	41–43
980(IR)	v(P-O-C)	33

Structural Study of the Organic Component by $^{13}C\{^1H\}$ CP-MAS and ^1H-^1H EXSY NMR. $^{13}C\{^1H\}$ CP-MAS NMR spectra and signal assignments are presented in **Figure 26** (a). The ^{13}C peak assignments are based on literature data and the identification of each carbon atom is represented in **Figure 26** (b)[27,35,44–50]. The carbonyl **(C1)** group from methacrylate, CH_2 from the ethyl group **(C4)** and methyl **(C9)** of the methacrylate were observed at 178, 60, and 17 ppm respectively. The CH_2 group closest to the hydroxyl group in HEMA **(C2)** and the one closest to the phosphate group in HEMA-P **(C3)** are assigned to the peaks at 66 and 63 ppm, respectively. Their chemical shift proximity results in a broad signal for low Al concentration samples. The weak signal at 31 ppm was attributed to the methyl group in the MAEAA diketone group **(C8)**. For high aluminum concentration samples, we observe a weak signal at 50 ppm which arises from the CH_2 units of the acetoacetate group **(C6)**. Weak carbonyl signals at 168 ppm **(C10)** from $Al(MAEAA)_2$ were also observed. The carbon atom (**C11)** from $Al(MAEAA)_2$ was not observed in the spectra, which is typically observed close to 200 ppm. Polymeric chain CH_2 **(C5)** units are observed at 55 ppm and the quaternary carbon **(C7)** at 45 ppm, respectively. The minor sharp signals at 10, 23, 32, and 69 ppm are characteristic of residual sec-butanol from the $Al(MAEAA)_2$ present in the samples. ^1H MAS and ^{13}C-^1H CP-HETCOR NMR data (**Figure S1** and **S2**) and assignments are presented in the Supporting Materials Section.

To complement the study of the polymeric chain formation in the polymerization process, the ^1H-^1H 2D-EXSY experiments serve to estimate the spatial separation between protons, providing structural information at the nanoscale[51]. Dipolar coupling and molecular motion are the main mechanisms for magnetization exchange in polymers and are distance and geometry dependent. ^2H-

^{2}H and ^{13}C-^{13}C EXSY have been already used to evaluate heterogeneities, domain sizes, chain motion and rheological properties in polymeric systems, however ^{1}H-^{1}H EXSY is rarely explored due to the poor resolution arising from strong proton dipolar coupling[52–57]. By employing high-speed MAS, it was possible to reduce the latter sufficiently, such that, ^{1}H-^{1}H EXSY spectra could be used to evaluate ^{1}H-^{1}H distances on a qualitative basis. Mixing times of 0.01 up to 100 ms were employed and the ^{1}H-^{1}H EXSY spectra are presented in **Figure 7** for the sample with x = Al/(Al+P) = 25%. Similar results were obtained for the x = 50% sample (data not shown). For short mixing time (0.01 ms), the correlation map shows the cross-peaks between the ethyl group with unreacted monomer **(H2, 3, 4 - H5 unpolymerized)** and CH_3 from $Al(MAEAA)_2$ **(H2, 3, 4 - H8)**. The CH_3 group from $Al(MAEAA)_2$ also shows correlation with the polymeric chain backbone **(H8-H5, 9)** units. For a mixing time of 0.5 ms, the ethyl group and polymer backbone **(H2, 3, 4 - H5, 9)** correlations were observed. At a mixing time of 100 ms, the spectrum is fully developed with correlations between protons belonging to the unreacted monomer and those of the polymeric chain backbone **(H5 unpolymerized - H5, 9)** and CH_3 from $Al(MAEAA)_2$ **(H5 unpolymerized – H8)**.

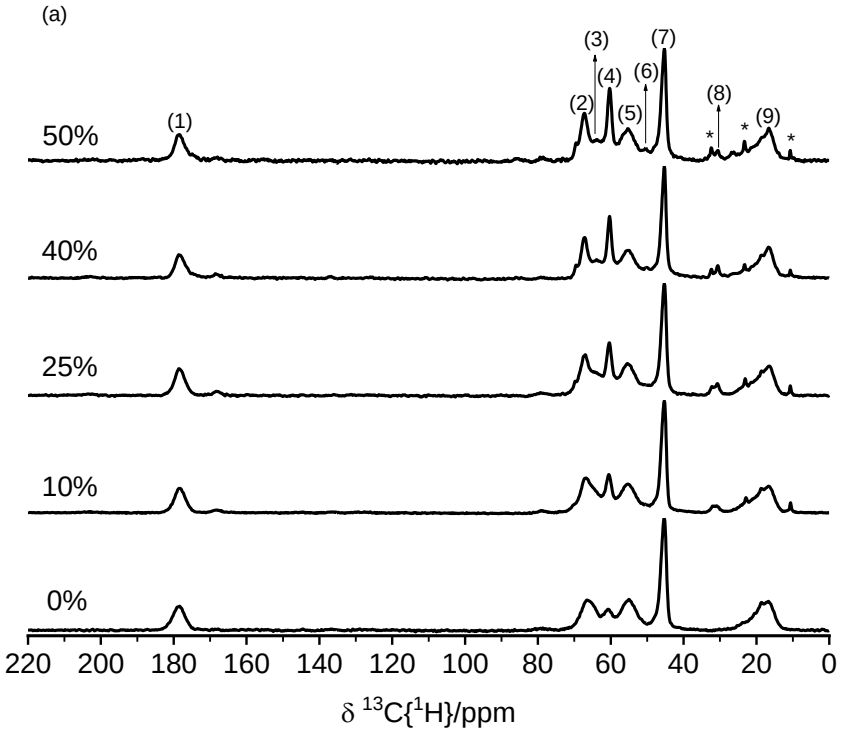

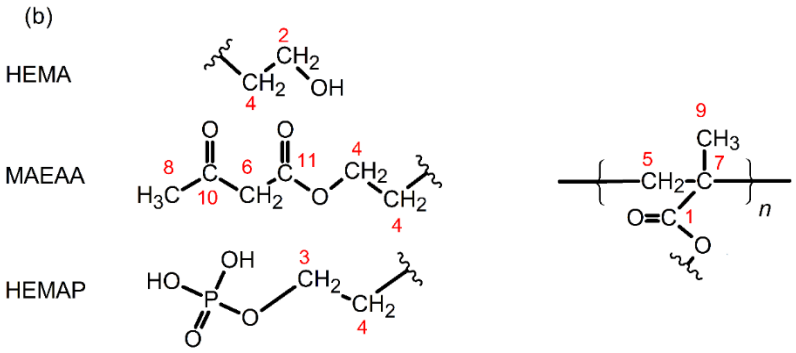

Figure 26. (a) $^{13}C\{^{1}H\}$ CP-MAS NMR spectra of the polymerized samples. The (*) denote sec-butanol signals. (b) structural sketch of the hybrid material.

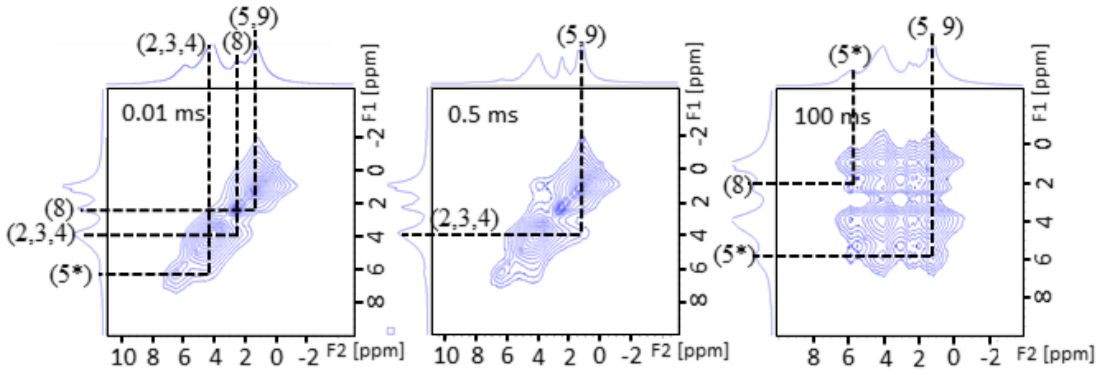

Figure 27. ^{1}H-^{1}H EXSY spectra collected at 60.00 kHz from the 25% Al/(Al+P) sample with mixing times of 0.01, 0.5, and 100 ms. 5* represents CH_2 from unpolymerized methacrylate.

Structural Studies of the Inorganic Component by ^{31}P and ^{27}Al NMR. The ^{31}P and ^{27}Al MAS NMR **Figure 28** (a) and (b), respectively. In the ^{31}P spectrum for the x = 0% sample, we can observe a sharp signal near 1.2 ppm. It can be deconvoluted into three components, associated with the three molecular structures of the HEMA-P reactant shown in **Figure 1**; in addition, orthophosphate units arising from hydrolysis may contribute. Increasing the $Al(MAEAA)_2$ concentration results in broad signals ranging from -5 to -30 ppm. The results are comparable to the ones reported by Zhang et. al[58,59] in a phosphoric acid/aluminum lactate sol-gel sample with signals at 1.2, -5, -12.2 and -18 ppm assigned to $Q^0{}_{0Al}$, $Q^0{}_{1Al}$, $Q^0{}_{2Al}$ and $Q^0{}_{3Al}$ units, respectively. In this terminology, the superscript 0 indicates the absence of P-O-P linkages, while the subscript denotes the number of P-O-Al linkages.

For all the samples studied,, these spectra were deconvoluted and their integrated areas are shown in **Table 4**.

The ^{27}Al MAS NMR spectra show dominantly hexacoordinated species (Al^6) with line positions observed between -20 and -10 ppm and tetracoordinated species (Al^4) with signals near 52 and 39 ppm. The broadening and downfield shift trend of the signals observed for the Al^6 species with increasing Al content indicates the presence of two overlapping Al^6 components, suggesting two distinct environments. Complementary data are obtained from the ^{27}Al TQMAS spectra; see **Figure 9** for a representative data set. The average isotropic chemical shift (δ_{iso}^{cs}) and quadrupolar coupling constants (C_Q) as extracted from the center of gravity of the spectra obtained in the F_1 and F_2 dimensions (see **Table 5**) confirm this result, even though the isotropic dimension does not result in increased resolution in this case. **Figure 8** (b) shows a tentative deconvolution of the MAS-NMR signals approximated by two Gaussian components for each the Al^4 and Al^6 units, assuming that second-order quadrupolar effects are weak. (The weakness of second-order effects is indicated by the near-Gaussian lineshapes as well as the analysis of the TQMAS experiments; see Table 4). The deconvolution parameters are shown in **Table 6**. We may assign these signals to species of the general formula $Al(OR)_y(PO_3)_x$[58,60], where the OR ligands are alkoxy or MAEAA groups. Similarly, both the ^{27}Al MAS spectra and the ^{27}Al TQMAS NMR contour map show two different Al^4 environments. In addition, small amounts of Al^5 units are detected in both experiments. Based on their ^{27}Al chemical shifts, all these environments appear to be linked to phosphate species. The latter conclusion is also in good agreement with the ^{31}P MAS NMR data.

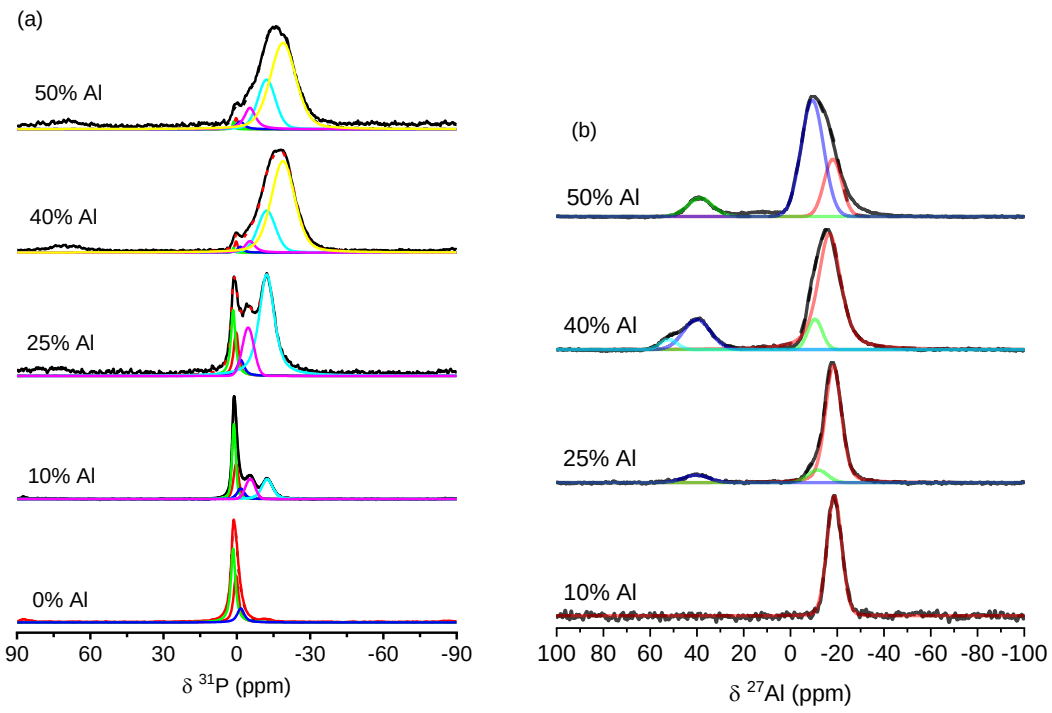

Figure 28.(a) ^{31}P and (b) ^{27}Al MAS NMR spectra from polymerized samples with different Al/ (Al+P) ratios. The solid black line represents the experimental spectrum and the dotted black line the deconvolution envelope.

Table 4. Fitting parameters and relative integrated area for deconvoluted data of ^{31}P MAS NMR spectra. Estimated errors are ±0.5 ppm for chemical shifts, ±2% for areas and ±0.1 for line width.

Composition Al/(P+Al)	Line position (ppm)	Line Width (ppm)	Integrated Area (%)
0%	1.5	2.2	52
	0.3	2.4	34
	-1.6	3.4	14
10%	1.2	1.8	31
	0.3	2.5	20
	-1.6	3.4	8
	-5.5	4.6	17
	-12.4	5.3	24
25%	1.5	2.2	13
	0.3	2.4	9
	-1.6	3.4	5
	-4.6	5.6	16
	-12.2	7.4	58

	1.4	0.7	<1
	0.3	1.6	1
40%	-1.4	2.8	1
	-5.3	4.8	4
	-12.2	8.6	23
	-18.9	11.4	69
	1.4	1.7	<1
	0.3	0.8	1
50%	-1.4	3.9	2
	-5.3	5.4	8
	-12.2	8.6	24
	-18.9	12.5	63

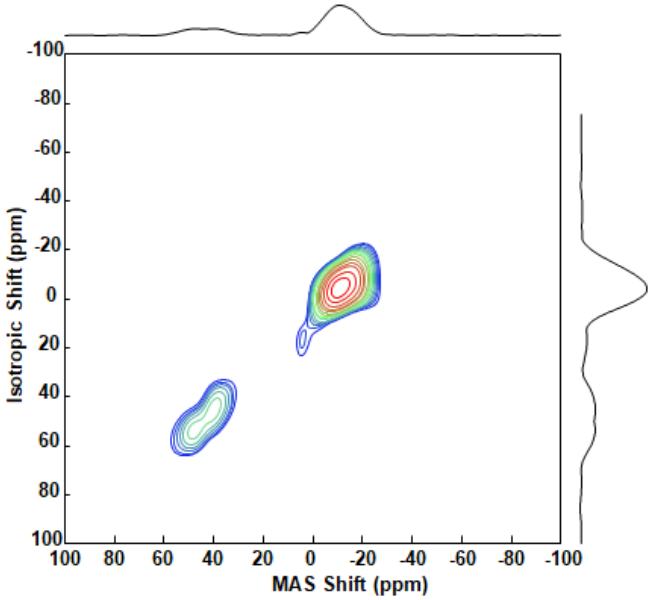

Figure 29. ^{27}Al TQMAS NMR spectrum of the sample with x =Al/(Al+P) = 50%:

Table 5. ^{27}Al NMR isotropic chemical shifts δ_{iso}^{cs} (±0.5 ppm) and SOQE values ($C_Q \times (1 + \eta^2/3)^{1/2}$) (±0.5 MHz) extracted from TQMAS, and $M_{2(Al-P)}$ values (±10%) leading to the estimated average number of Al-O-P linkages per Al species, $\langle m_P(Al^6) \rangle$, of the investigated hybrids.

Samples % Al	^{27}Al δ_{iso}^{cs}		SOQE (MHz)		$M_{2(Al-P)}$ (× 10^6 rad^2/s^2)		$\langle m_P(Al^6) \rangle$
	Al^4	Al^6	Al^4	Al^6	Al^4	Al^6	
10%		-16.2		3.9	-	3.6	3.7
25%						3.7	3.8

40%	53.0/42.2	-11.0	3.8/3.4	4.1	2.9	2.9	3.0
50%	51.5/41.9	-6.5	3.8/3.6	4.4	3.2	2.4	2.5
$Al(PO_3)_3$					-	5.8	6

Table 6. Deconvolution parameters obtained for the ^{27}Al MAS NMR spectra. Estimated errors are ±0.2 ppm for chemical shifts, ±2% for areas and ±0.1 for line width.

Composition Al/(P+Al)	Line position (ppm)	Line Width (ppm)	Integrated Area (%)
50%	-18.2	8.9	25
	-9.4	11.3	64
	38.6	12.5	11
40%	-18.8	12.	33
	-13.3	11.3	43
	40	14.2	20
	52.3	8.4	4
25%	-18.4	8.1	82
	-11.7	9.8	8
	40.3	13.2	10
10%	-18.8	7.4	100

$^{27}Al\{^{31}P\}$ REDOR. To further elucidate the number of Al-O-P linkages involved in these units $^{27}Al\{^{31}P\}$ REDOR experiments were conducted. As explained in the Experimental section, the second moments $M_{2(Al-P)}$ characterizing the strength of ^{27}Al---^{31}P dipolar coupling allow us to estimate the average number of phosphorus atoms bonded to aluminum, $\langle m_P(Al)\rangle$. Assuming that the Al---P distance across an Al-O-P linkage in the glass is the same as that in $Al(PO_3)_3$ we can make this estimate by comparing the $M_{2(Al-P)}$ values measured for the glasses with the value measured for $Al(PO_3)_3$ which features 6 Al-O-P linkages. The $^{27}Al\{^{31}P\}$ REDOR curves and the parabolic fits are shown in **Figure 30** and the $M_{2(Al-P)}$ values and the average numbers of phosphorus atoms coordinating hexacoordinated aluminum species calculated in this fashion are summarized in Table 5. As expected, this number increases with increasing P/Al ratio. Based on the $\langle m_P(Al)\rangle$ values thus obtained, we conclude that the dominant hexacoordinated unit in the sample with Al/(Al+P) = 10% is the $Al(OR)_2(PO_3)_4$ unit, whereas in case of the sample Al/(Al+P) = 50% both $Al(OR)_2(PO_3)_4$ and $Al(OR)_4(PO_3)_2$ units are present. The REDOR results indicate further that the four-coordinated Al species are involved in Al-O-P linkages as

well. As for four-coordinate Al species shorter Al-O-P distances are expected than for the six-coordinate Al species present in our calibration compound $Al(PO_3)_3$, the comparison of the M_2 value with that of $Al(PO_3)_3$ will likely lead to a moderate overestimate of the number of Al-O-P linkages. We may, however, conclude that the four-coordinated Al species possess at least two Al-O-P linkages.

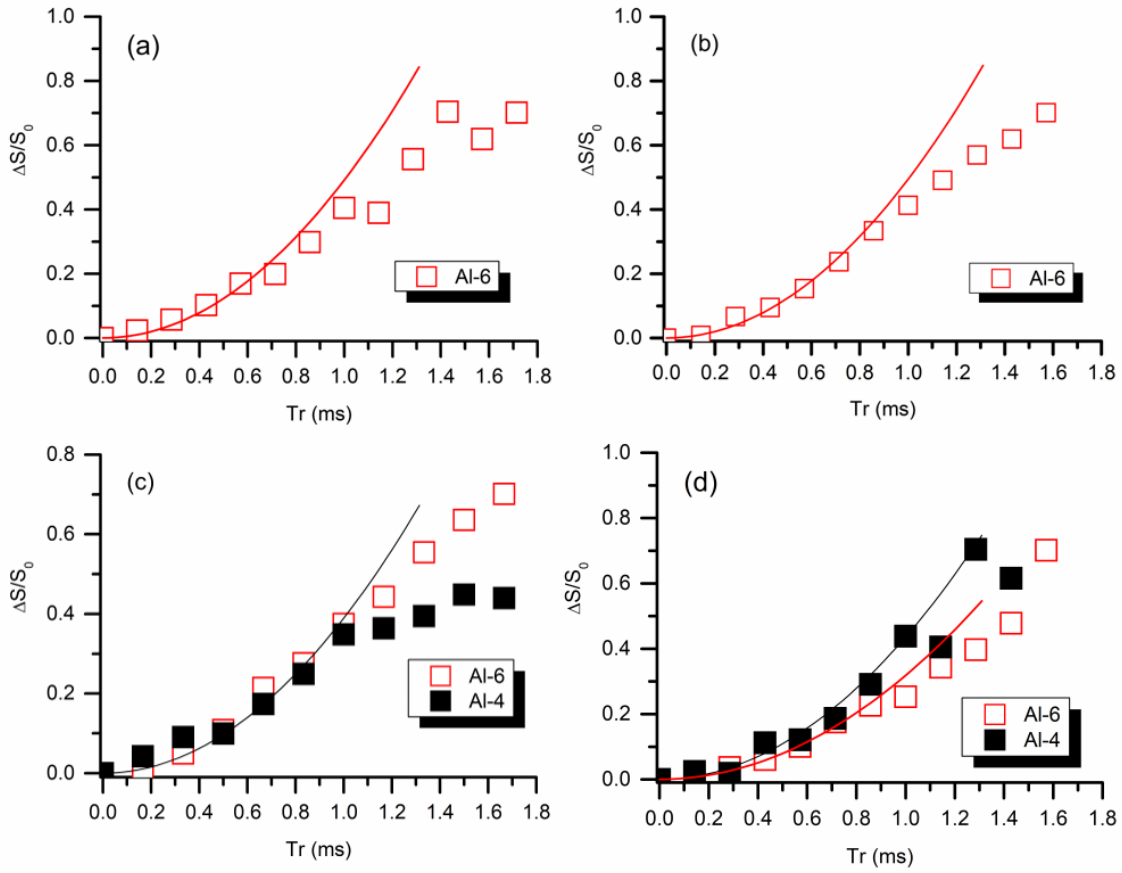

Figure 30. $^{27}Al\{^{31}P\}$ REDOR curves of tetracoordinated (Al^4) and hexacoordinated (Al^6) species for (a) 10%, (b) 25%, (c) 40% and (d) 50% Al/(Al+P) molar ratio. Solid curves are fits of the data points to eq. (1) within the data range $\Delta S/S_0 \leq 0.2$.

A final check on the validity of the analysis conducted here arises from the necessity that the connectivity estimates from ^{27}Al MAS NMR and from ^{31}P MAS NMR must be consistent. In other words, the average number of Al-O-P linkages, (moles Al)×$\langle m_P(Al) \rangle$ deduced from $^{27}Al\{^{31}P\}$ REDOR must be identical to the number of P-O-Al linkages, (moles P)×$\langle m_{Al}(P) \rangle$ deduced from the information in **Table 7**. Thus, the equation

$$(\text{moles P}) \times \{1 \times f_1 + 2 \times f_2 + 3 \times f_3\} = (\text{moles Al}) \times \langle m_P(Al) \rangle \quad (2)$$

must be fulfilled, where f_1, f_2, and f_3 are the fractional areas of the ^{31}P signal components near -5, -12, and -19 ppm, respectively. Table 7 summarizes the results of this analysis, indicating good consistency in three out of four samples. Only for the lowest-Al containing sample, a larger discrepancy between both values can be observed, which we are currently unable to explain. As we note that in the ^{27}Al MAS-NMR spectrum only a single spectral component is visible (based on its chemical shift to be attributed to $Al(OR)_2(PO_3)_4$ it appears likely that the REDOR method slightly under-estimates $<m_P(Al)>$ (yielding the value of 3.7 in Table 5 instead of the expected value of 4.0). The assumption that the calibration factor determined by REDOR on $Al(PO_3)_3$ can be applied to all of the glasses in a uniform manner may be an oversimplification.

Table 7. Number of P-O-Al and Al-O-P linkages analyzed by the different NMR methods.

Al/(Al + P)	mol Al	mol P	mol P-O-Al	mol Al-O-P
0.1	0.002	0.019	0.012	0.008
0.25	0.004	0.012	0.016	0.015
0.40	0.005	0.008	0.021	0.015
0.50	0.006	0.006	0.015	0.015

Discussion

FTIR/Raman and $^{13}C\{^1H\}$ CP MAS NMR data indicate that the organic components of these hybrid materials have a high polymerization degree, since only traces of unreacted monomer and weak signals at 1300 and 1320 cm^{-1} arising from C=C units conjugated with the ester group[41] are observed. Similarly, $^{13}C\{^1H\}$ CP MAS-NMR could not detect C=C signals (located at 126 and 136 ppm) due to their low concentration. Strong magnetic dipole-dipole couplings detected by ^1H-^1H EXSY MAS NMR offer additional information about the proximity of protons. At short mixing times (0.01 to 0.5 ms) only correlations between the closest protons are expected, as the magnetic dipole-dipole coupling strengths (and hence spin diffusion rates) are the greatest in this case, and the results we obtain in this regime are in good agreement with the molecular structure (see **Figure 27**). (**H8 - H2,3,4)** and **(H8 - H9,5)** correlations are the only cross peaks observed at 0.01 ms, and **(H2,3,4-H9,5)** correlations were observed at 0.05 ms. Considering intramolecular distances, **(H8 - H9,5)** correlations should not be observed at 0.01 ms. We conclude that the **(H8 - H9,5)** cross-peaks have an intermolecular nature, bringing the corresponding protons into proximity due to molecular packing. With long mixing time (100

ms), correlations between $C=CH_2$ unreacted monomer to CH_3 from MAEAA **(H5 unpolymerized-H8)** and the polymeric chain backbone **(H5 unpolymerized - H9,5)** are observed. Since the correlation **(H5 unpolymerized - H9,5)** must be intermolecular, we can assume that the **(H5 unpolymerized - H8)** correlations are also intermolecular, indicating that unpolymerized MAEEA is only a minority component.

These polymeric chains are covalently bonded to phosphate units through P-O-C bonds, as shown by the 980 cm^{-1} band in the FTIR spectra. On the other hand, chelating bonds from MAEAA are only observed as a weak signal for samples with Al/(P+Al) ratios of 50% and 40%. In these samples, the ^{27}Al MAS NMR spectra show a shift in the downfield direction since not all MAEAA ligand is replaced by phosphate species, resulting in 4- and 6-coordinated $Al(MAEAA)_x(PO_3)_y$ units. Increasing the Al((Al+P) ratio results in a reduction of the concentration of free phosphate and favors phosphate species with an increasing number of linkages to aluminum, as shown by ^{31}P MAS NMR. The ^{27}Al MAS and TQMAS spectra are consistent with the presence of two dominant Al^6 species characterized by two and four Al-O-P linkages. The average number of such linkages is available from dipolar second moments $M_{2(Al-P)}$ extracted via $^{27}Al\{^{31}P\}$ REDOR experiments. These values indicate a decrease from four to 2.5 linkages per Al species as the Al/(Al+P) ratio increases from 10% to 50%. These results support the presence of multiple $Al(MAEAA)_x(PO_3)_y$ species, with higher contribution of MAEAA ligands as the aluminum concentration increases. These aluminum-phosphate units are covalently bonded to the polymer backbone through phosphate groups, with a minor interaction of aluminate species for the samples with x = 40% and 50%. The formed network is directly correlated with the Al/(Al+P) ratio. For low aluminum concentrations (10% and 25%), the formation of Q^0_{1Al} and Q^0_{2Al} units is favored and the aluminate species are further bonded, on average, to 3 to 4 phosphate units. For high aluminum concentrations (40% and 50%), the Q^0_{2Al} and Q^0_{3Al} species become dominant, and the aluminate species are further bonded, on average, to 2 to 3 phosphate units. The phosphate groups incorporated within these inorganic-like structures act as crosslinkers, resulting in a highly connected and interlocked network of polymeric chains covalently bonded to an inorganic network. This highly polymerized structure avoids phase segregation and concomitant fluctuations in refractive index, yielding a transparent material.

Conclusions

Clear photopolymerizable aluminum-phosphate hybrid sols suitable for stereolithography technologies were presented. These sols are highly stable, presenting long shelf life at room temperature. Upon photopolymerization, hybrid materials optically transparent within the 420 nm - 1100 nm range with low volumetric retraction for acrylates are formed. The materials present an organic/inorganic nanocomposite structure described as poly (2-hydroxyethyl methacrylate) chains with aluminum-phosphate groups covalently bonded to the polymeric backbone. These aluminum-phosphate groups are formed by aluminate species connected, on average, to two up to four phosphate groups, and these phosphate species are linked to 1 to 3 aluminate units. The connectivity of aluminate and phosphate species depends on the Al/(Al+P) ratio as shown by a detailed NMR analysis. These structures provide numerous crosslinkers, generating a highly interconnected and interlocked inorganic/organic structure. These hybrid materials are considered promising candidates for the development of new optical devices and biomedical materials through stereolithography technologies, limited till now to alkoxysilane components. A wide range of new compositions can be explored and developed based on these new hybrid materials.

Acknowledgments

Authors would like to acknowledge the Brazilian funding agencies FAPESP (SPEC process 2015/ 22828-6 and 18/24735-3) is gratefully acknowledged. GT thanks FAPESP fellowship, process number 2018/06426-3.

Bibliographic References

(1) Faustini, M.; Nicole, L.; Ruiz-Hitzky, E.; Sanchez, C. History of Organic-Inorganic Hybrid Materials: Prehistory, Art, Science, and Advanced Applications. *Adv. Funct. Mater.* **2018**, *28*, 1704158

(2) Judeinstein, P.; Sanchez, C. Hybrid Organic–Inorganic Materials: A Land of Multidisciplinarity. *J Mater Chem* **1996**, *6*, 511–525.

(3) Sanchez, C.; Boissiere, C.; Cassaignon, S.; Chaneac, C.; Durupthy, O.; Faustini, M.; Grosso, D.; Laberty-Robert, C.; Nicole, L.; Portehault, D.; Ribot, F.; Rozes, L.; Sassoye, C. Molecular Engineering of Functional Inorganic and Hybrid Materials. *Chem. Mater.* **2014**, *26,* 221–238.

(4) Nicole, L.; Laberty-Robert, C.; Rozes, L.; Sanchez, C. Hybrid Materials Science: A Promised Land for the Integrative Design of Multifunctional Materials. *Nanoscale* **2014**, *6*, 6267–6292.

(5) Sanchez, C.; Shea, K. J.; Kitagawa, S. Applications of Advanced Hybrid Organic–Inorganic Nanomaterials: From Laboratory to Market. *Chem. Soc. Rev.* **2011**, *40*, 696–753.

(6) Mir, S. H.; Nagahara, L. A.; Thundat, T.; Mokarian-Tabari, P.; Furukawa, H.; Khosla, A. Review—Organic-Inorganic Hybrid Functional Materials: An Integrated Platform for Applied Technologies. *J. Electrochem. Soc.* **2018**, *165*, B3137–B3156.

(7) Drisko, G. L.; Sanchez, C. Hybridization in Materials Science - Evolution, Current State, and Future Aspirations. *Eur. J. Inorg. Chem.* **2012**, *2012*, 5097–5105.

(8) ASTM International. F2792-12a - Standard Terminology for Additive Manufacturing Technologies. *Rapid Manuf. Assoc.* **2013**, 10–12.

(9) Mellor, S.; Hao, L.; Zhang, D. Additive Manufacturing: A Framework for Implementation. *Int. J. Prod. Econ.* **2014**, *149*, 194–201.

(10) Goole, J.; Amighi, K. 3D Printing in Pharmaceutics: A New Tool for Designing Customized Drug Delivery Systems. *Int. J. Pharm.* **2016**, *499*, 376–394.

(11) Tack, P.; Victor, J.; Gemmel, P.; Annemans, L. 3D-Printing Techniques in a Medical Setting: A Systematic Literature Review. *Biomed. Eng. Online* **2016**, *15*, 1–22.

(12) Camposeo, A.; Persano, L.; Farsari, M.; Pisignano, D. Additive Manufacturing: Applications and Directions in Photonics and Optoelectronics. *Adv. Opt. Mater.* **2019**, *7* 1800419.

(13) Godoi, F. C.; Prakash, S.; Bhandari, B. R. 3d Printing Technologies Applied for Food Design: Status and Prospects. *J. Food Eng.* **2016**, *179*, 44–54.

(14) Gibson, I.; Rosen, D.; Stucker, B. *Additive Manufacturing Technologies: 3D Printing, Rapid Prototyping, and Direct Digital Manufacturing*.; Springer US, 2015.

(15) Redwood, B.; Schöffer, F.; Garret, B. *The 3D Printing Handbook*; 3D Hubs B. V.:, 2017.

(16) Shukrun, E.; Cooperstein, I.; Magdassi, S. 3D-Printed Organic–Ceramic Complex Hybrid Structures with High Silica Content. *Adv. Sci.* **2018**, *5* 1800061.

(17) Gailevičius, D.; Padolskytė, V.; Mikoliūnaitė, L.; Šakirzanovas, S.; Juodkazis, S.; Malinauskas, M. Additive-Manufacturing of 3D Glass-Ceramics down to Nanoscale Resolution. *Nanoscale Horiz.* **2019**, *4*, 647–651.

(18) Destino, J. F.; Dudukovic, N. A.; Johnson, M. A.; Nguyen, D. T.; Yee, T. D.; Egan, G. C.; Sawvel, A. M.; Steele, W. A.; Baumann, T. F.; Duoss, E. B.; Suratwala, T.; Dylla-Spears, R. 3D Printed Optical Quality Silica and Silica-Titania Glasses from Sol-Gel Feedstocks. *Adv. Mater. Technol.* **2018**, *1700323*.

(19) Ter-Mikirtychev, V. *Fundamentals of Fiber Lasers and Fiber Amplifiers*; Springer Series in Optical Sciences Vol. 181; Springer International Publishing: Cham, 2014.

(20) Krishnan, V.; Lakshmi, T. Bioglass: A Novel Biocompatible Innovation. *J. Adv. Pharm. Technol. Res.* **2013**, *4*, 78-83.

(21) Tilocca, A. Models of Structure, Dynamics and Reactivity of Bioglasses: A Review. *J. Mater. Chem.* **2010**, *20*, 6848-6858.

(22) Fernández-Lorenzo, C.; Esquivias, L.; Barboux, P.; Maquet, J.; Taulelle, F. Sol-Gel Synthesis of SiO2P2O5 Glasses. *J. Non-Cryst. Solids* **1994**, *176*, 189–199.

(23) Carta, D.; Pickup, D. M.; Knowles, J. C.; Ahmed, I.; Smith, M. E.; Newport, R. J. A Structural Study of Sol–Gel and Melt-Quenched Phosphate-Based Glasses. *J. Non-Cryst. Solids* **2007**, *353*, 1759–1765.

(24) Livage, J.; Barboux, P.; Vandenborre, M. T.; Schmutz, C.; Taulelle, F. Sol-Gel Synthesis of Phosphates. *J. Non-Cryst. Solids* **1992**, *147–148*, 18–23.

(25) Abo-Naf, S. M.; Ghoneim, N. A.; El-Batal, H. A. Preparation and Characterization of Sol-Gel Derived Glasses in the Ternatry Na2O-Al2O3-P2O5 System. *J. Mater. Sci. Mater. Electron. IS* **2004**, *15*, 273–282.

(26) Lichtenberger, R.; Schubert, U. Chemical Modification of Aluminium Alkoxides for Sol–Gel Processing. *J. Mater. Chem.* **2010**, *20*, 9287–9287.

(27) Lichtenberger, R.; Puchberger, M.; Baumann, S. O.; Schubert, U. Modification of Aluminum Alkoxides with β-Ketoesters: New Insights into Formation, Structure and Stability. *J. Sol-Gel Sci. Technol.* **2009**, *50*, 130–140

(28) Monteiro, G. Q. D. M.; Montes, M. A. J. R.; Rolim, T. V.; Mota, C. C. B. D. O.; Kyotoku, B. D. B. C.; Gomes, A. S. L.; Freitas, A. Z. D. Alternative Methods for Determining Shrinkage in Restorative Resin Composites. *Dent. Mater.* **2011**, *27*, 1–10.

(29) Bertmer, M.; Eckert, H. Dephasing of Spin Echoes by Multiple Heteronuclear Dipolar Interactions in Rotational Echo Double Resonance NMR Experiments. *Solid State Nucl. Magn. Reson.* **1999**, *15*, 139–152.

(30) van Wüllen, L.; Tricot, G.; Wegner, S. An Advanced NMR Protocol for the Structural Characterization of Aluminophosphate Glasses. *Solid State Nucl. Magn. Reson.* **2007**, *32*, 44–52.

(31) Lindsay, C. I.; Hill, S. B.; Hearn, M.; Manton, G.; Everall, N.; Bunn, A.; Heron, J.; Fletcher, I. Mechanisms of Action of Phosphorus Based Flame Retardants in Acrylic Polymers. *Polym. Int.* **2000**, *49*, 1183–1192.

(32) Rossos, A. K.; Banti, C. N.; Kalampounias, A. G.; Papachristodoulou, C.; Kordatos, K.; Zoumpoulakis, P.; Mavromoustakos, T.; Kourkoumelis, N.; Hadjikakou, S. K. PHEMA@AGMNA-1: A Novel Material for the Development of Antibacterial Contact Lens. *Mater. Sci. Eng. C* **2020**, *111*, 110770.

(33) Liang, H.; Shi, W. Thermal Behaviour and Degradation Mechanism of Phosphate Di/Triacrylate Used for UV Curable Flame-Retardant Coatings. *Polym. Degrad. Stab.* **2004**, *84*, 525–532.

(34) Ulu, A.; Koytepe, S.; Ates, B. Synthesis and Characterization of Biodegradable PHEMA-Starch Composites for Immobilization of L-Asparaginase. *Polym. Bull.* **2016**, *73*, 1891–1907.

(35) Ganesan, R.; Dinachali, S. S.; Lim, S. H.; Saifullah, M. S. M.; Chong, W. T.; Lim, A. H. H.; Yong, J. J.; Thian, E. S.; He, C.; Low, H. Y. Direct Nanoimprint Lithography of Al 2 O 3 Using a Chelated Monomer-Based Precursor. *Nanotechnology* **2012**, *23*, 315304.

(36) Jang, J.; Jeong, Y.-K. Synthesis and Flame-Retardancy of UV-Curable Methacryloyloxy Ethyl Phosphates. *Fibers Polym.* **2008**, *9*, 667–673.

(37) Yeniay, A.; Gao, R.; Takayama, K.; Gao, R.; Garito, A. F. Ultra-Low-Loss Polymer Waveguides. *J. Light. Technol.* **2004**, *22*, 154–158.

(38) Groh, W. Overtone Absorption in Macromolecules for Polymer Optical Fibers. *Makromol. Chem.* **1988**, *189*, 2861–2874.

(39) Lee, K.-S.; Lee, J.-S. Synthesis of Highly Fluorinated Poly(Arylene Ether Sulfide) for Polymeric Optical Waveguides. *Chem. Mater.* **2006**, *18*, 4519–4525.

(40) Watanabe, T.; Hayashida, S.; Imamura, S. Vibrational Overtone Absorption of Side Chain in Silicone at 1.55 Mm Wavelength Band. *Jpn. J. Appl. Phys.* **1999**, *38*, L318.

(41) Daimay Lin-Vien, N. B. C., William G. Fateley, Jeanette G. Grasselli. *The Handbook of Infrared and Raman Characteristic Frequencies of Organic*; Academic Press, 1991.

(42) Perova, T. S.; Vij, J. K.; Xu, H. Fourier Transform Infrared Study of Poly (2-Hydroxyethyl Methacrylate) PHEMA. *Colloid Polym. Sci.* **1997**, *275*, 323–332.

(43) Bertoluzza, A.; Monti, P.; Garcia-Ramos, J. V.; Simoni, R.; Caramazza, R.; Calzavara, A. Applications of Raman Spectroscopy to the Ophthalmological Field : Raman Spectra of Soft Contact Lenses Made of Poly-2-Hydroxyethylmethacrylate (PHEMA). *J. Mol. Struct.* **1986**, *143* (C), 469–472.

(44) Miwa, Y.; Ishida, H.; Tanaka, M.; Mochizuki, A. 2H-NMR and 13C-NMR Study of the Hydration Behavior of Poly(2-Methoxyethyl Acrylate), Poly(2-Hydroxyethyl Methacrylate) and Poly(Tetrahydrofurfuryl Acrylate) in Relation to Their Blood Compatibility as Biomaterials. *J. Biomater. Sci. Polym. Ed.* **2010**, *21*, 1911–1924.

(45) Ferrari, E.; Saladini, M.; Pignedoli, F.; Spagnolo, F.; Benassi, R. Solvent Effect on Keto–Enol Tautomerism in a New β-Diketone: A Comparison between Experimental Data and Different Theoretical Approaches. *New J. Chem.* **2011**, *35*, 2840–2840.

(46) Plummer, R.; Hill, D. J. T.; Whittaker, A. K. DOSY NMR Studies of Chemical Exchange Behavior of Poly(2-Hydroxyethyl Methacrylate). *Macromolecules* **2006**, *39*, 3878–3889.

(47) Kanai, T.; Mahato, T. K.; Kumar, D. Synthesis and Characterization of Novel Silicone Acrylate–Soya Alkyd Resin as Binder for Long Life Exterior Coatings. *Prog. Org. Coat.* **2007**, *58*, 259–264.

(48) Schiavoni, M. M.; Di Loreto, H. E.; Hermann, A.; Mack, H.-G.; Ulic, S. E.; Della Védova, C. O. Keto-Enol Tautomerism in β-Ketoesters: CH 3 C(O)CHXC(O)OY (X = H, Cl; Y = CH 3 , C 2 H 5

). Vibrational Analyses, NMR Spectra and Quantum Chemical Calculations. *J. Raman Spectrosc.* **2001**, *32*, 319–329.

(49) Ivanovici, S.; Puchberger, M.; Fric, H.; Kickelbick, G. Coordination Behavior of Acetoacetate Ligands with Attached Methacrylate Groups Containing Alkyl-Spacers of Different Length to Titanium and Zirconium Alkoxides. *Monatshefte Für Chem. - Chem. Mon.* **2007**, *138*, 529–539.

(50) Vilela, C.; Martins, A.; Sousa, N.; Silvestre, A.; Figueiredo, F.; Freire, C. Poly(Bis[2-(Methacryloyloxy)Ethyl] Phosphate)/Bacterial Cellulose Nanocomposites: Preparation, Characterization and Application as Polymer Electrolyte Membranes. *Appl. Sci.* **2018**, *8*, 1145.

(51) Davidowski, S. K.; Holland, G. P. Solid-State NMR Characterization of Mixed Phosphonic Acid Ligand Binding and Organization on Silica Nanoparticles. *Langmuir* **2016**, *32*, 3253–3261.

(52) Spiess, H. W. Multidimensional NMR Methods for Elucidating Structure and Dynamics of Polymers. Elsevier, 1997.

(53) Kuebler, S. C.; Schaefer, D. J.; Boeffel, C.; Pawelzik, U.; Spiess, H. W. 2D Exchange NMR Investigation of the α-Relaxation in Poly(Ethyl Methacrylate) as Compared to Poly(Methyl Methacrylate). *Macromolecules* **1997**, *30*, 6597–6609.

(54) Demco, D. E.; Hafner, S.; Fülber, C.; Graf, R.; Spiess, H. W. Two-dimensional Proton Magnetization-exchange NMR Spectroscopy in Cross-linked Elastomers. *J. Chem. Phys.* **1996**, *105*, 11285–11296.

(55) Spiess, H. W. Structure and Dynamics of Solid Polymers from 2D- and 3D-NMR. *Chem. Rev.* **1991**, *91*, 1321–1338.

(56) Schmidt-Rohr, K.; Spiess, H. W. Chain Diffusion between Crystalline and Amorphous Regions in Polyethylene Detected by 2D Exchange Carbon-13 NMR. *Macromolecules* **1991**, *24*, 5288–5293.

(57) Schmidt-Rohr, K.; Spiess, H. W. *Multidimensional Solid-State NMR and Polymers*; Acad. Press: London, 2005.

(58) Zhang, L.; Eckert, H. Sol–Gel Synthesis of Al 2 O 3 –P 2 O 5 Glasses: Mechanistic Studies by Solution and Solid State NMR. *J Mater Chem* **2004**, *14*, 1605–1615.

(59) Zhang, L.; de Araujo, C. C.; Eckert, H. Aluminum Lactate – An Attractive Precursor for Sol–Gel Synthesis of Alumina-Based Glasses. *J. Non-Cryst. Solids* **2007**, *353*, 1255–1260.

(60) Zhang, L.; Chan, J. C. C.; Eckert, H.; Helsch, G.; Hoyer, L. P.; Frischat, G. H. Novel Sol−Gel Synthesis of Sodium Aluminophosphate Glass Based on Aluminum Lactate. *Chem. Mater.* **2003**, *15*, 2702–2710.

CHAPTER 2. UNDERSTANDING THE MICROSTRUCTURE CONNECTIVITY IN PHOTOPOLYMERIZABLE ALUMINUM-PHOSPHATE-SILICATE SOL–GEL HYBRID MATERIALS FOR ADDITIVE MANUFACTURING

[1,2]Gabriel T. Tayama*, [1]Silvia Helena Santagneli*, [3]Marcos de Oliveira Junior, [1,2]Younes Messaddeq

1 - Chemistry Institute, São Paulo State University – UNESP, Rua Francisco Degni 55 Araraquara, SP 14800-900, Brazil

2-Centre de Optique, Photonique et Laser – COPL – Universite Laval, 2375 rue de la Terrase, Quebec, G1V 0A6, Canada

3- São Carlos Institute of Physics, University of São Paulo, PO Box 369, 13560-970, São Carlos, SP, Brazil.

KEYWORDS: Solid state NMR, Aluminum-phosphate-silicate, high speed MAS,

Abstract

In this paper, we report the synthesis and structural characterization of transparent and photopolymerizable aluminum-phosphate-silicate hybrid materials obtained via sol-gel route, with different aluminum:phosphate (Al:P) ratios. We explored the system $Si_{(1-x)}$ - $(Al:P)_{(x)}$ with x varying from 0.3 to 1, and atomic ratio Al:P = 1:3, 1:1 and 3:1. All compositions contain high inorganic mass content (up to 40 wt.%). Furthermore, they are compatible with vat-photopolymerization platforms. The structural evolution of the hybrid materials with the silicon concentration was investigated by SEM, phase contrast AFM and Solid-State NMR techniques, using single and double resonance experiments. The structure follows the build-up principle using aluminum-phosphate species and alkoxysilane chains as fundamental building blocks. These aluminum-phosphate species were identified as monomeric and dimeric chain structures by comparing different parameters obtained from

NMR data to compound models. Monomeric and dimeric aluminum-phosphate chain structures were predominant in 3:1 and 1:3 Al:P ratio samples, respectively, promoting and hindering the hetero-condensation with the alkoxysilane precursor, respectively. The photopolymerization mechanism leads to the percolation of the inorganic networks through a parallel PMMA network, resulting in a material with structural heterogeneities on the range of 5 nm, evidenced by phase contrast AFM.

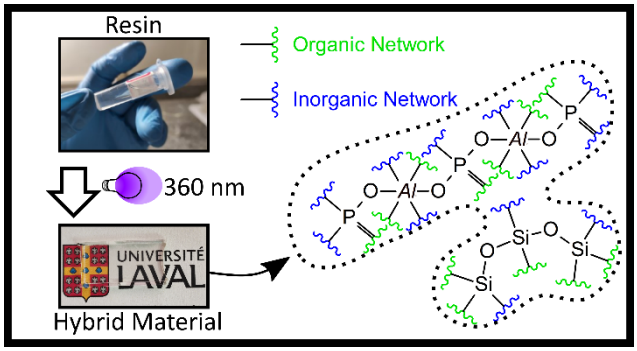

Resumo

Neste artigo, relatamos a síntese e caracterização estrutural de materiais híbridos transparentes e fotopolimerizáveis baseados em alumínio-fosfato-silicato obtidos pela rota sol-gel, com diferentes razões de alumínio:fosfato (Al:P). Exploramos o sistema $Si_{(1-x)}$ - $(Al:P)_{(x)}$ com x variando de 0,3 a 1, e razão atômica Al:P = 1:3, 1:1 e 3:1. Todas as composições contêm alta teor inorgânico (até 40% em peso). Além disso, esses materiais são compatíveis com plataformas de impressão 3D do tipo *vat-photopolymerization*. A evolução estrutural dos materiais híbridos com a concentração de silício foi investigada por MEV, contraste de fase por AFM e técnicas de RMN de estado sólido, usando experimentos de ressonância mono- e binuclear. A estrutura segue o princípio de construção *build-up* usando espécies de fosfato de alumínio e cadeias de alcoxissilano como blocos estruturais fundamentais. Essas espécies de fosfato de alumínio foram identificadas como estruturas de cadeias monoméricas e diméricas comparando diferentes parâmetros obtidos de dados de RMN com compostos modelo. Estruturas monoméricas e diméricas de cadeias fosfato de alumínio foram predominantes nas amostras com relação Al:P 3:1 e 1:3, respectivamente, promovendo e dificultando a heterocondensação com o precursor alcoxissilano, respectivamente. O mecanismo de fotopolimerização leva à percolação das redes inorgânicas através de uma rede PMMA paralela, resultando em um material com heterogeneidades estruturais na faixa de 5 nm, evidenciadas pelo contraste de fase AFM.

Résumé

Dans cet article, nous rapportons la synthèse et la caractérisation structurale de matériaux hybrides aluminium-phosphate-silicate transparents et photopolymérisables obtenus par voie sol-gel, avec différents rapports aluminium:phosphate (Al:P). Nous avons exploré le système Si(1-x) - (Al:P)(x) avec x variant de 0,3 à 1, et rapport atomique Al:P = 1:3, 1:1 et 3:1. Toutes les compositions contiennent une teneur élevée en masse inorganique (jusqu'à 40 % en poids). De plus, ils sont compatibles avec les plateformes de photopolymérisation en cuve. L'évolution structurelle des matériaux hybrides avec la concentration de silicium a été étudiée par SEM, contraste de phase AFM et techniques de RMN à l'état solide, en utilisant des expériences de résonance simple et double. La structure suit le principe d'accumulation en utilisant des espèces de phosphate d'aluminium et des chaînes d'alcoxysilane comme blocs de construction fondamentaux. Ces espèces de phosphate d'aluminium ont été identifiées comme des structures de chaînes monomères et dimères en comparant différents paramètres obtenus à partir des données RMN aux modèles composés. Les structures monomériques et dimères des chaînes de phosphate d'aluminium étaient prédominantes dans les échantillons de rapport Al:P de 3:1 et 1:3, respectivement, favorisant et entravant l'hétéro-condensation avec le précurseur d'alcoxysilane, respectivement. Le mécanisme de photopolymérisation conduit à la percolation des réseaux inorganiques à travers un réseau parallèle de PMMA, aboutissant à un matériau présentant des hétérogénéités structurales de l'ordre de 5 nm, mises en évidence par contraste de phase AFM.

Introduction

The hybrid sol-gel route is an attractive and widely explored method for synthesizing hybrid materials due to its mild processing conditions and compatibility with polymer processing techniques, including 3D printing platforms such as vat-photopolymerization (VPP) techniques.[1,2] This class of materials are commercially established products for scratch resistant and hydrophobic coatings under the trademark of ORMOCERs (organically modified ceramic),[3] but have been extensively investigated in many fields such as anticorrosive coatings, hosting matrices for photonics, chemical sensing, and medical applications, to cite a few.[4,5] This chemical route is well-described in literature,[6,7] and is based on reactants with a non-labile polymerizable group capable of undergoing condensation reactions, resulting in an inorganic network with pendant organic groups able to polymerize and form a parallel

organic network. The polymerization and condensation reactions can occur simultaneously or in different orders depending on the synthesis protocol,[8] which have profound impact on the organic and inorganic structure of the material and on its properties.[9,10]

Solid-state NMR spectroscopy is one of the most valuable and versatile techniques to elucidate the organic and inorganic structures in these materials.[11] However, most solid-state NMR studies are focused on silicate-based materials[12–15] since the alkoxysilane chemistry is well-stablished and easy to control.

Aluminum-phosphate hybrid sol-gel materials are promising candidates for the fabrication of active optical components due to promptly complexation of lanthanide ions by phosphate species, which is explored in numerous lanthanide phosphate synthesis.[16,17] This feature offers the possibility of immobilizing the rare earth ion in a low phonon energy chemical environment, improving its luminescent properties in near-infrared regime[18] without relying on high residue generating approaches such as nanoparticles synthesis[19,20] or expensive fluorinated ligands for organometallic complexes synthesis.[21] However these materials are little explored because of their poor gel forming ability and tendency to precipitate.[22–25] Such compositions are commonly used for the synthesis of metal-organic-frameworks (MOFs), due to its fast hetero-condensation and limited homo-condensation (both Al-O-Al and P-O-P)[26,27], yielding highly ordered structures. However, these materials are inappropriate for optical applications since monolithic and transparent samples are not feasible.

In a previous paper, we reported aluminum-phosphate hybrid materials obtained through photopolymerization of stable resins synthesized by the hybrid sol-gel route.[28] The materials were obtained by modifying an aluminum alkoxide with an acetylacetonate-based molecule to reduce its reactivity and using a methacrylate functionalized acidic phosphate precursor in a solventless approach. The presence of organic groups in the phosphate precursor promotes steric hindrance, reduces hetero-condensation rate and prevents the inorganic network percolation. These factors prevent gel formation, maintaining its liquid state despite the extensive formation of Al-O-P bonds in absence of solvents. Monolithic and transparent solid materials are readily available by polymerization, making these materials potential candidates for new rare-earth hosting matrices obtainable at low cost and processable by VPP.

Here, we improved these matrices by introducing a common alkoxysilane reactant - 3-(Trimethoxysilyl)propyl methacrylate (TMSPM)-, substituting the 2-hydroxyethyl methacrylate used as

solvent/monomer, resulting in an aluminum-phosphate-silicate hybrid material. Such approach increases the inorganic content (between 20 and 40% wt.) and improves the near-infrared transmission. These materials are compatible with VPP technologies, resulting in transparent bulky materials. Such compositions have been recently explored for the 3D printing of glasses, due to their potential use in the fabrication of active optical components,[29,30] however, the pristine hybrid materials are unsuitable for optical applications due to porosity or phase separation, leading to an opaque aspect. By contrast, our materials are synthesized under non-hydrolytic conditions, allowing a solventless route and pore-free bulk materials.[31] In this paper, we report the study of the Si-Al-P hybrid system formation with different concentrations of Si, Al and P, and characterization by scanning electron microscopy (SEM) and phase-contrast AFM to provide insights into the materials` structure from molecular scale, up to the microscopic scale. Because numerous parallel condensation reactions are accessible in sol-gel chemistry, the relationship between the structure and synthesis is complex. To better understand inorganic connectivity and organic-inorganic interactions in these materials, a series of ^{27}Al, ^{31}P, ^{13}C, ^{29}Si and ^{1}H single- and double-resonance NMR experiments were conducted to obtain structural insights into the speciation and distribution of silicon, phosphorus, aluminum, and organic components as well as the organic-inorganic connectivity. It is highlighted the use of the ^{1}H nuclei as a versatile probe able to study both the organic and inorganic structure, which was only possible due to the fast MAS employed in ^{1}H detection (60kHz), allowing signals to be resolved and assigned.

Materials and methods

Synthesis. Aluminum-tri-sec-butoxide 97% (Sigma-Aldrich), hydroxyethyl methacrylate phosphoric acid ester -HEMA-P- 90% (Sigma-Aldrich), 2-(Methacryloyloxy) ethyl acetoacetate-MAEAA- 95% (Sigma-Aldrich), methanol P.A. (Synth), TMSPM 98% (Sigma-Aldrich) and diphenyl (2, 4, 6- trimethyl benzoyl) phosphine oxide -TPO- 97% (Sigma-Aldrich) were used as received. HEMA-P is a mixture of phosphoric acid (32.5%), hydroxyethyl methacrylate phosphate (52.1%) and bis (hydroxyethyl methacrylate) phosphate (15%), with a calculated 189.6 $g.mol^{-1}$ molar mass based on its ^{31}P-NMR spectrum. MAEAA-modified aluminum-tri-sec-butoxide was synthesized by mixing aluminum-tri-sec-butoxide and MAEAA compound at a 1:2 molar ratio under water-free atmosphere (N_2 atmosphere, H_2O < 100 ppm) for 24 hours, yielding a clear liquid named $Al(MAEAA)_2$. HEMA-P was solubilized in methanol at 1:2 mass ratio to reduce its viscosity. TMSPM was hydrolyzed with a HCl solution (1 $mol.L^{-1}$) at 1:1 (H_2O:TMSPM) molar ratio and stirred until a clear solution was formed (typically a few minutes) and was used within an interval of 30 min after preparation.

In this paper, we explored compositions with nominal formula 0 < x < 70% TMSPM+(100-x)(1:3, 1:1 and 3:1 Al:P). Initially, HEMA-P and $Al(MAEAA)_2$ reactants were mixed for 24 h in closed vials yielding an aluminum-phosphate resin. Hydrolyzed TMSPM was added to the aluminum-phosphate resin and the mixture was stirred for another 24h. To achieve better optical quality, methanol and other solvents were removed under reduced pressure at room temperature. This step was impossible in 0% and 10% TMSPM (1:3 Al:P) compositions due to gelation upon evaporation. Compositions with 1:1 Al:P (shown in **Figure 31**) presented the best optical quality, stability, and printability through mask projection (MP) VPP process (Prusa SL1S) using 1% wt. TPO as photoinitiator. For optical characterization, monolithic samples were prepared through thermo-polymerization. AIBN was dissolved in the samples at 0.5% wt., and the resin was polymerized in plastic cuvettes at 75°C at 15 mmHg for 1 day using a vacuum oven.

Figure 31. Polished thermo-polymerized 30% TMSPM Al:P ratio of (a) 1:1, (b) 3:1, and (c) 1:3. Thickness between 2 and 4 mm, width of 10 mm and length of 15 to 30 mm. (d) 3D printed Voroni tower (5 cm height) with 0% TMSPM Al:P = 1:1 (1% wt. TPO) resin.

Absorption spectra for 30% TMSPM 1:1, 3:1 and 1:3 Al:P compositions are shown in **Figure S1** available in the Supporting Information in Annex B. These materials are transparent up to 1100 nm with a slight greenish aspect due to absorption in the blue region of the spectra associated with MAEAA. The observed absorption bands in the near-infrared region are assigned to overtones from C-H (1729 and 1176 nm), C=O (1382 nm) and O-H (1439 nm) vibrational bands.[32] Thermogravimetric analysis (TGA and DTG) for 1:3 and 3:1 Al:P compositions are presented in **Figure S2** available in the Supporting Information in Annex B. Thermal degradation in these materials occurs between 150°C and 700°C with inorganic content between 15 and 40% wt. depending on the composition.

Physicochemical Characterization. Thermogravimetric analysis (TGA) was done in a SDT Q600 (TA Instruments) equipment, with alumina crucible from 30°C up to 900°C at 10°C.min^{-1} with 100 mL.min^{-1} synthetic air dynamic atmosphere. Si, Al and P atomic contents were analyzed with an electron probe microanalyzer (EPMA) SX-100, equipped with a wavelength dispersive spectroscopy (WDS) with SiO_2, hydroxyapatite, and Al_2O_3 standards. Eight representative points were collected for each sample and the results were processed using PAP correction. Scanning electron microscopy (SEM) and atomic force microscopy (AFM) images were collected in a Quanta-3D-FEG (FEI) and Veeco Dimension V SPM. UV/VIS/NIR absorbance spectra were collected using 3mm thick polished samples in a Cary 5000 Spectrometer.

Solid State NMR: ^{31}P, ^{27}Al, and ^{13}C nuclei experiments were collected in a Bruker Avance III HD 400WB using a Triple Resonance probe under spinning speed at 14kHz. ^{27}Al MAS (Magic Angle Spinning) NMR spectra were recorded using short pulses of 1 μs length and a relaxation delay of 3 s. Chemical shifts are reported relative to a 1M $Al(NO_3)_3$ aqueous solution. ^{31}P MAS NMR spectra were recorded using $\pi/2$ pulses of 3.3 μs length and a relaxation delay of 240 s, which is long enough to ensure complete recovery of the equilibrium magnetization, yielding to quantitative ^{31}P spectra. Chemical shifts were referenced against an external 85% H_3PO_4 standard. $^{27}Al\{^{31}P\}$ rotational echo double resonance (REDOR) measurements were conducted under the same conditions, using π recoupling pulses on ^{31}P channel and acquisition of rotor-synchronized ^{27}Al spin echoes (the π pulse length was 4.5 μs in these experiments). The second moments $M_{2(Al-P)}$ characterizing the average dipolar coupling between the observed quadrupolar nuclei (^{27}Al in this case) and the neighboring ^{31}P nuclei (I = ½)[33], were obtained by applying a parabolic fit to the REDOR data within the range $\Delta S/S_0 \leq 0.2$, corresponding to the expression[34]:

$$\frac{\Delta S}{S_0} = \frac{4}{3\pi^2}(NT_R)^2 M_{2AlP}$$

$M_{2(Al-P)}$ values from the samples were compared to REDOR data on the crystalline compound model $Al(PO_3)_3$ (six Al-O-P linkages of 3.207 pm length) to estimate the average number of Al− O− P linkages. The $^{29}Si\{^1H\}$ CP-MAS and $^{13}C\{^1H\}$ CP-MAS spectra of samples were measured under spinning speed of 10 kHz, using a 2.5 and 1.0 ms CP contact time, and 5 s relaxation delay, respectively. All spectra were acquired with TPPM proton decoupling during data acquisition.[35]

^{1}H MAS and ^{1}H-X (X = ^{13}C, ^{29}Si, ^{31}P, ^{27}Al) double-resonance solid-state NMR spectra were measured on a Bruker Avance Neo spectrometer operating at 14.1 T (600 MHz for ^{1}H Larmor frequency) equipped with a Bruker HX 1.3 mm probe. ^{1}H MAS spectra were obtained with the EASY (Elimination of Artifacts in NMR Spectroscopy) pulse sequence,[36] which eliminates fast relaxing probe background signal. Spinning speed for MAS was of 60 kHz and π/2 pulse length of 1.0 μs. The recycle delays for the first and second blocks in the sequence were set to 2 s and 0.5 ms and 32 scans were acquired. ^{1}H-X-^{1}H double cross polarization (double-CP) experiments were performed at 60 kHz MAS, using the pulse sequence described by Baccile *et* al.,[37] where polarization is first transferred from ^{1}H to X spin followed by a block where X magnetization is stored on the z-axis while ^{1}H magnetization is saturated by a train of ten (10) π/2 pulses [21]. Finally, X magnetization is converted back to xy-plane and polarization is transferred from X to nearby ^{1}H and detected on ^{1}H channel. Adiabatic tangentially ramped contact pulses[38] on ^{1}H channel and squared pulses on X channel were used to achieve ^{1}H→X and X→^{1}H polarization transfer. No decoupling was employed in X-channel during ^{1}H acquisition. Typical π/2 pulse lengths for ^{1}H were 1.2 μs. For X = ^{13}C and ^{31}P the first contact pulse was fixed at 2 ms, while the second pulse was fixed at 500 μs to selectively excite the ^{1}H species in the local environment of ^{13}C/^{31}P species. For X = ^{29}Si the contact pulses were set to 4 and 1 ms respectively. For X = ^{27}Al short contact times of 500 μs were applied for both contact blocks. Typical π/2 pulse lengths for ^{13}C, ^{29}Si, ^{31}P and ^{27}Al were adjusted, respectively, to 2.0, 2.0, 1.6 and 1.0 μs. Typical nutation frequencies for the Hartman-Hahn matching condition were calibrated by fixing the ^{1}H power in 100 kHz and varying the X-channel power until a maximum was observed. Indirectly detected 2D ^{1}H-X heteronuclear correlation (HETCOR) spectra where also acquired with ^{1}H detection, using a modification of the double-CP sequence described above, after the first polarization transfer the X coherences are allowed to evolve during time t_1, while ^{1}H decoupling was achieved by a single 2.4 μs π pulse applied in the middle of the t_1 period, as described by Wiench *et* al.[39] The performance of HETCOR experiments with ^{1}H-detection and fast MAS rates provides an enhancement in sensitivity when compared to the conventional CP-HETCOR, where the low-γ nucleus is detected.[40] 2D ^{1}H−^{1}H double-quantum – single-quantum (DQ−SQ) correlation NMR experiments were performed at 60.8 kHz MAS, using $R14_4^5$ symmetry-based homonuclear recoupling scheme and no homonuclear decoupling during DQ evolution.[41] Excitation and reconversion times were of 65.8 μs (four rotor cycles) and the increment interval in the indirect dimension was set to 16.4 μs (rotor period); 256 t_1 increments were acquired, with 16 scans of accumulations for each t_1 increment and 2 s recycle delay. ^{13}C and ^{1}H chemical shifts are reported relative to tetramethylsilane (TMS) using α-glycine as secondary

reference, ^{13}C-$\delta_{(C=O)}$ = 176.5 ppm and ^{1}H-$\delta_{(NH3)}$ = 8.5 ppm.[42,43] ^{29}Si chemical shifts were referenced using kaolinite as a secondary standard (-91.5 ppm relative to tetramethylsilane) [44].

Results and discussion

Microstructure

The Si:Al:P atomic ratios of the hybrid materials were assessed using WDS to confirm the chemical composition. The data are presented in **Table S1** in the Supporting Information in Annex B and show good agreement with nominal compositions. SEM images are presented in **Figure 32 (a)** and **(b)**, showing a smooth and homogenous surface. Porosity associated with volatile components, such as residual methanol, was observed in 1:3 Al:P compositions and decreased as TMSPM concentration increased. As stated in the preparation, 0 and 10% TMSPM (1:3 Al:P) were not prepared with good optical quality due to premature gelation upon further evaporation of solvents, leaving methanol content between 10 - 20% wt. responsible for the porosity observed in the same samples' SEM images. Backscattered electron (BSE) images in **Figure 32 (c)** do not show chemical contrast, indicating chemical homogeneity at the micrometric scale. Signs of chemical inhomogeneity were observed for the 70% TMSPM (1:3 Al:P), where BSE images revealed some circular structures ranging between 5 and 10 µm scattered on the materials' surface, as shown in **Figure S3** in the Supporting Information in Annex B.

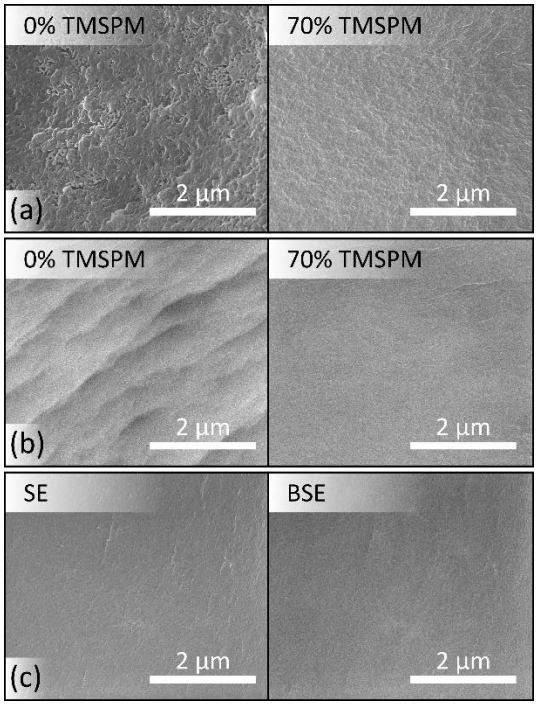

Figure 32. SEM and BSE imaging of 0% and 70% TMSPM 3:1 (a) and 1:3 Al:P (b) hybrid materials. (c) SE and BSE images of a 30% TMSPM 1:3 Al:P.

The microstructure was investigated at the nanometric scale using phase contrast AFM. This is an amplitude modulated technique in which the cantilever is driven by a fixed amplitude sinusoidal signal.[45] Conservative and non-conservative tip-surface interactions cause a phase shift, which reflects local changes in chemical and mechanical properties[46–48] allowing the study of polymers,[49,50] conjugated materials[51,52] and sol-gel hybrid materials.[12,53]

A representative phase and topography map from a 0% TMSPM (1:3 Al:P) composition is presented in **Figure 33 (a)** and **(b)**, respectively. The phase-contrast maps show nanometric domains with negative phase shift ($\varphi < -20°$) with an average equivalent radius of 5 nm embedded in the materials matrix ($\varphi > 0°$). The presence of these two domains is evident as two phase-shift distributions are observed in the distribution density plots presented in **Figure 33 (c)**. Relation plots between phase shift and topography maps presented in **Figure 33 (d)** show that these two distributions are microstructural heterogeneities since they are unrelated to topographic features, that is, these domains are randomly distributed on the sample surface.[54] Previous works in TMSPM-derived hybrid sol-gel materials have identified similar structures as inorganic domains arising from sol-gel condensation.[12] We lack information to confidently address the source of such heterogeneities in these materials. Phase-contrast and topography maps, and relation plots for the remaining 3:1 and 1:3 Al:P samples with 0%, 30%, and 70% TMSPM are presented in **Figure S4** and **Figure S5**, respectively, available in the Supporting Information in Annex B with similar results.

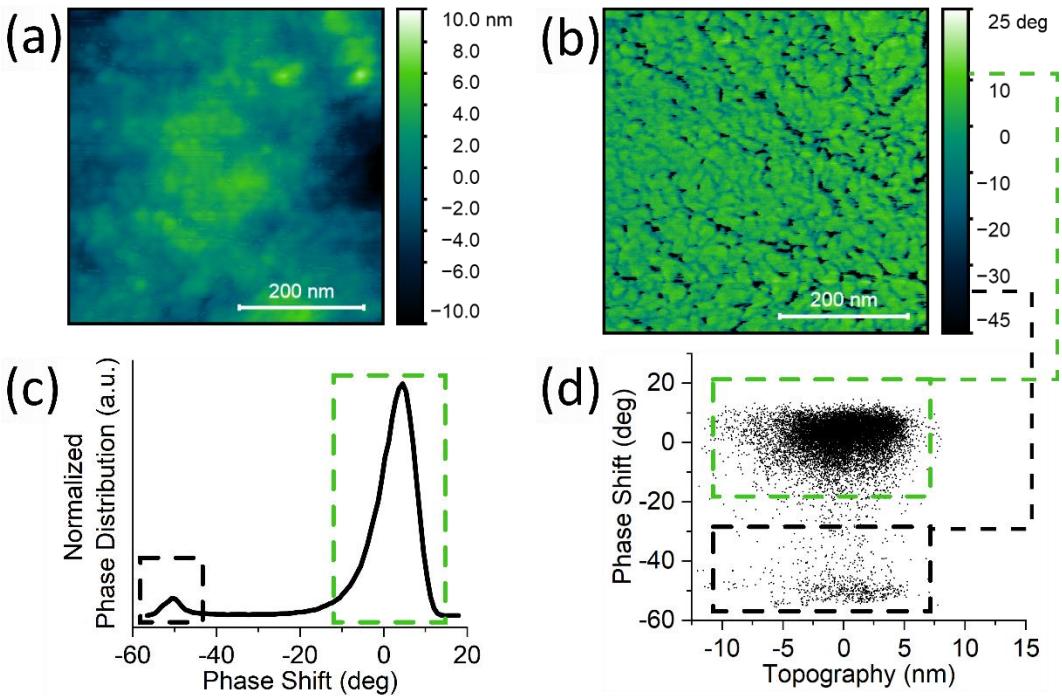

Figure 33. 0% TMSPM (1:3 Al:P) topography and phase map of a 500 nm square and phase-topography relation plot for the same sample.

^{31}P MAS-NMR

^{31}P MAS NMR spectra presented in **Figure 34** showed four ^{31}P chemical sites with characteristic chemical shift at 0, -5, -12, and -20 ppm. The spectra were deconvoluted according to the parameters presented in **Table S2** in the Supporting Information in Annex B and the structural evolution as function of TMSPM concentration is presented on **Figure 35**. Such species were identified as $Q^n_{mAl,lSi}$ phosphate sites where *n*, *m* and *l* respectively indicate the number of phosphates, aluminate and silicate structures bonded to the phosphate tetrahedron. The spectral lines observed for the sample with 0% TMSPM (3:1 Al:P) can be assigned based on previous studies on aluminum-phosphate sol-gel materials derived from aluminum-lactate.[55,56] The chemical shifts at -5.2, -11.6 and -19.9 are assigned respectively to $Q^0_{1Al,0Si}$, $Q^0_{2Al,0Si}$ and $Q^0_{3Al,0Si}$ species,[55,56] while the chemical shift at 0 ppm corresponds to isolated $Q^0_{0Al,0Si}$ units in HEMA-P.

Samples with low TMSPM content show preferential formation of $Q^0_{2Al,0Si}$ units for both Al:P ratios studied. Increasing TMSPM concentration increases the concentration of species with higher inorganic connectivity such as $Q^0_{3Al,0Si}$ and $Q^0_{2Al,1Si}$ (in general we may define these units as Q^0_3) at the expense of $Q^0_{2Al,0Si}$ and $Q^0_{1Al,1Si}$ units (which we define as Q^0_2 units). The weak sidebands indicate an

isotropic ^{31}P chemical environment with low P=O character as indicated by the fraction of Q^0_3 species around -20 ppm. The theoretical fraction of Q^0_3 species was calculated to further understand the participation of P=O bond on the aluminum-phosphate connectivity under the assumption that P=O bonds do not participate in the condensation reaction. Each P-O-C bond in the HEMA-P reactant hinders one phosphate site for the condensation reaction, since the P-O-C bond is very stable toward hydrolysis,[22,57] meaning that only the phosphoric acid (32% according to ^{31}P NMR analysis on the reactant) units present in the HEMA-P can form Q^0_3 species, while the hydroxyethyl methacrylate phosphate (52%) and bis (hydroxyethyl methacrylate) phosphate (15%) units can form only Q^0_2 and Q^0_1 species, respectively. For both Al:P ratios studied, the concentration of Q^0_3 species is superior to 32% for TMSPM concentrations higher than 30%, which is only possible if the P=O bond participates in the condensation reaction.

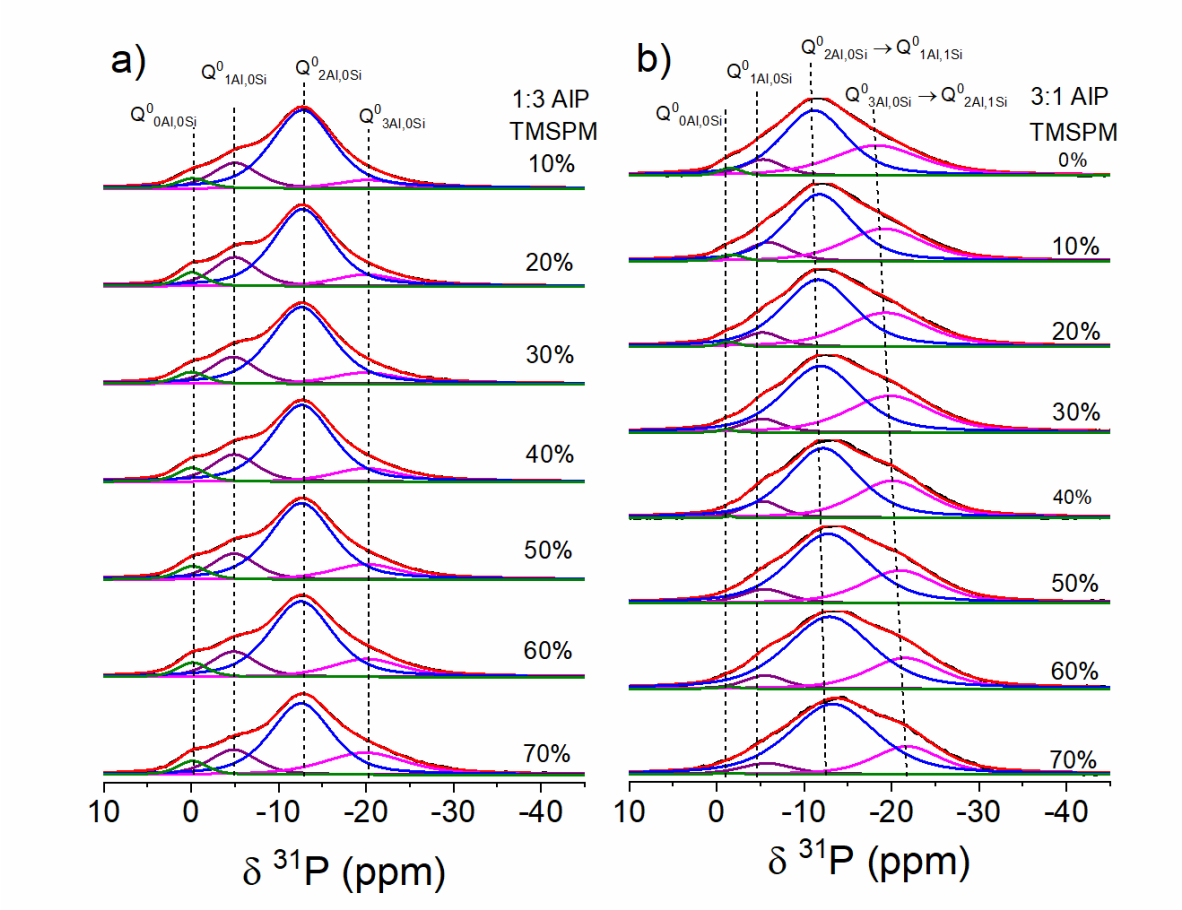

Figure 34. ^{31}P-MAS-NMR spectra from TMSPM 1:3 (a) and 3:1 (b) Al:P compositions. Experimental data is represented by black curves, and deconvolutions are presented in colored lines. The deconvolution envelope is presented by red curves.

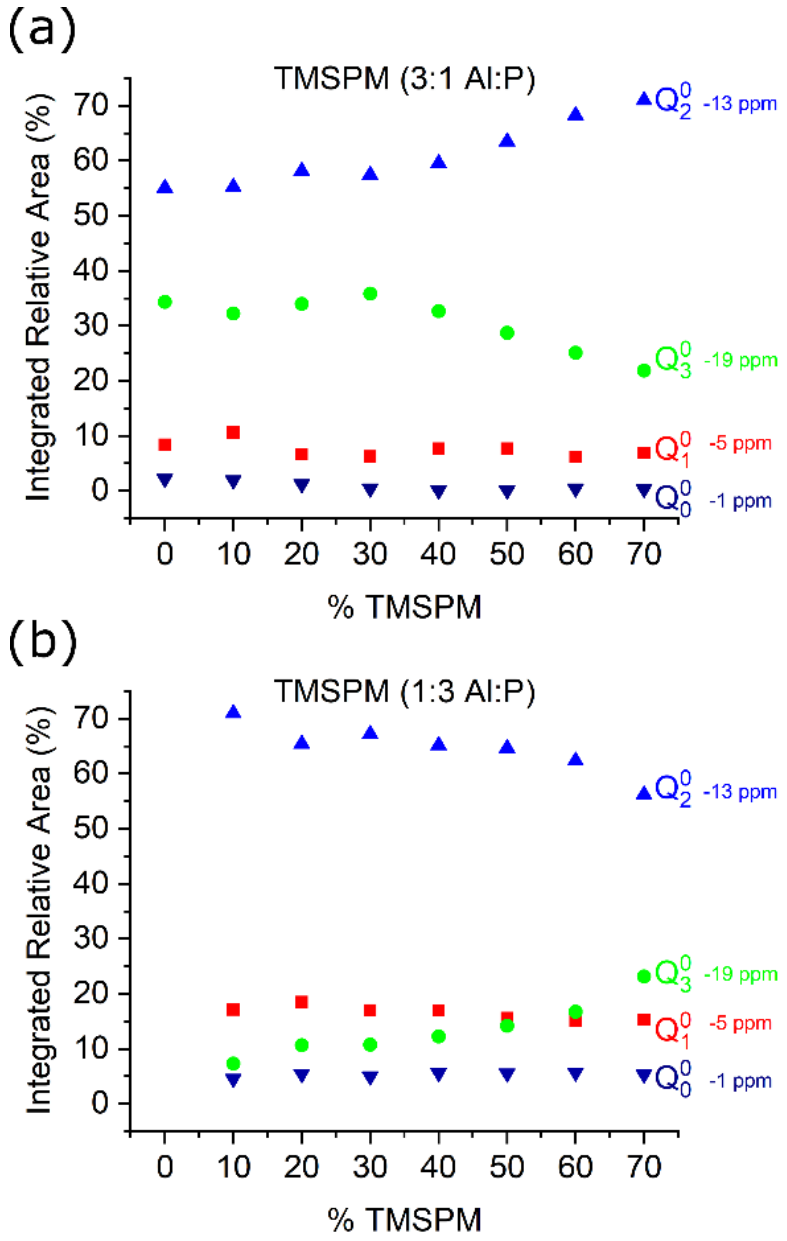

Figure 35. ^{31}P sites evolution in function of TMSPM concentration extracted from ^{31}P-MAS spectra for (a) 3:1 and (b) 1:3 Al:P ratios.

The ^{31}P peak positions for the high phosphate content (1:3 Al:P) compositions are independent of TMSPM concentration, indicating the absence of P-O-Si bonds. Low phosphate compositions (3:1 Al:P) show a monotonic upshift of Q^0_2 and Q^0_3 species with increasing TMSPM content for the 3:1 Al:P system. The most noticeable change is observed for the Q^0_3 ^{31}P species, shifting from -18 ppm to -22 ppm when TMSPM concentration increases from 0% to 70% TMSPM. This trend indicates that silicate species are gradually introduced into the first and/or second coordination sphere of phosphate sites. The formation of Si-O-P bonds in sol-gel chemistry is unlikely due to the susceptibility of the chemical

bound to hydrolysis,[23,24,58] while the formation of Al-O-Si bonds is favored.[59] Thus, it should be expected that the observed changes in the chemical environment of phosphate arise from modifications in the second coordination sphere through the formation of Si-O-Al bonds. Nonetheless, the observed chemical shift variation is comparable to phosphate species observed on silicate-phosphate and aluminum-phosphate systems[23,60] and by chemical shielding calculations in $Q^0_{mAl,nSi}$ systems, with *m,n* = *0, 1, 2, 3, 4,*[61] suggesting that the substitution of P-O-Al by P-O-Si is possible, i.e., the conversion of $Q^0_{2Al,0Si}$ units into $Q^0_{1Al,1Si}$ units and $Q^0_{3Al,0Si}$ units into $Q^0_{2Al,1Si}$ units.

^{27}Al MAS-NMR and ^{27}Al{^{31}P} REDOR

^{27}Al MAS NMR spectra for 3:1 and 1:3 Al:P compositions with different TMSPM concentrations are shown in **Figure 36 (a)**, and **(b)**, respectively. A representative ^{27}Al TQMAS spectra for 70% TMSPM 1:3 and 3:1 Al:P compositions are presented in **Figure S6** available in the Supporting Information in Annex B. Samples with 3:1 and 1:3 Al:P ratios showed ^{27}Al sites with peaks centered at around 0 ppm and -13 ppm, respectively. Such species are assigned to hexacoordinated (Al^6) aluminum-phosphate units and the signal upshift is associated to the number of phosphate species around (Al^6) species,[55] indicating a higher coordination of phosphate sites around the Al^6 site in phosphate rich samples. ^{27}Al TQMAS show only one Al^6 site in 1:3 Al:P compositions, while for 3:1 Al:P compositions at least two distinct Al^6 sites are observed.

Further information about P-O-Al connectivity is provided by ^{27}Al{^{31}P} REDOR experiments. The REDOR pulse sequence recovers the ^{27}Al-^{31}P dipole-dipole coupling, allowing the measurement of the dipolar second moment ($M_{2(Al-P)}$), which is related to the average number and distance of phosphate species coordinated to the aluminum site.[33] From the analysis of the ^{27}Al{^{31}P} REDOR lineshapes for 3:1 Al:P compositions (**Figure S7** in Supporting Information in Annex B), it is not possible to differentiate the REDOR dephasing for both Al^6 sites, due to the very low-concentration of the site at higher field. Therefore, the reported $M_{2(Al-P)}$ values correspond to the average taken from the integrated contribution of all Al^6 sites. The REDOR dephasing curves are shown in **Figures S8** and **S9**, available in the Supporting Information in Annex B. **Table 8** summarizes the dipolar second moments extracted from the parabolic analysis of the REDOR curves. By considering the measured second moment on the $Al(PO_3)_3$ crystal, the average number of P in the coordination environment of Al^6 can be estimated, giving average values around 0.7 and 4 for the 3:1 Al:P and 1:3 Al:P systems,

respectively. There is no noticeable variation in the average number of Al-O-P linkages [(Al^{6})-$(O\text{-}P)_n$] as a function of the TMSPM concentration.

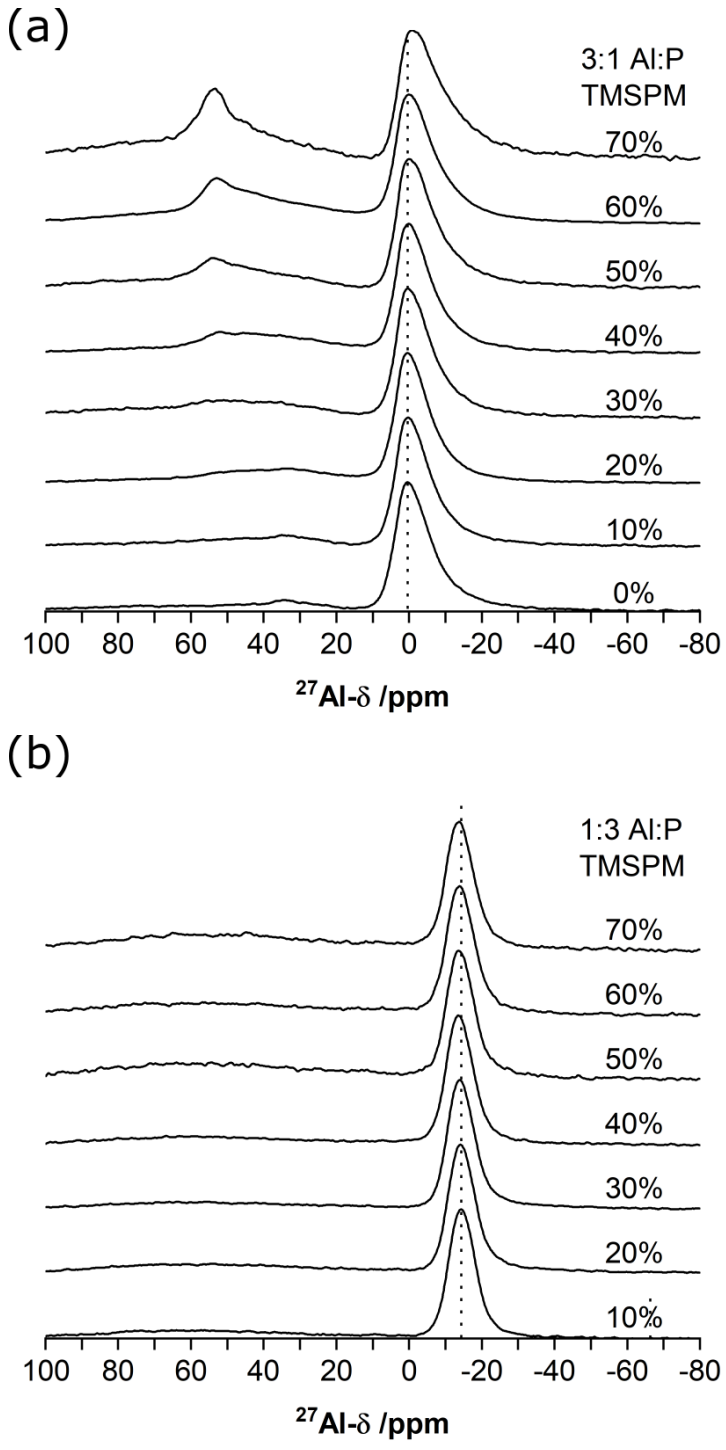

Figure 36. ^{27}Al-MAS-NMR spectra from TMSPM 3:1 (a) and 1:3 (b) Al:P compositions.

Table 8. Integrate area obtained from ^{27}Al MAS NMR spectra and M_2 values calculated from $^{27}Al\{^{31}P\}$ REDOR curves and estimated average number of phosphates bonded to each hexacoordinate aluminum in 1:3 and 3:1 Al:P compositions with different concentrations of TMSPM.

	3:1 Al:P				1:3 Al:P			
% TMSPM	M_2 ($x10^6$ rad^2s^{-2})	Al-$(O-P)_n$	Al^4 and Al^5(%area)	Al^6 (%area)	M_2 ($x10^6$ rad^2s^{-2})	Al-$(O-P)_n$	Al^4 and Al^5 (%area)	Al^6 (%area)
0	0.60	0.58	17	83	-	-		-
10	0.71	0.67	17	83	4.0	3.9	28	72
20	0.75	0.73	25	75	4.2	4.0	30	70
30	0.66	0.64	34	66	4.4	4.3	22	78
40	0.63	0.61	33	67	3.5	3.4	25	75
50	0.78	0.75	34	66	3.5	3.4	43	57
60	0.72	0.71	44	56	3.6	3.5	34	66
70	0.79	0.76	48	52	4.4	4.3	42	58
$Al(PO_3)_3$	5.8	6						

^{27}Al sites spawning from 100 to 0 ppm are observed and correspond to tetracoordinate (Al^4) and pentacoordinate (Al^5) species assigned to $Al[(-O-P)_n(-O-Al)_m(-O-Si)_l]$ (n+m+l = 4 or 5) sites. Al^4-$(O-P)_n$ and Al^4-$(O-Al)_m$ species show typical chemical shift between 0 and 45 ppm and between 60 and 100 ppm, respectively, while Al^4-$(O-Si)_l$ is found around 50 ppm.[62] The formation of Al-O-Al bonds is energetically unfavorable as stated by the Lowenstein's rule,[59,63] and the Al^4-$(O-Al)_m$ sites show a broad and weak signal suggesting a variety of different ^{27}Al sites in small quantity that are not observable in ^{27}Al TQMAS experiment.

Structural changes with the addition of TMSPM in the composition are observed only in 3:1 Al:P samples, with the appearance of ^{27}Al sites with characteristic chemical shift at 54 ppm, assigned to tetracoordinate aluminum-silicate species.[64] Previous studies on similar system have showed ^{27}Al lines at 45 ppm assigned to Al^4-$(O-P)_n$ units,[28] in clear distinction to the signals observed here. An upshift of 2 ppm is also observed at the Al^6 site for the same set of samples. These observations indicate that a small fraction of TMSPM bonds to Al^6 sites in 3:1 Al:P samples, resulting in $[(Al^4)(O-Si)_4]$ aluminum-silicate species,[64,65] in addition to the Al^4 site. Little interaction with Al^6 sites is observed, indicating that the $[(Al^6)(O-Si)_l]$ are not favorable. In opposition, ^{27}Al sites in 1:3 Al:P samples have poor reactivity with TMSPM, and the difference of phosphate coordination around the Al^6 site revealed by

$^{27}Al\{^{31}P\}$ REDOR analysis suggests that phosphate groups bonded to the Al^6 sites promote steric hindrance and limits the formation of Al-O-Si bond.

NMR is a versatile and robust technique, but structural elucidation is limited up to the second or third coordination sphere, meaning that network connectivity at long range is not directly accessible through NMR. Nonetheless, short range connectivity can still elucidate the materials' structure if prior information on the studied system is available. Fortunately, it is well-know that the inorganic network in aluminum-phosphate hybrid materials is formed through hetero-condensation process,[63] since Al-O-Al bond and P-O-P bonds are rarely formed due to Lowenstein rule[59,63] and the poor homo-condensation of phosphate species.[22,66] Furthermore, the NMR data presented here indicates that the build-up principle[2,67] is valid for such system since ^{31}P and ^{27}Al NMR data do not indicate appreciable substitution of Al-O-P bonds in favor of Al-O-Si or P-O-Si bonds. Thus, the formation of the inorganic network in these aluminum-phosphate-silicate hybrid materials can be understood in terms of aluminum-phosphate building blocks formed during the hetero-condensation of the aluminum alkoxides and phosphate precursor in the first step, followed by structural modifications in an additive way by the hydrolyzed TMSPM.

Further insight into the structure of these aluminum-phosphate building blocks for the two Al:P ratios studied was provided by comparing the data obtained through solid-state NMR data with the structure of the compound models presented in the **Figure 37**. The selected compound models were linear (1D) aluminum-phosphate structures, since they have been widely reported in literature during the synthesis of metal-phosphonate compounds employing similar experimental conditions found here (room temperature, and aluminum and phosphate reactants).[63] These units are known to self-assembly to form 2D (sheet-like) and 3D (cluster-like) networks by increasing the connectivity of the phosphate sites, forming Q^0_{3Al} (2D) and Q^0_{4Al} (3D) in addition to the Q_2 units present in the linear structures.[63] Particular attention was paid to the 1D units due to the abundance of Q^0_{2Al} phosphate units compared to Q^0_{3Al} as evidenced by NMR data. Furthermore, the organic group bonded to the phosphate unit hinders at least one site from forming bridging bonds. Thus, the formation of three-dimensional and bidimensional networks are unlikely since both hydroxyethyl methacrylate phosphate (52%) and bis (hydroxyethyl methacrylate) phosphate (15%) units hinder the formation of highly branched structures. $Al(PO_3)_3$ and $AlPO_4$ crystalline structures were also considered to highlight the discrepancies in the local coordination of phosphate and aluminate structures compared to the studied compounds.

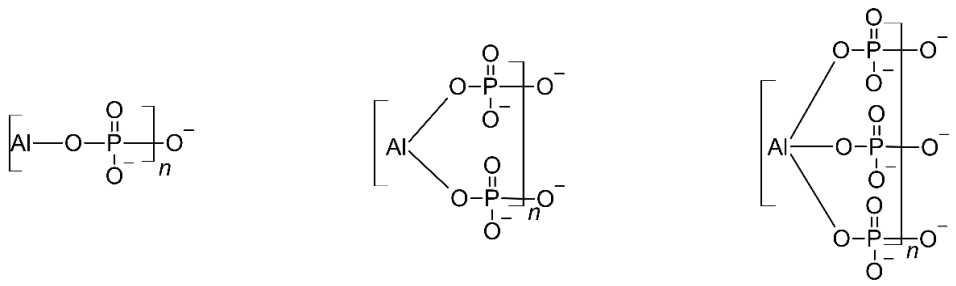

Aluminum Phosphate Chain Aluminum Phosphate Dimer Aluminum Phosphate Trimer

Figure 37. Linear aluminum-phosphate compound models for calculating the average number of phosphate and aluminate structures coordinated to each other and the distribution of Q_n phosphate and the coordination of the Al sites units.

The parameters employed for comparison were the distribution of Q^0_{nAl} ^{31}P species, the coordination of the Al sites, and the average P-O-Al linkage (aluminum around the phosphate $(PO_4)^{3-}(\text{-}Al^{3+})_{\bar{m}}$) as well the average Al-O-P linkage (phosphate around the aluminate $(AlO_6)^{9-}(\text{-}P^{5+})_{\bar{n}}$) on the unmodified aluminum-phosphate inorganic network. The distribution of the observed Q_n phosphate units $Q^0_{1Al,0Si}$, $Q^0_{2Al,0Si}$ and $Q^0_{3Al,0Si}$ bonded to Al^6 units is readily accessible from solid-state NMR data. The average number of aluminate bonded to phosphate sites ($(PO_4)^{3-}(\text{-}Al^{3+})_{\bar{m}}$) can be calculated using **Equation 1** with the ^{31}P MAS-NMR deconvolutions. The average number of phosphate bonded to aluminate species ($(AlO_6)^{9-}(\text{-}P^{5+})_{\bar{n}}$) requires additional information from $^{27}Al\{^{31}P\}$ REDOR data and can be calculated using **Equation 2**,

$$(\boldsymbol{PO_4})^{3-} - (f_1 + 2f_2 + 3f_3).\boldsymbol{Al^{3+}} \qquad \text{Equation 1}$$

$$(\boldsymbol{AlO_6})^{-9} - (f(Al^6) * \bar{n}).\boldsymbol{P^{5+}} \qquad \text{Equation 2}$$

where f_1, f_2, and f_3 are the fraction of $Q^0_{1Al,0Si}$, $Q^0_{2Al,0Si}$ and $Q^0_{3Al,0Si}$ units observed at -5, -12, and -20 ppm in ^{31}P MAS-NMR respectively, $f(Al^6)$ is the Al^6 sites fraction, and $\bar{n}$ is the average number of phosphate units bonded to Al^6 sites calculated from M^2 obtained from $^{27}Al\{^{31}P\}$ REDOR experiment. It is assumed that all phosphate is bonded to Al^6 sites, which is a reasonable assumption since no appreciable Al^4 or Al^5 sites were detected for the 0% and 10% TMSPM samples in both Al:P ratios. The calculated ($(PO_4)^{3-}(\text{-}Al^{3+})_{\bar{m}}$) and ($(AlO_6)^{9-}(\text{-}P^{5+})_{\bar{n}}$) ratios based on **Equation 1** and **2** for samples without TMSPM are presented in **Table 9**. For the compound models, these parameters are readily accessible in the literature for $Al(PO_3)_3$[68] and $AlPO_4$[69] crystalline structures. For the molecular, linear,

dimeric and trimeric aluminum-phosphate structures, structural models were drawn based on literature,[63,70,71] as presented in **Figure 37**. The $((PO_4)^{3-}(-Al^{3+})_m)$ and $((AlO_6)^{9-}(-P^{5+})_n)$ ratios were calculated by counting the number of Al-O-P bonds and dividing by the number of phosphorus and aluminum atoms within a molecule with n repeating units. These linear structures are composed only by Q^0_{2Al} ^{31}P species, with hexacoordinate Al sites.

For 3:1 Al:P samples, **Table 9** indicates that the aluminum-phosphate network is composed by aluminum-phosphate structures with the general formula $(Al)-(PO_4-(Al))_n$, with n=1 and n>1 corresponding to molecular units and aluminum-phosphate chains. The average fraction of P^{5+} to AlO_6 in 0% TMSPM 3:1 Al:P sample $((AlO_6)^{9-}(-P^{5+})_{0.5})$ below one indicates the presence of aluminate species that are not bonded to any phosphate species, and the two different Al^6 sites revealed by ^{27}Al TQMAS suggest that they correspond to unreacted aluminum alkoxide and the terminal aluminate group present in the aluminum-phosphate molecular structure. The Q^0_{3Al} units in ^{31}P MAS spectrum indicates that branched aluminum-phosphate chains are present but are less abundant than the molecular units. On the other hand, 1:3 Al:P compositions show an aluminum-phosphate inorganic network composed by dimeric and trimeric chain structures, and the presence of Q^0_{3Al} species suggests the formation of sheet-like structures through the percolation of these dimeric and trimeric chains. Such dimer and trimer structures have been observed in similar aluminum-phosphate materials with 1:3 Al:P stoichiometry synthesized from organic phosphates and aluminum alkoxide.[70,71] ^{27}Al TQMAS data showed only one Al^6 site, indicating a similar chemical environment for all ^{27}Al species, which agrees with the dimer/trimer structure proposed.

Table 9. The average number of aluminum atoms bonded to phosphate and phosphorus bonded to aluminate according to ^{31}P and ^{27}Al MAS spectra for 3:1 and 1:3 Al:P samples.

Compound	$(PO_4)^{3-}(-Al^{3+})_m^-$	$(AlO_6)^{9-}(-P^{5+})_n^-$	Q_n ^{31}P	$Al^{(CN)}$
3:1 Al:P (0% TMSPM)	2	0.5	Q_3 and Q_2	$Al^{(6)}$
Phosphate-complexed aluminum (Molecular Structure)	$n \leq 4$	1	Q_n	$Al^{(4)}$ and $Al^{(6)}$
Aluminum Phosphate chain	2	1-2	Q_2	
Aluminum Phosphate Dimer	2	2-4	Q_2	
1:3 Al:P (10% TMSPM)	2	3	Q_2	$Al^{(6)}$
Aluminum Phosphate chain	1-2	2	Q_2	$Al^{(4)}$ and $Al^{(6)}$

Aluminum Phosphate Dimer	1-2	4	Q_2	
Aluminum Phosphate Trimer	1-2	6	Q_2	$Al^{(6)}$
Aluminum Metaphosphate ($Al(PO_3)_3$)	2	6	Q_4	$Al^{(6)}$
Aluminum Phosphate ($AlPO_4$)	4	4	Q_4	$Al^{(4)}$

$^{29}Si\{^1H\}$ CP-MAS-NMR

Figure 38 shows $^{29}Si\{^1H\}$ CPMAS NMR spectra for the studied compounds. The CPMAS spectral intensities depend not only on the concentration of resonating species, but also on the efficiency of the ^1H-^{29}Si polarization transfer. Therefore, this experiment is not quantitative. Nevertheless, semiquantitative information about differences in the distribution of silicate species can be obtained. The spectra in **Figure 38** are composed of three main peaks, with maxima around of -50, -58, and -67 ppm. Resonances in this range can be assigned to trifunctional silicate T^n units $[RSi(OH)_{3-a}(O\text{-}P)_n(O\text{-}Al)_m(O\text{-}Si)_l$ where $n+m+l = a \leq 3$ and R is the organic groups] resulting from TMSPM condensation.[15,72] Unambiguous attribution for each ^{29}Si peak is not straightforward, since concurrent effects must be taken in account. Substitution of Si-O-Si linkages by Si-O-Al in T^n units causes a ^{29}Si downfield shift of up to ~10 ppm,[73] while connectivity to P species causes an upfield variation in the ^{29}Si chemical shifts.[74] Nevertheless, ^{31}P and ^{27}Al NMR has demonstrated that changes in the inorganic connectivity are observed only for samples with small amounts of P species and high concentrations of TMSPM. We can therefore assume that there is a preference for homo-condensation of the Si units and attribute the observed ^{29}Si chemical shifts of -50, -58, and -67 ppm to assigned to T^1, T^2, and T^3 units, respectively.

Based on the suggested ^{29}Si assignments, the 1:3 Al:P series experienced an increase in T^1 and T^2 units compared to T^3 units with higher TMSPM concentration, which correlates with an increase of the concentration of phosphorus Q^0_3 units (as revealed by ^{31}P NMR) without any changes in the ^{27}Al NMR spectra. These observations suggest a preferential homo-condensation mechanism in phosphate-rich samples, resulting in T^1 and T^2 structures corresponding to chain and terminal silicate groups, with minor hetero-condensation with phosphate, evidenced by the increase in Q^0_3 ^{31}P sites. In contrast, $^{29}Si\{^1H\}$ CPMAS spectra for 3:1 Al:P compositions do not experience significant changes in the relative intensities with the addition of TMSPM. On the other hand, the spectral linewidth is slightly larger for samples with low TMSPM concentration, which is an indication of a more heterogeneous environment, which may agree with the presence of a very minor amount of hetero-condensed Si-O-Al

and Si-O-P linkages. This assumption agrees with ^{27}Al and ^{31}P data, which also indicate the presence of these hetero-linkages. Nevertheless, the concentration of these species is small, as evidenced by the fact that they only affect the NMR spectra of the observed nuclei for very high relative concentration of the hetero-species.

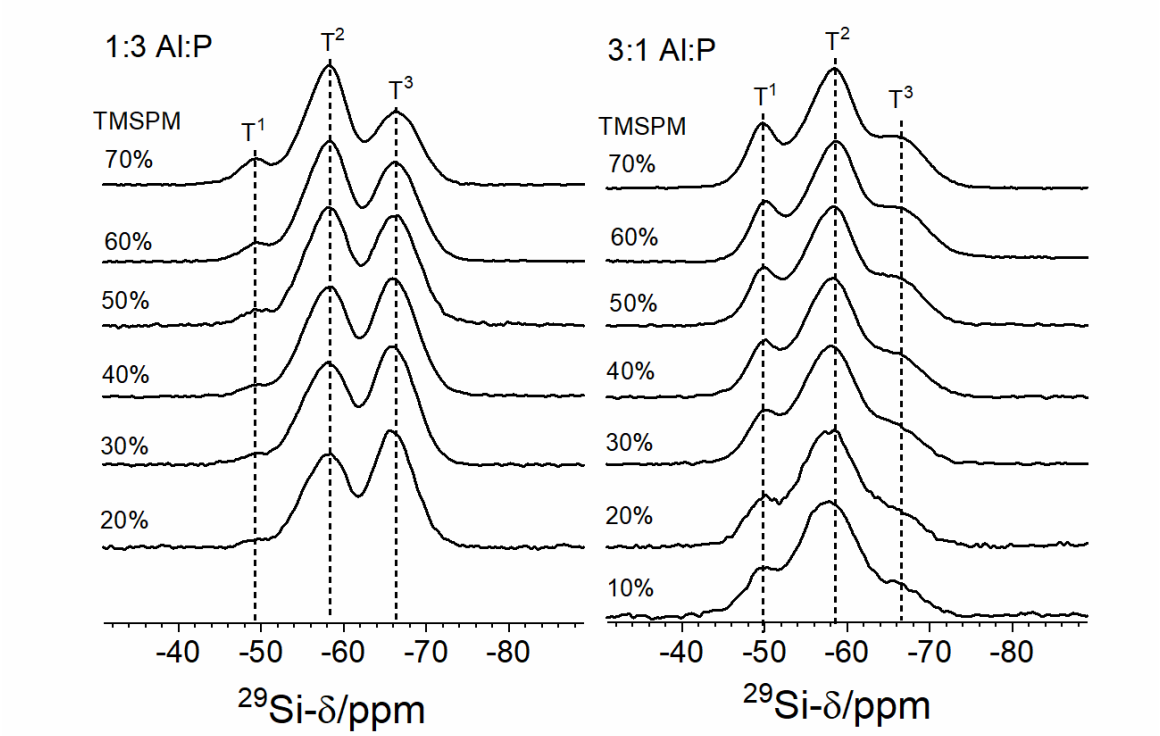

Figure 38. $^{29}Si\{^{1}H\}$ CP-MAS spectra from TMSPM 1:3 and 3:1 Al:P compositions as a function of TMSPM concentration. The spectra are normalized by the maximum intensity.

Altogether, the observed changes in ^{31}P and ^{27}Al MAS spectra suggest TMSPM condensation in 1:3 Al:P compositions result in alkoxysilane chains with limited interaction/bonding to aluminum-phosphate structures. On the other hand, 3:1 Al:P samples exhibit aluminum-phosphate and TMSPM interactions to some extent, suggesting that the hetero-condensation and homo-condensation mechanism compete, and shorter silicate chains must be formed. These NMR experiments showed that TMSPM is prone towards hetero-condensation with aluminum in both Al:P ratios studied is hindered by steric effects introduced by the phosphate species coordination around the Al^{6} site. In opposition, hetero-condensation with phosphate is little expressive in both Al:P ratios studied, and is possibly associated to the weakness of the Si-O-P chemical bonds, which readily undergo hydrolysis.[23,57,58] For the synthesis of this samples, water is only present in trace amounts during

TMSPM hydrolysis, and residual water is removed from the medium, since the aluminum-phosphate precursor itself act as a drying agent. Despite the introduced synthesis conditions, the formation of Si-O-P bonds is little expressive and TMSPM mostly undergoes homo-condensation. Based on these considerations, the aluminum-phosphate-silicate inorganic structure is defined by the building blocks formed during the aluminum and phosphate hetero-condensation. In 3:1 Al:P samples, the hexacoordinate aluminum-phosphate building blocks consist in molecular and chain (Al)-(PO_4-(Al))$_n$ structures ($n \geq 1$) and unreacted aluminum alkoxide. The aluminum sites are less hindered by phosphate groups and readily interact with the hydrolyzed TMSPM, resulting in competing alkoxysilane homo-condensation and hetero-condensation mechanism, which should lead to short silicate chains crosslinking the aluminum phosphate building blocks. In comparison, 1:3 Al:P compositions result in aluminum-phosphate dimeric/trimeric chain structures, and the aluminum coordination is saturated by phosphate species. The TMSPM shows little interaction with the aluminum-phosphate building blocks and the homo-condensation mechanism predominates, resulting in silicate chains. There are no microstructural differences between the 3:1 and 1:3 Al:P samples, despite their structure being fundamentally different, which suggests that the polymerization of the sol through the methacrylate groups promotes the anchoring and formation of an interpenetrating network of the aluminum-phosphate building blocks and silicate chains.

^{1}H MAS and ^{13}C[^{1}H] CP-MAS NMR

The organic functionalities present in the hybrid materials were characterized with high speed ^{1}H NMR MAS (60kHz) and ^{13}C{^{1}H} CP-MAS NMR experiments. A representative ^{13}C{^{1}H} CP-MAS NMR spectra and the signal assignment are presented in **Figure 39** and **Table 10**. These assignments were based on literature data[14,15,72,75–85] and on 1D and 2D ^{1}H{^{13}C}, ^{1}H{^{29}Si} and ^{1}H{^{31}P} double-CP HETCOR experiments discussed on the sections below. All ^{13}C signals were assigned to the polymethylmethacrylate (PMMA) structure with a functional group according to the reactants used (propyl silyl from TMSPM, ethyl acetyl acetonate from MAEAA and ethyl phosphate from HEMA-P). The ^{13}C assignments in **Figure 39** show two tautomer configurations for the MAEAA reactant in its keto (C3, C4, C5, and C6, with peaks at 168, 50, 202, and 30 ppm respectively) and enol form (C3‘, C4’, C5’, and C6’, with peaks at 175, 85, 190, and 26 ppm respectively). The enol tautomer chelates the aluminum alkoxide and is observed only in the 3:1 Al:P compositions, indicating the presence of unreacted aluminum sites.[78] The relative intensity of the enol tautomer compared to the keto tautomer decreases with higher TMSPM concentration. This observation is coherent with the appearance of Al^{4}

sites assigned to aluminum-silicate species in ^{27}Al MAS-NMR spectra, indicating the formation of Si-O-Al bonds with elimination of MAEAA from the aluminum coordination.

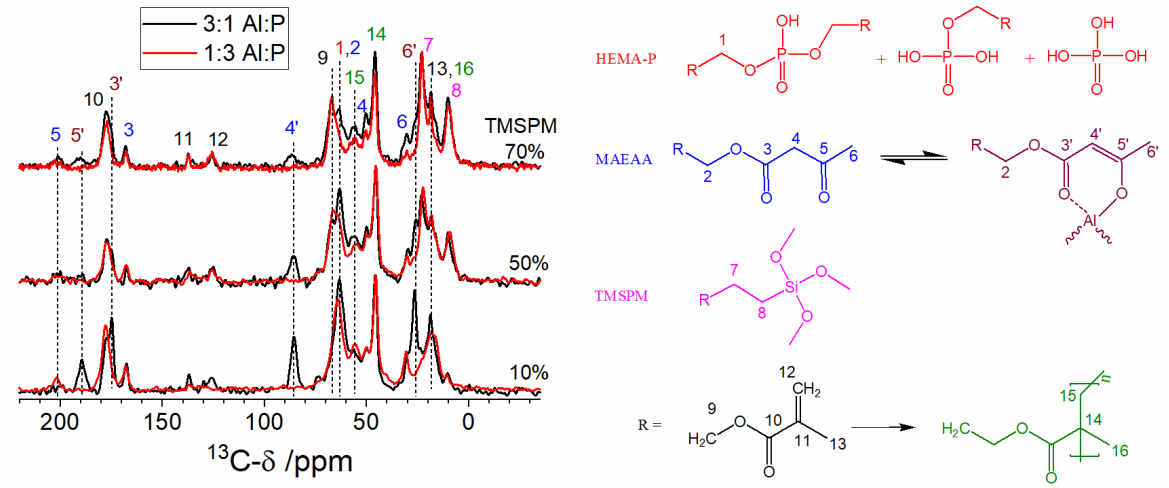

Figure 39. ^{13}C{^{1}H} CPMAS spectra of hybrid samples (right). The numbers correspond to line attributions based on the C-labels shown in the scheme on the right.

Table 10. Assignments of ^{13}C NMR lines observed in this work and ^{1}H chemical shifts of the ^{1}H-^{13}C cross peaks observed in ^{1}H{^{13}C} CP HETCOR spectra. Values in brackets correspond to the ^{1}H second neighbors to the highlighted ^{13}C site according to the cross peaks at ^{1}H{^{13}C} CP HETCOR spectra.

Assignment	^{13}C-δ_{iso} (±1 ppm)	^{1}H-δ_{iso} (±0.5 ppm)	Reference
1,2 (O**C**H$_2$CH$_2$O)^{1,2}	64	4.1	75,78,79,83
3 (O**C**OCH$_2$)^{2,3}	168	(4.1)	75,80,81,83,84
4 (CO**C**H$_2$CO)^{2,3}	50	3.5[a]	
5 (CH$_2$**C**OCH$_3$)^{2,3}	202	(4.1) (2.6) (1.3)	
6 (CO**C**H$_3$)^{2,3}	30	2.1 (4.3)	
3' (O**C**OCH)^{2,3}	175	(5.0) (1.8)	
4' (CO**C**HCO)^{2,3}	85	5.1	
5' (CH**C**OCH$_3$)^{2,3}	190	(5.0) (1.8)	
6' (CHCO**C**H$_3$)^{2,3}	26	1.7 (4.1)	
7 (OCH$_2$**C**H$_2$CH$_2$Si)	22	1.2	14,15,72,76,77,82
8 (CH$_2$**C**H$_2$Si)	10	0.6	
9 (CH$_2$**C**H$_2$O)^{1}	67	4.1	
10 (O**C**(O)C(CH$_3$)=CH$_2$)^{1}	178	(1.2)	14,15,78,86
11 (OC(O)**C**(CH$_3$)=CH$_2$)^{1}	137	(5.8) (1.7)	
12 (OC(O)C(CH$_3$)=**C**H$_2$)^{1}	125	5.5/6.1	
13 (OC(O)C(**C**H$_3$)=CH$_2$)^{1}	18	1.7 (3.2)	
14 (OC(O)**C**(CH$_3$)(CH$_2$))^{4}	179[a]	(1.3) (3.2)	85,87,88

15 (OC(O)C(CH_3)(**C**H_2))[4]	56	1.7[a]	
16 (OC(O)C(**C**H_3)(CH_2))[4]	20	1.0[a]	

[a] Expected chemical shift values for sites not observed due to overlapping signals.

Figure 40 shows the ^{1}H NMR spectra under fast MAS (60 kHz) for both series of samples (1:3 and 3:1 Al:P). Peak assignment in ^{1}H spectra was based on one- and two-dimensional ^{1}H{X} double-CP experiments (X = ^{29}Si, ^{13}C, ^{27}Al and ^{31}P) and ^{1}H single-quantum/double-quantum (SQ/DQ) correlation experiments detailed below. The peaks that can be resolved were assigned as presented in **Figure 40** and compiled in **Table 10**, using the same numerical labels as in **Figure 39** for ^{13}C nuclei. Similar to ^{13}C NMR results, ^{1}H peaks assigned to the enol and keto tautomer of MAEAA are clearly observed in the samples. The H6 line at 2.1 ppm from the keto form is evident in 1:3 Al:P compositions, while the 1.9 and 4.9 ppm lines (H6' and H4' respectively) assigned to the enol tautomer are visible in the 3:1 Al:P composition. The increase in TMSPM concentration for both Al:P ratios studied showed a decrease in MAEAA concentration observed by the simultaneous reduction of H4, H6`, and H6 sites, while the 1 ppm line increases with higher abundance of H7 and H8 sites from TMSPM.

The ^{1}H signal at 1.9 ppm is an overlap between the resonance of H6' (from MAEAA), H13 (unpolymerized methacrylate), and H15 (polymerized methacrylate). Unpolymerized methacrylate groups are observed as ^{1}H peaks at 6.0 and 5.5 ppm assigned to the non-equivalent C=CH_2 protons (H12 in **Figure 39**). The 1.9 ppm signal is sensitive to the polymerization degree because the H13 (α-methyl of unpolymerized methacrylate) and H15 (CH_2 polymer backbone) have similar chemical shift but differ by one proton. The 1:3 Al:P samples show an increase at the H13 and the H12 (relative to the C=C) species as TMSPM concentration increases, suggesting a higher fraction of unpolymerized methacrylate groups in these samples. In opposition, the 3:1 Al:P compositions show a constant relative intensity of H12 species compared to the 1.9 ppm band intensity, indicating that the overall decrease of 1.9 ppm signal arises from the reduction of MAEAA species, while the concentration of unreacted C=C bonds throughout this series of samples remains constant. These assignments are in complete agreement with ^{1}H DQ-SQ NMR measurements shown in **Figure S10**.

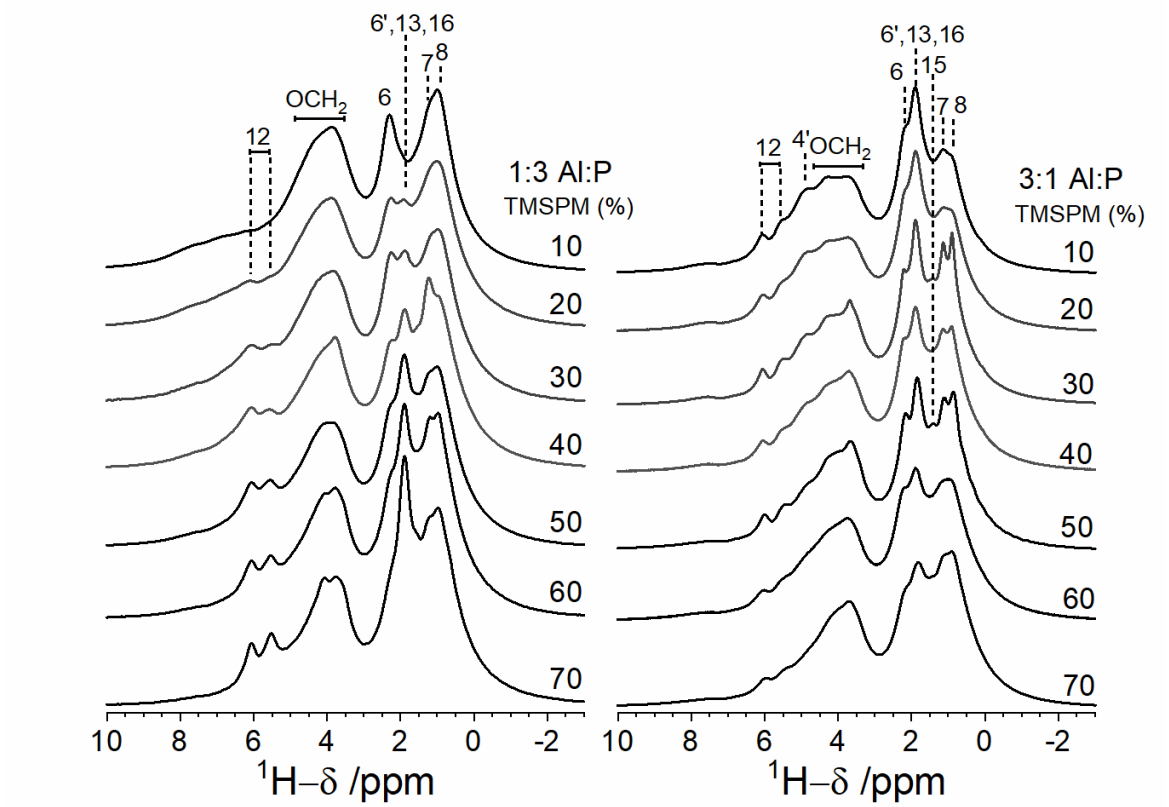

Figure 40. ^{1}H MAS spectra for the investigated hybrid compounds and attributions based on C-labels in **Figure 39**.

$^{1}H\{^{13}C\}$ and $^{1}H\{^{29}Si\}$ double-CP HETCOR

The bonding between inorganic and organic moieties in these series of hybrid materials was studied with two-dimensional $^{1}H\{X\}$ double-CP experiments (X=^{13}C or ^{29}Si). These experiments recover X-^{1}H dipolar coupling and reveal the spatial correlation between the studied nuclei. **Figure 41** shows $^{1}H\{^{13}C\}$ and $^{1}H\{^{29}Si\}$ double-CP HETCOR spectra measured at 60 kHz MAS with ^{1}H detection for samples with 50% TMSPM from 1:3 and 3:1 Al:P series. The experiments were performed using long contact times to probe second neighbors' connectivity. The $^{1}H\{^{29}Si\}$ 2D spectra show correlations of T^1, T^2 and T^3 ^{29}Si species with CH_2 protons covalently attached to Si (H8 in the scheme of **Figure 39**, δ-^{1}H = 0.6) and weaker correlations with the second neighbor CH_2 (H7, δ-^{1}H = 1.2). Additional correlations with ^{1}H site around 4 ppm are observed and are assigned to the third CH_2 neighbor (H9 δ-^{1}H = 4.1) or protons H1 from HEMA-P. The H9/H1 correlation is more evident in 1:3 Al:P samples compared to 3:1 Al:P, supporting that the Si-O-P hetero-condensation mechanism has a higher contribution in these series of samples.

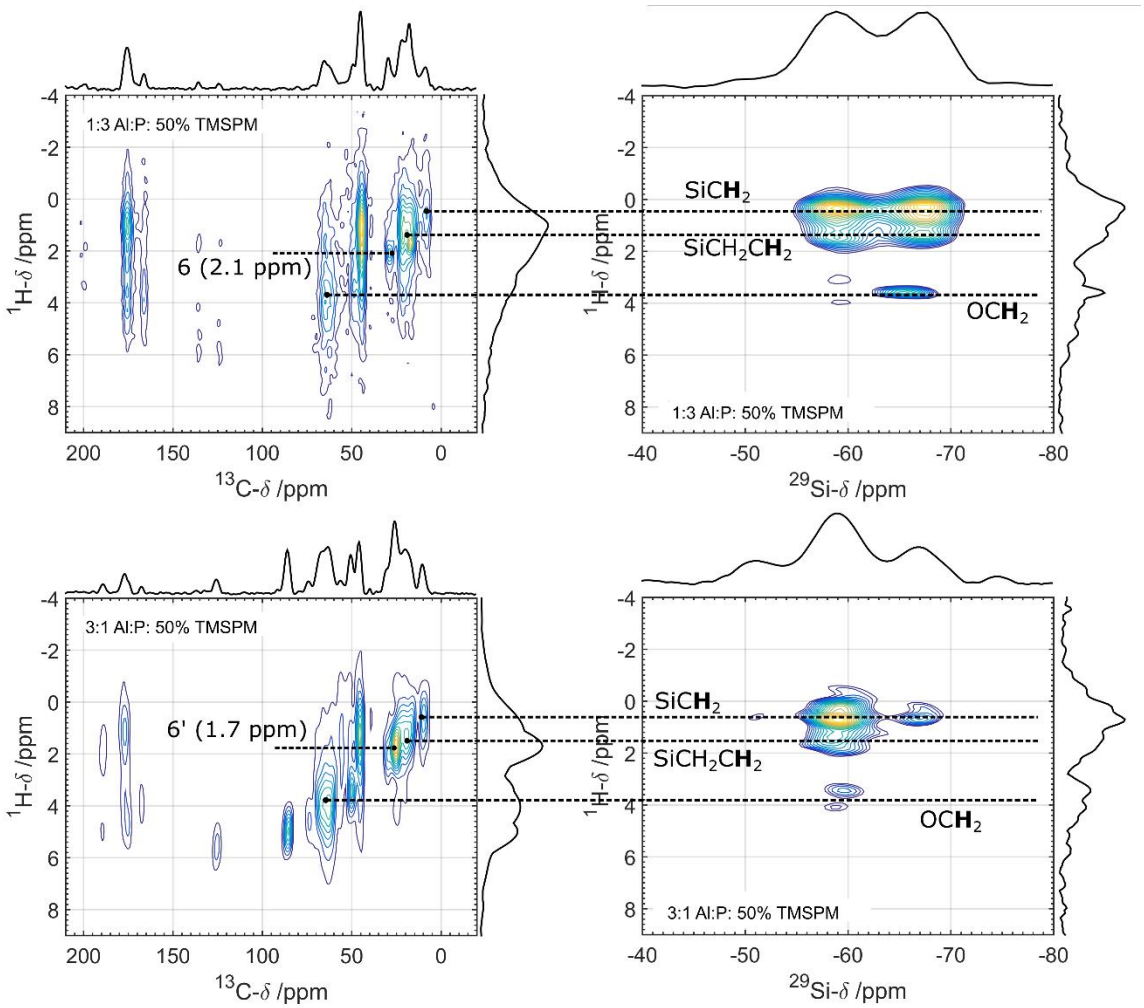

Figure 41. $^{1}H\{^{13}C\}$ (right) and $^{1}H\{^{29}Si\}$ (left) double-CP HETCOR spectra measured at 60 kHz MAS with ^{1}H detection (see experimental section for details). 2D spectra are show for representative samples, 50% MTMS for both, 1:3 (top) and 3:1 (bottom) Al:P systems. The dashed lines extending over the $^{1}H\{^{29}Si\}$ spectra show correlation with ^{1}H species dipolar coupled to both, ^{29}Si and ^{13}C nuclei. The dashed lines on the $^{1}H\{^{13}C\}$ spectra call the attention to the chemical shift difference for protons in CH_3 from keto (C6) and enol (C6') species belonging to MAEAA moieties.

The $^{1}H\{^{13}C\}$ HETCOR spectra confirm the ^{1}H and ^{13}C assignments presented on **Table 10**. The cross-peaks between keto (C6) and enol (C6') tautomer of the acetoacetate group with the CH_3 groups at H6 and H6' are clearly identified in agreement with ^{1}H chemical shifts assignments in the work of Yamada et al.[89]. The cross-peaks H12 – C12 further confirm their assignment to non-polymerized methacrylate species.

$^{1}H\{X\}$ double CP-MAS-NMR - X = ^{13}C, ^{31}P, ^{29}Si and ^{27}Al

Unidimensional $^{1}H\{X\}$ double CP experiments (X = ^{13}C, ^{31}P, ^{29}Si and ^{27}Al) probe ^{1}H sites through a $^{1}H \rightarrow X \rightarrow {}^{1}H$ cross-polarization pathway and reveals proton sites spatially close to the X nucleus. Thus, the proton assignments from ^{1}H MAS NMR spectra can be employed to elucidate inorganic connectivity through organic-inorganic interactions. **Figure 42** shows a $^{1}H\{X\}$ double CP spectra for representative samples (50% TMSPM) for 1:3 and 3:1 Al:P compositions. ^{1}H MAS NMR spectra are also displayed for comparison. The double-CP spectra in **Figure 42** show line-broadening compared to ^{1}H single-pulse representatives, caused by the selective excitation of ^{1}H with restricted mobility, due to the more efficient $^{13}C \rightarrow {}^{1}H$ polarization transfer. The spectra show four regions of interest, comprehending the lines centered at 7, 4, 2 and 1 ppm. The signal at 7 ppm is assigned to P-OH groups, in agreement with ^{31}P-MAS results indicating the presence of $Q^{0}_{mAl,nSi}$ units, with $m+n < 3$. The signal around 4 ppm corresponds to OCH_2 species (H1, H2, and H9) from the ethyl groups. The proton sites around 2 ppm (H6, H6', H13, and H15) are associated to CH_3 sites from MAEAA, and the CH_2 unit from the polymeric backbone. The 1 ppm region is assigned to protons (H8, H7, H16) from the propyl group (TMSPM) and CH_3 from the polymeric backbone.

The $^{1}H\{^{31}P\}$ double-CP spectra show resonances in all four regions, confirming the stability of P-O-C bonds and the direct bonding between the polymeric and inorganic networks. Both $^{1}H\{^{29}Si\}$ and $^{1}H\{^{13}C\}$ double-CP spectra have similar shape, showing resonance with the regions at 4, 2 and 1 ppm. Particularly, the lack of resonance for the $^{1}H\{^{29}Si\}$ double-CP spectra at 7 ppm indicates non-preferential Si-O-P hetero-condensation, in agreement with the results obtained in a previous study.[28] The same spectra show strong resonance in the 1 ppm region, suggesting that homo-condensation is a dominant process. Lastly, the $^{1}H\{^{27}Al\}$ double CP-spectrum shows distinct behaviors for 1:3 and 3:1 Al:P compositions. The phosphate rich samples (1:3 Al:P) show resonance with 7 ppm species, indicating a phosphate rich coordination around the ^{27}Al sites, as confirmed by REDOR data. In opposition, the 3:1 Al:P series show resonance in the region of 4, 2 and 1 ppm, suggesting expressive Al-O-Si hetero-condensation, which is in good agreement with the appearance of tetracoordinated aluminum-silicate species in ^{27}Al MAS NMR spectra.

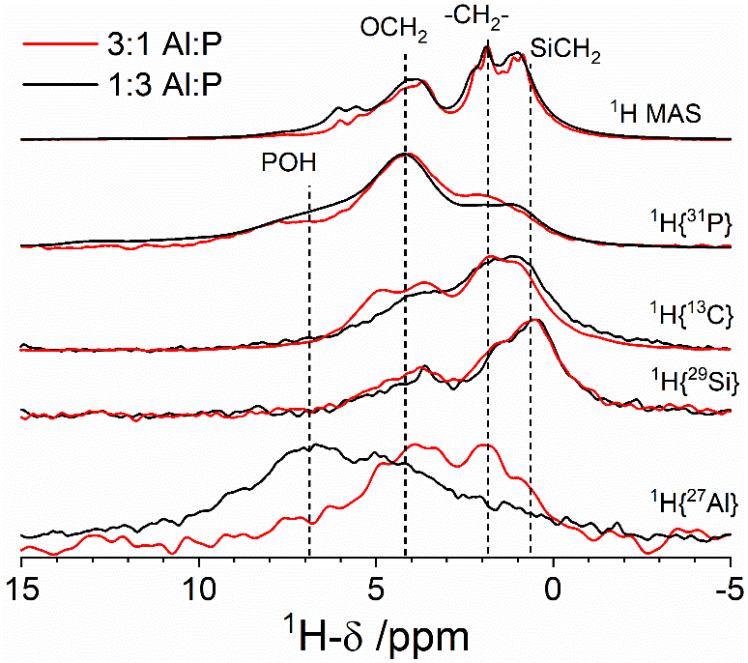

Figure 42. (a) ^{1}H{X} double CP MAS of 50% TMSPM 1:3 and 3:1 Al:P hybrids. The ^{1}H MAS spectra obtained with direct excitation are also shown for the sake of comparison.

Conclusions

Aluminum-phosphate-silicate hybrid materials in the system $Si_{(1-x)}$- $(Al:P)_{(x)}$ with x varying from 0.3 to 1, and atomic ratio Al:P = 1:3, 1:1 and 3:1 were synthesized using a hybrid sol-gel approach, resulting in photopolymerizable solutions. These solutions are compatible with VPP technologies, resulting in transparent hybrid materials with high inorganic mass content. The structural evolution with Si concentration for polymerized samples with different Al:P ratios was investigated by means of solid-state NMR, combined with SEM and phase contrast AFM imaging. It is highlighted the use of the ^{1}H nucleus as a probe to analyze both the organic and inorganic structure, as well their interaction, due to high MAS (60 kHz) experiments. Structural heterogeneities were observed only at nanoscale (< 5 nm) using phase-contrast AFM, and the NMR analysis shows that these materials structure follow the build-up principle with aluminum-phosphate species and alkoxysilane chains acting as fundamental building blocks. The Al:P ratio dictates the hetero-condensation of aluminum and phosphate precursors, resulting in linear aluminum-phosphate units. Insight into these aluminum-phosphate species was possible by analyzing certain structural features of these species and comparing to compound models. The features analyzed were the distribution of ^{31}P sites, the coordination of the hexacoordinate ^{27}Al sites, and the average $(PO_4)^{3-}(-Al^{3+})_m^-$ and $(AlO_6)^{9-}(-P^{5+})_n^-$ linkage, which were obtained from ^{27}Al and

^{31}P MAS, ^{27}Al TQ-MAS and ^{27}Al{^{31}P} REDOR-MAS experiments. These results suggest that monomeric chains are formed for 3:1 Al:P ratio, and dimeric chains are formed for 1:3 Al:P ratio with one and two phosphate units bridging the hexacoordinate aluminum (Al^6) sites, respectively. ^{1}H{^{27}Al} and ^{1}H{^{31}P} double-CP and ^{27}Al MAS-NMR data show that monomeric aluminum-phosphate chains, compared to the dimeric one, are more prone to hetero-condensation with the alkoxysilane chains since Al-O-Si hetero-condensation is more expressive than P-O-Si hetero-condensation. This suggests that the steric hindrance around the hexacoordinate aluminum site controls how the alkoxysilane participates in the materials inorganic structure. The dimeric chains in 1:3 Al:P samples show Al^6 sites strongly hindered by phosphate tetrahedrons, and the alkoxysilane undergoes homo-condensation, resulting in separate silicate and aluminum-phosphate inorganic networks. In contrast, the 3:1 Al:P samples show Al^6 sites readily available to react with the alkoxysilane, and the hetero-condensation Al-O-Si competes with the homo-condensation, resulting in an inorganic network composed by aluminum-phosphate units interconnected by silicate chains. In both cases, the alkoxysilane homo-condensation predominates, as evidenced by ^{29}Si{^{1}H} CP-MAS experiments. Furthermore, the Al^6 sites are converted to Al^4 sites during Al-O-Si hetero-condensation in 3:1 Al:P samples. Despite their structural differences, the polymerization of the organic group results in numerous organic crosslinks, immobilizing the inorganic network and hindering phase separation, with the parallel formation of a PMMA polymeric network according to ^{1}H high-speed MAS, ^{13}C{^{1}H} CP-MAS, ^{1}H DQ-SQ, ^{1}H{^{27}Al} and ^{1}H{^{31}P} double CP-MAS, and ^{1}H-^{13}C{^{1}H} and ^{1}H-^{29}Si{^{1}H} double CP-HETCOR-MAS experiments. These structural features present these materials as potential candidates to immobilize lanthanide ions for developing active optical components.

Acknowledgements

Authors would like to acknowledge the Brazilian funding agencies FAPESP (SPEC process 2015/ 22828-6 and 18/24735-3). GT thanks FAPESP fellowship process number 2018/06426-3 and 2019/24637-7. MOJr acknowledges the Brazilian National Council for Scientific and Technological Development (grant number 311069/2020-7). This research was also supported by the Canadian Excellence Research Chair program (CERC) in Photonics Innovations. The authors are also grateful to the Natural Sciences and Engineering Research Council of Canada (NSERC), the Fonds de Recherche Québecois sur la Nature et les Technologies (FRQNT) and the Canadian Foundation for Innovation (CFI) for the financial support. The author would like to thank Wagner Correr for the SEM images.

Bibliographic References

(1) Faustini, M.; Nicole, L.; Ruiz-Hitzky, E.; Sanchez, C. History of Organic-Inorganic Hybrid Materials: Prehistory, Art, Science, and Advanced Applications. *Adv. Funct. Mater.* **2018**, *28* (27), 1704158–1704158. https://doi.org/10.1002/adfm.201704158.

(2) Faustini, M.; Grosso, D.; Boissière, C.; Backov, R.; Sanchez, C. "Integrative Sol–Gel Chemistry": A Nanofoundry for Materials Science. *J. Sol-Gel Sci. Technol.* **2014**, *70* (2), 216–226. https://doi.org/10.1007/s10971-014-3321-9.

(3) Albert, P.; Lohden, G.; Gall, C.; Borup, B. Ormocers, Method for Their Production and Their Use. 2009023471, 2001. https://doi.org/10.1037/t24245-000.

(4) Parola, S.; Julián-López, B.; Carlos, L. D.; Sanchez, C. Optical Properties of Hybrid Organic-Inorganic Materials and Their Applications. *Adv. Funct. Mater.* **2016**, *26* (36), 6506–6544. https://doi.org/10.1002/adfm.201602730.

(5) Sanchez, C.; Shea, K. J.; Kitagawa, S. Applications of Advanced Hybrid Organic–Inorganic Nanomaterials: From Laboratory to Market. *Chem. Soc. Rev.* **2011**, *40*, 696–753. https://doi.org/10.1039/c0cs00076k.

(6) Judeinstein, P.; Sanchez, C. Hybrid Organic–Inorganic Materials: A Land of Multidisciplinarity. *J Mater Chem* **1996**, *6* (4), 511–525. https://doi.org/10.1039/JM9960600511.

(7) C. Brinker; Scherer, G. Sol-Gel Science: The Physics and Chemistry of Sol-Gel Processing. *Adv. Mater.* **1990**, *3* (10), 912–912. https://doi.org/10.1186/1471-2105-8-444.

(8) Belon, C.; Chemtob, A.; Croutxé-Barghorn, C.; Rigolet, S.; Le Houérou, V.; Gauthier, C. A Simple Method for the Reinforcement of UV-Cured Coatings via Sol-Gel Photopolymerization. *Macromol. Mater. Eng.* **2011**, *296* (6), 506–516. https://doi.org/10.1002/mame.201000350.

(9) Nicole, L.; Rozes, L.; Sanchez, C. Integrative Approaches to Hybrid Multifunctional Materials: From Multidisciplinary Research to Applied Technologies. *Adv. Mater.* **2010**, *22* (29), 3208–3214. https://doi.org/10.1002/adma.201000231.

(10) Schubert, U.; Huesing, N.; Lorenz, A. Hybrid Inorganic-Organic Materials by Sol-Gel Processing of Organofunctional Metal Alkoxides. *Chem. Mater.* **1995**, *7* (11), 2010–2027. https://doi.org/10.1021/cm00059a007.

(11) Grosso, D.; Ribot, F.; Boissiere, C.; Sanchez, C. Molecular and Supramolecular Dynamics of Hybrid Organic–Inorganic Interfaces for the Rational Construction of Advanced Hybrid Nanomaterials. *Chem Soc Rev* **2011**, *40* (2), 829–848. https://doi.org/10.1039/C0CS00039F.

(12) Maçon, A. L. B.; Page, S. J.; Chung, J. J.; Amdursky, N.; Stevens, M. M.; Weaver, J. V. M.; Hanna, J. V.; Jones, J. R. A Structural and Physical Study of Sol–Gel Methacrylate–Silica Hybrids: Intermolecular Spacing Dictates the Mechanical Properties. *Phys. Chem. Chem. Phys.* **2015**, *17* (43), 29124–29133. https://doi.org/10.1039/C5CP04656D.

(13) Oubaha, M.; Dubois, M.; Murphy, B.; Etienne, P. Structural Characterisation of a Sol-Gel Copolymer Synthesised from Aliphatic and Aromatic Alkoxysilanes Using29Si-NMR Spectroscopy. *J. Sol-Gel Sci. Technol.* **2006**, *38* (2), 111–119. https://doi.org/10.1007/s10971-006-7114-7.

(14) Bag, D. S.; Rao, K. U. B. Synthesis of UV-Curable Difunctional Silane Monomer Based on 3-Methacryloxy Propyl Trimethoxysilane (3-MPTS) and Its UV-Curing Characteristics and Thermal Stability. *J. Appl. Polym. Sci.* **2010**, *115* (4), 2352–2358. https://doi.org/10.1002/app.31266.

(15) El hadad, A. A.; Carbonell, D.; Barranco, V.; Jiménez-Morales, A.; Casal, B.; Galván, J. C. Preparation of Sol–Gel Hybrid Materials from γ-Methacryloxypropyltrimethoxysilane and Tetramethyl Orthosilicate: Study of the Hydrolysis and Condensation Reactions. *Colloid Polym. Sci.* **2011**, *289* (17–18), 1875–1883. https://doi.org/10.1007/s00396-011-2504-y.

(16) Lehmann, O.; Meyssamy, H.; Kömpe, K.; Schnablegger, H.; Haase, M. Synthesis, Growth, and Er 3+ Luminescence of Lanthanide Phosphate Nanoparticles †. *J. Phys. Chem. B* **2003**, *107* (30), 7449–7453. https://doi.org/10.1021/jp030012h.

(17) Boakye, E. E.; Mogilevsky, P.; Hay, R. S.; Fair, G. E. Synthesis and Phase Composition of Lanthanide Phosphate Nanoparticles LnPO4 (Ln=La, Gd, Tb, Dy, Y) and Solid Solutions for Fiber Coatings. *J. Am. Ceram. Soc.* **2008**, *91* (12), 3841–3849. https://doi.org/10.1111/j.1551-2916.2008.02737.x.

(18) Mataki, H.; Tsuchii, K.; Mibuka, N.; Suzuki, A.; Sun, J.; Taniguchi, H.; Yamashita, K.; Oe, K. Polymer Waveguide Optical Amplifier Using Organic/Inorganic Nanocomposites Doped With Rare-Earth-Metal Nanoclusters. *J. Photopolym. Sci. Technol.* **2007**, *20* (1), 67–72. https://doi.org/10.2494/photopolymer.20.67.

(19) Talapin, D. V.; Shevchenko, E. V. Introduction: Nanoparticle Chemistry. *Chem. Rev.* **2016**, *116* (18), 10343–10345. https://doi.org/10.1021/acs.chemrev.6b00566.

(20) Duan, H.; Wang, D.; Li, Y. Green Chemistry for Nanoparticle Synthesis. *Chem. Soc. Rev.* **2015**, *44* (16), 5778–5792. https://doi.org/10.1039/C4CS00363B.

(21) Nehra, K.; Dalal, A.; Hooda, A.; Bhagwan, S.; Saini, R. K.; Mari, B.; Kumar, S.; Singh, D. Lanthanides β-Diketonate Complexes as Energy-Efficient Emissive Materials: A Review. *J. Mol. Struct.* **2022**, *1249*, 131531. https://doi.org/10.1016/j.molstruc.2021.131531.

(22) Livage, J.; Barboux, P.; Vandenborre, M. T.; Schmutz, C.; Taulelle, F. Sol-Gel Synthesis of Phosphates. *J. Non-Cryst. Solids* **1992**, *147–148* (C), 18–23. https://doi.org/10.1016/S0022-3093(05)80586-1.

(23) Fernández-Lorenzo, C.; Esquivias, L.; Barboux, P.; Maquet, J.; Taulelle, F. Sol-Gel Synthesis of SiO2P2O5 Glasses. *J. Non-Cryst. Solids* **1994**, *176* (2–3), 189–199. https://doi.org/10.1016/0022-3093(94)90077-9.

(24) Carta, D.; Knowles, J. C.; Guerry, P.; Smith, M. E.; Newport, R. J. Sol–Gel Synthesis and Structural Characterisation of P 2 O 5 –B 2 O 3 –Na 2 O Glasses for Biomedical Applications. *J Mater Chem* **2009**, *19* (1), 150–158. https://doi.org/10.1039/B813288G.

(25) Willinger, M.-G.; Clavel, G.; Di, W.; Pinna, N. A General Soft-Chemistry Route to Metal Phosphate Nanocrystals. *J. Ind. Eng. Chem.* **2009**, *15* (6), 883–887. https://doi.org/10.1016/j.jiec.2009.09.017.

(26) Yu, J.; Xu, R. Insight into the Construction of Open-Framework Aluminophosphates. *Chem. Soc. Rev.* **2006**, *35* (7), 593. https://doi.org/10.1039/b505856m.

(27) Wang, Y.; Pan, S.; Han, S.; Dong, L.; Zhang, M.; Wu, K. Synthesis and Characterization of a New Aluminophosphate with a $Al_3P_6O_{24}^{9-}$ Three-Dimensional Framework. *New J Chem* **2014**, *38* (3), 889–892. https://doi.org/10.1039/C3NJ01484C.

(28) Tayama, G. T.; Santagneli, S. H.; Eckert, H.; Pawsey, S.; Messaddeq, Y. Preparation and Structural Characterization of New Photopolymerizable Transparent Aluminum-Phosphate Hybrid Materials as Resins for 3D Printing. *J. Phys. Chem. C* **2020**, *124* (46), 25621–25631. https://doi.org/10.1021/acs.jpcc.0c08289.

(29) Moore, D. G.; Barbera, L.; Masania, K.; Studart, A. R. Three-Dimensional Printing of Multicomponent Glasses Using Phase-Separating Resins. *Nat. Mater.* **2020**, *19* (2), 212–217. https://doi.org/10.1038/s41563-019-0525-y.

(30) Wang, J.; Zheng, B.; Wang, P. 3D Printed Er3+/Yb3+ Co-Doped Phosphosilicate Glass Based on Sol-Gel Technology. *J. Non-Cryst. Solids* **2020**, *550*, 120362. https://doi.org/10.1016/j.jnoncrysol.2020.120362.

(31) Hay, J. N.; Raval, H. M. Synthesis of Organic - Inorganic Hybrids via the Non-Hydrolytic Sol - Gel Process. **2001**, 3396–3403. https://doi.org/10.1021/cm011024n.

(32) Yeniay, A.; Gao, R.; Takayama, K.; Gao, R.; Garito, A. F. Ultra-Low-Loss Polymer Waveguides. *J. Light. Technol.* **2004**, *22* (1), 154–158. https://doi.org/10.1109/JLT.2003.822206.

(33) Van Vleck, J. H. The Dipolar Broadening of Magnetic Resonance Lines in Crystals. *Phys. Rev.* **1948**, *74* (9), 1168–1183. https://doi.org/10.1103/PhysRev.74.1168.

(34) Gullion, T. Measurement of Dipolar Interactions between Spin- 1 2 and Quadrupolar Nuclei by Rotational-Echo, Adiabatic-Passage, Double-Resonance NMR. *Chem. Phys. Lett.* **1995**, *246* (3), 325–330. https://doi.org/10.1016/0009-2614(95)01120-X.

(35) Bennett, A. E.; Rienstra, C. M.; Auger, M.; Lakshmi, K. V.; Griffin, R. G. Heteronuclear Decoupling in Rotating Solids. *J. Chem. Phys.* **1995**, *103* (16), 6951–6958. https://doi.org/10.1063/1.470372.

(36) Jaeger, C.; Hemmann, F. EASY: A Simple Tool for Simultaneously Removing Background, Deadtime and Acoustic Ringing in Quantitative NMR Spectroscopy--Part I: Basic Principle and Applications. *Solid State Nucl. Magn. Reson.* **2014**, *57–58*, 22–28. https://doi.org/10.1016/j.ssnmr.2013.11.002.

(37) Baccile, N.; Laurent, G.; Bonhomme, C.; Innocenzi, P.; Babonneau, F. Solid-State NMR Characterization of the Surfactant−Silica Interface in Templated Silicas: Acidic versus Basic Conditions. *Chem. Mater.* **2007**, *19* (6), 1343–1354. https://doi.org/10.1021/cm062545j.

(38) Christiansen, S. C.; Hedin, N.; Epping, J. D.; Janicke, M. T.; del Amo, Y.; Demarest, M.; Brzezinski, M.; Chmelka, B. F. Sensitivity Considerations in Polarization Transfer and Filtering Using Dipole-Dipole Couplings: Implications for Biomineral Systems. *Solid State Nucl. Magn. Reson.* **2006**, *29* (1–3), 170–182. https://doi.org/10.1016/j.ssnmr.2005.10.010.

(39) Wiench, J. W.; Bronnimann, C. E.; Lin, V. S.-Y.; Pruski, M. Chemical Shift Correlation NMR Spectroscopy with Indirect Detection in Fast Rotating Solids: Studies of Organically Functionalized Mesoporous Silicas. *J. Am. Chem. Soc.* **2007**, *129* (40), 12076–12077. https://doi.org/10.1021/ja074746+.

(40) Ishii, Y.; Yesinowski, J. P.; Tycko, R. Sensitivity Enhancement in Solid-State 13C NMR of Synthetic Polymers and Biopolymers by 1H NMR Detection with High-Speed Magic Angle Spinning. *J. Am. Chem. Soc.* **2001**, *123* (12), 2921–2922. https://doi.org/10.1021/ja015505j.

(41) Mafra, L.; Siegel, R.; Fernandez, C.; Schneider, D.; Aussenac, F.; Rocha, J. High-Resolution 1H Homonuclear Dipolar Recoupling NMR Spectra of Biological Solids at MAS Rates up to 67 KHz. *J. Magn. Reson. San Diego Calif 1997* **2009**, *199* (1), 111–114. https://doi.org/10.1016/j.jmr.2009.04.004.

(42) Kimura, H.; Nakamura, K.; Eguchi, A.; Sugisawa, H.; Deguchi, K.; Ebisawa, K.; Suzuki, E.; Shoji, A. Structural Study of α-Amino-Acid Crystals by 1H CRAMPS NMR Spectroscopy. *J. Mol. Struct.* **1998**, *447* (3), 247–255. https://doi.org/10.1016/S0022-2860(98)00329-9.

(43) Potrzebowski, M. J.; Tekely, P.; Dusausoy, Y. Comment to 13C-NMR Studies of Alpha and Gamma Polymorphs of Glycine. *Solid State Nucl. Magn. Reson.* **1998**, *11* (3–4), 253–257. https://doi.org/10.1016/s0926-2040(98)00028-9.

(44) Massiot, D.; Dion, P.; Alcover, J. F.; Bergaya, F. 27Al and 29Si MAS NMR Study of Kaolinite Thermal Decomposition by Controlled Rate Thermal Analysis. *J. Am. Ceram. Soc.* **1995**, *78* (11), 2940–2944. https://doi.org/10.1111/j.1151-2916.1995.tb09067.x.

(45) Garcia, R. Nanomechanical Mapping of Soft Materials with the Atomic Force Microscope: Methods, Theory and Applications. *Chem Soc Rev* **2020**, *49* (16), 5850–5884. https://doi.org/10.1039/d0cs00318b.

(46) Tamayo, J.; García, R. Effects of Elastic and Inelastic Interactions on Phase Contrast Images in Tapping-Mode Scanning Force Microscopy. *Appl. Phys. Lett.* **1997**, *71* (16), 2394–2396. https://doi.org/10.1063/1.120039.

(47) Tamayo, J.; García, R. Deformation, Contact Time, and Phase Contrast in Tapping Mode Scanning Force Microscopy. *Langmuir* **1996**, *12* (18), 4430–4435. https://doi.org/10.1021/la960189l.

(48) Phani, A.; Jung, H. S.; Kim, S. Deconvolution of Dissipative Pathways for the Interpretation of Tapping-Mode Atomic Force Microscopy from Phase-Contrast. *Commun. Phys.* **2021**, *4* (1), 1–13. https://doi.org/10.1038/s42005-021-00576-6.

(49) Knoll, A.; Magerle, R.; Krausch, G. Phase Behavior in Thin Films of Cylinder-Forming ABA Block Copolymers: Experiments. *J. Chem. Phys.* **2004**, *120* (2), 1105–1116. https://doi.org/10.1063/1.1627324.

(50) Sundrani, D.; Darling, S. B.; Sibener, S. J. Guiding Polymers to Perfection: Macroscopic Alignment of Nanoscale Domains. *Nano Lett.* **2004**, *4* (2), 273–276. https://doi.org/10.1021/nl035005j.

(51) Rodríguez Hernández, J. C.; Salmerón Sánchez, M.; Gómez Ribelles, J. L.; Monleón Pradas, M. Polymer–Silica Nanocomposites Prepared by Sol–Gel Technique: Nanoindentation and Tapping Mode AFM Studies. *Eur. Polym. J.* **2007**, *43* (7), 2775–2783. https://doi.org/10.1016/j.eurpolymj.2007.04.021.

(52) Sangermano, M.; Amerio, E.; Priola, A.; Di Gianni, A.; Voit, B. Preparation and Characterization of Acrylic Resin/Titania Hybrid Nanocomposite Coatings by Photopolymerization and Sol–Gel Process. *J. Appl. Polym. Sci.* **2006**, *102* (5), 4659–4664. https://doi.org/10.1002/app.24707.

(53) Mohseni, M.; Bastani, S.; Jannesari, A. Influence of Silane Structure on Curing Behavior and Surface Properties of Sol–Gel Based UV-Curable Organic–Inorganic Hybrid Coatings. *Prog. Org. Coat.* **2014**, *77* (7), 1191–1199. https://doi.org/10.1016/j.porgcoat.2014.04.008.

(54) *From Images to Interactions: High-Resolution Phase Imaging in Tapping-Mode Atomic Force Microscopy | Elsevier Enhanced Reader*. https://doi.org/10.1016/S0006-3495(01)76266-2.

(55) Zhang, L.; Eckert, H. Sol–Gel Synthesis of Al 2 O 3 –P 2 O 5 Glasses: Mechanistic Studies by Solution and Solid State NMR. *J Mater Chem* **2004**, *14* (10), 1605–1615. https://doi.org/10.1039/B400651H.

(56) Zhang, L.; Chan, J. C. C.; Eckert, H.; Helsch, G.; Hoyer, L. P.; Frischat, G. H. Novel Sol−Gel Synthesis of Sodium Aluminophosphate Glass Based on Aluminum Lactate. *Chem. Mater.* **2003**, *15* (14), 2702–2710. https://doi.org/10.1021/cm030155g.

(57) Schrotter, J. C.; Cardenas, A.; Smaihi, M.; Hovnanian, N. Silicon and Phosphorus Alkoxide Mixture: Sol-Gel Study by Spectroscopic Technics. *J. Sol-Gel Sci. Technol.* **1995**, *4* (3), 195–204. https://doi.org/10.1007/BF00488374.

(58) Tian, F.; Pan, L.; Wu, X.; Wu, F. The NMR Studies of the P2O5□SiO2 Sol and Gel Chemistry. *J. Non-Cryst. Solids* **1988**, *104* (1), 129–134. https://doi.org/10.1016/0022-3093(88)90191-3.

(59) Catlow, C. R. A.; George, A. R.; Freeman, C. M. Ab Initio and Molecular-Mechanics Studies of Aluminosilicate Fragments, and the Origin of Lowenstein's Rule. *Chem. Commun.* **1996**, No. 11, 1311. https://doi.org/10.1039/cc9960001311.

(60) Coelho, C.; Babonneau, F.; Azaïs, T.; Bonhomme-Coury, L.; Maquet, J.; Laurent, G.; Bonhomme, C. Chemical Bonding in Silicophosphate Gels: Contribution of Dipolar and J-Derived Solid State NMR Techniques. *J. Sol-Gel Sci. Technol.* **2006**, *40* (2–3), 181–189. https://doi.org/10.1007/s10971-006-7431-x.

(61) Cody, G. D.; Mysen, B.; Sághi-Szabó, G.; Tossell, J. A. Silicate-Phosphate Interactions in Silicate Glasses and Melts: I. A Multinuclear (27Al,29Si,31P) MAS NMR and Ab Initio Chemical Shielding (31P) Study of Phosphorous Speciation in Silicate Glasses. *Geochim. Cosmochim. Acta* **2001**, *65* (14), 2395–2411. https://doi.org/10.1016/S0016-7037(01)00597-X.

(62) Martineau, C.; Taulelle, F.; Haouas, M. The Use of 27 Al NMR to Study Aluminum Compounds: A Survey of the Last 25 Years. In *PATAI'S Chemistry of Functional Groups*; John Wiley & Sons, Ltd: Chichester, UK, 2016; pp 1–51. https://doi.org/10.1002/9780470682531.pat0840.

(63) Oliver, S.; Kuperman, A.; Ozin, G. A. A New Model for Aluminophosphate Formation: Transformation of a Linear Chain Aluminophosphate to Chain, Layer, and Framework Structures. *Angew. Chem. Int. Ed.* **1998**, *37* (1–2), 46–62. https://doi.org/10.1002/(SICI)1521-3773(19980202)37:1/2<46::AID-ANIE46>3.0.CO;2-R.

(64) Deshpande, R. R.; Eckert, H. Sol-Gel Preparation of Mesoporous Sodium Aluminosilicate Glasses: Mechanistic and Structural Investigations by Solid State Nuclear Magnetic Resonance. *J. Mater. Chem.* **2009**, *19* (21), 3419. https://doi.org/10.1039/b900864k.

(65) Prabakar, S.; Rao, K. J.; Rao, C. N. R. A MAS NMR Investigation of Aluminosilicate, Silicophosphate, and Aluminosilicophosphate Gels and the Evolution of Crystalline Structures on Heating the Gels. *J. Mater. Res.* **1991**, *6* (3), 592–601. https://doi.org/10.1557/JMR.1991.0592.

(66) Mutin, P. H.; Guerrero, G. Hybrid Materials from Organophosphorus Coupling Molecules. *J. Mater. Chem.* **2005**, *15*, 3761–3768. https://doi.org/10.1039/b505422b.

(67) Sanchez, C.; Soler-Illia, G. J. de A. A.; Ribot, F.; Lalot, T.; Mayer, C. R.; Cabuil, V. Designed Hybrid Organic−Inorganic Nanocomposites from Functional Nanobuilding Blocks. *Chem. Mater.* **2001**, *13* (10), 3061–3083. https://doi.org/10.1021/cm011061e.

(68) Pauling, L.; Sherman, J. The Crystal Structure of Aluminum Metaphosphate, Al(PO $_3$) $_3$. *Z. Für Krist. - Cryst. Mater.* **1937**, *96* (1–6), 481–487. https://doi.org/10.1524/zkri.1937.96.1.481.

(69) Mooney, R. C. L. The Crystal Structure of Aluminium Phosphate and Gallium Phosphate, Low-Cristobalite Type. *Acta Crystallogr.* **1956**, *9* (9), 728–734. https://doi.org/10.1107/S0365110X56001996.

(70) Dębowski, M.; Łokaj, K.; Wolak, A.; Żurawski, K.; Plichta, A.; Zachara, J.; Ostrowski, A.; Florjańczyk, Z. Linear Coordination Polymers Based on Aluminum Phosphates: Synthesis, Crystal Structure and Morphology. *Dalton Trans.* **2016**, *45* (19), 8008–8020. https://doi.org/10.1039/C6DT00153J.

(71) Pinkas, J.; Chakraborty, D.; Yang, Y.; Murugavel, R.; Noltemeyer, M.; Roesky, H. W. Reactions of Trialkyl Phosphates with Trialkyls of Aluminum and Gallium: New Route to Alumino- and Gallophosphate Compounds via Dealkylsilylation. *Organometallics* **1999**, *18* (4), 523–528. https://doi.org/10.1021/om9806702.

(72) Wei, L.; Yonggang, W.; Shukun, S.; Shaofei, S.; Daodao, H. Ultraviolet Light Catalyzed Gelation of 3-Methacryloxypropyltrimethoxysilane via Altered Silicate Spatial Structure. *J. Phys. Chem. B* **2016**, *120* (35), 9513–9522. https://doi.org/10.1021/acs.jpcb.6b05477.

(73) Engelhardt, G.; Michel, D. *High-Resolution Solid-State NMR of Silicates and Zeolites*; John Wiley & Sons, 1987.

(74) de Oliveira, M.; Aitken, B.; Eckert, H. Structure of P2O5–SiO2 Pure Network Former Glasses Studied by Solid State NMR Spectroscopy. *J. Phys. Chem. C* **2018**, *122* (34), 19807–19815. https://doi.org/10.1021/acs.jpcc.8b06055.

(75) Ganesan, R.; Dinachali, S. S.; Lim, S. H.; Saifullah, M. S. M.; Chong, W. T.; Lim, A. H. H.; Yong, J. J.; Thian, E. S.; He, C.; Low, H. Y. Direct Nanoimprint Lithography of Al 2 O 3 Using a Chelated Monomer-Based Precursor. *Nanotechnology* **2012**, *23* (31), 315304–315304. https://doi.org/10.1088/0957-4484/23/31/315304.

(76) R. Di Maggio, E. C., F. Girardi, S. Dire` Dipartimento. Structure-Related Behavior of Hybrid Organic–Inorganic Materials Prepared in Different Synthesis Conditions from Zr-Based NBBs and 3-Methacryloxypropyl Trimethoxysilane R. *J. Appl. Polym. Sci.* **2010**, *116* (5), 2658–2667. https://doi.org/10.1002/app.

(77) Delattre, L.; Dupuy, C.; Babonneau, F. Characterization of the Hydrolysis and Polymerization Processes of Methacryloxypropyltrimethoxysilane. *J. Sol-Gel Sci. Technol.* **1994**, *2* (1–3), 185–188. https://doi.org/10.1007/BF00486238.

(78) Lichtenberger, R.; Puchberger, M.; Baumann, S. O.; Schubert, U. Modification of Aluminum Alkoxides with β-Ketoesters: New Insights into Formation, Structure and Stability. *J. Sol-Gel Sci. Technol.* **2009**, *50* (2), 130–140. https://doi.org/10.1007/s10971-008-1890-1.

(79) Vilela, C.; Martins, A.; Sousa, N.; Silvestre, A.; Figueiredo, F.; Freire, C. Poly(Bis[2-(Methacryloyloxy)Ethyl] Phosphate)/Bacterial Cellulose Nanocomposites: Preparation, Characterization and Application as Polymer Electrolyte Membranes. *Appl. Sci.* **2018**, *8* (7), 1145. https://doi.org/10.3390/app8071145.

(80) Schiavoni, M. M.; Di Loreto, H. E.; Hermann, A.; Mack, H.-G.; Ulic, S. E.; Della Védova, C. O. Keto-Enol Tautomerism in β-Ketoesters: CH 3 C(O)CHXC(O)OY (X = H, Cl; Y = CH 3 , C 2 H 5

). Vibrational Analyses, NMR Spectra and Quantum Chemical Calculations. *J. Raman Spectrosc.* **2001**, *32* (5), 319–329. https://doi.org/10.1002/jrs.701.

(81) Ivanovici, S.; Puchberger, M.; Fric, H.; Kickelbick, G. Coordination Behavior of Acetoacetate Ligands with Attached Methacrylate Groups Containing Alkyl-Spacers of Different Length to Titanium and Zirconium Alkoxides. *Monatshefte Für Chem. - Chem. Mon.* **2007**, *138* (6), 529–539. https://doi.org/10.1007/s00706-007-0632-3.

(82) Abe, Y.; Honda, Y.; Gunji, T. Preparation and Properties of Silicon-Containing Polymer Hybrids from 3-Methacryloxypropyltrimethoxysilane. *Appl. Organomet. Chem.* **1998**, *12* (10–11), 749–753. https://doi.org/10.1002/(SICI)1099-0739(199810/11)12:10/11<749::AID-AOC782>3.0.CO;2-2.

(83) Kurajica, S.; Mali, G.; Mandić, V.; Minga, I. Multinuclear Magnetic Resonance Study on Aluminium Sec-Butoxide Chelated with Ethyl Acetoacetate in Various Amounts. *Croat. Chem. Acta* **2019**, *92* (1), 17–28. https://doi.org/10.5562/cca3426.

(84) Yamada, N.; Yoshinaga, I.; Katayama, S. Formation Behavior and Optical Properties of Transparent Inorganic-Organic Hybrids Prepared from Metal Alkoxides and Polydimethylsiloxane. *J. Sol-Gel Sci. Technol.* **2000**, *17* (2), 123–130. https://doi.org/10.1023/A:1008787200364.

(85) Kim, Y.; Harwood, H. J. Analysis of Sequence Distribution in Methyl Methacrylate–Methyl Acrylate Copolymers by 13C NMR Spectroscopy. *Polymer* **2002**, *43* (11), 3229–3237. https://doi.org/10.1016/S0032-3861(02)00153-2.

(86) Spěváček, J.; Schneider, B.; Mihailov, M.; Dirlikov, S. 1H-NMR Study of Interactions in the Systems Methyl Methacrylate-Dimethylformamide and Methyl Methacrylate-Poly(Methyl Methacrylate-Dimethylformamide. *Eur. Polym. J.* **1977**, *13* (8), 625–630. https://doi.org/10.1016/0014-3057(77)90192-6.

(87) Miwa, Y.; Ishida, H.; Tanaka, M.; Mochizuki, A. 2H-NMR and 13C-NMR Study of the Hydration Behavior of Poly(2-Methoxyethyl Acrylate), Poly(2-Hydroxyethyl Methacrylate) and Poly(Tetrahydrofurfuryl Acrylate) in Relation to Their Blood Compatibility as Biomaterials. *J. Biomater. Sci. Polym. Ed.* **2010**, *21* (14), 1911–1924. https://doi.org/10.1163/092050610X489682.

(88) Momose, H.; Maeda, T.; Hattori, K.; Hirano, T.; Ute, K. Statistical Determination of Chemical Composition and Monomer Sequence Distribution of Poly(Methyl Methacrylate-Co-Tert-Butyl

Methacrylate)s by Multivariate Analysis of 13C NMR Spectra. *Polym. J.* **2012**, *44* (8), 808–814. https://doi.org/10.1038/pj.2012.110.

(89) Kaji, H.; Hayashi, H.; Yamada, T.; Fukuchi, M.; Fujimura, S.; Ueda, M.; Kang, S.; Umeyama, T.; Matano, Y.; Imahori, H. Local Stoichiometry in Amorphous Supramolecular Composites Analyzed by Solid-State C13 Nuclear Magnetic Resonance. *Appl. Phys. Lett.* **2011**, *98* (11), 113301. https://doi.org/10.1063/1.3565237.

CHAPTER 3. PROCESS MODELING OF LASER SCANNING VAT-PHOTOPOLYMERIZATION OPERATING UNDER INTERMITTENT EXPOSURE CONDITIONS

Mykola Posternak [1], Gabriel Toshiaki Tayama [1 2*], Sandra Helena Messaddeq [1], and Younes Messaddeq [1, 2]

Center for Optics, Photonics and Lasers, Laval University, 2375 de la Terrasse, Quebec City, QC, G1V 0A6, Canada;

Chemistry Institute of Araraquara, Sao Paulo State University (UNESP), 55 Av. Prof. Francisco Degni, Araraquara, SP, 14800-900, Brazil;

KEYWORDS: stereolithography; pulsed laser; intermittent exposure; process modelling; work curve.

Abstract

Process modeling is an important tool in additive manufacturing (AM) because it elucidates the relationship between processing parameters and material properties. Ultraviolet laser scanning vat-photopolymerization (VPP-UVL) is a common additive manufacturing technique, with a strong physical modeling based on the Jacobs work curve framework. The work curve model was developed for continuous UV exposure (CE) systems, however most VPP-UVL systems to date operate under intermittent exposure (IE) conditions due to the wide adoption of solid-state pulsed-laser sources. Despite their fundamental differences, the Jacobs work curve model is still successfully employed in IE systems under high overlap conditions between pulses, however there are few investigations regarding the limiting conditions for the applicability of the Jacobs work curve model to describe the total exposure profile in intermittent exposure (IE) setups. To address this issue, a model describing a VPP-UVL-IE process was developed. The VPP-UVL-IE model presented here has the same logarithmic dependence as the Jacobs work curve model, but with the addition of a multiplying factor

carrying information on the spatial distribution of energy, that is, the overlap of individual pulses. The model is adaptable for non-gaussian beam profiles and can be solved for bidimensional analysis representing layer fabrication. To test the model, a custom-built VPP-UVL-IE additive manufacturing system was used, and structures were printed and characterized using SEM and stylus profilometry. The model`s reliability was investigated under constant overlap and exposure conditions. The model is very robust under constant overlap conditions, with good agreement between experimental data and simulation. For constant exposure, there is good qualitative agreement, but discrepancies occur due to insufficient modeling of the spatial distribution of energy. The 3D printing of complex structures is demonstrated, and the model indicates that VPP-UVL-IE can offer, theoretically, faster printing compared to VPP-UVL-CE for large beam radius (>275 μm), under the assumption of Gaussian beam profile, constant irradiance during the pulses, and dwell time longer than beam travel time. Conversely, same levels of exposure can be achieved at higher scan speed using CW laser sources instead of pulsed sources for small beam radius (<275 μm).

Resumo

A modelagem de processo é uma ferramenta importante na manufatura aditiva (AM) porque elucida a relação entre os parâmetros de processamento e as propriedades do material. A fotopolimerização por varredura a laser ultravioleta (VPP-UVL) é uma técnica de manufatura aditiva muito comum, com uma forte modelagem física baseada na curva de trabalho de Jacobs. O modelo de curva de trabalho foi desenvolvido para sistemas de exposição UV contínua (CE), no entanto, a maioria dos sistemas VPP-UVL opera sob condições de exposição intermitente (IE) devido à ampla adoção de fontes de laser pulsado de estado sólido. Apesar de suas diferenças fundamentais, o modelo de curva de trabalho de Jacobs ainda é empregado com sucesso em sistemas IE sob condições de elevada sobreposição entre pulsos, porém existem poucas investigações sobre as condições limitantes para a aplicabilidade do modelo de curva de trabalho de Jacobs para descrever o perfil de exposição total em regime de exposição intermitente (IE). Para explorar esse problema, um modelo que descreve um processo VPP-UVL-IE foi desenvolvido. O modelo VPP-UVL-IE aqui apresentado tem a mesma dependência logarítmica do modelo da curva de trabalho de Jacobs, mas com a adição de um fator multiplicador que carrega informações sobre a distribuição espacial da energia, ou seja, a sobreposição de pulsos individuais. O modelo é adaptável para perfis de feixe não gaussianos e pode ser resolvido para análises bidimensionais representando a fabricação de camadas. Para testar o modelo, foi usado um sistema de manufatura aditiva VPP-UVL-IE customizado,

e as estruturas foram impressas e caracterizadas usando SEM e perfilometria. A confiabilidade do modelo foi investigada sob condições de sobreposição e exposição constantes. O modelo é bastante robusto sob condições de sobreposição constante, com boa concordância entre os dados experimentais e simulados. Para exposição constante, há boa concordância qualitativa, mas discrepâncias ocorrem devido à modelagem insuficiente da distribuição espacial de energia. A impressão 3D de estruturas complexas é demonstrada, e o modelo indica que VPP-UVL-IE pode oferecer, teoricamente, impressão mais rápida em comparação com VPP-UVL-CE para grandes raios de feixe (>275 µm), sob a hipótese de perfil de feixe gaussiano , irradiância constante durante os pulsos e tempo de permanência maior que o tempo de viagem do feixe. Por outro lado, os mesmos níveis de exposição podem ser alcançados em velocidade de varredura mais alta usando fontes de laser CW em vez de fontes pulsadas para raio de feixe pequeno (<275 µm).

Résumé

La modélisation des processus est un outil important dans la fabrication additive (FA) car elle élucide la relation entre les paramètres de traitement et les propriétés des matériaux. La photopolymérisation en cuve à balayage laser ultraviolet (VPP-UVL) est une technique de fabrication additive courante, avec une modélisation physique solide basée sur le cadre de la courbe de travail de Jacobs. Le modèle de courbe de travail a été développé pour les systèmes d'exposition continue aux UV (CE), mais la plupart des systèmes VPP-UVL fonctionnent à ce jour dans des conditions d'exposition intermittente (IE) en raison de la large adoption de sources laser pulsées à semi-conducteurs. Malgré leurs différences fondamentales, le modèle de courbe de travail de Jacobs est toujours utilisé avec succès dans les systèmes IE dans des conditions de chevauchement élevé entre les impulsions, mais il existe peu d'études concernant les conditions limitantes de l'applicabilité du modèle de courbe de travail de Jacobs pour décrire le profil d'exposition totale en intermittent. configurations d'exposition (IE). Pour résoudre ce problème, un modèle décrivant un processus VPP-UVL-IE a été développé. Le modèle VPP-UVL-IE présenté ici a la même dépendance logarithmique que le modèle de courbe de travail de Jacobs, mais avec l'ajout d'un facteur multiplicateur portant des informations sur la distribution spatiale de l'énergie, c'est-à-dire le chevauchement des impulsions individuelles. Le modèle est adaptable pour des profils de faisceau non gaussiens et peut être résolu pour une analyse bidimensionnelle représentant la fabrication de couches. Pour tester le modèle, un système de fabrication additive VPP-UVL-IE sur mesure a été utilisé, et les structures ont été imprimées et caractérisées à l'aide de la profilométrie SEM et du stylet. La fiabilité du modèle a été

étudiée dans des conditions de chevauchement et d'exposition constants. Le modèle est très robuste dans des conditions de chevauchement constant, avec un bon accord entre les données expérimentales et la simulation. Pour une exposition constante, il y a un bon accord qualitatif, mais des écarts se produisent en raison d'une modélisation insuffisante de la distribution spatiale de l'énergie. L'impression 3D de structures complexes est démontrée et le modèle indique que VPP-UVL-IE peut offrir, en théorie, une impression plus rapide par rapport à VPP-UVL-CE pour un rayon de faisceau important (> 275 µm), sous l'hypothèse d'un profil de faisceau gaussien , irradiance constante pendant les impulsions et temps de séjour supérieur au temps de parcours du faisceau. Inversement, les mêmes niveaux d'exposition peuvent être obtenus à une vitesse de balayage plus élevée en utilisant des sources laser CW au lieu de sources pulsées pour un petit rayon de faisceau (<275 µm).

Introduction

VPP-UVL was one of the first AM techniques developed and offers high resolution, fast printing times and excellent surface quality compared to other AM technologies [1,2]. Most VPP-UVL setups employed continuous exposure (CE) conditions in the early years of the technique by scanning a photopolymerizable resin at a constant speed using a continuous wave (CW) UV laser as illustrated in **Figure 43** [3]. Process modeling offers a reference framework to understand the influence of different experimental parameters into the final product dimensions and properties, which is essential to produce high-quality parts [4]. The pioneer work of Jacob can successfully describe the VPP-UVL-CE process, resulting in a simple yet robust model capable of predicting the cured layer thickness as function of the energy dose [3,5,6]. The model shows some limitations in addressing the lateral resolution of printed features and can be imprecise when dynamical and photochemical [7,8] factors play a major role into the polymerization reaction, because the applied energy dose is not enough to describe the entire polymerization reaction. Nonetheless, Jacob's model is still used as the foundation for more precise VPP-UVL-CE models encompassing factors, such as reaction rate dependence on light intensity [9], scattering centers [10–14], diffusion [15,16], photobleaching [17], oxygen inhibition [16,18], heat diffusion [19], and self-focusing effects [20].

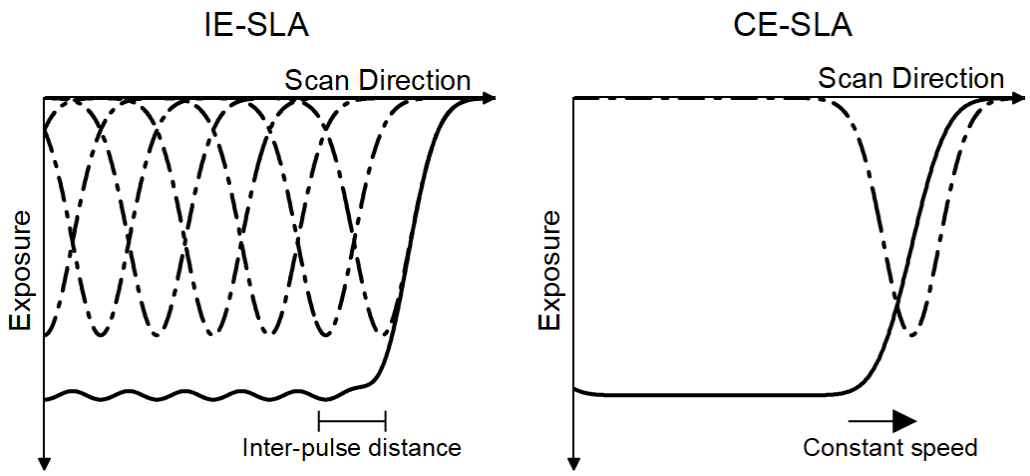

Figure 43. Exposure profile outputted by a VPP-UVL process under continuous exposure (CE), and intermittent exposure (IE) conditions. Profiles calculated using a 250 µm beam radius with 1W power output. Dwell time of 1 s and inter-pulse distance of 250 µm were employed for IE process and scan speed of 250 $\mu m.s^{-1}$ for CE process.

An intermittent exposure (IE) process is a variant of VPP-UVL in which single laser pulses overlap to result in a homogenous exposure profile, as illustrated in **Figure 43**. The overlap between pulses depends on the inter-pulse distance, which is directly linked to the laser repetition rate and the laser scan speed. VPP-UVL-IE process has been typically represented by multiphoton-polymerization (MPP) setups [21] as well single-photon processes using pulsed lamp sources [22–24]. However, IE process has been commercially dominant [25] due to the superior lifetime and efficiency of frequency-multiplied solid-state lasers compared to traditional CW gas lasers used in CE systems [22,26]. The distinction between CE and IE processes is often overlooked despite their fundamental differences, and process modeling in VPP-IE has been mostly focused on MPP setups, with emphasis on photopolymerization kinetics [27] and lateral resolution [28–30]. Physical models for VPP-UVL-IE are far less prevalent in literature compared to CE process.

Recent studies simulating on VPP-UVL-IE have indicated higher lateral resolution compared to VPP-UVL-CE if the dwell time is less than the time scale of molecular species diffusion (10^{-3} s for 1,6 Hexanediol diacrylate monomer) [31], allowing polymerization to occur strictly within the exposed area. Nonetheless, any technological developments on VPP-UVL-IE requires a process model capable of predicting: (1) the polymerized layer thickness as a function of the energy dose, and (2) under which conditions a homogenous energy dose profile is delivered to fabricate continuous structures. Experimentally, it has been verified that the work curve equation can be used for addressing (1),

however the Jacobs work curve model (CW laser scanning at constant speed) is inappropriate to model the spatial distribution of exposure introduced by the pulsed regime observed in VPP-UVL-IE systems since it does not acquaint for the overlap between subsequent pulses. Concerning (2), published literature [22–24] typically employ high overlap conditions between laser pulses to achieve conditions similar to continuous exposure, however the limiting conditions to achieve homogeneous exposure are still little explored.

This work presents and validates a VPP-UVL-IE process model with experimental results from a custom-built additive manufacturing system. The model employ the same boundary conditions of the Jacobs work curve model, but approximates the total exposure by a summation of the exposure function of individual laser pulses as if they occurred simultaneously, which is similar to a recent approach employed for another CE process using a VPP-UVM (mask projection) system [32]. Photochemical and dynamical factors, such as self-focusing, scattering and photobleaching are not considered, and polymerization is solely determined by the levels of exposure. The derived VPP-UVL-IE model describes the total exposure as two separable contributions associated with the energy dose of a single pulse and the overlap from adjacent pulses. The model was tested experimentally by fabricating and characterizing line structures under constant overlap and constant single-pulse exposure conditions. The model highlights the limitations of using the Jacob`s work curve to predict (1) and offers a reference framework to select the printing parameters to achieve a homogenous energy dose profile (2). Furthermore, the printing speed between VPP-UVL-IE and -CE process is compared from a theoretical point of view and the -IE process can be faster depending on the laser beam radius.

Materials and Methods

IE-SLA printer

The custom-made VPP-UVL-IE additive manufacturing system employed in this work is equipped with a CW-diode laser (Laserglow Technology, model LRS-0360-WFO) operating at 360 nm. The laser beam is corrected by a lens (f=100 mm) to achieve a gaussian-like profile. A x-y galvanometric mirror (Dual-Axis Galvo Scan Head Systems, Thorlabs) with fast response (250 µs for $\Delta\theta$=0.4°) guides the laser beam from spot to spot during the printing process. Typical dwell time at each spot is between 10 ms and 100 ms (with 10 ms temporal resolution), with an estimated 125 µs travel time between spots (100 µm displacement between spots with the galvanometric mirror at 30 cm from the platform). The dwell time is at least 3 orders of magnitude slower than the travel time, and the

process can be approximated as VPP-UVL-IE process with constant irradiance during the laser pulses, as evidenced by the results presented below. Laser irradiance is adjusted using a series of ND filters located at the exit of the laser, achieving a variable laser power between 30 µW and 20 mW. The resulting beam diameter ($1/e^2$) at the printing platform is 550 ± 10 µm. Printing platform vertical movement is achieved using a high-resolution linear stage. The hardware is controlled through a MATLAB software that reads G-Code files and send the instructions through a National Instruments multifunction data acquisition unit (USB-6009) connected to the computer's universal serial bus. Inter-pulse distance, dwell time, and platform vertical displacement between layers are user-defined parameters inputted through the software. The collection of individual exposures allowing the fabrication of continuous structures is demonstrated in **Video S1** available in supplementary information. The VPP-UVL-IE setup`s printing capability is demonstrated in **Figure 44**, showing different complex and intricate scaffold structures.

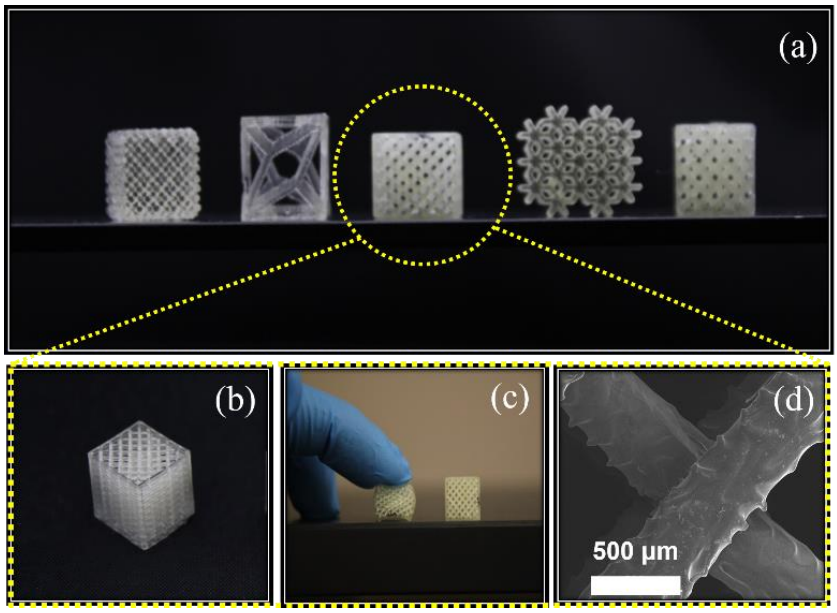

Figure 44. (a) Pictures of different geometries printed using 0.73 wt.% [PETA/BAPO]-[MPTMS-HAD] resin, (b) the side view of the 3D printed scaffold (10 mm cube), (c) the scaffold compressive strength response in the perpendicular direction of the printed structure, (d), SEM image of 3D printed scaffold wall. Printing parameters were 100 $mW.cm^{-2}$, dwell time between 50 to 70 ms and 100 µm inter-pulse distance.

Resin Preparation

Resins for VPP-UVL were prepared according to literature [33]. Pentaerythritol tetraacrylate-PETA (Sigma-Aldrich), 1, 6-hexanediol diacrylate-HDA (Sigma-Aldrich), 3-(trimethoxysilyl)propyl

methacrylate-MPTMS (Sigma-Aldrich), and phenylbis (2,4,6-trimethylbenzoyl)-phosphine oxide-BAPO (Sigma-Aldrich 97%) were used as received. BAPO was dissolved in PETA at 0.73 w.t. % concentration. The container was wrapped in aluminum foil to reduce premature polymerization under ambient light and the mixture was stirred for 90 min. MPTMS was hydrolyzed with a HCl solution (0.1 mol.L^{-1}) using a 1:2 (H_2O:MPTMS) molar ratio for 1 h, and hydrolysis byproducts were eliminated under low pressure conditions for 40 min (25 mbar at 30 °C). Lastly, pre-hydrolyzed MPTMS and HAD were added to the BAPO solution at [HDA]/[PETA]=0.13 and [MPTMS]/[PETA]=0.25 molar ratio and the mixture was stirred for another 30 min.

Linear structures fabrication and characterization

Lines were printed in a glass slide substrate using a vat structure as presented in **Figure 45 (a).** For constant overlap experiments, inter-pulse distance (*h*) was kept constant and laser irradiance and dwell time were varied. For constant energy experiments (E_{SE}), laser irradiance and dwell time were kept constant and different inter-pulse distances were tested. Once printed, residual resin was removed from the structures using lens tissue resulting in the lines presented in **Figure 45 (b).** The height profile was measured using a surface stylus profilometer equipped with a 45° and 3µm curvature radius stylus (Form Taylorsurf PGI Optics). SEM images were collected using a Quanta 3D FEG (FEI) at 3 keV to avoid surface damage.

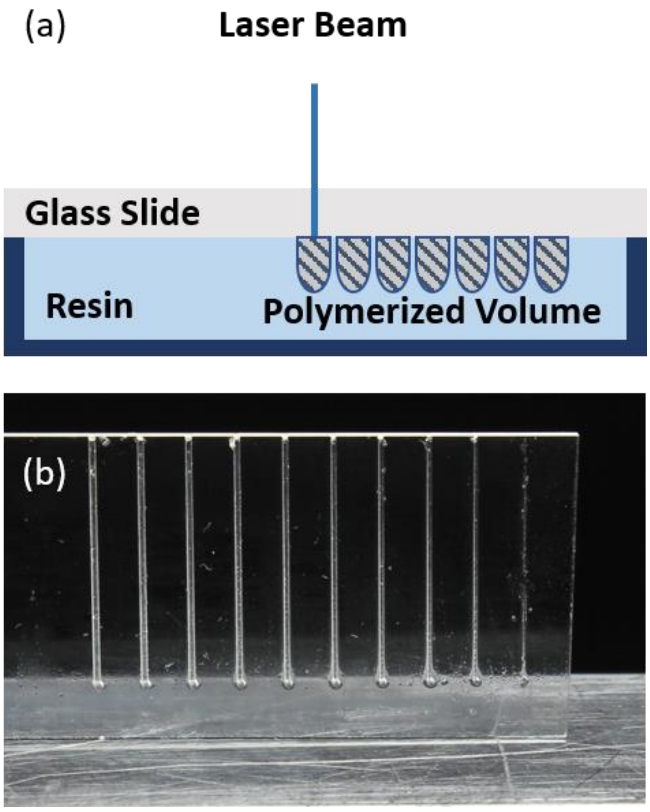

Figure 45. (a) Illustration of the vat setup used to fabricate line structures using VPP-UVL-IE process. (b) The resulting line structures fabricated with different exposure conditions.

Intermittent exposure modeling – VPP-UVL-IE

The developed model for the VPP-UVL-IE process is based on the main steps and assumptions present in the Jacob`s work curve model, which is well-described in literature [3,5,6]. According to Beer-Lambert law, when light passes through an absorbing medium, its irradiance H (mW.cm^{-2}) and exposure E (mJ.cm^{-2}) decay exponentially with distance until it reaches 1/e of its original value at a characteristic penetration depth (D_p), as shown in **Equation 1**. A resin for VPP is a photoreactive medium, and the extent of the polymerization reaction is directly associated to the total exposure. These resins are composed by multifunctional monomers, and a percolated network, or gel structure, is formed when the exposure exceeds a critical exposure value ($E>E_c$). The surface of the polymerized volume is described by **Equation 1** when the boundary condition $E(x,y,C_d)=E_c$ is introduced, resulting in **Equation 2a**, where C_d is the cure depth, or the layer thickness. The vertical platform movement is a process parameter directly correlated to the cure depth, and **Equation 2a** can be reorganized as **Equation 2b.** Based on such considerations, any VPP process can be modeled if

the exposure can be adequately described. Jacobs work curve model corresponds to the solution of **Equation 2b** using a gaussian beam laser with W_o (μm) beam radius (1/e² of peak exposure) moving at constant speed V_{CE} (μm.s^{-1}) and with P_l output power (mW), resulting in **Equation 2c**.

$$\int_{t=0}^{t} H(x,y).e^{-z/D_p}.dt = E(x,y,z) = E(x,y).e^{-z/D_p} \quad \textbf{Equation 1}$$

$$E_c = E(x,y).e^{-C_d(x,y)/D_p} \quad \textbf{Equation 2a}$$

$$C_d(x,y) = D_P * \ln\frac{E(x,y)}{E_c} \quad \textbf{Equation 2b}$$

$$C_d = D_P * \ln\sqrt{\frac{2}{\pi W_o^2}}\frac{P_l}{V_{CE}E_c} \quad \textbf{Equation 2c}$$

In the case of VPP-UVL-IE, the simplest approximation for calculating the total exposure is to sum the exposure of all individual pulses assuming they occur simultaneously. Assuming that the printing process occurs by scanning a pulsed laser along the X direction, followed by translation along the Y axis for bidimensional fabrication, in such a way that all individual pulses are aligned to each other, the total exposure assumes the form of **Equation 3.**

$$E(x,y) = P_l.t\frac{2}{\pi W_o^2}\sum_{m=0}\sum_{n=0} exp(-2(x-nh_1)^2/W_o^2).exp(-2(y-mh_2)^2/W_o^2)$$

Equation 3

Here, h_2 (m) is the hatch distance (spacing in the Y axis between two), h_1 (m) is the inter-pulse distance in the X axis, P_l (W) is the laser power, and t (s) is the dwell time of each pulse. Such description assumes that the exposure is spatially confined to the pulse spot, that is, the laser beam is stationary during the pulse. The spatial coordinate along the x and y axis (μm) are represented by *x* and *y*, respectively. The parameters *n* and *m* refer to the nth individual exposure at the mth line. The overlap of parallel lines has been studied in literature, thus only the exposure profile from a line scan is of interest in such analysis. Studying the peak exposure profile (y=0) of a single line scan (m=0) results in **Equation 4.**

$$E(x) = \sum_{n=0} E_n(x) = P_l.t\frac{2}{\pi W_o^2}\sum_{n=0} exp(-2(x-nh_1)^2/W_o^2) \quad \textbf{Equation 4}$$

Dwell time and laser power are parameters inputted by the user, and the total exposure is more conveniently expressed as **Equation 5a**:

$$E(x,h,W_o) = E_{SE}(P_l,t).EOF(x,h,W_o) \quad \textbf{Equation 5a}$$

$$E_{SE}(P_l,t) \equiv P_l.t\frac{2}{\pi W_o^2} \quad \textbf{Equation 5b}$$

$$EOF(x,h,W_o) \equiv \sum_{n=0} exp(-2(x-nh_1)^2/W_o^2) \quad \textbf{Equation 5c}$$

where E_{SE} represent the peak exposure value associated to a single exposure as defined by **Equation 5b**, and EOF(x,h,W_o) is an Exposure Overlap Factor carrying the information on the spatial profile of exposure as defined by **Equation 5c**. The model for the VPP-UVL-IE process is identical to that of VPP-UVL-CE, with the addition of a factor describing the spatial distribution of exposure. It is highlighted that the critical exposure hypothesis and the summation of individual exposures overlook the complexity of the laser-resin interaction. Literature indicates that the critical exposure hypothesis is quite robust [34], but that is not the case for the summation hypothesis [5], and many factors such as photobleaching, and self-focusing effects, can hinder an accurate description of EOF. Because of insufficient EOF modeling, calculating critical exposure values for various overlap conditions can be unreliable as will be shown in the following sections. However, the VPP-UVL-IE model present EOF and E_{SE} as separable factors that can be tested independently. Such separation is not limited to the gaussian beam case but can be observed for any beam profile as long as E_{SE} can be expressed as a normalizing factor.

A simulation of EOF profile is presented in **Figure 46 (a)**. A 7 mm line scan with different inter-pulse distances using the same beam diameter (Ø=550 µm) employed in the experimental part was calculated by numerically solving **Equation 5c** for discrete points spaced 2 µm along the scan line. EOF values fluctuate along the scan line and the inter-pulse distance determines its periodicity and magnitude. Decreasing inter-pulse distance increases the overlap between subsequent exposures, resulting in more homogenous and higher values for the EOF profile along the scan line. These findings point to a minimum inter-pulse distance, depending on the beam diameter, in which EOF fluctuations are minimized and a homogenous energy dose profile is delivered. To evaluate such hypothesis, the coefficient of variation for EOF values was calculated for different inter-pulse distances using average (μ_{EOF}) and standard deviation (σ_{EOF}) values according to **Equation 6**. These values were calculated by performing a discrete statistical analysis over the EOF values calculated using **Equation 5c** of a 7 mm line scan simulation. Only the central 5 mm of the scan line were used for the discrete statistical analysis

to avoid deviations introduced by the low overlap conditions found at the beginning and end of the line scan.

$$EOF\ Coef.of\ variation = \frac{\sigma_{EOF(x,h,W_O)}}{\mu_{EOF(x,h,W_O)}} \qquad \textbf{Equation 6}$$

The simulations were done for different beam diameters (500 µm ≤ Ø ≤700 µm) and the calculated EOF coefficient of variation is presented in **Figure 46 (b)** as a function of h/W_o ratio to allow a direct comparison between the overlap conditions of laser beams with different diameters. According to these simulations, homogenous exposure is achievable at longer inter-pulse distances using larger beam radius. Using the 1% coefficient of variation as an arbitrary threshold for exposure homogeneity, it can be seen that the corresponding inter-pulse distance shifts from h/W_o=0.91 at W_o=250 µm to h/W_o=1.28 at W_o=350 µm. However, a larger beam radius compromises the achievable lateral resolution as demonstrated by simulating the EOF profile (values were normalized by the maximum EOF for direct comparison) at the start of a line scan for different beam radius at constant inter-pulse distance, as presented in **Figure 46 (c).** It can be seen that exposure builds up over hundreds of micrometers until it becomes stable. Nonetheless, the final lateral resolution will depend on the E_{SE}/E_{CE} ratios because the critical exposure act as an energy cutoff to form structures.

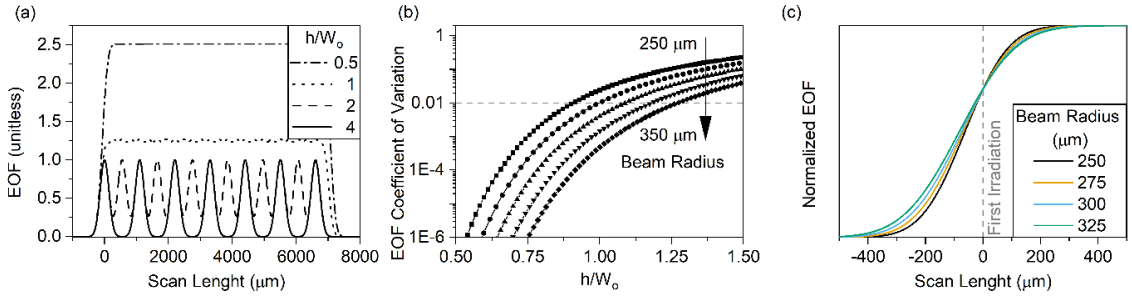

Figure 46. (a) EOF values along a 7 mm scan line using a W_o=275 µm gaussian laser beam with different inter-pulse distances, (b) EOF coefficient of variation calculated over a 5 mm long scan line with different inter-pulse distances, and (c) normalized values of EOF at the beginning of a line scan using different beam diameters with fixed inter-pulse distance (0.5 = h/W_o).

The VPP-UVL-IE model derived is similar to the Jacobs work curve describing -CE process, allowing a direct comparison between the printing speed of -IE and -CE process. Assuming the same laser beam parameters (W_o and P_l), and that beam speed in VPP-UVL-IE (V_{IE}) can be approximated by *h/t* (i.e. dwell time is about two to three orders of magnitude longer than the beam travel time between spots), **Equation 2c** and **5a** describing the peak exposure can be equaled resulting in **Equation 7**.

$$E_{CE} = \frac{P_l}{V_{CE}}\sqrt{\frac{2}{\pi W_o^2}} = P_l.t\frac{2}{\pi W_o^2}EOF(x,h,W_o) = E_{IE}(x,h,W_o)$$

$$V_{IE} \cong h/t$$

$$V_{CE} = V_{IE}\sqrt{\frac{\pi}{2}}\frac{W_o}{EOF(x,h,W_o).h} \qquad \textbf{Equation 7}$$

Thus, the difference in scan speed between -CE and -IE process is a function of EOF. The dependence of EOF with beam radius and inter-pulse distance was evaluated by calculating average EOF values for gaussian beams with different diameters (500 μm ≤ Ø ≤ 700 μm) as function of h/W_o ratio. The data was fitted using an allometric equation (R^2=1), as shown in **Figure 47 (a)**. The coefficient of the allometric fitting was plotted as function of the beam radius and fitted using a linear equation (R^2=1), yielding **Equation 8a** which express EOF as a function of beam radius and inter-pulse distance as shown in **Figure 47 (b)**. Introducing the fitting into **Equation 7** shows that VPP-UVL-IE could theoretically offer faster printing compared to -CE process when the beam radius is larger than 275 μm under same laser intensity conditions with constant power output during the pulses of a gaussian beam, where the laser beam is stationary during the pulse and the dwell time is much longer than the travel time between two spots, as indicated by **Equation 8b**. Interestingly, the difference in scan speed between -CE and -IE process does not depend on dwell time and inter-pulse distance, thus the inter-pulse distance can be freely modulated to achieve homogenous exposure levels along the scan line. Such counter-intuitive conclusion indicates that the faster scan speed of -IE process is a direct result of the higher coverage area and pulse overlap provided by wide laser beams. Conversely, this result also suggests that higher scan speeds are achievable using -CE process for most commercial VPP platforms, which employ pulsed laser sources with beam diameter between 100 and 200 μm with typical pulse duration of dozens of nanoseconds, while the pulse interval is on the order of microseconds [22]. It is worth highlighting that increasing the laser beam diameter also results in decreased lateral resolution, especially at the edges, the ending and beginning of scan lines.

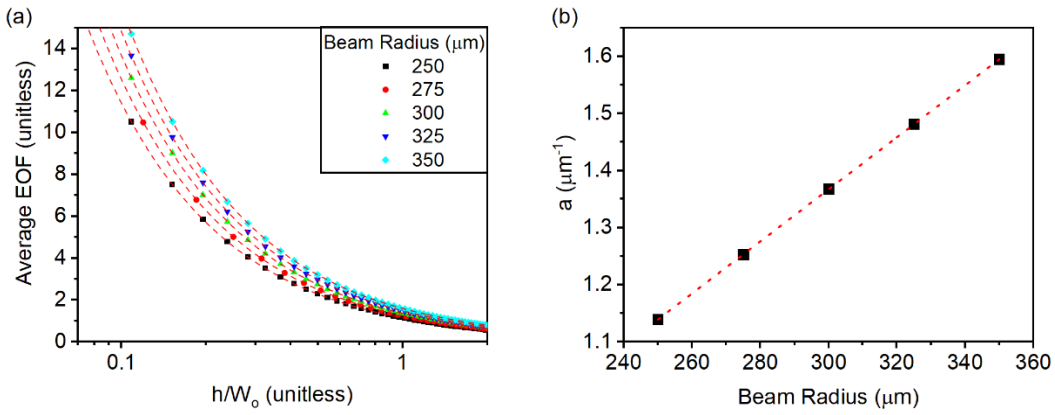

Figure 47. (a) Average EOF value for a gaussian beam with different radius (250, 275, 300, 325, and 350 μm) at different inter-pulse distances. Fitting in red line with an allometric equation $y=ax^{-1}$ ($R^2=1$). The values of *a* parameter are plotted in (b) and fitted with a linear equation $a=0.00456W_o$ ($R^2=1$).

$$\mu_{EOF}\,(h, W_o) \cong 0.00456\frac{W_o^2}{h}.\mu m^{-1}\ 250\ \mu m \leq W_o \leq 350\ \mu m \qquad \textbf{Equation 8a}$$

$$V_{CE} \cong \frac{275}{W_o} V_{IE}.\mu m \qquad \textbf{Equation 8b}$$

The model applicability depends on its robustness since the EOF profile can present insufficient modeling. The impact of such deviations will mostly depend on the exposure conditions used (E_{SE}/E_C ratios). This is evident in **Equation 9** obtained by combining **Equation 5a** and **2b**, showing that an accurate EOF modeling has greater importance under low exposure conditions ($\ln E_{SE}/E_C \approx \ln EOF$) compared to high exposure conditions ($\ln E_{SE}/E_{CE} > \ln EOF$).

$$C_d(x) = D_p\left(\ln\frac{E_{SE}}{E_C} + \ln\ EOF(x, h, W_o)\right) \qquad \textbf{Equation 9}$$

All the above presented analysis is done for a line scan; however, the model can be expanded for bidimensional (layer fabrication) analysis by solving **Equation 3** in y axis. Simulations for the plane fabrication are presented in **Figure S1** available on the Supporting Information in Annex C and the same conclusions can be drawn. It is highlighted that EOF values are different in bidimensional analysis due to overlap in y axis.

Results and discussion

IE-SLA model at constant EOF

Unidimensional (lines) structures were printed at a constant inter-pulse distance of 100 µm. Dwell time ranging from 10 ms up to 100 ms and laser power output from 0.1 mW up to 1.4 mW (irradiance between 42-589 $mWcm^{-2}$) were used. Exposure and cure depth data is presented in **Figure 48**. The data show good adjustment with **Equation 9** (R^2=0.994), with critical exposure (E_c/EOF) estimated in 2.3 $mJ.cm^{-2}$ (simulated EOF≈3.4) and penetration depth of 401 µm. The data at different irradiances can be satisfactorily fitted with a single curve, suggesting that dynamical factors associated to photopolymerization such as oxygen inhibition and reaction rate dependence on light intensity have little effect over the VPP-UVL-IE for these resins. If these factors have an appreciable contribution, the work curves should shift for higher energy as the irradiance increases [9].

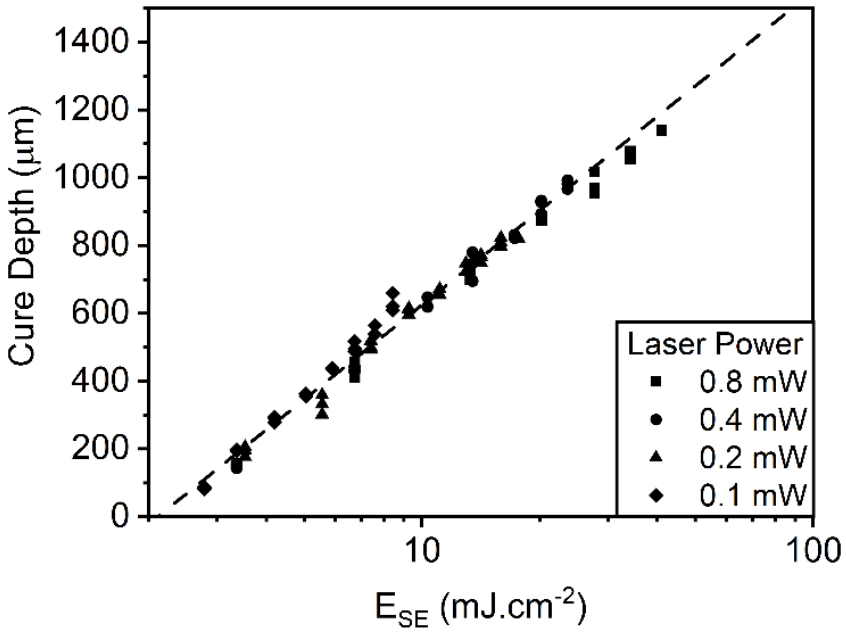

Figure 48. Cure depth (C_d) as a function of exposure for the 0.73 wt.% [PETA/BAPO]-[MPTMS-HAD] resin.

According to **Equation 7**, the VPP-UVL-IE model assumes the same form of Jacobs work curve when inter-pulse distance and beam diameter are fixed, resulting in constant EOF values. This prediction is in excellent agreement with the presented data, and explains why the Jacobs work curve model can be used to model cure depth and exposure data from pulsed laser VPP experiments [22,24]. These observations have been confirmed with a series of other photopolymerizable resins explored by the authors research group and confirm the non-dependence between E_{SE} and EOF factors (data to be published in future works).

IE-SLA model at constant E_{SE}

Linear structures were fabricated under constant laser irradiance and dwell time while the inter-pulse distance was varied from 1 mm to 0.1 mm. Two sets of samples were fabricated under low ($E_{SE} \approx E_C$) and high ($E_{SE} \approx 8E_C$) exposure conditions. The lines were characterized by SEM and stylus profilometry, and experimental data was compared to the simulated VPP-UVL-IE model under the same experimental parameters using E_c and D_p calculated from work curves obtained with 0.1 mm inter-pulse distance.

SEM images and the VPP-UVL-IE model simulation for the high exposure samples is presented in **Figure 49.** The simulated and experimental height profile is consistent, and the model correctly describes the evolution from single and spaced exposures to continuous structures associated to the higher overlap. The spacing between each exposure spot shows good agreement with experimental data and the width of resulting structures at long inter-pulse distance ($h/W_o=3.63$) are comparable (~500μm). The height profile becomes homogenous for $h/W_o<0.91$, which is consistent with the calculated 1% EOF coefficient of variation threshold at $h/W_o<1$. The model overestimates height oscillations on the $h/W_o=1.82$ sample, suggesting that the overlap between individual exposures are higher compared to the model prediction, and real EOF values are superior to simulated ones.

Topography maps obtained from profilometry data presented in **Figure S2** available on the Supporting Information in Annex C reveal further discrepancies. The model overestimates the lines absolute height by about 20%, except the $h/W_o=0.36$ sample whose values are consistent with the model and corresponds to the inter-pulse distance used to calculate the work curve parameters. These inconsistencies indicate real EOF values differ from calculated ones, which is reasonable since the model was simulated for a gaussian beam, and the laser employed in this work is not gaussian ($M^2 < 2$). As noted in the $h/W_o=1.82$ sample, EOF values are higher compared to calculation, leading to underestimation of critical exposure. Ultimately, a systematic error is introduced and the height profile at different inter-pulse distances is overestimated by the model. Nonetheless, the VPP-UVL-IE model offers good insight into the evolution of the exposure and height profile obtained at high exposure conditions.

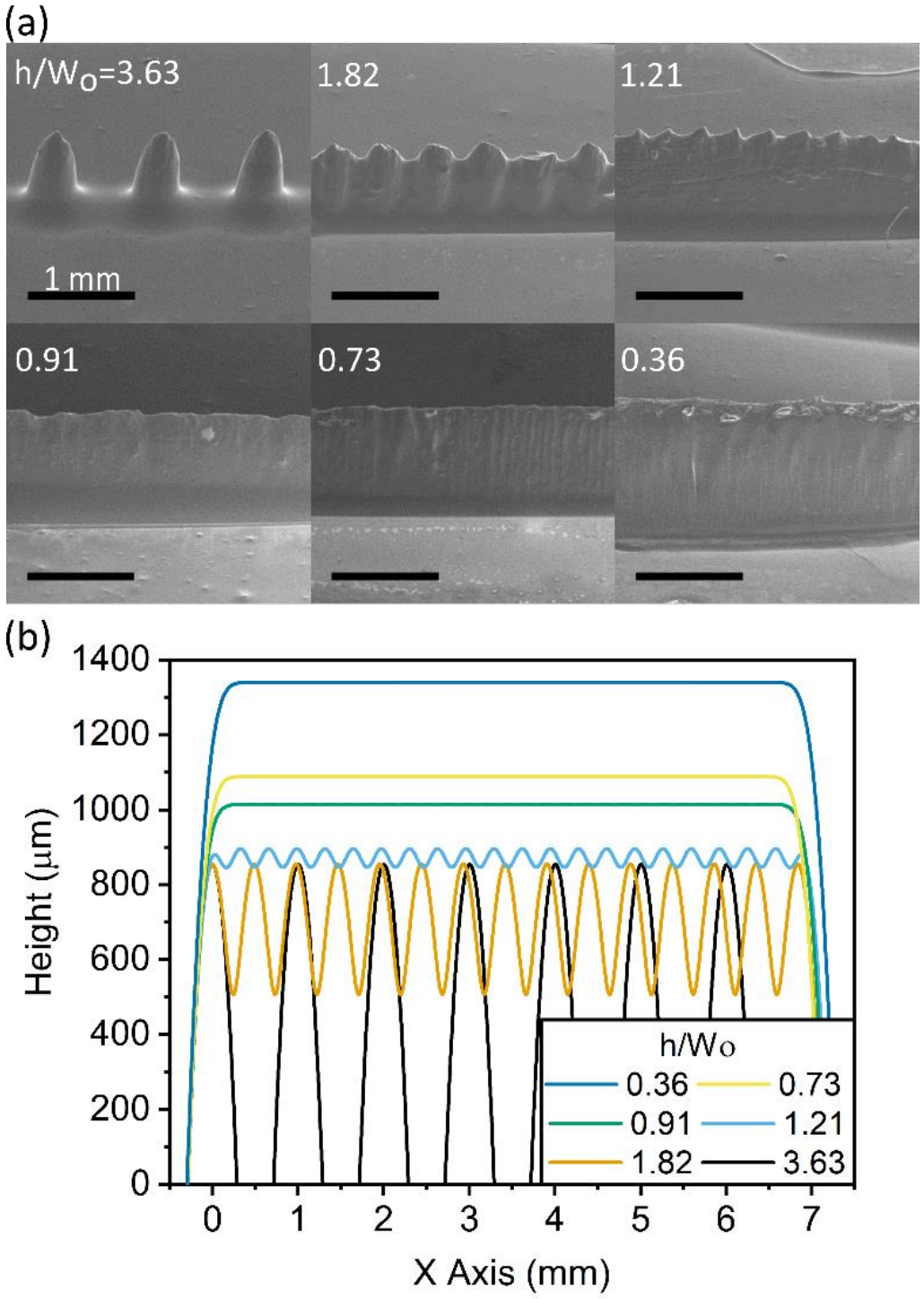

Figure 49. (a) SEM image of a line scan at different inter-pulse distances using 0.73 wt% [PETA/BAPO]-[MPTMS-HAD] resin with a 360 nm laser (Ø=550±10 μm) 800 μW (336.7 mW.cm^{-2}) laser and 100 ms of dwell time. Bar scale of 1 mm; (b) Topography profile according to VPP-UVL-IE model using the same experimental parameters.

Experimental data and simulation for low exposure sample is presented in **Figure 50.** There are discrepancies in the height profile for long inter-pulse distance (h/W_o>0.87) samples. The h/W_o=3.63 and 1.82 samples show wider and taller structures, and h/W_o=1.21 and 0.91 samples show significant height oscillations compared to the simulation. Topography maps presented in **Figure S3** available in the Supporting Information in Annex C indicate significant differences in height values, which are underestimated for all samples, except the h/W_o=0.36 sample. It can be noted that the error increases as h/W_o departs from 0.36, and the predicted height deviates about 10% for h/W_o=0.73 and are higher than 100% at h/W_o=1.21. According to **Equation 7**, EOF values have a large influence in the height profile under low exposure conditions, meaning that the observed deviations are associated with inadequate modeling of total exposure. Thus, the dynamical aspects of photopolymerization, such as self-focusing, scattering and photobleaching phenomena cannot be overlooked when describing the VPP-UVL-IE process at low exposure conditions. In such cases, it is recommended that critical energy and penetration depth must be experimentally determined under the specific overlap conditions employed.

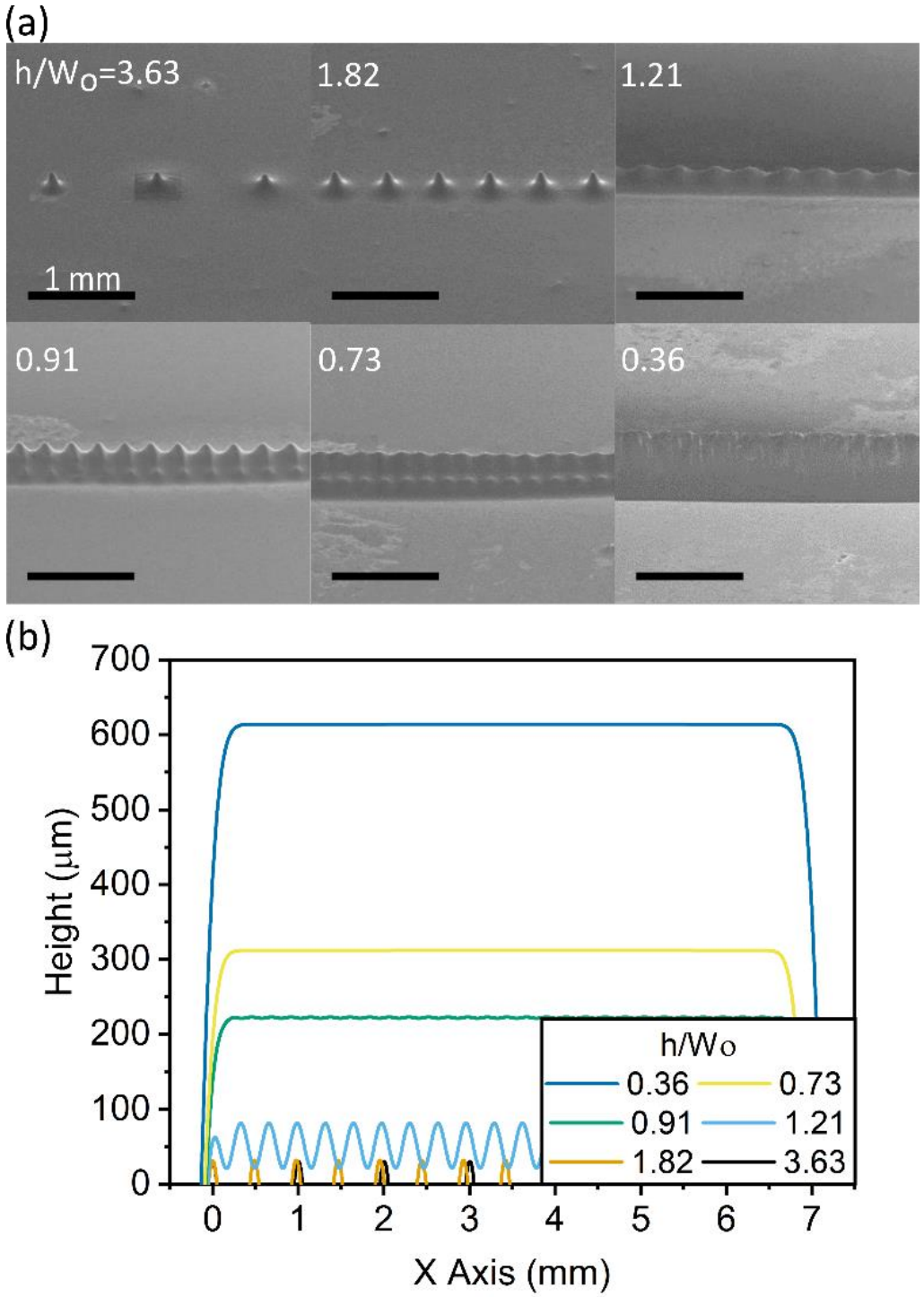

Figure 50. (a) SEM image of a line scan at different inter-pulse distances using 0.73 wt% [PETA/BAPO]-[MPTMS-HAD] resin with a 360 nm 100μW (42.1 mW.cm^{-2}) laser and 100 ms of dwell time. Bar scale of 1 mm; (b) Topography profile according to VPP-UVL-IE model using the same experimental parameters.

In addition to the model's reliability, high exposure conditions offer better surface quality compared to low exposure conditions, as observed in the SEM images of line structures printed with different exposure conditions with fixed inter-pulse distance (h/W_o=0.35) presented in **Figure 51**. At low exposure, as showed by **Figure 51 (a-b)**, the surface is irregular and shows many printing defects, however it becomes smoother as exposure increases, as indicated by **Figure 51 (e-f)**. These findings can be analyzed in the scope of **Equation 7**, since fluctuations in the beam profile and local heterogeneities in the resin will affect EOF values, which are more critical when E/E_c ratio is small.

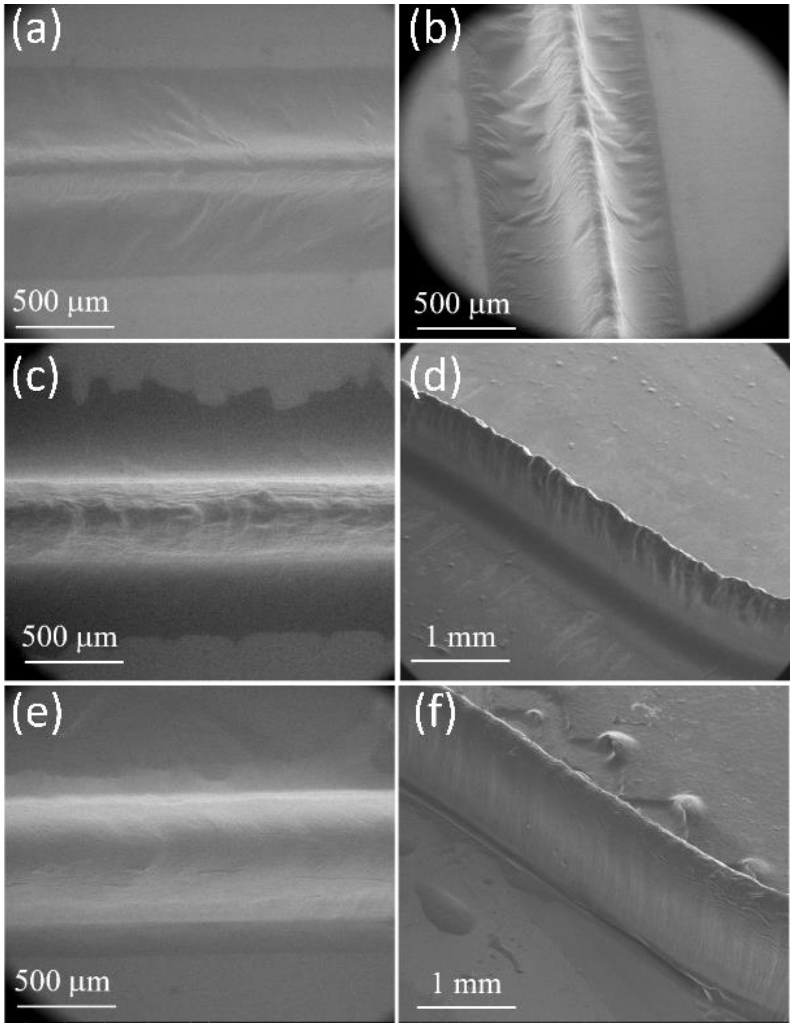

Figure 51. Top (a), (c), and (e) and side view (b), (d), and (f) SEM images of 3D-printed lines prepared from [PETA/BAPO] -[MPTMS-HAD] printed with 10, 30 and 100 ms of dwell time, respectively. Laser irradiance was fixed at 336.7 $mW.cm^{-2}$ and inter-pulse distance of 100 µm was used. Total exposure values of 11.4, 34.3 and 114 $mJ.cm^{-2}$ were calculated based on estimated EOF values (EOF = 3.4).

Conclusion

A VPP-UVL-IE process was modeled and tested using a custom-built printer. The model does not consider dynamical aspects of the photopolymerization process such as reaction kinetics, photobleaching, diffusion and self-focus effects, and the total exposure is described as a summation of individual exposures. The model has the same logarithmic dependence of Jacobs work curve, and the total exposure separates in the exposure of a single pulse and the overlap from adjacent pulses. The model describes with good precision experimental data when the printing parameters related to the spatial distribution of energy are fixed. When fixed exposure conditions are used, only good qualitative agreement is found, and a more robust exposure overlap model is needed to accurately simulate the complexity of the laser-resin interaction. Nonetheless, good agreement with experimental data is still possible under high ($E_{SE} \approx 8E_C$) exposure conditions since the single exposure contribution becomes more important than the overlap one. The VPP-UVL-IE model is less reliable at low exposure ($E_{SE} \approx E_C$) conditions. Insufficient modelling on EOF is eliminated by experimentally determining the critical energy and penetration depth of the resin under fixed overlap conditions, which in most commercial platforms would mean using same scan speed and pulse frequency. These findings highlight intrinsic limitations of the Jacobs work curve model in describing the VPP-UVL-IE process because critical energy values cannot be compared without taking into consideration the overlapping factor between pulse, which are dictated by pulse frequency and scan speed. Lastly, the model indicates that VPP-UVL-IE can, in theory, offer faster printing compared to -CE process for wide laser beam radius (<275 μm) with gaussian profile, considering constant laser output between pulses with dwell time much larger than travel time. Conversely, the model points out that commercial system where laser beam radius is typically inferior than 275 μm could be faster using CW laser sources.

Acknowledgments

The authors would like to thanks Patrick LaRochelle (COPL- University Laval) for his assistance with Software design, 3D printing, and access to fabrication equipment.

Bibliographic References

(1) Ngo, T. D.; Kashani, A.; Imbalzano, G.; Nguyen, K. T. Q.; Hui, D. Additive Manufacturing (3D Printing): A Review of Materials, Methods, Applications and Challenges. *Compos. Part B Eng.* **2018**, *143* (December 2017), 172–196. https://doi.org/10.1016/j.compositesb.2018.02.012.

(2) Quan, H.; Zhang, T.; Xu, H.; Luo, S.; Nie, J.; Zhu, X. Photo-Curing 3D Printing Technique and Its Challenges. *Bioact. Mater.* **2020**, *5* (1), 110–115. https://doi.org/10.1016/j.bioactmat.2019.12.003.

(3) Gibson, I.; Rosen, D.; Stucker, B. *Additive Manufacturing Technologies: 3D Printing, Rapid Prototyping, and Direct Digital Manufacturing*, Second edi.; Springer US, 2015; p 510. https://doi.org/10.1520/F2792-12A.2.

(4) Bikas, H.; Stavropoulos, P.; Chryssolouris, G. Additive Manufacturing Methods and Modelling Approaches: A Critical Review. *Int. J. Adv. Manuf. Technol.* **2016**, *83* (1–4), 389–405. https://doi.org/10.1007/s00170-015-7576-2.

(5) Jacobs, P. F. *Rapid Prototyping & Manufacturing: Fundamentals of StereoLithography*; American Society of Mechanical Engineers, 1992; p 369.

(6) Jacobs, P. F. *Stereolithography and Other RP&M Technologies from Rapid Prototyping to Rapid Tooling*; American Society of Mechanical Engineers, 1996; p 450.

(7) Lee, J. H.; Prud'homme, R. K.; Aksay, I. A. Cure Depth in Photopolymerization: Experiments and Theory. *J. Mater. Res.* **2001**, *16* (12), 3536–3544. https://doi.org/10.1557/JMR.2001.0485.

(8) Goodner, M. D.; Bowman, C. N. Modeling Primary Radical Termination and Its Effects on Autoacceleration in Photopolymerization Kinetics. *Macromolecules* **1999**, *32* (20), 6552–6559. https://doi.org/10.1021/ma9901947.

(9) Uzcategui, A. C.; Muralidharan, A.; Ferguson, V. L.; Bryant, S. J.; McLeod, R. R. Understanding and Improving Mechanical Properties in 3D Printed Parts Using a Dual-Cure Acrylate-Based Resin for Stereolithography. *Adv. Eng. Mater.* **2018**, *20* (12), 1800876. https://doi.org/10.1002/adem.201800876.

(10) Abouliatim, Y.; Chartier, T.; Abelard, P.; Chaput, C.; Delage, C. Optical Characterization of Stereolithography Alumina Suspensions Using the Kubelka–Munk Model. *J. Eur. Ceram. Soc.* **2009**, *29* (5), 919–924. https://doi.org/10.1016/j.jeurceramsoc.2008.07.008.

(11) Tomeckova, V.; Halloran, J. W. Cure Depth for Photopolymerization of Ceramic Suspensions. *J. Eur. Ceram. Soc.* **2010**, *30* (15), 3023–3033. https://doi.org/10.1016/j.jeurceramsoc.2010.06.004.

(12) Tomeckova, V.; Halloran, J. W. Predictive Models for the Photopolymerization of Ceramic Suspensions. *J. Eur. Ceram. Soc.* **2010**, *30* (14), 2833–2840. https://doi.org/10.1016/j.jeurceramsoc.2010.01.027.

(13) Tarabeux, J.; Pateloup, V.; Michaud, P.; Chartier, T. Development of a Numerical Simulation Model for Predicting the Curing of Ceramic Systems in the Stereolithography Process. *J. Eur. Ceram. Soc.* **2018**, *38* (11), 4089–4098. https://doi.org/10.1016/j.jeurceramsoc.2018.03.052.

(14) Tomeckova, V.; Halloran, J. W. Critical Energy for Photopolymerization of Ceramic Suspensions in Acrylate Monomers. *J. Eur. Ceram. Soc.* **2010**, *30* (16), 3273–3282. https://doi.org/10.1016/j.jeurceramsoc.2010.08.003.

(15) Li, H.; Qi, Y.; Sheridan, J. T. Three-Dimensional Extended Nonlocal Photopolymerization Driven Diffusion Model Part II Photopolymerization and Model Development. *J. Opt. Soc. Am. B* **2014**, *31* (11), 2648. https://doi.org/10.1364/JOSAB.31.002648.

(16) Jariwala, A. S.; Ding, F.; Boddapati, A.; Breedveld, V.; Grover, M. A.; Henderson, C. L.; Rosen, D. W. Modeling Effects of Oxygen Inhibition in Mask-based Stereolithography. *Rapid Prototyp. J.* **2011**, *17* (3), 168–175. https://doi.org/10.1108/13552541111124734.

(17) Emami, M. M.; Rosen, D. W. An Improved Vat Photopolymerization Cure Model Demonstrates Photobleaching Effects. In *Solid Freeform Fabrication 2018: Proceedings of the 29th Annual International*; pp 1940–1952. http://dx.doi.org/10.26153/tsw/17195.

(18) Cramer, N. B.; O'Brien, C. P.; Bowman, C. N. Mechanisms, Polymerization Rate Scaling, and Oxygen Inhibition with an Ultra-Rapid Monovinyl Urethane Acrylate. *Polymer* **2008**, *49* (22), 4756–4761. https://doi.org/10.1016/j.polymer.2008.08.051.

(19) Tang, Y.; Henderson, C.; Muzzy, J.; Rosen, D. W. Stereolithography Cure Modelling and Simulation. *Int. J. Mater. Prod. Technol.* **2004**, *21* (4), 255. https://doi.org/10.1504/IJMPT.2004.004941.

(20) Belgacem, M. B.; Kamoun, S.; Gargouri, M.; Dorkenoo, K. D. H.; Barsella, A.; Mager, L. Light Induced Self-Written Waveguides Interactions in Photopolymer Media. *Opt. Express* **2015**, *23* (16), 20841–20848. https://doi.org/10.1364/OE.23.020841.

(21) Lee, K.-S.; Kim, R. H.; Prabhakaran, P.; Yang, D.-Y.; Lim, T. W.; Park, S. H. TWO-PHOTON STEREOLITHOGRAPHY. *J. Nonlinear Opt. Phys. Mater.* **2007**, *16* (01), 59–73. https://doi.org/10.1142/S021886350700355X.

(22) Partanen, J. P. Solid State Lasers for Stereolithography. In *International Congress on Applications of Lasers & Electro-Optics*; Laser Institute of America: Detroit, Michigan, USA, 1996; pp E115–E123. https://doi.org/10.2351/1.5059069.

(23) Satoh, S.; Tanaka, T.; Ihara, S.; Yamabe, C. Excimer Lamp Stereolithography. In *Laser Applications in Microelectronic and Optoelectronic Manufacturing V*; SPIE, 2000; Vol. 3933, pp 272–279. https://doi.org/10.1117/12.387563.

(24) Beke, S.; Anjum, F.; Tsushima, H.; Ceseracciu, L.; Chieregatti, E.; Diaspro, A.; Athanassiou, A.; Brandi, F. Towards Excimer-Laser-Based Stereolithography: A Rapid Process to Fabricate Rigid Biodegradable Photopolymer Scaffolds. *J. R. Soc. Interface* **2012**, *9* (76), 3017–3026. https://doi.org/10.1098/rsif.2012.0300.

(25) Cooper, G. Stereolithography Systems and Methods Using Internal Laser Modulation. EP2646223B1, June 28, 2017. https://patents.google.com/patent/EP2646223B1/en?q=solid+state+laser&assignee=3D+Systems%2c+Inc.&oq=solid+state+laser+assignee:(3D+Systems%2c+Inc.) (accessed 2022-09-01).

(26) Partanen, J. P.; Smalley, D. R. Apparatus and Method for Controlling Exposure of a Solidifiable Medium Using a Pulsed Radiation Source in Building a Three-Dimensional Object Using Stereolithography. US6215095B1, April 10, 2001. https://patents.google.com/patent/US6215095/en (accessed 2022-09-01).

(27) Pingali, R.; Saha, S. K. Reaction-Diffusion Modeling of Photopolymerization During Femtosecond Projection Two-Photon Lithography. *J. Manuf. Sci. Eng.* **2021**, *144* (2). https://doi.org/10.1115/1.4051830.

(28) Bhole, K.; Gandhi, P.; Kundu, T. On the Evolution of Cured Voxel in Bulk Photopolymerization upon Focused Gaussian Laser Exposure. *J. Appl. Phys.* **2014**, *116* (4), 043105. https://doi.org/10.1063/1.4891109.

(29) Sun, H.-B.; Takada, K.; Kim, M.-S.; Lee, K.-S.; Kawata, S. Scaling Laws of Voxels in Two-Photon Photopolymerization Nanofabrication. *Appl. Phys. Lett.* **2003**, *83* (6), 1104–1106. https://doi.org/10.1063/1.1599968.

(30) Nakamura, Y.; Fushinobu, K.; Tamura, A. Numerical Analysis of Pulse Laser Assisted Curing Region of Photocurable Resins. In *ASME 2019 International Technical Conference and Exhibition on Packaging and Integration of Electronic and Photonic Microsystems*; American Society of Mechanical Engineers: Anaheim, California, USA, 2019; p V001T05A001. https://doi.org/10.1115/IPACK2019-6356.

(31) Fang, N.; Sun, C.; Zhang, X. Diffusion-Limited Photopolymerization in Scanning Micro-Stereolithography. *Appl. Phys. A* **2004**, *79* (8), 1839–1842. https://doi.org/10.1007/s00339-004-2938-x.

(32) Kang, H.-W.; Park, J. H.; Cho, D.-W. A Pixel Based Solidification Model for Projection Based Stereolithography Technology. *Sens. Actuators Phys.* **2012**, *178*, 223–229. https://doi.org/10.1016/j.sna.2012.01.016.

(33) Park, H. K.; Shin, M.; Kim, B.; Park, J. W.; Lee, H. A Visible Light-Curable yet Visible Wavelength-Transparent Resin for Stereolithography 3D Printing. *NPG Asia Mater.* **2018**, *10* (4), 82–89. https://doi.org/10.1038/s41427-018-0021-x.

(34) Bennett, J. Measuring UV Curing Parameters of Commercial Photopolymers Used in Additive Manufacturing. *Addit. Manuf.* **2017**, *18*, 203–212. https://doi.org/10.1016/j.addma.2017.10.009.

CHAPTER 4. CORRELATION BETWEEN CRITICAL ENERGY, PENETRATION DEPTH, AND PHOTOPOLYMERIZATION KINETICS IN ALUMINUM-PHOSPHATE-SILICATE HYBRID MATERIALS FOR VAT-PHOTOPOLYMERIZATION

Gabriel Toshiaki Tayama [1 2 *], Sandra Helena Messaddeq [1], Silvia Helena Santagneli [2] and Younes Messaddeq [1, 2]

Center for Optics, Photonics and Lasers, Laval University, 2375 de la Terrasse, Quebec City, QC, G1V 0A6, Canada;

Chemistry Institute of Araraquara, Sao Paulo State University (UNESP), 55 Av. Prof. Francisco Degni, Araraquara, SP, 14800-900, Brazil;

KEYWORDS: Work curve, stereolithography, sol-gel, photo-DSC, photopolymerization, hybrid materials.

Abstract

The photopolymerization of aluminum-phosphate-silicate resins obtained from the hybrid sol-gel route for Vat Photopolymerization (VPP) process was investigated. The printing parameters derived from Jacob's work curve model, critical energy (E_c) and penetration depth (D_p), were determined as a function of laser power and MPTMS (silicate) concentration for materials with stoichiometry $Si_{(x)}$- $(Al+P)_{(1-x)}$, $0 \leq x \leq 0.7$. The kinetics of photopolymerization were further explored using steady- and unsteady-state photo-DSC experiments. The oxygen inhibition, and primary termination had similar contributions to the polymerization process for all compositions, while the propagation and bimolecular termination constants increased with MPTMS concentration. These experimental results were used to test the validity of the $E_c \propto ({k_t}^{1/2}/k_p)$ and $D_p \propto \epsilon$ relationship derived from a photochemical model for VPP assuming steady-state kinetics. Both $E_c \propto ({k_t}^{1/2}/k_p)$ and $D_p \propto \epsilon$ may be used to predict critical

energy and penetration values for an arbitrary resin without calculating its work curve function, according to our study.

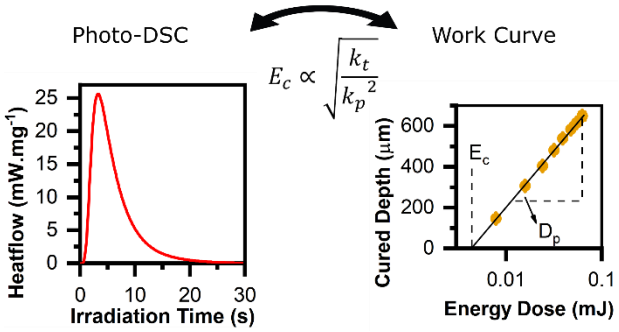

Resumo

Neste trabalho foi investigado a fotopolimerização de resinas a base de alumínio-fosfato-silicato obtidas a partir da rota sol-gel para impressão 3D via fotopolimerização em cuba (VPP). Os parâmetros de impressão energia crítica (E_c) e profundidade de penetração (D_p), derivados do modelo de curva de trabalho de Jacob, foram determinados em função da potência do laser e da concentração de MPTMS (silicato) para materiais com estequiometria $Si_{(x)}$- $(Al+P)_{(1-x)}$, $0 \leq x \leq 0.7$. Complementarmente, foi estudado a cinética da fotopolimerização através de experimentos de foto-DSC utilizando modelos cinéticos de polimerização em estado estacionário e não-estacionário. Os resultados obtidos indicaram que a inibição por oxigênio e a terminação primária tiveram contribuições similares para o processo de polimerização em todas as composições, enquanto as constantes de propagação e terminação bimolecular aumentaram com a concentração de MPTMS. Esses resultados experimentais foram utilizados para validar as relações $E_c \propto ({k_t}^{1/2}/k_p)$ e $D_p \propto \epsilon$ obtidas a partir de um modelo fotoquímico para VPP assumindo cinética polimerização em estado estacionário. Ambos $E_c \propto ({k_t}^{1/2}/k_p)$ e $D_p \propto \epsilon$ podem ser usados para prever valores de energia crítica e de profundida de penetração, dispensando a necessidade de construir a curva de trabalho do material.

Résumé

La photopolymérisation des résines d'aluminium-phosphate-silicate obtenues à partir de la voie sol-gel pour le processus de photopolymérisation en cuve (VPP) a été étudiée. Les paramètres d'impression dérivés du modèle de courbe de travail de Jacob, énergie critique (E_c) et profondeur de pénétration (D_p), ont été déterminés en fonction de la puissance du laser et de la concentration de

MPTMS (silicate) pour les matériaux de stœchiométrie $Si_{(x)}$- $(Al+P)_{(1-x)}$, $0 \leq x \leq 0.7$. La cinétique de la photopolymérisation a été explorée à l'aide d'expériences de photo-DSC en utilisant des modelés cinétiques de polymérisation avec d'approximation des états quasi stationnaires e non stationnaires. L'inhibition de l'oxygène et la terminaison primaire avaient des contributions similaires au processus de polymérisation pour toutes les compositions, tandis que les constantes de propagation et de terminaison bimoléculaire augmentaient avec la concentration de MPTMS. Ces résultats expérimentaux ont été utilisés pour tester la validité de la relation $E_c \propto ({k_t}^{1/2}/k_p)$ et $D_p \propto \epsilon$ dérivée d'un modèle photochimique pour VPP en supposant une cinétique à l'état d'équilibre. Selon notre étude, $E_c \propto ({k_t}^{1/2}/k_p)$ et $D_p \propto \epsilon$ peuvent être utilisés pour prédire l'énergie critique et les valeurs de pénétration pour une résine arbitraire sans calculer sa fonction de courbe de travail.

Introduction

Laser scanning vat photopolymerization (VPP-UV), also known as stereolithography (SLA), is a well-established additive manufacturing (AM) technique based on the selective photopolymerization of a resin using a laser source [1]. VPP presents one of the greatest printing resolutions and best surface quality among other AM techniques, making it a suitable microfabrication technology for applications in photonics [2,3] and microfluidics [4,5]. The lack of a wide variety of processable materials is one of the main factors hindering the extensive application of VPP techniques [6,7], since only acrylate, epoxy and thiol-ene organic functions can react through the photopolymerization mechanism [8,9]. Recently, numerous studies have been conducted to expand the range of materials that can be processed by VPP, with a focus on ceramics and inorganic glasses. One of the most promising methods is the hybrid sol-gel process to achieve a photopolymerizable resin, resulting in a hybrid material [10–14], which can be further heat treated to remove the organic components, and form a ceramic material [15–17] or an inorganic glass [18–23].

Modeling the laser-resin interaction is a crucial aspect for developing new materials for VPP technologies, as it enables the selection of optimal exposure conditions (processing parameters) to produce the desired 3D printed objects [24]. Consequently, a model describing the VPP process must consider the physics and chemistry of light penetration and polymerization kinetics. This is not a simple task since many factors must be considered to create accurate models, such as the numerous parallel

reactions leading to polymerization [25,26], the dependence of kinetic constants on light intensity [27], presence of scattering centers [28–32], diffusion of active centers and monomers [33,34], photobleaching of photoinitiator fragments [35], oxygen inhibition [34,36], heat diffusion [37], self-focusing effects [38], polymerization shrinkage and cyclization reaction [39–41], and the gel effect [25,26,42,43]. The most relevant factors affecting the laser-resin interaction are summarized in **Figure 52.**

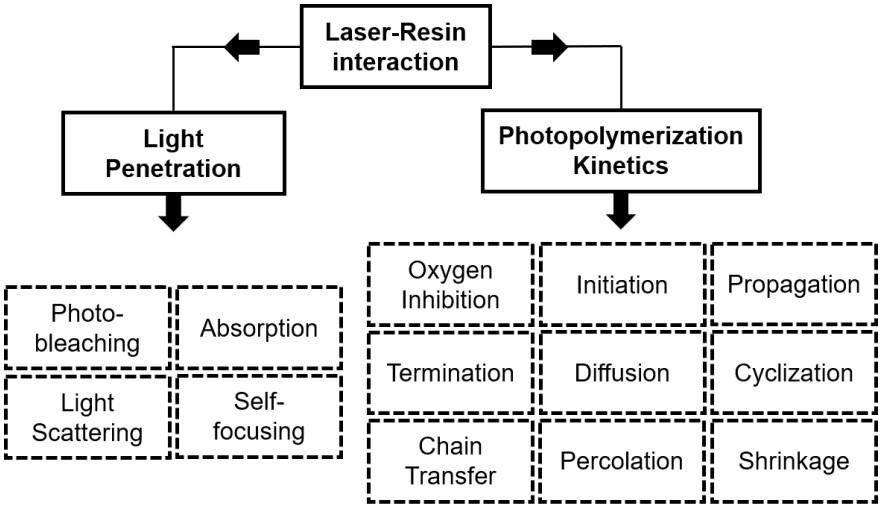

Figure 52. The main factors determining the laser-resin interaction during the photopolymerization process in vat-photopolymerization techniques.

Jacob deduced the work curve model in the early 1960, when the VPP process was in its infancy [44,45]. The model describes the light penetration of a Gaussian beam using the Lambert-Beer law, and it assumes the existence of a critical exposure (E_c) required for the resin to reach the gel point, i.e., the formation of a percolated network [1,44,45], as well a characteristic penetration depth (D_p) related to the absorption properties of the resin. The Jacobs work curve model is shown in **Equation 1**, and the model is successful in fitting layer thickness (C_d) vs energy dose (E) data straightforwardly. It is important to highlight that the E_c and D_p obtained can only be applied under the irradiation conditions studied.

$$C_d = D_p \ln \frac{E}{E_c} \quad (1)$$

Constructing the Jacobs work curve has become the most popular procedure for characterizing a new photocurable resin for VPP, nevertheless the critical exposure hypothesis oversimplifies the complexity and dynamic nature of the photopolymerization phenomenon. For instance, the kinetics of

photopolymerization, and the resulting polymer properties do not scale linearly with the applied energy dose, that is, reciprocity law is not respected in most cases [46] because the photoscission is the primary reaction while the photopolymerization is a secondary process. In the case of VPP, it means that E_c and D_p values of different materials can only be compared if they are measured at the same light intensity [27,47]. The Trommsdorff–Norrish effect (gel effect) increases the complexity of the photopolymerization because the percolation of the polymeric network greatly affects the kinetics of the photopolymerization process [48,49]. Traditional methods to model the gel effect such as Flory-Stockmayer theory for polycondensation systems and statistical methods do not consider the evolution of the polymerization kinetics and cannot address the laser-resin interaction [25].To date, there is no reliable approach for modeling the gel effect.

The most robust photopolymerization models encompassing all these factors can be divided into phenomenological and mechanistic approaches. Phenomenological methods describe the photopolymerization process as a single reaction, which facilitates its implementation in engineering processes [50], at the expense of information on the numerous parallel reactions occurring during the photopolymerization process [51]. In contrast, mechanistic models try to capture all the reactions associated with the polymerization process, but still require a significant number of assumptions and simplifications [51] due to the complexity of the photopolymerization reaction. Nonetheless, mechanistic models are the most interesting approaches to understand the correlation between photopolymerization kinetics and the printing parameters of VPP. The most robust mechanistic models available require experimental data to fit a free-volume factor describing the network percolation and the reduced mobility of chemical species, i.e., the gel effect [52]. Furthermore, there are few works in the literature concerning the photopolymerization process under high initiation rates with high crosslink density, which is the case for VPP-UV techniques [49,53–55]. Consequently, most descriptions of the photochemistry of VPP resins presented in the literature fail to grasp the significant primary termination, recombination, and cyclization reactions [9,56,57], as well the gel effect at C=C conversion as low as 5% present in the photopolymerization of these materials.

Few works have been published in the literature concerning the photochemistry of VPP, and they rely on simulations employing mechanistic [58–60] or phenomenological models [50,61–63]. It is important to highlight, however, that none of these studies were developed in the same framework of the work curve model. Consequently, there is no connection between the work curve model parameters (critical energy and penetration depth), and the physico-chemical properties of a resin for VPP-UV (such as

photopolymerization kinetic constants, structure, crosslinking density, viscosity, concentration of reactive groups, and polymerization shrinkage). Such a gap in the literature results in time-consuming and tedious experiments to acquire energy dose vs cure depth data for each material under specific exposure conditions since there is no reliable method of estimating these values for an arbitrary resin. In this sense, the work of Lee et al. [64] is the only one in the literature addressing such issue, where the authors applied a steady-state approach toward the polymerization kinetics to derive the same work curve relationship deduced by Jacobs. In particular, the authors have derived **Equation 2** and **3** that express the dependence of the critical energy and penetration depth on polymerization kinetic constants for bimolecular termination and propagation (k_t and k_p respectively), critical conversion (p_c), photoinitiator concentration [PI], and absorption coefficient (ε). However, the experimental validity of this relationship has not been further explored.

$$E_c \propto \frac{1}{[PI]^{1/2}} \sqrt[2]{\frac{k_t[\ln 1 - p_c]^2}{k_p^2}} \tag{2}$$

$$D_p = \frac{2}{2.303\epsilon[PI]} \tag{3}$$

In this study, we characterized the critical energy and penetration depth parameters for a set of resins obtained through the hybrid sol-gel method. These materials comprehend silicate-aluminum-phosphate hybrids described in a prior work [10] with nominal composition $Si_{(x)}$- $(Al+P)_{(1-x)}$ where x ranges from 0 to 0.7. The parameters of the work curve were measured at various irradiance intensities and as a function of the MPTMS (silicate) content. Steady-state and unsteady-state photo-DSC experiments were conducted to further follow the evolution of the photopolymerization kinetic constants with irradiance and MPTMS concentration. Additionally, its UV-VIS absorption, and polymerization shrinkage were assessed. We analyzed the evolution of the Jacobs work curve parameters based on the photopolymerization kinetics of initiation, propagation, and termination with MPTMS content and light intensity to verify the validity of **Equation (2)** and **(3)**.

Materials and methods

Materials synthesis. The photopolymerizable aluminum-phosphate-silicate organic-inorganic hybrid resins were prepared by sol-gel method using a procedure described in detail elsewhere [10,11].

Aluminum-tri-sec-butoxide 97% (Sigma-Aldrich), hydroxyethyl methacrylate phosphoric acid ester - HEMA-P- 90% (Sigma-Aldrich), 2-(Methacryloyloxy) ethyl acetoacetate-MAEAA- 95% (Sigma-Aldrich), methanol P.A. (Synth), [3-(Methacryloyloxoxy)propyl]trimethoxisilane – MPTMS - 98% (Sigma-Aldrich) and diphenyl (2, 4, 6- trimethyl benzoyl) phosphine oxide -TPO- 97% (Sigma-Aldrich) was used as received. In short, appropriate quantities of a modified aluminum alkoxide and a methanol solution of HEMA-P were mixed at a 1:1 molar ratio for 24 h, followed by the addition of pre-hydrolyzed MPTMS. The mixture was stirred another 24 h to allow the condensation reaction to occur. The solvents were evaporated under reduced pressure, resulting in a yellowish liquid. The photoinitiator TPO was dissolved at 1w.t. % and the solutions were stored in closed vessels. The resins do not undergo gelation when stored in closed vials, and can be photopolymerized after at least four years of storage.

Characterizations. The resins UV/VIS absorption spectra were collected using a Cary 5000 with quartz cuvettes of 10 mm optical path. Resin density (ρ_{resin}) was determined using a microscale and a transfer pipette by weighing different volumes of resin and fitting the data through linear regression. Polymerized hybrid materials' density ($\rho_{polymer}$) was measured with a helium pycnometer (Quantachrome Ultrapyc 1200e). The polymerization volumetric retraction was determined using Archimedes's principle.

$$\Delta V = \left(\frac{1}{\rho_{resin}} - \frac{1}{\rho_{polymer}}\right) \times \frac{1}{\rho_{polymer}} \times 100\%$$

Solid State NMR ^{29}Si nuclei were obtained on a Bruker Avance III HD 400WB spectrometer equipped with a 4 mm probe. The samples were measured under ν_{ro} = 10.0 kHz. ^{29}Si single pulse NMR spectra were acquired using an excitation π/2 single pulse (3.5 μs length) under TPPM proton decoupling during data acquisition, and relaxation time of 400 s. The ^{29}Si NMR spectra were referenced externally to tetramethyl silane (TMS).

Additive manufacturing. Critical energy and penetration depth of the resins were characterized using a procedure and custom-made VPP-UV setup described elsewhere [47]. In short, lines were printed in microscope slides using a vat structure with different energy doses and light intensities. The glass slide was removed from the vat structure and washed with anhydrous ethanol to remove residual resin, and the line height was measured using a stylus profilometer (Dektak 150, Veeco) equipped with a 45-angle cone, and 9 μm curvature radius stylus. For this work, lines were printed using laser intensities ranging from 30 μW up to 1 mW.

Photo DSC. The photopolymerization was studied by photo-DSC using a Mettler Toledo (DSC 822e) equipped with a Hamamatsu LC5 Spot Light Source L8333-02, operating with a mercury-xenon lamp coupled to a quartz waveguide. The full spectrum of the lamp was used in the study. The photopolymerization was carried out under a dynamic N_2 atmosphere (50 mL.min^{-1}) with an uncovered aluminum pan and 10 mm of distance between the sample and the waveguide. Between 1 and 2 mg of sample was spread in the aluminum pan to achieve thin film polymerization conditions, with an estimated thickness of 10 µm. Steady state experiments were employed to measure the lumped kinetic constant at three different light intensities of 0.5, 2.5, and 25 mW cm^{-2}. Unsteady- and steady-state experiments with 0.1 mW cm^{-2} light intensity were explored to evaluate the K_p/K_t ratios between the compositions. The heat flow curves were normalized by the samples mass, and the polymerization rate was calculated assuming a polymerization heat of 14.1 kcal.mol^{-1} per methacrylate group (corresponding to the polymerization of ethyl methacrylate [65]).

Results and discussion

Work Curve Measurements

Representative work curves of 0% and 70% MPTMS resin measured at different laser intensities are presented in **Figure 53 (a)** and **(b)**, respectively. The experimental data show good fitting quality with the work curve equation with R^2>0.98. Critical energy and penetration depth values are compiled in **Figure 53 (c)** and **(d)**, indicating a systematic increase in the average critical energy and penetration depth with MPTMS concentration. For instance, the average critical energy increases about four times, from 3.3 µJ to 12.0 µJ from 0 to 70% MPTMS concentration. This trend is contradictory with the increase in the average penetration depth, from 234 to 370 µm, since more photons can penetrate the resin, resulting in higher initiation rates. Furthermore, it can be seen that critical energy values are shifted towards higher energy as the laser intensity increases for all compositions. The trend is similar for all laser intensities studied, except for the measurements at low laser power, in which case the 70% MPTMS sample shows a smaller increase in critical energy compared to the ones observed at higher laser power, indicating a higher dependency of the photopolymerization kinetics with light intensity for the 70% sample compared to other compositions. Conversely, it can be seen that the increase of light penetration with MPTMS concentration follows different trends with the laser intensity employed. For instance, the increase in penetration depth with MPTMS concentration observed for measurements with 0.13 and 0.34 mW of laser power show a higher increase compared to the ones collected at 1.09

and 0.73 mW. The fitted values of critical energy and penetration depth are shown in Table S1 available in the Supporting Information in Annex D.

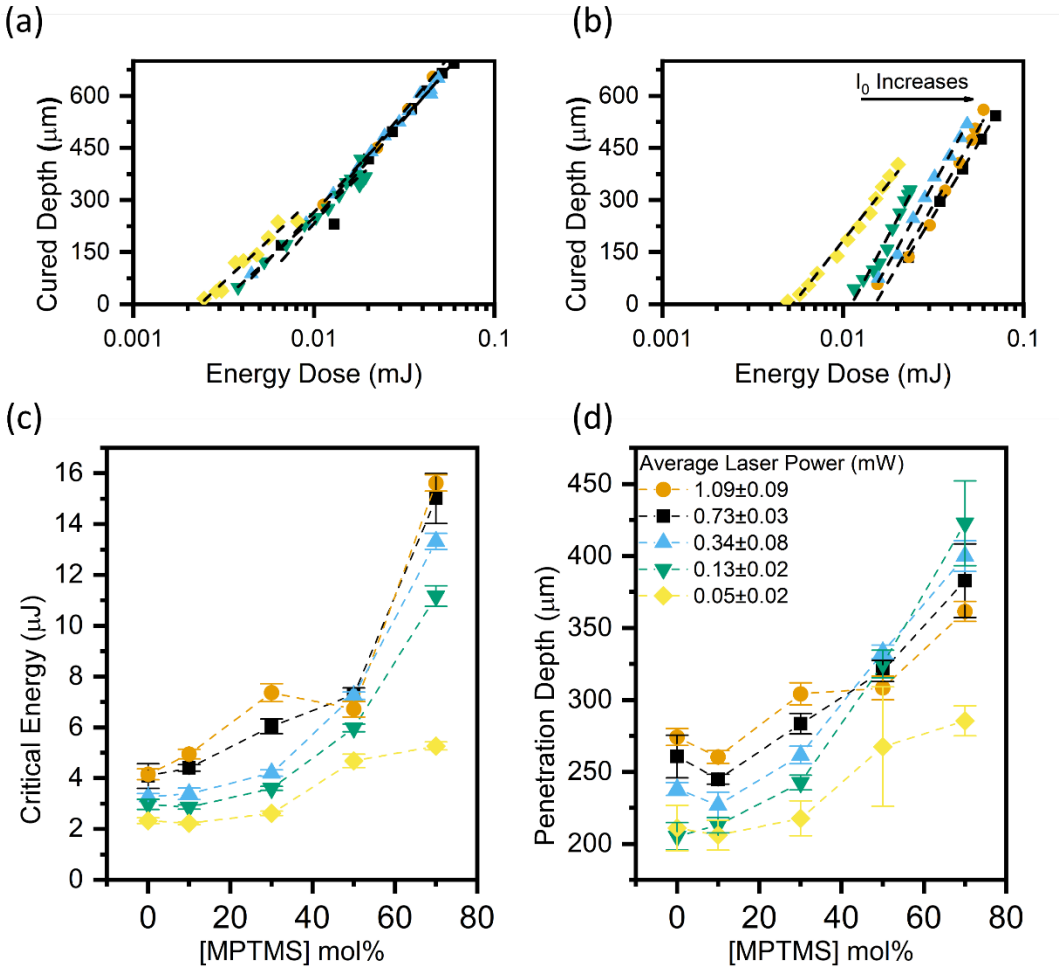

Figure 53. Work curve fitting of cure depth by energy dose for 0% (a) and 70% (b) MPTMS resins measured at average laser powers of 1.09, 0.73, 0.34, 0.13, and 0.05 mW. Critical energy and penetration depth values according to MPTMS concentration are compiled in (c) and (d), respectively.

Average penetration depth evolution with MPTMS concentration

Penetration depth is directly associated with resin`s absorption properties at the irradiation wavelength according to **Equation 3**. The resins' absorption coefficient was estimated from the photoinitiator absorption and the resins' intrinsic absorption. **Figure 54 (a)** shows the photoinitiator absorption coefficients measured at different concentrations. The data were fitted using Lambert-Beer law and extrapolated to the photoinitiator concentration employed in this work (1 w.t. %), revealing an absorption coefficient of 15 cm^{-1}. **Figure 54 (b)** presents the UV/Vis absorption spectra of the resins

without photoinitiator with different MPTMS concentrations, showing a characteristic absorption band between 330 and 380 nm assigned to the modified aluminum alkoxide. The evolution of penetration depth with MPTMS concentration is coherent with the UV/Vis absorption spectra of the resins. Penetration depth values were calculated using **Equation 3** based on the absorption values measured using UV/Vis absorption data. A comparison with experimental data is presented in **Figure 54 (c)**. It can be seen that the penetration depth values measured at low laser intensity agree with the calculated values. Deviations were observed for the measurements at higher laser intensity, suggesting the presence of other phenomena such as photobleaching.

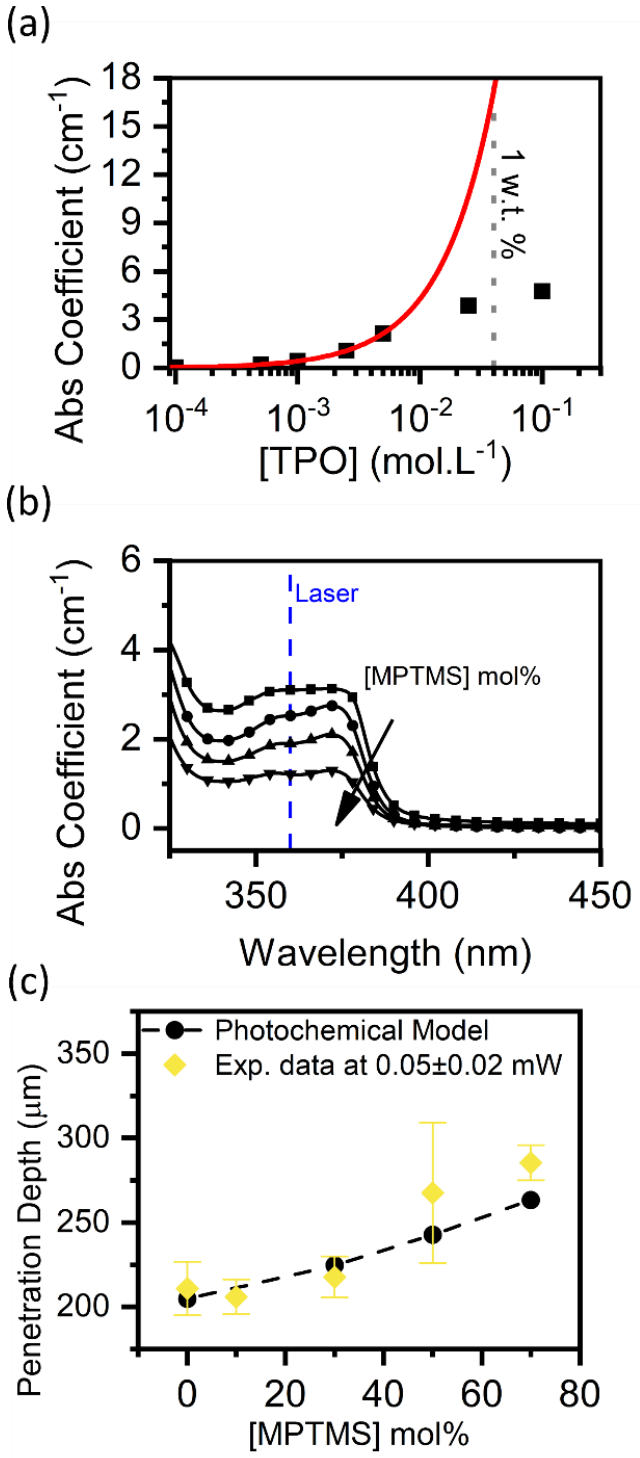

Figure 54. (a) Absorption coefficient spectra of TPO dispersed in ethanol at different concentrations fitted with Lambert-Beer law. The dotted line indicates the equivalent molar concentration to 1 w.t.% used in this study. (b) Absorption coefficient spectra of resins with 0%, 30%, 50%, and 70% MPTMS concentrations without photoinitiator. (c) Penetration depth values extracted from the work curve data collected at 0.05 mW laser power, and calculated penetration depth values based on **Equation 3** [64].

Penetration depth evolution with light intensity

Penetration depth evolution with laser power for all compositions was investigated, and the values are presented in **Figure 55**. All samples with MPTMS concentrations below 30% showed an increase in penetration depth with laser power. The increase in light penetration with laser power suggests the presence of the photobleaching effect, which would explain why only penetration depth values obtained at low laser power follow the photochemical model, as seen in **Figure 54 (c)**. In contrast, the penetration depth of samples with MPTMS concentrations higher than 50% decreased with laser power for laser intensities higher than 50 uW, suggesting the presence of light scattering. Light scattering is a well-known phenomenon in laser photopolymerization, however its modeling has been an object of investigation in many published works without a general accepted approach of modeling [66]. The main mechanisms responsible for light scattering during photopolymerization of homogeneous photopolymer system are Rayleigh scattering and phase separation[67] due to the micro heterogenous nature of the photopolymerization process[25]. Solid-state NMR studies in these materials have revealed that their structure is composed by fundamental building blocks of aluminum-phosphate and alkoxysilane branched chains of high molecular weight, with low interaction with each other[11]. These alkoxysilane units could act as scattering centers, resulting in appreciable light scattering.

The contribution of light scattering and photobleaching with higher laser power introduces deviations in the observed trends of penetration depth versus MPTMS concentration according to the laser power employed as shown in **Figure 53**. For instance, it can be seen that the increase of penetration depth with MPTMS concentration is higher for the measurements at 0.13, and 0.34 mW, compared to those at 1.09, and 0.73 mW. As showed in **Figure 55**, photobleaching is more evident in the 0, 10 and 30% MPTMS concentration, while the light scattering has a stronger effect in the 50% and 70% samples. The light penetration increases and decreases with photobleaching and scattering, respectively, which would explain the differences observed in the penetration depth evolution for measurements at different laser powers. Both photobleaching and light scattering are not phenomena considered in Lee's photochemical model, consequently **Equation 3** is unable to model the dependence of penetration depth with light intensity. Nonetheless, **Equation 3** is valid when these factors are mitigated using low laser power.

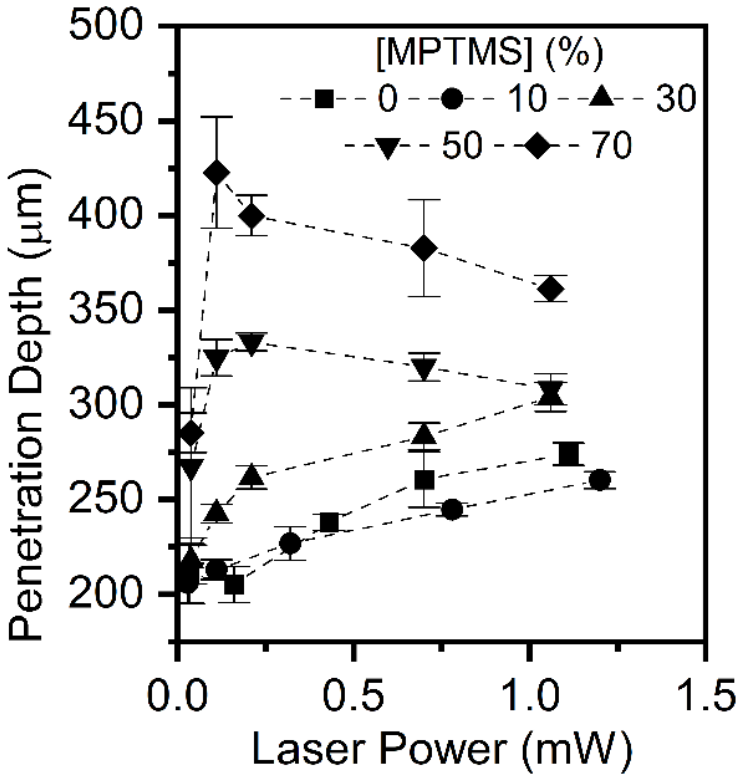

Figure 55. The evolution of penetration depth values extracted from work curve data collected at different laser intensities for resins with 0% (a), 10% (b), 30% (c), 50% (d), and 70% (e) MPTMS concentration.

Photopolymerization kinetics evolution with MPTMS concentration

The photopolymerization kinetics of the samples was studied by photo-DSC under three irradiation intensities (0.25, 2.5 and 25 mW.cm^{-2}). Photo-DSC curves measured under the irradiance of 25, 2.5, and 0.25 mW.cm^{-2} are presented in **Figure 56 (a)**, **(b)**, and **(c)**, respectively. These materials show typical sigmoidal curves with auto-acceleration and auto-deacceleration behavior and induction time in the order of 1 second. The induction period is caused by oxygen inhibition, because dissolved molecular oxygen scavenges radical centers or quenches the excited photoinitiator molecules' triplet state, depending on the type of photoinitiator [68]. The kinetic constant for inhibition is orders of magnitude higher than other reactions, and it is often assumed that no significant polymerization occurs until the dissolved oxygen concentration is below a certain threshold, usually representing a reduction by three to four orders of magnitude in dissolved oxygen according to Decker and Jenkins [69].

The induction time increases monotonically with the light intensity, with the average inhibition regime lasting 1.00 s, 1.30 s, and 1.60 s under irradiation of 25, 2.5, and 0.5 $mW.cm^{-2}$, respectively. There is no correlation between MPTMS concentration and the induction period, despite the concentration of stabilizing agents (MEHQ/TBH) decreasing with MPTMS concentration since the manufacturer adds these compounds in the aluminum and the phosphate precursors. These stabilizing agents are polymerization retardants, since they are only effective in inhibiting the polymerization in the presence of oxygen [70,71], which suggests similar concentrations of dissolved oxygen in all samples studied. Thus, compositional differences in these resins has little influence over the oxygen inhibition mechanics, despite the high oxygen permeability typically shown by alkoxysilane species formed during MPTMS condensation [72].

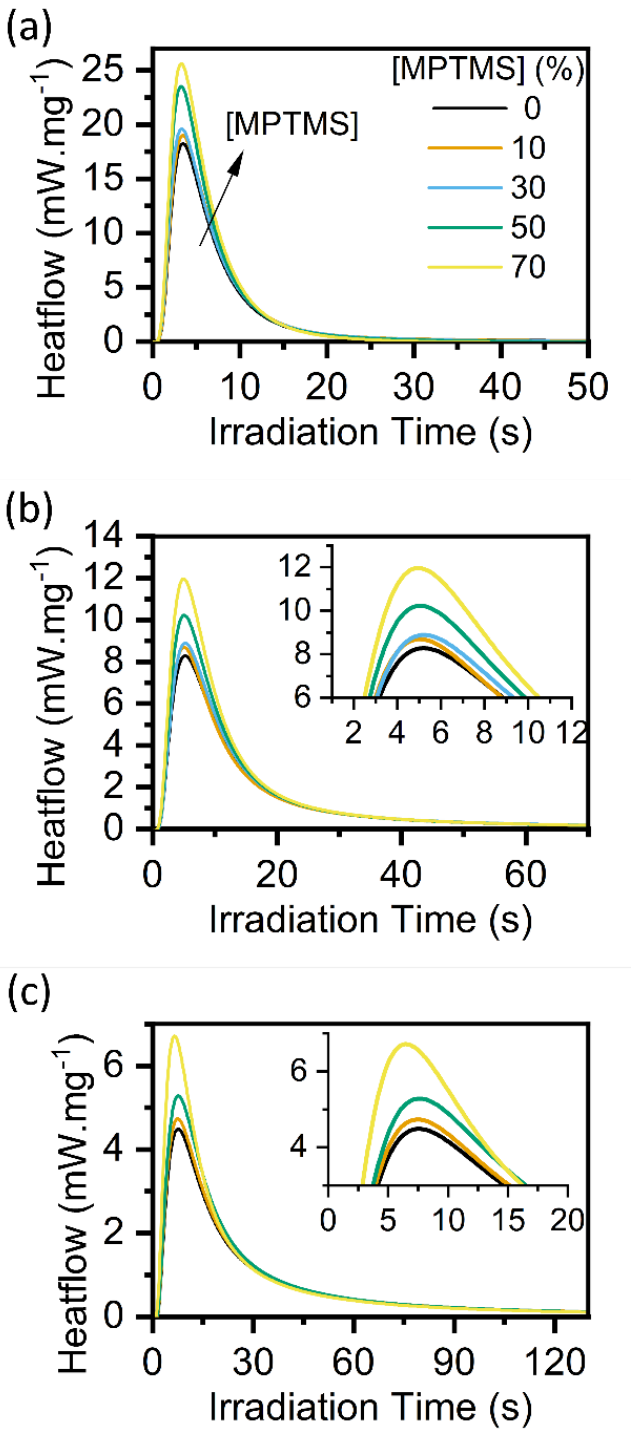

Figure 56. Photo-DSC curves for the photopolymerization of 0% (black), 10% (orange), 30% (blue), 50% (green) and 70% (yellow) [MPTMS] resins under irradiation of 25 mW.cm^{-2}, 2.5 mW.cm^{-2}, and 0.5 mW.cm^{-2},

The calorimetric data were analyzed using pseudo-steady-state mechanics with bimolecular termination, according to **Equation (4)**, which describes the polymerization rate (R_p) as a function of the lumped kinetic constant, which is a combination of the initiation (k_i), propagation (k_p), and termination (k_t) rates.

$$\frac{R_p}{[M]} = \frac{k_p k_i^{1/2}}{k_t^{1/2}} \quad (4)$$

The evolution of the lumped kinetic constant with irradiation time for samples with different MPTMS concentrations measured at 25 mW.cm^{-2} is presented in **Figure 57 (a)**. It can be seen that the kinetic constant increases with the MPTMS concentration, under the assumption of a constant initiation rate between compositions. Such assumption is plausible since the efficiency of the photoinitiator, the absorption coefficient, and the light intensity determine the kinetics of initiation. The final two criteria are believed to be constant across samples because the analysis was conducted using a small sample mass (1.5 mg) to ensure thin film conditions and comparable exposure levels across the sample. The efficiency of photoinitiators depends on the monomer's reactivity towards the produced radical species [73,74]. Different polymerizable functional groups show discernible changes in initiation rates, but these differences have been reported to be rather minor in the case of methacrylate-based monomers.

The lumped kinetic constant was plotted as a function of C=C conversion, as presented in **Figure 57 (b)**. It can be seen that auto deacceleration behavior occurs at higher C=C conversion for high MPTMS compositions, shifting from 0.2 to 0.3 C=C conversion at 0% and 70% MPTMS concentration, respectively. These results suggest a shift in the gel point toward higher C=C-conversion, delaying the onset in which the propagation reaction becomes diffusion limited as the MPTMS concentration increases. Ultimate conversion values shown in **Figure 57 (c)** exhibit the same trend, which agrees with the increase in the polymerization rate. The dependence of ultimate conversion with polymerization rate is related to the higher heating rate in the polymerization spot, promoting the mobility of propagating species and shifting the materials vitrification towards higher ultimate conversion [46,52]. The phenomenon is related to the gel effect since both are diffusion-dependent. The same conclusions can be extracted from measurements performed at 2.5 and 0.5 mW.cm^{-2} presented in **Figure S1** available in the Supporting Information in Annex D.

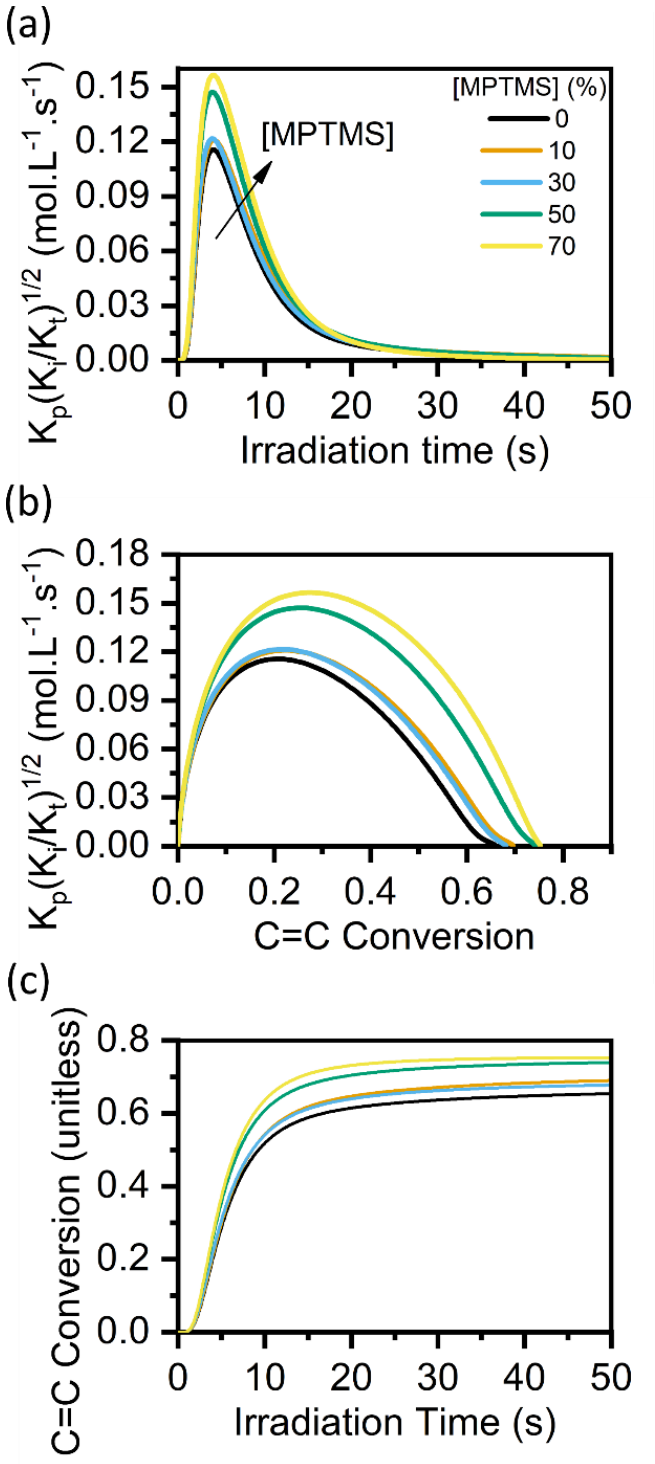

Figure 57. Lumped kinetic constant vs irradiation time (a), and vs C=C conversion (b) for resins with 0% (black), 10% (orange), 30% (blue), 50% (green) and 70% (yellow) [MPTMS] concentration at light intensity of 25 mW.cm-2. In (c), C=C conversion vs irradiation time for the same compositions.

To further comprehend the photo-curing of these materials, 70% and 0% MPTMS were studied using unsteady-state photo-DSC experiments. These experiments were conducted by shutting off the irradiation at different stages of polymerization and following the dark cure reaction. The measurements were performed under irradiation of 0.1 $mW.cm^{-2}$ for 70% and 0% MPTMS resins, and the results for the 70% MPTMS samples are presented in **Figure 58 (a)**. The heat flow curves were analyzed using **Equation (5)** over a short dark cure period (less than 2% of C=C conversion), yielding average K_t/K_p ratios at different C=C-conversion degrees for 70% and 0% MPTMS resins, as presented in **Figure 58 (b)**. The steady state photo-DSC curves for the same light intensity for 70% and 0% MPTMS resins are presented in **Figure 58 (c)**.

$$\frac{k_t}{k_p} = \frac{1}{2(t - t_0)}\left[\frac{[M](t)}{R_p(t)} - \frac{[M](t_0)}{R_p(t_0)}\right] \quad (5)$$

As can be seen in **Figure 58 (b)**, the K_t/K_p ratio evolution with C=C conversion follows the same behavior for 70% and 0% MPTMS compositions. The rapid decrease of K_t/K_p at low conversions is coherent with the polymerization of highly cross-linked systems, because the bimolecular termination mechanism is diffusion-controlled [75], and the gel effect occurs at very low C=C conversions. It can be seen that K_t/K_p reaches its minimum at C=C conversion of 6%, indicating that the propagation reaction becomes diffusion controlled at a low conversion. These observations agree with the onset of auto-deacceleration observed in steady-state measurements presented in **Figure 58 (c)**. Then K_t/K_p ratio reaches a plateau because molecular mobility occurs in the space between gel particles, meaning that micro-viscosity becomes more important than macroviscosity [25]. While K_t/K_p are constant for both MPTMS concentration samples according to unsteady state experiments, the $K_t/K_p^{0.5}$ ratio is higher in 70% MPTMS sample. These results indicate that both propagation and bimolecular termination constants are higher for 70% MPTMS compositions in comparison to 0% MPTMS, although the bimolecular termination constant does not increase in the same proportion as the propagation one.

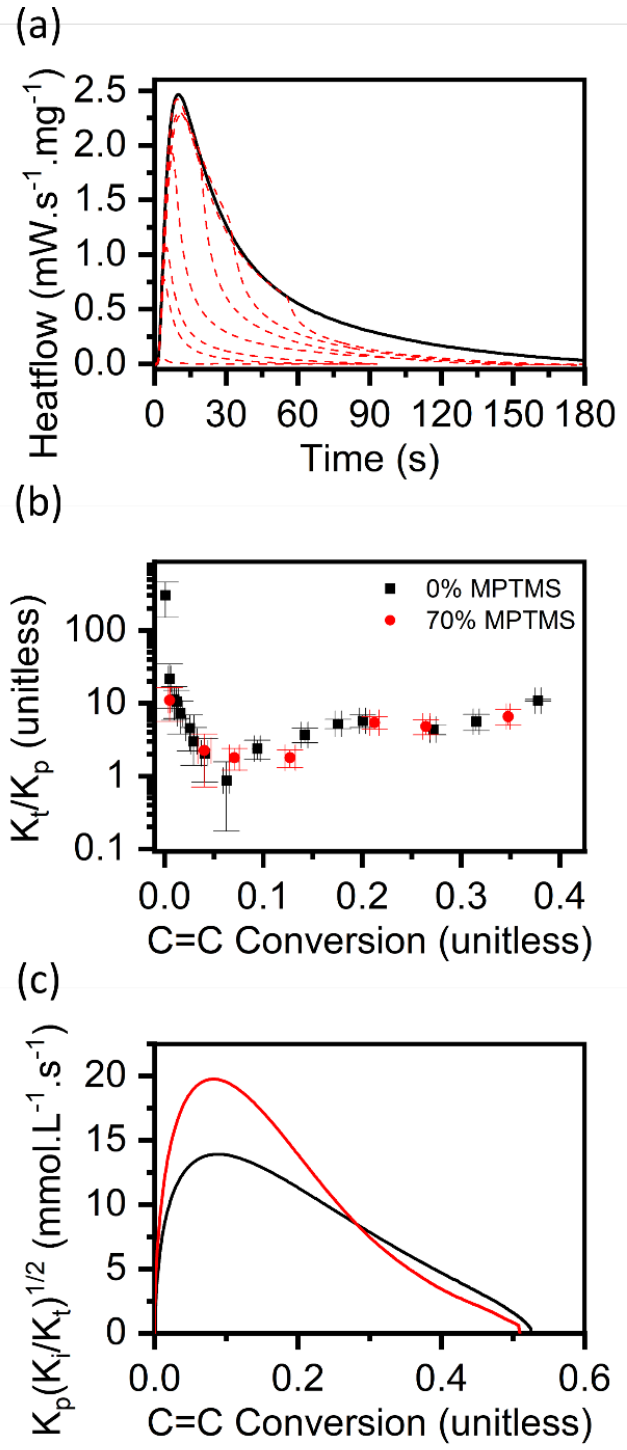

Figure 58. Heat flow from a 70% MPTMS resin as a function of exposure time (a) and C=C conversion with light intensity of 0.1 mW.cm-2 collected under steady state (solid line) and unsteady state (dotted grey line) conditions. (b) Kt/Kp as a function of C=C conversion for 0% and 70% MPTMS resins.

Photopolymerization kinetics evolution with light intensity

The dependence of the peak lumped kinect constant, and ultimate conversion, and C=C conversion at the maximum polymerization rate as a function of light intensity for samples with different MPTMS concentrations are presented in **Figure 59 (a), (b)** and **(c),** respectively. The curves were fitted using a power law, and the fitting parameters are presented in **Table S2** available in the Supporting Information in Annex D. The power law fitting of the peak lumped kinetic constant versus light intensity presented in **Figure 59 (a)** shows a constant exponential factor of 0.37 for all MPTMS concentrations. The exponential factor below 0.5 suggests that the primary radical termination has an important contribution to the photopolymerization process. The primary termination is an alternative reaction pathway where the reactive centers of growing polymeric chains react with free-radical species, interrupting the polymeric chain growth [76]. Primary termination introduces deviations from pseudo-steady state assumption, and the polymerization rate scales to the light intensity by an exponential factor inferior to half [46,76,77]. In opposition, an exponential factor close to unit suggests important contribution of oxygen inhibition towards the polymerization, which is not supported by the short inhibition periods measured in steady state photo-DSC measurements [68]. The similar values of exponential factor between all compositions reveal that the propagation, primary termination, oxygen inhibition and bimolecular termination reactions have similar dependence on the light intensity in all MPTMS concentration samples. Furthermore, it indicates that the MPTMS concentration has little influence on the contribution of primary termination, which is especially important for VPP since primary termination does not contribute toward network percolation, ultimately affecting the critical energy values of a given resins. Unfortunately, there are few investigations concerning such process, especially in the case of highly crosslinked systems such as resins for VPP-UV; however, these findings suggest that primary termination is not responsible for the variation of critical energy (E_c) with light intensity and MPTMS concentration in these materials.

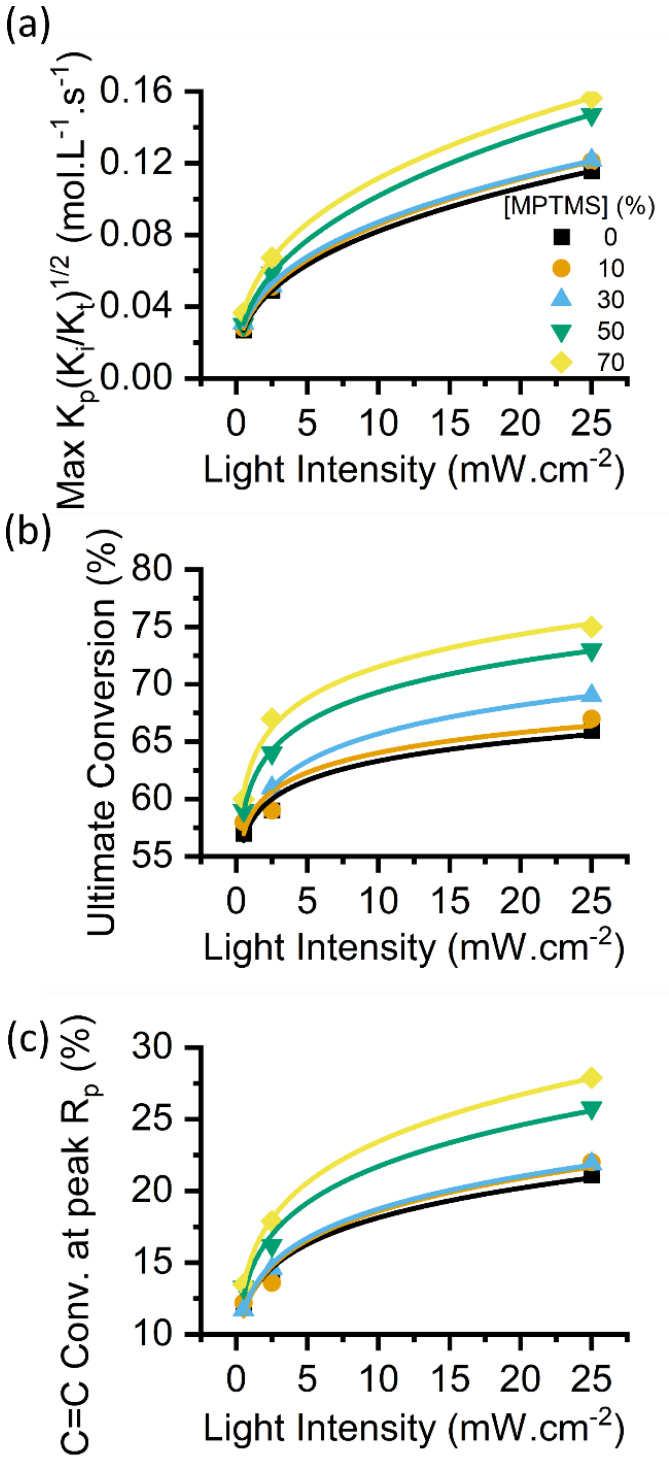

Figure 59. Peak lumped kinetic constant (a), ultimate conversion (b) and C=C conversion at peak polymerization rate (c) for 0% (diamond), 10% (inverted triangle), 30% (triangle), 50% (circle) and 70% (square) MPTMS concentrations as functions of light intensity.

The power law fitting of the ultimate conversion versus light intensity in **Figure 59 (b))** showed an increase in the exponential factor value from 0.039 to 0.056 from 0 to 70% MPTMS samples. Thus, the molecular mobility during the polymerization process has a higher dependency with light intensity as the MPTMS concentration increases. As prior discussed, the polymerization rate is one of the main factors determining the molecular mobility due to the localized heating within the polymerization spot. Based on this, it would be expected that a similar dependence of the peak lumped kinetic constant with light intensity between all compositions, as shown in **Figure 59 (a)**, should be followed by similar dependence of ultimate conversion with light intensity between all compositions. These observations indicate the presence of other factors that must increase the molecular mobility during the polymerization, besides the heating due to the polymerization reaction. Further support is found by inspecting the C=C conversion at the maximum polymerization rate with higher MPTMS concentration, as presented in **Figure 59 (c)**. Similar to ultimate conversion data, the exponential factor values increase from 0.15 to 0.19 from 0 to 70% MPTMS samples, indicating that the gel point shift toward higher C=C conversion with light intensity is more intense in high MPTMS concentration samples compared to low MPTMS concentration. These results may indicate the increase of cyclization during the polymerization of high MPTMS concentration samples.

Contribution of cyclization

Cyclization refers to a special type of propagation reaction where the reactive center in a growing polymeric chain reacts with a pendant group present in the same chain, forming a loop [39,78]. These loops do not contribute toward network percolation and the restriction of molecular mobility, delaying the gel point toward higher C=C conversions [25]. The participation of the cyclization reaction in the polymerization of such systems is often neglected but has an important effect on the dynamics of network connectivity. Studying cyclization is still a challenge, with most research on literature relying on models and comparison with experimental data on the overall polymerization process, since cyclization itself cannot be directly measured or evaluated [78,79]. Cyclization is more prone to occur under low conversion, with long polymeric chains [39] and under high initiation rates [80]. The molecular structure also plays an important role, since polymeric backbones with high rotational freedom are more prone towards cyclization, as shown by Elliot et al.[40], where the authors modeled the polymerization of two different monomers (TEGDMA and bis-GMA), and they have found that the molecular stiffness caused by the aromatic ring between the two polymerizable groups hinders the primary cyclization reaction.

In a previous work, the structure of these resins was studied by solid-state NMR technique [10,11]. The results showed that these materials are composed of fundamental building blocks of dimeric aluminum-phosphate chains and linear alkoxysilane chains. Both chains show little interaction with each other, although both react through the polymerization of methacrylate groups. The dimeric nature of the aluminum-phosphate chains results in a stiff linear structure, while the alkoxysilane chains are free to rotate around the Si-O-Si bound. To better understand these alkoxysilane chain's structure, ^{29}Si MAS experiments were conducted and are presented in **Figure 60 (a)**. The spectra are composed of three main signals, with maxima centered at -50, -58, and -67 ppm, comprehending T^n units (where n represents the number of other silicate tetrahedrons bonded to the T^n unit) [81,82]. The broad line observed in 110 ppm correspond to the background probe signal, due to the low ^{29}Si concentration in the resin`s composition. According to these results, T^2 units are predominant (70%) while the terminal T^1 units acquaint for only 17%, suggesting that these alkoxysilane chains are roughly composed of 7 T^2 units, where these chains can easily bend. The presence of T^3 units (13%) suggests that some chains are branched, which should further contribute to cyclization.

Further evidence for cyclization is found in the polymerization volumetric retraction data presented in **Figure 60 (b).** Shrinkage always follows the photopolymerization process due to changes in the functional group structure. The magnitude of such shrinkage depends on the type of monomer, and for acrylates is typically in the range of 15 to 20% [1]. One-important aspect of polymerization shrinkage is that it is directly correlated to the polymerization degree [83]. It can be seen that the high MPTMS concentration samples show smaller shrinkage values, despite the higher overall conversion. Cyclization is reported in literature to not contribute appreciably to polymerization shrinkage due to pre-orientation of segmental chains leading to cyclic structures of similar-volume [41,84,85], which would explain the observed trend. Thus, the data indicate that MPTMS rich compositions are more prone to cyclization compared low MPTMS ones. These results indicate that cyclization is a plausible hypothesis to explain why the lumped kinetic constant dependence with light intensity is similar for all compositions, while the ultimate conversion and gel point dependence with light intensity increase with higher MPTMS concentration.

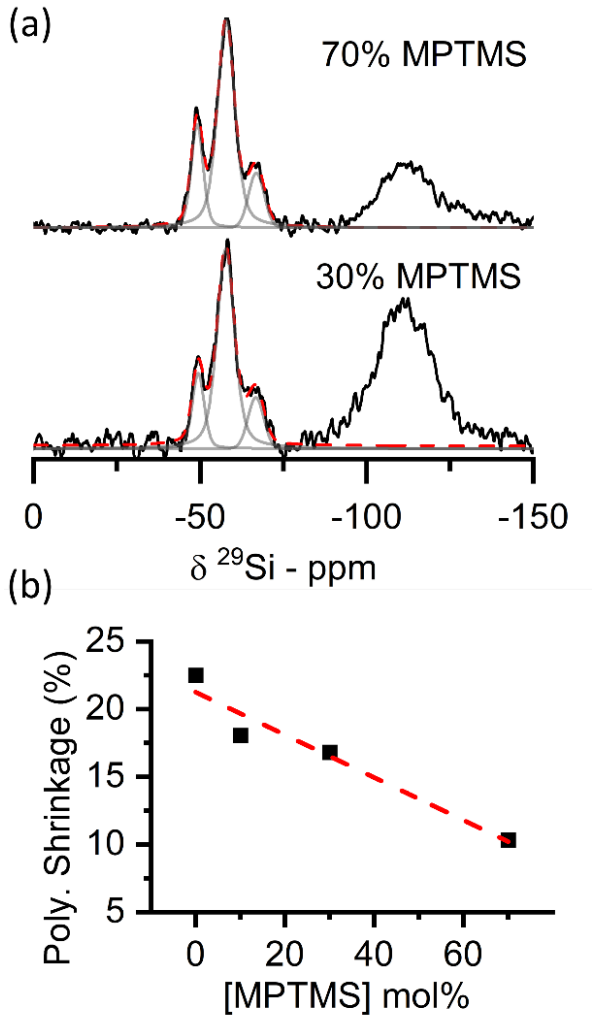

Figure 60. (a) ^{29}Si -MAS spectra of 70% and 30% MPTMS Deconvolutions are shown in the gray line and the envelope in the red line. (b) Polymerization shrinkage as a function of MPTMS concentration for photopolymerized samples.

Critical energy evolution with light intensity

Critical energy versus light intensity for resins with different MPTMS concentrations are presented in **Figure 61.** It can be seen that critical energy increases with light intensity due to the higher polymerization rates achieved, leading to higher local heating and molecular mobility, delaying the vitrification onset. Our results contradict some reports in the literature where the critical energy decreases with irradiance due to oxygen diffusion [86,87]. In these works, the polymerization proceeds slowly at low light intensity, and molecular oxygen is constantly replenished in the exposed areas, resulting in inefficient conversion and higher critical energy values. At high irradiance, the polymerization is fast enough so that dissolved oxygen cannot diffuse to the exposed area, and

saturation is observed with critical energy remaining constant [72]. Particularly, oxygen diffusion is an additional factor for long exposures (higher than 5 ms in the monomeric system studied by the Decker et al. [69]). Nonetheless, our results show an expressive increase in critical energy, indicating that oxygen inhibition has little influence on the photopolymerization of these resins in the VPP process.

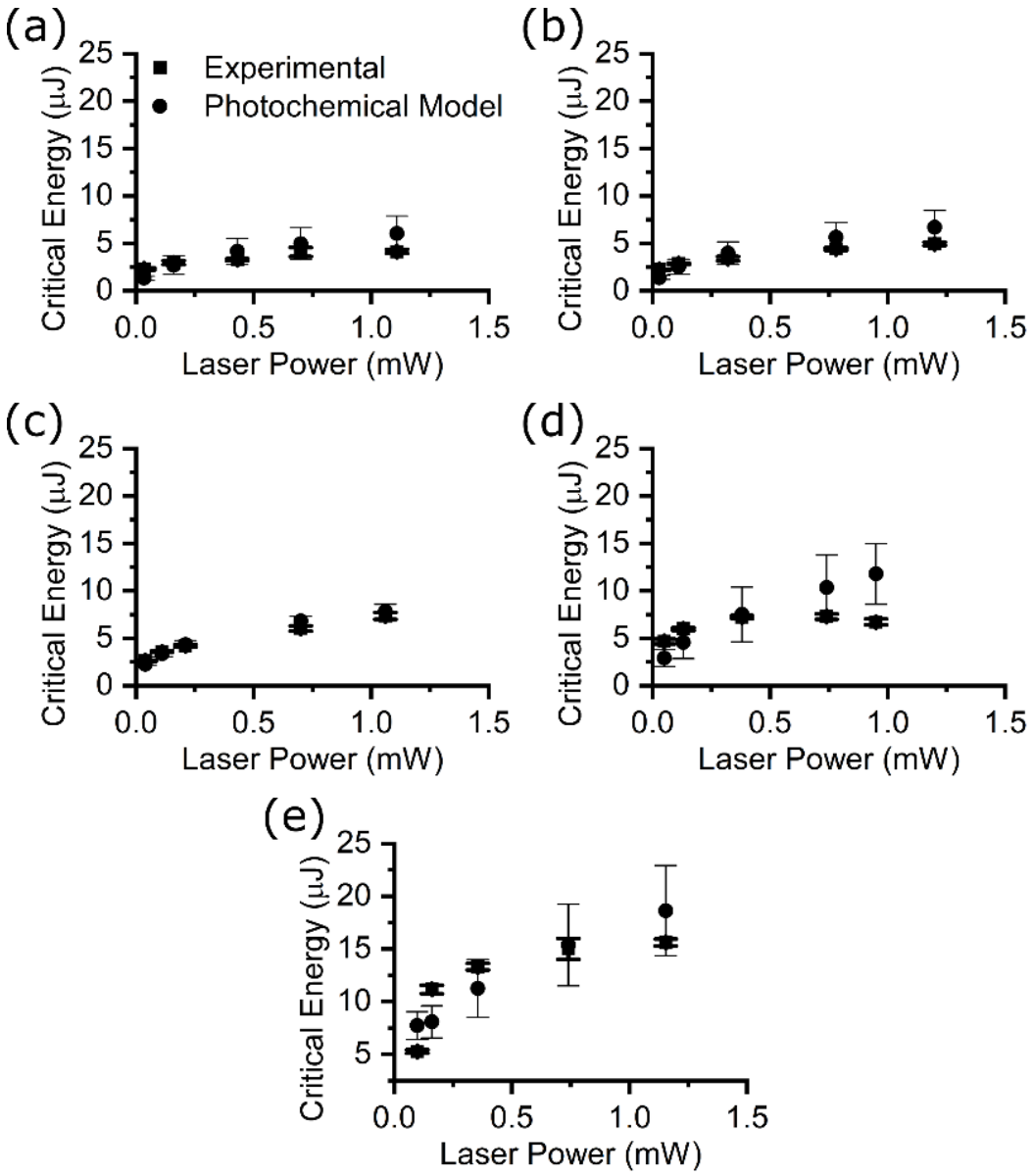

Figure 61. The evolution of critical energy values extracted from work curve data collected at different laser intensities for resins with 0% (a), 10% (b), 30% (c), 50% (d), and 70% (e) MPTMS concentration.

To test the validity of **Equation 2**, critical energy values $E_c(I_1)$ acquired at I_1 light intensity were extrapolated to other light intensity values (I_n) for the same MPTMS concentration. The extrapolation

used the direct proportionality between the lumped kinetic constant and the critical energy according to Lee`s model, as presented in **Equation 2**. By introducing the dependence of the lumped kinetic constant with light intensity approximated using the power law fitting ($k_t^{1/2}/k_p=a.I^b$) presented in **Figure 59**, **Equation 2** can be restated as **Equation 6**. Thus, the extrapolation can be done by calculating the proportional increase in the lumped kinetic constant from I_1 to I_n light intensities, resulting in **Equation 7**. The a and b fitting parameters are the same (constant MPTMS concentration), and **Equation 7** is simplified into **Equation 8**. Based on this procedure, the critical energy values for each light intensity were extrapolated to all other light intensities, as presented in **Table S3** available in the Supporting Information in Annex D. The averaged extrapolated values were compared to experimental data and are presented in **Figure 61.** These calculations assume that the critical conversion remains constant through all ranges of laser power employed for samples with the same MPTMS concentration.

$$E_c \propto \sqrt[2]{\frac{k_t}{k_p^2}} \sim aI^b \tag{6}$$

$$E_c(I_n) = E_c(I_1)\frac{a_n}{a_1}\frac{{I_n}^{b_n}}{{I_1}^{b_1}} \tag{7}$$

$$E_c(I_n) = E_c(I_1)\left(\frac{I_n}{I_1}\right)^b \tag{8}$$

It can be seen that **Equation 8** matches experimental data satisfactorily for 0%, 10%, and 30% MPTMS samples, as shown in **Figure 61 (a), (b),** and **(c),** respectively. The extrapolated values well match the experimental points acquired until 0.38 mW of laser power for the 50% MPTMS samples but does not satisfactorily fits the 70% MPTMS one. Furthermore, it can be seen that standard deviation values for 50% and 70% MPTMS samples are higher compared to the other samples, as shown in **Figure 61 (d),** and **(e)**, respectively. These samples exhibited higher dependency of ultimate conversion with the light intensity as shown in **Figure 59 (b)**, suggesting that they are more prone toward cyclization reaction, which shifts the gel point, and are more affected by light scattering as shown in **Figure 55 (d)** and **(e)**, which are factors not considered by Lee`s model. The results for the 0%, 10% and 30% MPTMS samples support the validity of **Equation 6**, however it seems that the presence of the cyclization reaction and light scattering can render **Equation 6** imprecise. These results demonstrate that pseudo-steady-state models can still be used to describe the dependency of critical

energy with kinetic constants, despite clear evidence that the high initiation conditions found in the photopolymerization of these resins result in deviations of pseudo-steady-state behavior, i.e., expressive primary termination. Recent attempts to model the critical energy evolution with light intensity have relied on the use of a power-law to describe the critical energy on the basis of reciprocity law ($E_c \propto I^n$) [27], however we highlight that Wydra et al.[46] have demonstrated that the main hypothesis supporting their modified model is not accurate because of the bimolecular termination mechanism. Nonetheless, the power law model could still fit experimental data to some success, which is reasonable given the similarity between **Equation 6** and the power law model derived in [27].

Lastly, we would like to highlight one of the comments raised by peer-reviewers regarding the correlation between the exposure conditions in the photo-DSC and 3D printing process. The photo-DSC measurements at high light intensity (25 $mW.cm^{-2}$) are comparable to 3D printing results obtained at the lowest laser power (30 µW ≈ 15 $mW.cm^{-2}$). Furthermore, we employed the full spectrum of a xenon-mercury lamp, which should induce higher initiation rates since the photoinitiator (TPO) employed in this study has a higher absorption cross-section below 365 nm (the wavelength used in the VPP setup). Thus, while the measurements using the 3D printing system employ initiation rates much higher than the photo-DSC measurements, there is still an overlap between the experimental conditions of both experiments. Nonetheless, our conclusions are not drawn based on the absolute values of initiation rate and other photopolymerization kinetic constants, but on the dependence of the k_t/k_p ratio with light intensity, which were analyzed under light intensity ranges that, although not the same, are overlapping. Furthermore, the photo-DSC experiments employed the full spectrum of the xenon-mercury lamp, which could introduce deviations in the measurements due to an inner filter effect. However, we ensured thin film conditions during the experiment, mitigating light penetration issues in the sample in order to achieve homogenous photopolymerization in the sample`s volume.

Critical energy evolution with MPTMS concentration

The validity of **Equation 2** was further assessed by extrapolating critical energy values from one MPTMS concentration to other concentrations under the same light intensity using **Equation 7**. The averaged extrapolated values were compared to experimental data and are presented in **Figure 62**. Critical energy values for each MPTMS concentration under the same light intensity are presented in **Table S4** available in the Supporting Information in Annex D. The photochemical model shows good agreement with experimental data at low MPTMS concentration but deviates for 50% and 70% MPTMS

samples. These results indicate that the light scattering and the different dependence of critical conversion with light intensity between different MPTMS concentration samples result in significant deviations from the photochemical model. We highlight that 0%, 10%, and 30% MPTMS concentration samples have similar evolution of ultimate conversion and C=C conversion at the maximum polymerization rate with the composition, as presented in **Figure 59 (b)** and **(c)**, consequently, their critical conversion values should also be similar as well. These findings further support the validity of the direct proportionality between the lumped kinetic constant and critical energy stated by **Equation 6**, as long as light scattering has little influence over the resins photopolymerization and the critical conversion between remains fairly constant. Further study must validate if $E_c \propto \ln p_c$ holds true as well.

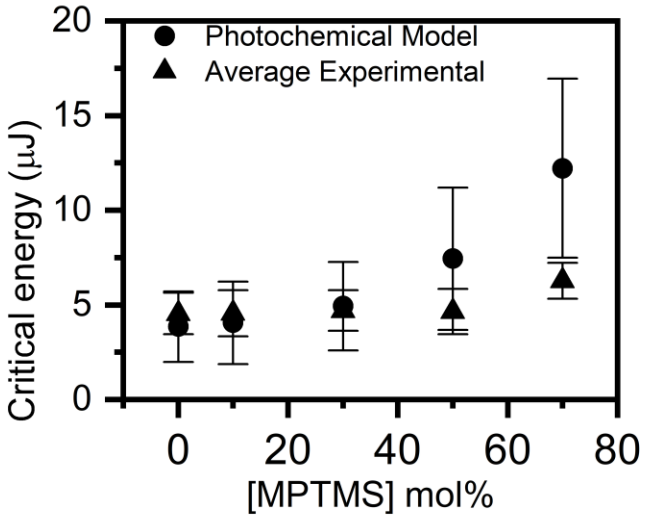

Figure 62. Average and predicted critical energy values as functions of MPTMS concentrations for 0%, 10%, 30%, 50%, and 70% MPTMS concentration.

One of the main problems with testing the dependence of the gel point and the critical energy is that there is no standard method to measure the gel point. Various techniques are reported in the literature, such as DMA [88] or DSC [43] analysis, however it is uncertain if the gel point measured by these techniques is the same as the one measured in the work curves. Furthermore, the most robust models for the study of gel formation are kinetics models based on the balance of populations [25,79,89] that are hard to implement, without a direct connection between the kinetic parameters and the critical conversion. In the last years, simulation studies have been employed to better understand the

polymerization process in such systems, however it is still difficult to stablish a correlation between the kinetic constants and the critical energy values measured in such systems.

Conclusions

The photopolymerization of aluminum-phosphate-silicate resins obtained from the hybrid sol-gel route for the VPP process with stoichiometry $Si_{(1-x)}$- $(Al+P)_{(x)}$, $0 \leq x \leq 0.7$ and 1 w.t. % of TPO as photoinitiator was studied. Critical energy and penetration depth were measured as a function of laser power in the range of 50 uW up to 1.2 mW, and of MPTMS (silicate) concentration for samples. The photopolymerization kinetics evolution with light intensity and MPTMS concentration were studied by steady- and unsteady-state photo-DSC measurements. The experimental data were used to validate a photochemical model published in the literature describing the VPP process. The model predicts that $E_c \propto ({k_t}^{1/2}/k_p) \ln p_c$ and $D_p \propto \epsilon$, where k_t k_p, p_c, and ϵ are the kinetic constant of bimolecular termination, kinetic constant of propagation, critical conversion, and absorption coefficient at the laser wavelength, respectively.

Photo-DSC measurements showed little difference in the oxygen inhibition dynamics between compositions with different MPTMS concentrations. The evolution of the lumped kinetic constants k_t/k_p and ${k_t}^{1/2}/k_p$ with composition indicated higher propagation and bimolecular termination rates as the MPTMS concentration increased. The dependence of peak ${k_t}^{1/2}/k_p$, ultimate conversion, and C=C conversion at the maximum polymerization rate with light intensity was fitted using a power law. These results showed a similar and significant contribution of primary termination for all samples, as well a shift of the gel point with MPTMS concentration. According to our hypothesis, this shift is associated with the cyclization reaction, which was supported by the polymerization shrinkage measurements, and structural data from ^{29}Si MAS-NMR coupled to a previous structural study.

The critical energy values were predicted based on the ${k_t}^{1/2}/k_p$ evolution with light intensity and MPTMS concentration. Predicted values agreed with experimental values for low MPTMS concentration samples, while a substantial deviation was found for higher MPTMS samples. These results indicated a significant difference of critical conversion between the high and low MPTMS concentration samples due to the cyclization. The $D_p \propto \epsilon$ relationship adequately described the evolution of penetration depth with MPTMS concentration, however photobleaching and light scattering can result in a substantial deviation from the model, which are more evident at high laser power. Our

study reveals that both $E_c \propto ({k_t}^{1/2}/k_p)$ and $D_p \propto \epsilon$ relationships can be used to predict critical energy and penetration depth values for an arbitrary resin without the need of constructing a work curve function, as long as critical conversion values are similar. Further study must validate the entire model, particularly to elucidate if $E_c \propto \ln p_c$ holds true as well. Nonetheless, our findings indicate a solid link between the critical energy and the kinetic constants describing the polymerization process of a given material.

Acknowledgments

The Brazilian funding agency FAPESP (SPEC process 2015/ 22828–6 and 18/24735-3) is gratefully acknowledged. GT thanks the FAPESP fellowship process numbers 2018/06426-3 and 2019/24637-7. This research was also supported by the Sentinel Nord, the Natural Sciences and Engineering Research Council of Canada (NSERC), the Fonds de Recherche Québecois sur la Nature et les Technologies (FRQNT) and the Canadian Foundation for Innovation (CFI) for the financial support.

Bibliographic References

(1) Gibson, I.; Rosen, D.; Stucker, B. *Additive Manufacturing Technologies: 3D Printing, Rapid Prototyping, and Direct Digital Manufacturing*, Second edi.; Springer US, 2015; p 510. https://doi.org/10.1520/F2792-12A.2.

(2) Gvishi, R.; Sokolov, I. 3D Sol–Gel Printing and Sol–Gel Bonding for Fabrication of Macro- and Micro/Nano-Structured Photonic Devices. *J. Sol-Gel Sci. Technol.* **2020**, *95*, 635–648. https://doi.org/10.1007/s10971-020-05270-7.

(3) Camposeo, A.; Persano, L.; Farsari, M.; Pisignano, D. Additive Manufacturing: Applications and Directions in Photonics and Optoelectronics. *Adv. Opt. Mater.* **2019**, *7* (1). https://doi.org/10.1002/adom.201800419.

(4) Ho, C. M. B.; Ng, S. H.; Li, K. H. H.; Yoon, Y.-J. 3D Printed Microfluidics for Biological Applications. *Lab. Chip* **2015**, *15* (18), 3627–3637. https://doi.org/10.1039/C5LC00685F.

(5) Waheed, S.; Cabot, J. M.; Macdonald, N. P.; Lewis, T.; Guijt, R. M.; Paull, B.; Breadmore, M. C. 3D Printed Microfluidic Devices: Enablers and Barriers. *Lab. Chip* **2016**, *16* (11), 1993–2013. https://doi.org/10.1039/c6lc00284f.

(6) Layani, M.; Wang, X.; Magdassi, S. Novel Materials for 3D Printing by Photopolymerization. *Adv. Mater.* **2018**, *30* (41), 1706344–1706344. https://doi.org/10.1002/adma.201706344.

(7) Wilts, E. M.; Pekkanen, A. M.; White, B. T.; Meenakshisundaram, V.; Aduba, D. C.; Williams, C. B.; Long, T. E. Vat Photopolymerization of Charged Monomers: 3D Printing with Supramolecular Interactions. *Polym. Chem.* **2019**, *10* (12), 1442–1451. https://doi.org/10.1039/C8PY01792A.

(8) Zhang, J.; Xiao, P. 3D Printing of Photopolymers. *Polym. Chem.* **2018**, *9* (13), 1530–1540. https://doi.org/10.1039/C8PY00157J.

(9) Crivello, J. V.; Reichmanis, E. Photopolymer Materials and Processes for Advanced Technologies. *Chem. Mater.* **2014**, *26* (1), 533–548. https://doi.org/10.1021/cm402262g.

(10) Tayama, G. T.; Santagneli, S. H.; Eckert, H.; Pawsey, S.; Messaddeq, Y. Preparation and Structural Characterization of New Photopolymerizable Transparent Aluminum-Phosphate Hybrid Materials as Resins for 3D Printing. *J. Phys. Chem. C* **2020**, *124* (46), 25621–25631. https://doi.org/10.1021/acs.jpcc.0c08289.

(11) Tayama, G. T.; Santagneli, S. H.; de Oliveira Junior, M.; Messaddeq, Y. Understanding the Microstructure Connectivity in Photopolymerizable Aluminum-Phosphate-Silicate Sol–Gel Hybrid Materials for Additive Manufacturing. *J. Phys. Chem. C* **2023**, acs.jpcc.2c08027. https://doi.org/10.1021/acs.jpcc.2c08027.

(12) Rosa, M.; Barou, C.; Esposito, V. Zirconia UV-Curable Colloids for Additive Manufacturing via Hybrid Inkjet Printing-Stereolithography. *Mater. Lett.* **2018**, *215*, 214–217. https://doi.org/10.1016/j.matlet.2017.12.096.

(13) Serbin, J.; Egbert, A.; Ostendorf, A.; Chichkov, B. N.; Houbertz, R.; Domann, G.; Schulz, J.; Cronauer, C.; Fröhlich, L.; Popall, M. Femtosecond Laser-Induced Two-Photon Polymerization of Inorganic–Organic Hybrid Materials for Applications in Photonics. *Opt. Lett.* **2003**, *28* (5), 301. https://doi.org/10.1364/OL.28.000301.

(14) Chiappone, A.; Fantino, E.; Roppolo, I.; Lorusso, M.; Manfredi, D.; Fino, P.; Pirri, C. F.; Calignano, F. 3D Printed PEG-Based Hybrid Nanocomposites Obtained by Sol–Gel Technique. *ACS Appl. Mater. Interfaces* **2016**, *8* (8), 5627–5633. https://doi.org/10.1021/acsami.5b12578.

(15) Shlomo, M.; Cooperstein, I.; Shukrun, E. 3D Polymerizable Ceramic Inks. WO2017029673A1, 2017.

(16) Zanchetta, E.; Cattaldo, M.; Franchin, G.; Schwentenwein, M.; Homa, J.; Brusatin, G.; Colombo, P. Stereolithography of SiOC Ceramic Microcomponents. *Adv. Mater.* **2016**, *28* (2), 370–376. https://doi.org/10.1002/adma.201503470.

(17) Goodman, W. A. A Review on the Advances in 3D Printing and Additive Manufacturing of Ceramics and Ceramic Matrix Composites for Optical Applications. In *SPIE 10372, Material Technologies and Applications to Optics, Structures, Components, and Sub-Systems III*; 2017; pp 10–10. https://doi.org/10.1117/12.2269394.

(18) Cooperstein, I.; Shukrun, E.; Press, O.; Kamyshny, A.; Magdassi, S. Additive Manufacturing of Transparent Silica Glass from Solutions. *ACS Appl. Mater. Interfaces* **2018**, *10* (22), 18879–18885. https://doi.org/10.1021/acsami.8b03766.

(19) Shukrun, E.; Cooperstein, I.; Magdassi, S. 3D-Printed Organic–Ceramic Complex Hybrid Structures with High Silica Content. *Adv. Sci.* **2018**, *5* (8), 1–7. https://doi.org/10.1002/advs.201800061.

(20) Wang, J.; Zheng, B.; Wang, P. 3D Printed Er3+/Yb3+ Co-Doped Phosphosilicate Glass Based on Sol-Gel Technology. *J. Non-Cryst. Solids* **2020**, *550*, 120362. https://doi.org/10.1016/j.jnoncrysol.2020.120362.

(21) Sasan, K.; Lange, A.; Yee, T. D.; Dudukovic, N.; Nguyen, D. T.; Johnson, M. A.; Herrera, O. D.; Yoo, J. H.; Sawvel, A. M.; Ellis, M. E.; Mah, C. M.; Ryerson, R.; Wong, L. L.; Suratwala, T.; Destino, J. F.; Dylla-Spears, R. Additive Manufacturing of Optical Quality Germania–Silica Glasses. *ACS Appl. Mater. Interfaces* **2020**, *12* (5), 6736–6741. https://doi.org/10.1021/acsami.9b21136.

(22) Arita, R.; Iijima, M.; Fujishiro, Y.; Morita, S.; Furukawa, T.; Tatami, J.; Maruo, S. Rapid Three-Dimensional Structuring of Transparent SiO2 Glass Using Interparticle Photo-Cross-Linkable Suspensions. *Commun. Mater.* **2020**, *1* (1), 30. https://doi.org/10.1038/s43246-020-0029-y.

(23) Destino, J. F.; Dudukovic, N. A.; Johnson, M. A.; Nguyen, D. T.; Yee, T. D.; Egan, G. C.; Sawvel, A. M.; Steele, W. A.; Baumann, T. F.; Duoss, E. B.; Suratwala, T.; Dylla-Spears, R. 3D Printed Optical Quality Silica and Silica-Titania Glasses from Sol-Gel Feedstocks. *Adv. Mater. Technol.* **2018**, *1700323*, 1–10. https://doi.org/10.1002/admt.201700323.

(24) Bennett, J. Measuring UV Curing Parameters of Commercial Photopolymers Used in Additive Manufacturing. *Addit. Manuf.* **2017**, *18*, 203–212. https://doi.org/10.1016/j.addma.2017.10.009.

(25) Irzhak, T. F.; Irzhak, V. I. Critical Conversion in Polymerization Processes. *Russ. Chem. Rev.* **2010**, *79* (10), 921–944. https://doi.org/10.1070/RC2010v079n10ABEH004155.

(26) Irzhak, V. Methods of Description of the Polycondensation Kinetics and the Structures of the Polymers Formed. *Russ. Chem. Rev.* **2007**, *66*, 541. https://doi.org/10.1070/RC1997v066n06ABEH000346.

(27) Uzcategui, A. C.; Muralidharan, A.; Ferguson, V. L.; Bryant, S. J.; McLeod, R. R. Understanding and Improving Mechanical Properties in 3D Printed Parts Using a Dual-Cure Acrylate-Based Resin for Stereolithography. *Adv. Eng. Mater.* **2018**, *20* (12), 1800876. https://doi.org/10.1002/adem.201800876.

(28) Abouliatim, Y.; Chartier, T.; Abelard, P.; Chaput, C.; Delage, C. Optical Characterization of Stereolithography Alumina Suspensions Using the Kubelka–Munk Model. *J. Eur. Ceram. Soc.* **2009**, *29* (5), 919–924. https://doi.org/10.1016/j.jeurceramsoc.2008.07.008.

(29) Tomeckova, V.; Halloran, J. W. Cure Depth for Photopolymerization of Ceramic Suspensions. *J. Eur. Ceram. Soc.* **2010**, *30* (15), 3023–3033. https://doi.org/10.1016/j.jeurceramsoc.2010.06.004.

(30) Tomeckova, V.; Halloran, J. W. Predictive Models for the Photopolymerization of Ceramic Suspensions. *J. Eur. Ceram. Soc.* **2010**, *30* (14), 2833–2840. https://doi.org/10.1016/j.jeurceramsoc.2010.01.027.

(31) Tarabeux, J.; Pateloup, V.; Michaud, P.; Chartier, T. Development of a Numerical Simulation Model for Predicting the Curing of Ceramic Systems in the Stereolithography Process. *J. Eur. Ceram. Soc.* **2018**, *38* (11), 4089–4098. https://doi.org/10.1016/j.jeurceramsoc.2018.03.052.

(32) Tomeckova, V.; Halloran, J. W. Critical Energy for Photopolymerization of Ceramic Suspensions in Acrylate Monomers. *J. Eur. Ceram. Soc.* **2010**, *30* (16), 3273–3282. https://doi.org/10.1016/j.jeurceramsoc.2010.08.003.

(33) Li, H.; Qi, Y.; Sheridan, J. T. Three-Dimensional Extended Nonlocal Photopolymerization Driven Diffusion Model Part II Photopolymerization and Model Development. *J. Opt. Soc. Am. B* **2014**, *31* (11), 2648. https://doi.org/10.1364/JOSAB.31.002648.

(34) Jariwala, A. S.; Ding, F.; Boddapati, A.; Breedveld, V.; Grover, M. A.; Henderson, C. L.; Rosen, D. W. Modeling Effects of Oxygen Inhibition in Mask-based Stereolithography. *Rapid Prototyp. J.* **2011**, *17* (3), 168–175. https://doi.org/10.1108/13552541111124734.

(35) Emami, M. M.; Rosen, D. W. An Improved Vat Photopolymerization Cure Model Demonstrates Photobleaching Effects. In *Solid Freeform Fabrication 2018: Proceedings of the 29th Annual International*; pp 1940–1952. http://dx.doi.org/10.26153/tsw/17195.

(36) Cramer, N. B.; O'Brien, C. P.; Bowman, C. N. Mechanisms, Polymerization Rate Scaling, and Oxygen Inhibition with an Ultra-Rapid Monovinyl Urethane Acrylate. *Polymer* **2008**, *49* (22), 4756–4761. https://doi.org/10.1016/j.polymer.2008.08.051.

(37) Tang, Y.; Henderson, C.; Muzzy, J.; Rosen, D. W. Stereolithography Cure Modelling and Simulation. *Int. J. Mater. Prod. Technol.* **2004**, *21* (4), 255. https://doi.org/10.1504/IJMPT.2004.004941.

(38) Belgacem, M. B.; Kamoun, S.; Gargouri, M.; Dorkenoo, K. D. H.; Barsella, A.; Mager, L. Light Induced Self-Written Waveguides Interactions in Photopolymer Media. *Opt. Express* **2015**, *23* (16), 20841–20848. https://doi.org/10.1364/OE.23.020841.

(39) Elliott, J. E.; Bowman, C. N. Kinetics of Primary Cyclization Reactions in Cross-Linked Polymers: An Analytical and Numerical Approach to Heterogeneity in Network Formation. *Macromolecules* **1999**, *32* (25), 8621–8628. https://doi.org/10.1021/ma990797i.

(40) Elliott, J. E.; Lovell, L. G.; Bowman, C. N. Primary Cyclization in the Polymerization of Bis-GMA and TEGDMA: A Modeling Approach to Understanding the Cure of Dental Resins. *Dent. Mater.* **2001**, *17* (3), 221–229. https://doi.org/10.1016/S0109-5641(00)00075-0.

(41) Stansbury, J. W. Cyclopolymerizable Monomers for Use in Dental Resin Composites. *J. Dent. Res.* **1990**, *69* (3), 844–848. https://doi.org/10.1177/00220345900690030201.

(42) Camp, W. V.; Gao, H.; Prez, F. E. D.; Matyjaszewski, K. Effect of Crosslinker Multiplicity on the Gel Point in ATRP. *J. Polym. Sci. Part Polym. Chem.* **2010**, *48* (9), 2016–2023. https://doi.org/10.1002/pola.23970.

(43) O'Neil, G. A.; Wisnudel, M. B.; Torkelson, J. M. A Critical Experimental Examination of the Gel Effect in Free Radical Polymerization: Do Entanglements Cause Autoacceleration? *Macromolecules* **1996**, *29* (23), 7477–7490. https://doi.org/10.1021/ma9606263.

(44) Jacobs, P. F. *Stereolithography and Other RP&M Technologies from Rapid Prototyping to Rapid Tooling*; American Society of Mechanical Engineers, 1996; p 450.

(45) Jacobs, P. F. *Rapid Prototyping & Manufacturing: Fundamentals of StereoLithography*; American Society of Mechanical Engineers, 1992; p 369.

(46) Wydra, J. W.; Cramer, N. B.; Stansbury, J. W.; Bowman, C. N. The Reciprocity Law Concerning Light Dose Relationships Applied to BisGMA/TEGDMA Photopolymers: Theoretical Analysis and Experimental Characterization. *Dent. Mater.* **2014**, *30* (6), 605–612. https://doi.org/10.1016/j.dental.2014.02.021.

(47) Posternak, M.; Tayama, G. T.; Messaddeq, S. H.; Messaddeq, Y. Process Modeling of Laser Scanning Vat-Photopolymerization Operating under Intermittent Exposure Conditions. *Addit. Manuf.* **2022**, *60*, 103234. https://doi.org/10.1016/j.addma.2022.103234.

(48) Khudyakov, I. V.; Legg, J. C.; Purvis, M. B.; Overton, B. J. Kinetics of Photopolymerization of Acrylates with Functionality of 1−6. *Ind. Eng. Chem. Res.* **1999**, *38* (9), 3353–3359. https://doi.org/10.1021/ie990306i.

(49) Decker, C.; Elzaouk, B.; Decker, D. Kinetic Study of Ultrafast Photopolymerization Reactions. *J. Macromol. Sci. Part A* **1996**, *33* (2), 173–190. https://doi.org/10.1080/10601329608010861.

(50) Matias, J. M.; Bartolo, P. J.; Pontes, A. V. Modeling and Simulation of Photofabrication Processes Using Unsaturated Polyester Resins. *J. Appl. Polym. Sci.* **2009**, *114* (6), 3673–3685. https://doi.org/10.1002/app.30405.

(51) Lang, M.; Hirner, S.; Wiesbrock, F.; Fuchs, P. A Review on Modeling Cure Kinetics and Mechanisms of Photopolymerization. *Polymers* **2022**, *14* (10), 2074. https://doi.org/10.3390/polym14102074.

(52) Goodner, M. D.; Bowman, C. N. Development of a Comprehensive Free Radical Photopolymerization Model Incorporating Heat and Mass Transfer e Ects in Thick Ÿlms. *Chem. Eng. Sci.* **2002**, 14.

(53) Decker, C. Laser-Induced Curing of Functional Polymers. *Des. Monomers Polym.* **1998**, *1* (1), 47–64. https://doi.org/10.1163/156855598X00107.

(54) Decker, C.; Moussa, K. A New Method for Monitoring Ultra-Fast Photopolymerizations by Real-Time Infra-Red (RTIR) Spectroscopy. *Makromol. Chem.* **1988**, *189* (10), 2381–2394. https://doi.org/10.1002/macp.1988.021891016.

(55) Dickey, M. D.; Willson, C. G. Kinetic Parameters for Step and Flash Imprint Lithography Photopolymerization. *AIChE J.* **2006**, *52* (2), 777–784. https://doi.org/10.1002/aic.10666.

(56) Schwartz, J. J. Additive Manufacturing: Frameworks for Chemical Understanding and Advancement in Vat Photopolymerization. *MRS Bull.* **2022**, *47* (6), 628–641. https://doi.org/10.1557/s43577-022-00343-0.

(57) Anastasio, R.; Peerbooms, W.; Cardinaels, R.; van Breemen, L. C. A. Characterization of Ultraviolet-Cured Methacrylate Networks: From Photopolymerization to Ultimate Mechanical Properties. *Macromolecules* **2019**, *52* (23), 9220–9231. https://doi.org/10.1021/acs.macromol.9b01439.

(58) Perry, M. F.; Young, G. W. A Mathematical Model for Photopolymerization From a Stationary Laser Light Source. *Macromol. Theory Simul.* **2005**, *14* (1), 26–39. https://doi.org/10.1002/mats.200400056.

(59) Nakamura, Y.; Fushinobu, K.; Tamura, A. Numerical Analysis of Pulse Laser Assisted Curing Region of Photocurable Resins. In *ASME 2019 International Technical Conference and Exhibition on Packaging and Integration of Electronic and Photonic Microsystems*; American Society of Mechanical Engineers: Anaheim, California, USA, 2019; p V001T05A001. https://doi.org/10.1115/IPACK2019-6356.

(60) Gao, Y.; Xu, L.; Zhao, Y.; You, Z.; Guan, Q. 3D Printing Preview for Stereo-Lithography Based on Photopolymerization Kinetic Models. *Bioact. Mater.* **2020**, *5* (4), 798–807. https://doi.org/10.1016/j.bioactmat.2020.05.006.

(61) Bartolo, P. J. ; G., I. ;. Munhoz, A. L. J. ;. Filho, R. M.; Bertsch, A. ; R., P. ;. Davis, F. J. ;. Mitchell, G. R. ;. Corbel, S. ;. Dufaud, O. ;. Roques-Carmes, T. ;. Stampfl, j. ;. Liska, R. ;. Sager, B. ;. Rosen, D. W. ;. Harris, R. ;. Ovsianikov, A. ;. Farsari, M. ;. Chichkov, B. N. ;. Arcaute, K. ;. Mann, B. K. ;. Wickers, R. B. ; *Stereolitography: Materials, Processes and Applications*; Bártolo, P. J., Ed.; Springer, 2011; p 353.

(62) da Silva Bartolo, P. J. Photo-Curing Modelling: Direct Irradiation. *Int. J. Adv. Manuf. Technol.* **2007**, *32* (5–6), 480–491. https://doi.org/10.1007/s00170-005-0374-5.

(63) Yang, Y.; Li, L.; Zhao, J. Mechanical Property Modeling of Photosensitive Liquid Resin in Stereolithography Additive Manufacturing: Bridging Degree of Cure with Tensile Strength and Hardness. *Mater. Des.* **2019**, *162*, 418–428. https://doi.org/10.1016/j.matdes.2018.12.009.

(64) Lee, J. H.; Prud'homme, R. K.; Aksay, I. A. Cure Depth in Photopolymerization: Experiments and Theory. *J. Mater. Res.* **2001**, *16* (12), 3536–3544. https://doi.org/10.1557/JMR.2001.0485.

(65) Roberts, D. E. Heats of Polymerization - a Summary of Published Values and Their Relation to Structure. *J. Res. Natl. Bur. Stand.* **1950**, *44* (3), 221. https://doi.org/10.6028/jres.044.021.

(66) Désilles, N.; Gautrelet, C.; Lecamp, L.; Lebaudy, P.; Bunel, C. Effect of UV Light Scattering during Photopolymerization on UV Spectroscopy Measurements. *Eur. Polym. J.* **2005**, *41* (6), 1296–1303. https://doi.org/10.1016/j.eurpolymj.2004.12.019.

(67) You, S.; Wang, P.; Schimelman, J.; Hwang, H. H.; Chen, S. High-Fidelity 3D Printing Using Flashing Photopolymerization. *Addit. Manuf.* **2019**, *30*, 100834. https://doi.org/10.1016/j.addma.2019.100834.

(68) Ligon, S. C.; Husár, B.; Wutzel, H.; Holman, R.; Liska, R. Strategies to Reduce Oxygen Inhibition in Photoinduced Polymerization. *Chem. Rev.* **2014**, *114* (1), 557–589. https://doi.org/10.1021/cr3005197.

(69) Decker, C.; Jenkins, A. D. Kinetic Approach of Oxygen Inhibition in Ultraviolet- and Laser-Induced Polymerizations. *Macromolecules* **1985**, *18* (6), 1241–1244. https://doi.org/10.1021/ma00148a034.

(70) Cutié, S. S.; Henton, D. E.; Powell, C.; Reim, R. E.; Smith, P. B.; Staples, T. L. The Effects of MEHQ on the Polymerization of Acrylic Acid in the Preparation of Superabsorbent Gels. *J. Appl. Polym. Sci.* **1997**, *64* (3), 577–589. https://doi.org/10.1002/(SICI)1097-4628(19970418)64:3<577::AID-APP14>3.0.CO;2-V.

(71) Becker, H.; Vogel, H. The Role of Hydroquinone Monomethyl Ether in the Stabilization of Acrylic Acid. *Chem. Eng. Technol.* **2006**, *29* (10), 1227–1231. https://doi.org/10.1002/ceat.200500401.

(72) Dendukuri, D.; Panda, P.; Haghgooie, R.; Kim, J. M.; Hatton, T. A.; Doyle, P. S. Modeling of Oxygen-Inhibited Free Radical Photopolymerization in a PDMS Microfluidic Device. *Macromolecules* **2008**, *41* (22), 8547–8556. https://doi.org/10.1021/ma801219w.

(73) Lalevée, J.; Allonas, X.; Jradi, S.; Fouassier, J.-P. Role of the Medium on the Reactivity of Cleavable Photoinitiators in Photopolymerization Reactions. *Macromolecules* **2006**, *39* (5), 1872–1879. https://doi.org/10.1021/ma052173k.

(74) Fouassier, J. P.; Allonas, X.; Laleve, J.; Dietlin, C. Photoinitiators for Free Radical Polymerization Reactions. In *Photochemistry and Photophysics of Polymer Materials*; John Wiley & Sons, Inc.: Hoboken, NJ, USA, 2010; pp 351–419. https://doi.org/10.1002/9780470594179.ch10.

(75) Buback, M.; Egorov, M.; Gilbert, R. G.; Kaminsky, V.; Olaj, O. F.; Russell, G. T.; Vana, P.; Zifferer, G. Critically Evaluated Termination Rate Coefficients for Free-Radical Polymerization, 1. The Current Situation. *Macromol. Chem. Phys.* **2002**, *203* (18), 2570–2582. https://doi.org/10.1002/macp.200290041.

(76) Goodner, M. D.; Bowman, C. N. Modeling Primary Radical Termination and Its Effects on Autoacceleration in Photopolymerization Kinetics. *Macromolecules* **1999**, *32* (20), 6552–6559. https://doi.org/10.1021/ma9901947.

(77) Schmidt, L. E.; Leterrier, Y.; Schmäh, D.; Månson, J.-A. E.; James, D.; Gustavsson, E.; Svensson, L. S. Conversion Analysis of Acrylated Hyperbranched Polymers UV-Cured below

Their Ultimate Glass Transition Temperature. *J. Appl. Polym. Sci.* **2007**, *104* (4), 2366–2376. https://doi.org/10.1002/app.25826.

(78) Polanowski, P.; Jeszka, J. K.; Krysiak, K.; Matyjaszewski, K. Influence of Intramolecular Crosslinking on Gelation in Living Copolymerization of Monomer and Divinyl Cross-Linker. Monte Carlo Simulation Studies. *Polymer* **2015**, *79*, 171–178. https://doi.org/10.1016/j.polymer.2015.10.018.

(79) Hamzehlou, S.; Reyes, Y.; Leiza, J. R. A New Insight into the Formation of Polymer Networks: A Kinetic Monte Carlo Simulation of the Cross-Linking Polymerization of S/DVB. *Macromolecules* **2013**, *46* (22), 9064–9073. https://doi.org/10.1021/ma4016054.

(80) Li, L.; Lee, L. J. Photopolymerization of HEMA/DEGDMA Hydrogels in Solution. *Polymer* **2005**, *46* (25), 11540–11547. https://doi.org/10.1016/j.polymer.2005.10.051.

(81) El hadad, A. A.; Carbonell, D.; Barranco, V.; Jiménez-Morales, A.; Casal, B.; Galván, J. C. Preparation of Sol–Gel Hybrid Materials from γ-Methacryloxypropyltrimethoxysilane and Tetramethyl Orthosilicate: Study of the Hydrolysis and Condensation Reactions. *Colloid Polym. Sci.* **2011**, *289* (17–18), 1875–1883. https://doi.org/10.1007/s00396-011-2504-y.

(82) Wei, L.; Yonggang, W.; Shukun, S.; Shaofei, S.; Daodao, H. Ultraviolet Light Catalyzed Gelation of 3-Methacryloxypropyltrimethoxysilane via Altered Silicate Spatial Structure. *J. Phys. Chem. B* **2016**, *120* (35), 9513–9522. https://doi.org/10.1021/acs.jpcb.6b05477.

(83) Sun, G.; Wu, X.; Liu, R. A Comprehensive Investigation of Acrylates Photopolymerization Shrinkage Stress from Micro and Macro Perspectives by Real Time MIR-Photo-Rheology. *Prog. Org. Coat.* **2021**, *155*, 106229. https://doi.org/10.1016/j.porgcoat.2021.106229.

(84) Spinell, T.; Schedle, A.; Watts, D. C. Polymerization Shrinkage Kinetics of Dimethacrylate Resin-Cements. *Dent. Mater.* **2009**, *25* (8), 1058–1066. https://doi.org/10.1016/j.dental.2009.04.008.

(85) Stansbury, J. W. Dimethacrylate Network Formation and Polymer Property Evolution as Determined by the Selection of Monomers and Curing Conditions. *Dent. Mater.* **2012**, *28* (1), 13–22. https://doi.org/10.1016/j.dental.2011.09.005.

(86) Soppera, O.; Jradi, S.; Lougnot, D. J. Photopolymerization with Microscale Resolution: Influence of the Physico-Chemical and Photonic Parameters. *J. Polym. Sci. Part Polym. Chem.* **2008**, *46* (11), 3783–3794. https://doi.org/10.1002/pola.22727.

(87) Deeb, C.; Ecoffet, C.; Bachelot, R.; Plain, J.; Bouhelier, A.; Soppera, O. Plasmon-Based Free-Radical Photopolymerization: Effect of Diffusion on Nanolithography Processes. *J. Am. Chem. Soc.* **2011**, *133* (27), 10535–10542. https://doi.org/10.1021/ja201636y.

(88) Korolev, G. V. Current Trends in Investigations into the Microheterogeneous Mechanism of Three-Dimensional Radical Polymerisation. *Russ. Chem. Rev.* **2003**, *72* (3), 197–216. https://doi.org/10.1070/RC2003v072n03ABEH000771.

(89) Kryven, I.; Iedema, P. D. Transition into the Gel Regime for Free Radical Crosslinking Polymerisation in a Batch Reactor. *Polymer* **2014**, *55* (16), 3475–3489. https://doi.org/10.1016/j.polymer.2014.06.013.

CHAPTER 5. REFRACTIVE INDEX DISTRIBUTION AND OPTICAL ANISOTROPIES IN ADDITIVE MANUFACTURED MATERIALS

Gabriel T. Tayama[1 2 *], Sandra H. Messaddeq[1], Tigran Galstian[1], and Younes Messaddeq[1, 2]

Center for Optics, Photonics and Lasers, Laval University, 2375 de la Terrasse, Quebec City, QC, G1V 0A6, Canada;

Chemistry Institute of Araraquara, Sao Paulo State University (UNESP), 55 Av. Prof. Francisco Degni, Araraquara, SP, 14800-900, Brazil;

KEYWORDS: Vat-Photopolymerization, Anistropy, Refractive Index, Additive Manufacturing

Abstract

The use of vat-photopolymerization (VPP) for photonic applications represents growing interest since it may solve the major disadvantages of traditional manufacturing methods for photonics, which have impeded the development of integrated optical and electro-optical devices. There are few investigations dedicated to the optical properties of 3D printed parts via VPP, such as the formation of optical anisotropy and refractive index homogeneity. In this work, we have investigated the optical properties of the fundamental structure obtained by using VPP method, i.e., a line, using an organic-inorganic hybrid material obtained by sol-gel method. The printed line was investigated using polarized and unpolarized micro-Raman spectroscopy, quantitative phase imaging, and confocal microscopy. Our results demonstrate the presence of a gradient of polymerization degree associated to the spatial distribution of light intensity. Nonetheless, the lines are optically homogeneous with no refractive index differences above 10^{-4}. However, polarimetric images have revealed optical anisotropy in these lines, and polarized micro-Raman spectroscopy indicates that they arise from the shear stress formed due to the influx of monomers to the center of the polymerization spot.

Resumo

O uso da fotopolimerização em cuba (VPP) para aplicações fotônicas tem recebido crescente interesse, pois pode contornar as principais limitações dos métodos tradicionais de fabricação fotônica, que têm impedido o desenvolvimento de dispositivos ópticos e eletro-ópticos integrados. Existem poucas investigações dedicadas às propriedades ópticas de peças impressas em 3D via VPP, como a formação de anisotropia óptica e homogeneidade do índice de refração. Neste trabalho, investigamos as propriedades ópticas da estrutura fundamental produzida pelo processo VPP, isto é, uma linha, usando um material híbrido orgânico-inorgânico obtido pelo método sol-gel. A linha impressa foi investigada usando espectroscopia micro-Raman polarizada e não polarizada, imageamento de fase quantitativo e microscopia confocal. Nossos resultados demonstraram a presença de um gradiente de grau de polimerização associado à distribuição espacial da intensidade luminosa. No entanto, as linhas são opticamente homogêneas sem diferenças de índice de refração acima de 10^{-4}. Entretanto, imagens polarimétricas revelaram anisotropia óptica nessas linhas, e os resultados da espectroscopia micro-Raman polarizada sugere que elas surgem da tensão de cisalhamento formada devido ao influxo de monômeros para o centro do ponto de polimerização.

Résumé

L'utilisation de la photopolymérisation en cuve (VPP) pour les applications photoniques représente un intérêt croissant car elle peut résoudre les principaux inconvénients des méthodes de fabrication traditionnelles pour la photonique, qui ont entravé le développement de dispositifs optiques et électro-optiques intégrés. Il existe peu d'études consacrées aux propriétés optiques des pièces imprimées en 3D via VPP, telles que la formation d'anisotropie optique et l'homogénéité de l'indice de réfraction. Dans ce travail, nous avons étudié les propriétés optiques de la structure fondamentale obtenue en utilisant la méthode VPP, c'est-à-dire une ligne, en utilisant un matériau hybride organique-inorganique obtenu par la méthode sol-gel. La ligne imprimée a été étudiée à l'aide de la spectroscopie micro-Raman polarisée et non polarisée, de l'imagerie de phase quantitative et de la microscopie confocale. Nos résultats démontrent la présence d'un gradient de degré de polymérisation associé à la distribution spatiale de l'intensité lumineuse. Néanmoins, les lignes sont optiquement homogènes sans différences d'indice de réfraction supérieures à 10^{-4}. Cependant, les images polarimétriques ont révélé une anisotropie optique dans ces lignes, et la spectroscopie micro-Raman polarisée indique

qu'elles proviennent de la contrainte de cisaillement formée en raison de l'afflux de monomères au centre de la tache de polymérisation.

Introduction

Additive manufacturing (AM) refers to a family of different manufacturing techniques sharing the same layer-by-layer approach for fabricating objects. AM technologies allow the fabrication of complex structures with reduced time and cost, with a simplified process planning, being ideal to manufacture highly customizable products on small-scale [1]. There are extensive reviews in the scientific literature about how promising AM technologies for a wide range of applications are [2–4].

Traditional manufacturing methods for photonic devices are costly, have low customizability, and are usually restricted to bidimensional construction, making difficult the integration with other optical components [5,6]. These factors are the main challenges to overcome in order to achieve a new generation of integrated photonic circuits [7,8], three-dimensional lenses and waveguides at microscale/nanoscale [9,10]. AM is considered a promising manufacturing technique for photonics [5,11] since it addresses all the above-mentioned issues. To be applied in photonics, AM must have relatively high resolution (<10 um) and high surface finishing quality [5]. These requirements are met by a few AM techniques, such as, ultraviolet laser scanning vat-photopolymerization (VPP-UV). Vat photopolymerization refers to a family of AM technologies that are based on the selective photopolymerization of a resin, such as localized UV laser exposure in the case of VPP-UV [12,13]. These techniques excel in spatial resolution, printing time, and surface finishing compared to other AM technologies, allowing the fabrication of objects with numerous fine features/structures[14,15].

Additive manufactured parts are intrinsically anisotropic due to its layer-by-layer fabrication method [16]. The vast majority of AM parts are designed for structural applications, and there is intensive research on the anisotropy of mechanical properties between the Z axis (plane adhesion direction) and the X and Y axes (plane of fabrication) [17,18]. However, studies, addressing optical anisotropies in VPP-UV-produced parts, are scarce and have been limited to evaluating the potential of VPP-UV in fabricating photoelastic models for stress analysis [19,20]. These works have identified the presence of birefringence in the core and edges of printed parts, but they have not determined its magnitude. Further post-processing with thermal treatment could remove the optical anisotropies in the core of the printed parts, but it was ineffective in eliminating them on the edges.

Additionally, the laser sources employed in VPP-UV have a characteristic irradiance profile across the beam. Thus, the photopolymerization process is initiated by different light intensity values depending on the region of the beam profile. At the same time, it is well-known that the photopolymerization kinetics is strongly dependent on the light intensity value, meaning that the polymerization rate will vary with light intensity. It is well-stablished also that the ultimate conversion (final degree of polymerization) increase with the irradiance because of higher initiation rates achieved, and therefore polymerization rates, result in higher localized heating, increasing the molecular mobility and shifting the vitrification point to higher C=C conversion values [21]. Particularly, the ultimate conversion is a major factor responsible for the material's refractive index changes from a resin to a solid, since the polymerization reaction is followed by shrinkage due to the formation of covalent bonds between monomers, resulting in smaller distance between the species, densifying and increasing the materials refractive index [22]. Thus, it is expected that the VPP-UV process should create a distribution of refractive index values within the polymerized regions. There have been some investigations in the past concerning the variation of C=C conversion during photopolymerization using diffraction mask and laser, but these works have relied on simulations using a phenomenological photopolymerization models, which fail to grasp the dependence between light intensity and ultimate polymerization [23–25]. Nonetheless, these works have estimated refractive index differences on the order of 10^{-3} to 10^{-4} between the edges and the center of irradiation[23–27].

To date, there is little investigation on the optical anisotropy and refractive index distribution of VPP-produced parts. Nonetheless, it has been reported the presence of chords in the final object, which are sometimes referred as plane fabrication or line effects [28–30], as shown in **Figure 63 (c)** and **(d)**. The lack of any systematic approach to observe, measure, and control the optical anisotropy and heterogeneities in 3D printed parts is a challenge that must be overcome to enable the use of AM technologies in photonics.

In this work, we studied the refractive index distribution and optical anisotropy in the fundamental structure, produced by VPP-UV equipment, i.e., a line, as shown in **Figure 63 (a)** and **(b)**. We employed polarimetry imaging to study the optical anisotropy in these materials. Micro-Raman was used to map the distribution of polymerization degree, and a combination of quantitative phase imaging (QPI) and confocal microscopy allowed the mapping of refractive index distribution in the fabricated line.

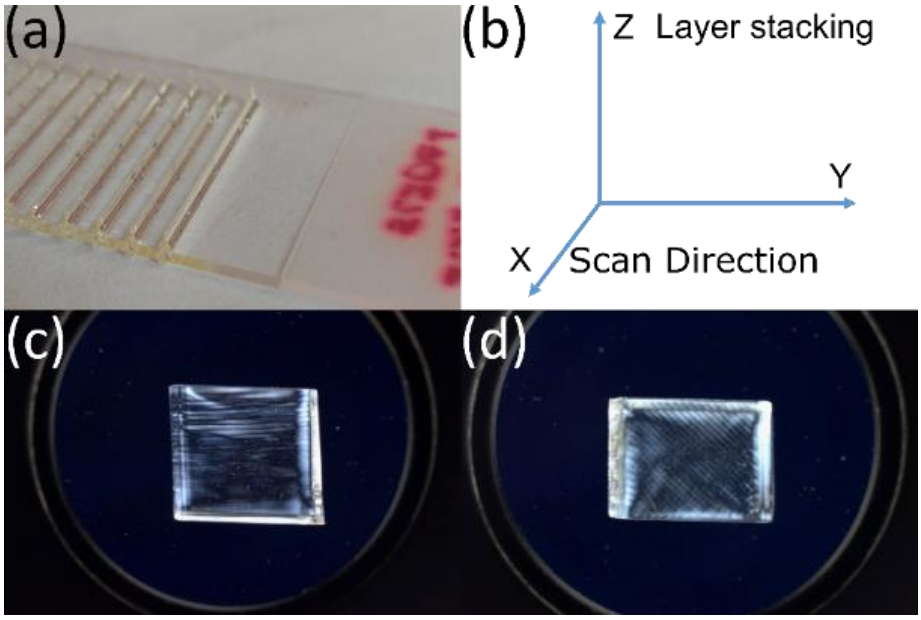

Figure 63. (a) 3D printed lines with a 50% MPTMS (1:1 Al:P) resin, and (b) the coordinates system for the line printing used in this work. (c) polarimetry image of polished 3D printed cube in the XZ plane. (d) polarimetry image of polished 3D printed cube in the XY plane.

Materials and methods

Material synthesis and sample preparation. The photopolymerizable resin was prepared by sol-gel method according to the synthesis procedure described in detail elsewhere [31,32]. Here, we synthesized the composition corresponding to the nominal formula 10% TMSPM+90% (1:1 Al:P) described in [32]. The reactants aluminum-tri-sec-butoxide 97% (Sigma-Aldrich), hydroxyethyl methacrylate phosphoric acid ester 90% (Sigma-Aldrich), 2-(Methacryloyloxy) ethyl acetoacetate 95% (Sigma-Aldrich), methanol P.A. (Synth), and trimethylsilyl propyl metachrylate 98% (Sigma-Aldrich)) were used as received. The photoinititor diphenyl (2, 4, 6- trimethyl benzoyl) phosphine oxide 97% (Sigma-Aldrich) was added to the resin in a concentration of 5% w.t.. Samples were prepared by printing line structures on top of a glass slide using a vat structure in a custom-made SLA platform equipped with a 360 nm CW-diode laser (Laserglow Technology, model LRS-0360-WFO) with a beam diameter of 500 µm. The details of this device are described elsewhere [33]. For this work, lines were printed using laser intensities of 70 µW and exposure time of 50 ms. Once printed, the glass slide was washed with anhydrous ethanol to remove the residual resin.

Optical Characterizations. QPI images were acquired using quadriwave lateral shearing interferometry (QWLSI) approach with a Phasics SID4 Bio camera, coupled to a microscope.

Polarimetry images were obtained using the microscope in transmission mode with an external crossed polarizer and analyzer setup. The sample was immersed in a refractive index matching oil (n=1.5064, Cargille Series E) using a glass-slide as a slipcover and positioned parallel to the substrate by the aid of spacers for QWLSI and polarimetry images. The use of the index matching oil serves two purposes: (1) it removes lensing effects for the polarimetry measurement and (2) it reduces optical path difference (OPD) values to allow the measurements of QWLSI technique. Photos for polarimetry were taken with the sample along the X axis (scan direction) at different angles to the polarizer and analyzer direction. The camera gain, shutter time, and white balance were manually adjusted to remain constant during the whole experiment.

Confocal images were obtained using a Leica SP8 with a 405 nm laser excitation source and by observing the fluorescence of the photoinitiator. Micro-Raman scattering spectra were collected in the backscattering geometry using a 633 nm laser excitation source in a Renishaw inVia equipment coupled to a Leica DM2700 microscope. Micro-Raman analysis was employed to analyze the line's cross-section by griding and polishing the printed line with a cylinder in order to expose the cross-section in a tilted angle so that the material can be probed at different depths, as shown in **Figure 64 (a)** and **(b)**.

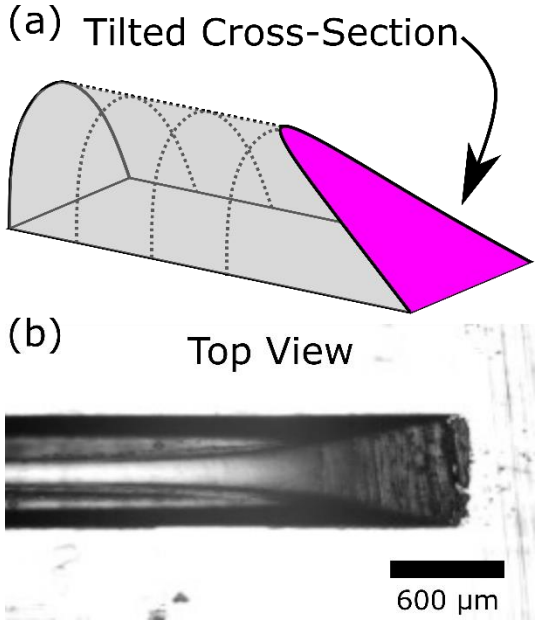

Figure 64. Schematic drawing of the 3D printed line with its tilted cross-section in (a) and the top view of a 3D printed line with an exposed tilted cross-section in (b).

Detection limits of QWLSI. QWLSI is a wavefront analyzer technique using a modified Shack-Hartmann mask. The mask introduces a destructive interference to the zeroth-order diffracted components, preserving only the first-order, resulting in an interferogram carrying information on the distortion introduced to the wavefront [34]. A robust mathematical treatment on the interferogram allows the mapping of OPD in the analyzed image, which is the difference of optical path length (OPL) between two pixels. The OPL is the product of refractive index (n) by distance (L), as shown in **Equation 1**. The OPD, measured using QWLSI is the difference between OPL from two pixels. For an irregular surface, such as the one depicted in **Figure 65**, the OPD can be deducted to yield **Equation 2**, where Δh is the materials height difference between the two pixels, Δn is material's refractive index difference between the two pixels, n is the index matching oil refractive index, and $n(x_1)$ is the material's refractive index at the x_1 pixel. As a consequence of **Equation 2**, if the refractive index is constant along the sample, the OPD and the topography profile should match perfectly. Furthermore, the refractive index information is available as long as reliable topography information is obtainable.

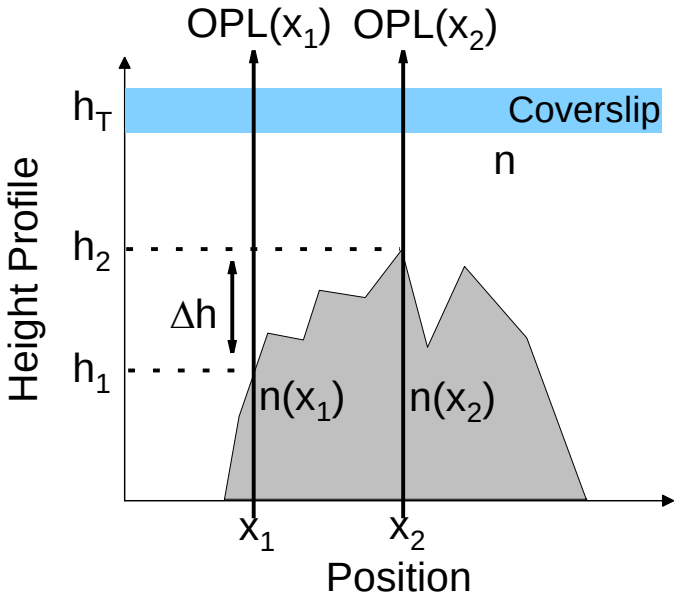

Figure 65. Schematic OPL from two different positions in a sample with arbitrary height profile and non-homogeneous refractive index.

$$OPL = \int_0^L n(z).dz \qquad \textbf{Equation 1}$$

$$OPD = OPL(x_2) - OPL(x_1) = \Delta h.n(x_1) + h_2.\Delta n - \Delta h.n \qquad \textbf{Equation 2}$$

A fundamental limitation of any QPI method is that the phase shift between two pixels must be inferior to **π**. For an irregular surface, such as the one presented in **Figure 65 (b)**, the phase shift is directly associated to the variation of the refractive index (Δn) of the material between two pixels and height from one pixel to the other (Δh), as shown in **Equation 3**. The distance between two pixels for the equipment, described in the section below (calibrated at 530 nm ~10^{-7} m), is between 2.7 μm and 0.4 μm, corresponding to a Δh of 10^{-7} m and h_2 of 10^{-4} m. The estimated ($n(x_1)$-n) difference is at the order of 10^{-3} or below, which sets a maximum detectable (by the technique) Δn between pixels of 10^{-3}. Variation of Δn between pixels higher than 10^{-3} will result in unstable measurements, which is easily observed during analysis. Furthermore, the equipment sensitivity is on the order of OPD=10 nm, meaning the technique can detect variations of refractive index down to 10^{-4}, setting the lower detection limit of the technique.

$$\pi > \frac{2\pi}{\lambda}.OPD \qquad \textbf{Equation 3}$$

$$\frac{0.532}{2}10^{-7} > \Delta h.(n(x_1) - n) + h_2.\Delta n$$

Results and Discussion

Polymerization degree mapping

Raman scattering spectroscopy is a standard technique for measuring the polymerization degree of a polymer. The Raman spectra of these materials have been previously studied, and their vibrational spectrum are similar to polymethylmethacrylate (PMMA) [31,32]. For methacrylate-based polymers, the polymerization degree can be measured by calculating the ratio between the vibrational bands assigned to the stretching of the C=C and C=O bond, with characteristic Raman shifts around 1630 and 1720 cm^{-1}, respectively. Micro-Raman scattering maps were collected on the cleaved surface, presented in **Figure 64**, and the data were deconvoluted to measure the ratio between the relative areas of the C=C and C=O bands. The map scan in **Figure 66 a** and **b** highlights the C=C conversion profile as function of the laser penetration depth. The map scan in **Figure 66 c** and **d** highlights the C=C conversion profile across the laser beam from the center to the edges of the irradiation center..

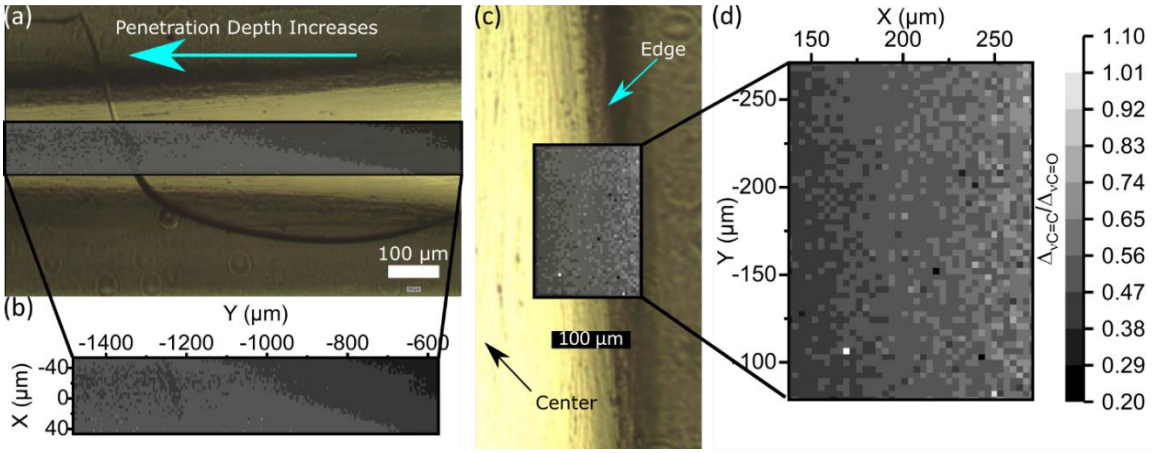

Figure 66. Micro-Raman scattering mapping of the tilted cross-section of a line. The ratio between the integrated areas of the vibrational bands at 1630 and 1720 cm^{-1} assigned to the stretching of the C=C and C=O bonds, respectively, were monitored: (a) the microscope image of the scanned area, (b) the corresponding map, (c) the microscope image of the scanned area and (d) the corresponding map with indications of the center and edges of irradiation.

It can be seen that the polymerization degree decreases with the penetration depth and with the distance from the beam center, as shown in **Figure 66 a** and **b**, and in **Figure 66 c** and **d**, respectively. These observations are coherent with the exposure profile introduced by the laser beam profile, and the exponential decrease of irradiance with the penetration depth caused by the photoinitiators absorption in the resin. When the profile of C=C conversion is plotted as a function of the Y coordinate (penetration depth) for each X coordinate in **Figure 66 b**, it can be seen that $\Delta_{C=C}/\Delta_{C=O}$ ratio starting values are 0.35 and 0.44 for the -53 and 46 µm X position, decreasing until they reach a plateau. The ratios for each plateau also increase as it gets farther away from the center of the irradiation. Similarly, the profile of C=C conversion as a function of the penetration depth for each Y coordinate in **Figure 66 b** shows a similar trend when evaluated from the center to the edge of the irradiation. These results clearly indicate the formation of a C=C conversion profile, thus it is expected that a refractive index profile should be present in the materials.

Refractive index distribution

Mapping the refractive index of curved surfaces is challenging since most refractive index measuring methods rely on coupling the surface of the sample with a reference material. This means that the sample must be prepared (cut, ground and polished) and flat in most cases, which is not convenient for these 3D printed lines. Here, we employed a combination of QWLSI and confocal microscopy to evaluate the average refractive index distribution of the 3D printed lines along the cross-

section. The OPD mapping of the 3D printed line is presented in **Figure 67 a**, and the average OPD profile of the cross-section is shown in **Figure 67 b**. The height profile image of a cross-section obtained from confocal microscopy is presented in **Figure 67 c**, and the extracted values are presented in **Figure 67 b**. It can be seen that both the OPD and the height profile of the lines cross-section are identical, indicating that the average refractive index of the material along the cross-section remains constant, despite the C=C conversion profile observed in the Raman scattering maps. According to calculations using **Equation 3**, the method should be able to detect refractive differences between 10^{-3} and 10^{-4}, indicating that the refractive index in these 3D printed lines is homogenous up to 10^{-4} despite the presence of a C=C conversion profile.

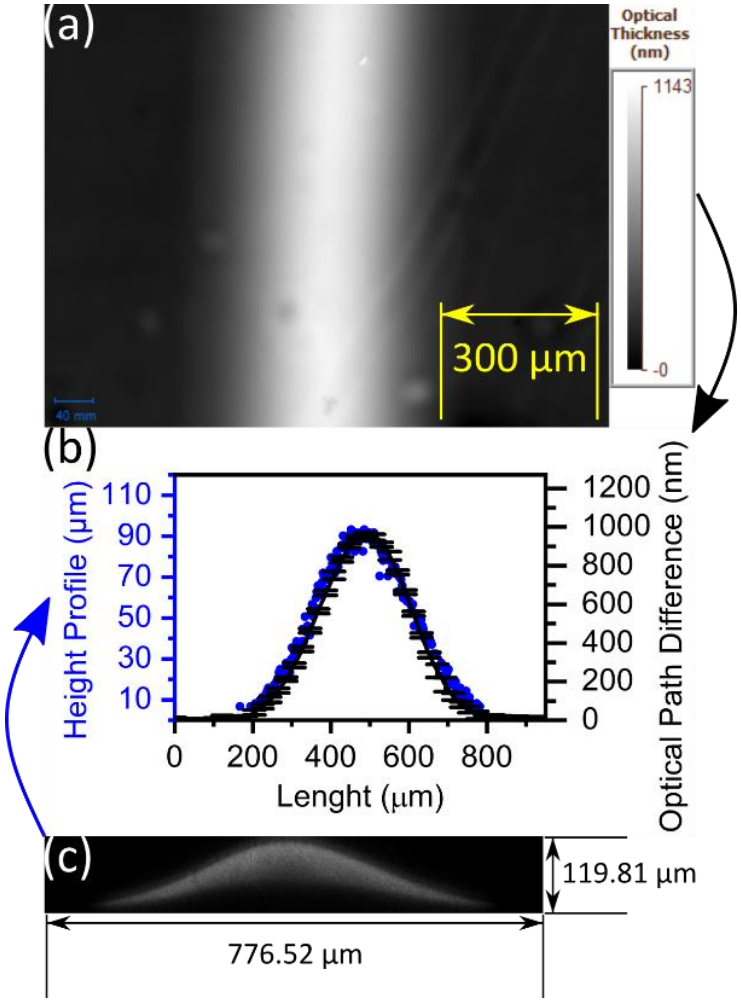

Figure 67. (a) QWLSI image of an additive manufactured line. In (b) the OPD and height profile of an additive manufactured line extracted from QWLSI and confocal microscopy images. (c) the height profile of a cross section obtained by confocal microscopy.

Optical anisotropies

Polarimetry images of the 3D printed lines are presented in **Figure *74***. No image is observed when the line is positioned parallel to either the polarizer or the analyzer in crossed configuration, however, a bright strip is observed when the line is tilted by 45 degrees to either the polarizer or analyzer. The images obtained at 45 and -45 degrees are symmetrical. These observations indicate that these lines are birefringent with their optical axis aligned or perpendicular to the laser scan direction, suggesting a biaxial refractive index distribution [35,36]. Kobayashi et al. studied the photopolymerization of oxetane-based monomers using a scanning light source [37], and the author have found a preferential alignment of the monomers with the scan direction, resulting in birefringence. In another investigation by the same group [38], the authors employed structured light instead of a scanning light source, and have identified the presence of optical anisotropies as well. The authors assigned their findings to the polymerization gradient introduced by the localized light source, inducing the diffusion of monomers to the irradiated area and creating shear stresses perpendicular to the scan direction. These stresses are then frozen by the vitrification of the polymeric network, resulting in the observed anisotropies.

In this work, we employed an intermittent exposure (IE) VPP setup under a high overlap regime. Thus, a line scan consists of multiple stationary overlapping exposures as described in [33], meaning that the printing process is a combination of both structured light and a scanning light source. Based on this, both mechanisms, that are molecular orientation and shear stress, could explain the birefringence in the 3D printed lines observed in this work. To further elucidate their origin, we employed polarized micro-Raman experiments to verify the existence of preferential molecular alignments in these lines.

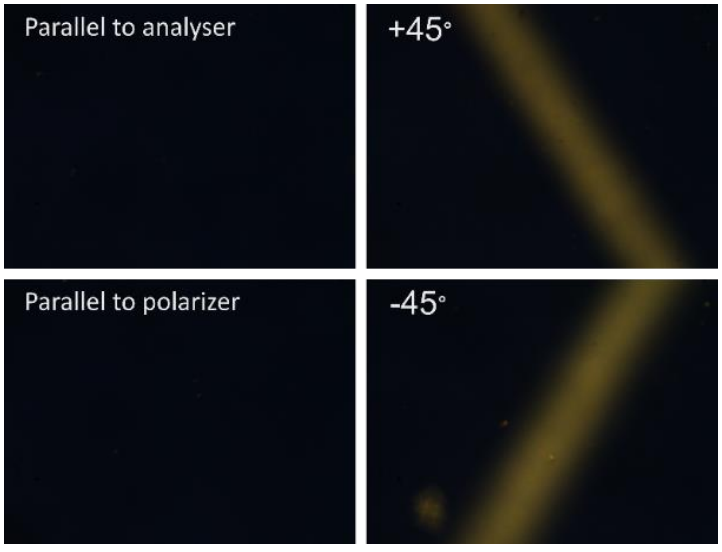

Figure 68. Polarimetry images of 3D printed line immersed in refractive index matching oil. Photos were taken with the line aligned parallel, +45, -45, and perpendicular to the polarizer.

Polarized micro-Raman mapping

Polarized Raman has been employed for evaluating the molecular orientation of PMMA [39], by analyzing the intensity of the 486, 562, 604, and 1732 cm^{-1} vibrational bands as a function of the polarizer/analyzer orientations. Detailed information on the direction and degree of molecular alignment can be acquired by comparing to tensor models describing the Raman scattering, however this approach is particularly challenging for complex systems where vibrational bands with different symmetries overlap. Here, we used a simplified analysis by comparing the polarized Raman spectra with different polarizer/analyzer orientations to identify the presence of preferential alignment of segments associated to the organic structure.

The surface shown in **Figure 64** was mapped using polarized micro-Raman acquired in the HH (horizontally aligned polarizer and analyzer)and VV (vertically aligned polarizer and analyzer) configurations, as shown in the representative spectra presented in **Figure 69.** The vibrational bands located at 1744 and 1719 cm^{-1} are assigned to the stretching of the C=O bond. The stretching of the C=C bonds from unreacted monomer is observed at 1639 $cm^{-1.}$ The stretching of the C-O and C-C bond from the chelating ring of MAEAA can be observed at 1610 and 1530 cm^{-1}. The stretching of the P=O can be seen at 1242 cm^{-1}. Lastly, the bands are 1454, 1410, 1375, and 1181 cm^{-1} are assigned to the wagging and rocking of CH_2 and CH_3 groups. It can be seen that the spectrum acquired with HH and VV polarizer/analyzer orientation match perfectly. Similar results were observed for all spectra collected in the mapping. The spectra were deconvoluted and the ratio between each vibrational band acquired in HH and VV configuration was calculated and plotted in **Figure S1** available in the supporting information in Annex E. These results indicate the absence of preferential alignment between the organic groups, suggesting that the observed optical anisotropies arise due to shear stresses created by the localized photopolymerization during the additive manufacturing process.

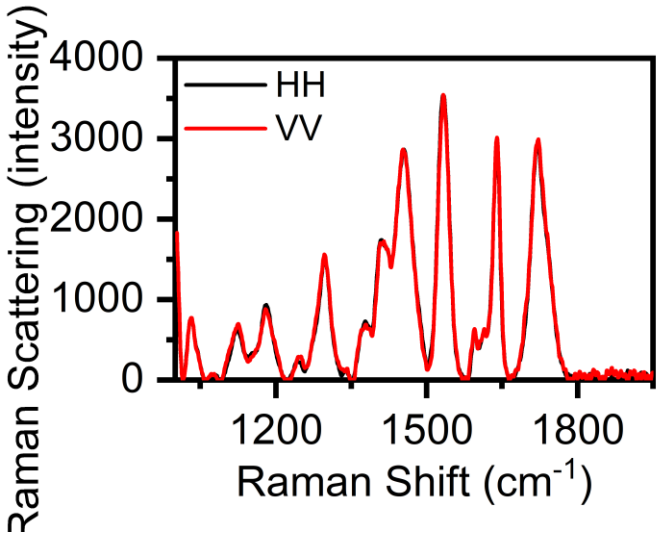

Figure 69. Raman scattering spectra acquired in HH and VV configurations.

Summary and Conclusions

A 3D printed line of an aluminum-phosphate-silicate hybrid material was fabricated using VPP-UV. This line was used to study the refractive index distribution and the presence of optical anisotropies resulting from the laser scan during the VPP-UV process, by combining micro-Raman, quantitative phase imaging, confocal microscopy and polarized micro-Raman techniques. Micro-Raman was used to map the distribution of polymerization degrees across the cross-section of the line, and a combination of quantitative phase imaging (QPI) and confocal microscopy allowed the mapping of refractive index distribution in the fabricated line. Micro-Raman revealed different degrees of polymerization in the line, where smaller C=C conversions were achieved as the light intensity decreased (deeper light penetration and farther from the beam center). Despite this distribution of C=C conversion, the combination of QPI and confocal microscopy did not reveal any refractive index heterogeneities above 10^{-4}. To the best of our knowledge, this is the first observation and mapping of conversion profiles introduced by the VPP process. Polarimetry images revealed optical anisotropies in these lines. Polarized micro-Raman showed that these anisotropies do not arise due to molecular alignment, suggesting that the mechanism responsible for the birefringence is related to the localized polymerization, which induces the diffusion of monomer to the polymerization spot, resulting in shear stress perpendicular to the scan direction. These results demonstrate that further application of VPP techniques to additive manufacturing of photonic materials is not straightforward, and must require additional effort into elucidating the optical properties at microscale in these materials.

Acknowledgments

The Brazilian funding agency FAPESP (SPEC process 2015/ 22828–6 and 18/24735-3) is gratefully acknowledged. GT thanks the FAPESP fellowship process numbers 2018/06426-3 and 2019/24637-7. This research was also supported by the Canadian Excellence Research Chair program (CERC) in Photonics Innovations. The authors are also grateful to the Natural Sciences and Engineering Research Council of Canada (NSERC), the Fonds de Recherche Québecois sur la Nature et les Technologies (FRQNT) and the Canadian Foundation for Innovation (CFI) for the financial support. The authors would like to thank Prof. Réal Vallée for the use of the Phasics microscope.

Bibliographic References

(1) Mellor, S.; Hao, L.; Zhang, D. Additive Manufacturing: A Framework for Implementation. *International Journal of Production Economics* **2014**, *149*, 194–201. https://doi.org/10.1016/j.ijpe.2013.07.008.

(2) Ngo, T. D.; Kashani, A.; Imbalzano, G.; Nguyen, K. T. Q.; Hui, D. Additive Manufacturing (3D Printing): A Review of Materials, Methods, Applications and Challenges. *Composites Part B: Engineering* **2018**, *143* (December 2017), 172–196. https://doi.org/10.1016/j.compositesb.2018.02.012.

(3) Bhushan, B.; Caspers, M. An Overview of Additive Manufacturing (3D Printing) for Microfabrication. *Microsystem Technologies* **2017**, *23* (4), 1117–1124. https://doi.org/10.1007/s00542-017-3342-8.

(4) Weber, C. L.; Pena, V.; Micali, M. K.; Yglesias, E.; Rood, S.; Scott, J. A.; Lal, B. *The Role of the National Science Foundation in the Origin and Evolution of Additive Manufacturing in the United States*; 2013; p 175 pages-175 pages. https://www.ida.org/idamedia/Corporate/Files/Publications/STPIPubs/ida-p-5091.ashx.

(5) Camposeo, A.; Persano, L.; Farsari, M.; Pisignano, D. Additive Manufacturing: Applications and Directions in Photonics and Optoelectronics. *Advanced Optical Materials* **2019**, *7* (1). https://doi.org/10.1002/adom.201800419.

(6) Zhu, Y.; Tang, T.; Zhao, S.; Joralmon, D.; Poit, Z.; Ahire, B.; Keshav, S.; Raje, A. R.; Blair, J.; Zhang, Z.; Li, X. Recent Advancements and Applications in 3D Printing of Functional Optics. *Additive Manufacturing* **2022**, *52*, 102682. https://doi.org/10.1016/j.addma.2022.102682.

(7) Cao, Y.; Yi, Y. J.; Lin, B. Z.; Sun, Y.; Che, X. C.; Zheng, J.; Wang, F.; Zhang, D. M. Polymer/Glass Hybrid DC-MZI Thermal Optical Switch for 3D-Integrated Chips. *RSC Advances* **2019**, *9* (19), 10651–10656. https://doi.org/10.1039/c9ra00037b.

(8) Gvishi, R.; Sokolov, I. 3D Sol–Gel Printing and Sol–Gel Bonding for Fabrication of Macro- and Micro/Nano-Structured Photonic Devices. *Journal of Sol-Gel Science and Technology* **2020**, *95*, 635–648. https://doi.org/10.1007/s10971-020-05270-7.

(9) Gissibl, T.; Thiele, S.; Herkommer, A.; Giessen, H. Two-Photon Direct Laser Writing of Ultracompact Multi-Lens Objectives. *Nature Photonics* **2016**, *10* (8), 554–560. https://doi.org/10.1038/nphoton.2016.121.

(10) Juodkazis, S. Manufacturing: 3D Printed Micro-Optics. *Nature Photonics* **2016**, *10* (8), 499–501. https://doi.org/10.1038/nphoton.2016.150.

(11) Vaidya, N.; Solgaard, O. 3D Printed Optics with Nanometer Scale Surface Roughness. *Microsyst Nanoeng* **2018**, *4* (1), 18. https://doi.org/10.1038/s41378-018-0015-4.

(12) Zhang, J.; Xiao, P. 3D Printing of Photopolymers. *Polymer Chemistry*. Royal Society of Chemistry 2018, pp 1530–1540. https://doi.org/10.1039/c8py00157j.

(13) Liska, R.; Schuster, M.; Inführ, R.; Turecek, C.; Fritscher, C.; Seidl, B.; Schmidt, V.; Kuna, L.; Haase, A.; Varga, F.; Lichtenegger, H.; Stampfl, J. Photopolymers for Rapid Prototyping. *Journal of Coatings Technology and Research* **2007**, *4* (4), 505–510. https://doi.org/10.1007/s11998-007-9059-3.

(14) Bhushan, B.; Caspers, M. An Overview of Additive Manufacturing (3D Printing) for Microfabrication. *Microsystem Technologies* **2017**, *23* (4), 1117–1124. https://doi.org/10.1007/s00542-017-3342-8.

(15) Mao, M.; He, J.; Li, X.; Zhang, B.; Lei, Q.; Liu, Y.; Li, D. The Emerging Frontiers and Applications of High-Resolution 3D Printing. *Micromachines* **2017**, *8* (4), 1–20. https://doi.org/10.3390/mi8040113.

(16) Gao, W.; Zhang, Y.; Ramanujan, D.; Ramani, K.; Chen, Y.; Williams, C. B.; Wang, C. C. L.; Shin, Y. C.; Zhang, S.; Zavattieri, P. D. The Status, Challenges, and Future of Additive Manufacturing in Engineering. *CAD Computer Aided Design* **2015**, *69*, 65–89. https://doi.org/10.1016/j.cad.2015.04.001.

(17) Schmidt, K.; Zimmermann, A. Evaluation of Process and Anisotropy of Thermosetting Adhesives with Ultraviolet-Assisted 3D Dispensing. *Additive Manufacturing* **2020**, *34*, 101262. https://doi.org/10.1016/j.addma.2020.101262.

(18) Dulieu-Barton, J. M.; Fulton, M. C. Mechanical Properties of a Typical Stereolithography Resin. *Strain* **2000**, *36* (2), 81–87. https://doi.org/10.1111/j.1475-1305.2000.tb01177.x.

(19) Curtis, J. D.; Hanna, S. D.; Patterson, E. A.; Taroni, M. On the Use of Stereolithography for the Manufacture of Photoelastic Models. **2003**, 15.

(20) Karalekas, D. E.; Agelopoulos, A. On the Use of Stereolithography Built Photoelastic Models for Stress Analysis Investigations. *Materials & Design* **2006**, *27* (2), 100–106. https://doi.org/10.1016/j.matdes.2004.09.028.

(21) Goodner, M. D.; Bowman, C. N. Development of a Comprehensive Free Radical Photopolymerization Model Incorporating Heat and Mass Transfer e Ects in Thick Ÿlms. *Chemical Engineering Science* **2002**, 14.

(22) Sun, G.; Wu, X.; Liu, R. A Comprehensive Investigation of Acrylates Photopolymerization Shrinkage Stress from Micro and Macro Perspectives by Real Time MIR-Photo-Rheology. *Progress in Organic Coatings* **2021**, *155*, 106229. https://doi.org/10.1016/j.porgcoat.2021.106229.

(23) Belgacem, M. B.; Kamoun, S.; Gargouri, M.; Dorkenoo, K. D. H.; Barsella, A.; Mager, L. Light Induced Self-Written Waveguides Interactions in Photopolymer Media. *Opt. Express, OE* **2015**, *23* (16), 20841–20848. https://doi.org/10.1364/OE.23.020841.

(24) Monro, T. M.; Poladian, L.; de Sterke, C. M. Analysis of Self-Written Waveguides in Photopolymers and Photosensitive Materials. *Phys. Rev. E* **1998**, *57* (1), 1104–1113. https://doi.org/10.1103/PhysRevE.57.1104.

(25) Li, H.; Qi, Y.; Malallah, R.; Sheridan, J. T. Modeling the Nonlinear Photoabsorptive Behavior during Self-Written Waveguide Formation in a Photopolymer. *J. Opt. Soc. Am. B, JOSAB* **2015**, *32* (5), 912–922. https://doi.org/10.1364/JOSAB.32.000912.

(26) Barsella, A.; Dorkenoo, H.; Mager, L. Near Infrared Two-Photon Self-Confinement in Photopolymers for Light Induced Self-Written Waveguides Fabrication. *Appl. Phys. Lett.* **2012**, *100* (22), 221102. https://doi.org/10.1063/1.4722925.

(27) Bielykh, S. P.; Galstian, T.; Reshetnyak, V. Y. Theoretical Modeling of Photo-Induced Lens Formation in a Polymerizable Matrix Containing Quantum Dots. *J. Opt. Soc. Am. B* **2018**, *35* (8), 2029. https://doi.org/10.1364/JOSAB.35.002029.

(28) Blachowicz, T.; Ehrmann, G.; Ehrmann, A. Optical Elements from 3D Printed Polymers. *e-Polymers* **2021**, *21* (1), 549–565. https://doi.org/10.1515/epoly-2021-0061.

(29) Shrotri, A.; Beyer, M.; Stübbe, O. Manufacturing and Analyzing of Cost-Efficient Fresnel Lenses Using Stereolithography. In *3D Printed Optics and Additive Photonic Manufacturing II*; von Freymann, G., Herkommer, A. M., Flury, M., Eds.; SPIE: Online Only, France, 2020; p 25. https://doi.org/10.1117/12.2555367.

(30) Vallejo-Melgarejo, L. D.; Reifenberger, R. G.; Newell, B. A.; Narváez-Tovar, C. A.; Garcia-Bravo, J. M. Characterization of 3D-Printed Lenses and Diffraction Gratings Made by DLP Additive Manufacturing. *Rapid Prototyping Journal* **2019**, *25* (10), 1684–1694. https://doi.org/10.1108/RPJ-03-2019-0074.

(31) Tayama, G. T.; Santagneli, S. H.; Eckert, H.; Pawsey, S.; Messaddeq, Y. Preparation and Structural Characterization of New Photopolymerizable Transparent Aluminum-Phosphate Hybrid Materials as Resins for 3D Printing. *J. Phys. Chem. C* **2020**, *124* (46), 25621–25631. https://doi.org/10.1021/acs.jpcc.0c08289.

(32) Tayama, G. T.; Santagneli, S. H.; de Oliveira Junior, M.; Messaddeq, Y. Understanding the Microstructure Connectivity in Photopolymerizable Aluminum-Phosphate-Silicate Sol–Gel Hybrid Materials for Additive Manufacturing. *J. Phys. Chem. C* **2023**, acs.jpcc.2c08027. https://doi.org/10.1021/acs.jpcc.2c08027.

(33) Posternak, M.; Tayama, G. T.; Messaddeq, S. H.; Messaddeq, Y. Process Modeling of Laser Scanning Vat-Photopolymerization Operating under Intermittent Exposure Conditions. *Additive Manufacturing* **2022**, *60*, 103234. https://doi.org/10.1016/j.addma.2022.103234.

(34) Baffou, G. Quantitative Phase Microscopy Using Quadriwave Lateral Shearing Interferometry (QLSI): Principle, Terminology, Algorithm and Grating Shadow Description. *J. Phys. D: Appl. Phys.* **2021**, *54* (29), 294002. https://doi.org/10.1088/1361-6463/abfbf9.

(35) Galstian, T. *Introduction à La Photonique*; Loze-Dion: Quebec, 2015.

(36) Wu, S.-T.; Efron, U.; Hess, L. D. Birefringence Measurements of Liquid Crystals. *Appl. Opt.* **1984**, *23* (21), 3911. https://doi.org/10.1364/AO.23.003911.

(37) Kobayashi, Y.; Hisano, K.; Aizawa, M.; Ishizu, M.; Akamatsu, N.; Shishido, A. Liquid Crystal Polymer Networks Directed by Scanning Wave Photopolymerization of Oxetane Monomer and Crosslinker. *Molecular Crystals and Liquid Crystals* **2020**, *713* (1), 37–45. https://doi.org/10.1080/15421406.2020.1856531.

(38) Hashimoto, S.; Akamatsu, N.; Kobayashi, Y.; Hisano, K.; Aizawa, M.; Kubo, S.; Shishido, A. Direct Surface Patterning of Microscale Well and Canal Structures by Photopolymerization of

Liquid Crystals with Structured Light. *ACS Appl. Mater. Interfaces* **2023**. https://doi.org/10.1021/acsami.2c20739.

(39) Purvis, J.; Bower, D. I. A Study of Molecular Orientation in Poly(Methyl Methacrylate) by Means of Laser-Raman Spectroscopy. *Polymer* **1974**, *15* (10), 645–654. https://doi.org/10.1016/0032-3861(74)90055-X.

CONCLUSION AND OUTLOOKS

In this project, we developed aluminum-phosphate-based hybrid materials using the sol-gel route for additive manufacturing. We characterized in-depth the structure of these materials using solid-state NMR. These materials are candidates for the fabrication of active and passive additive manufactured photonic devices. For this project, we employed a custom-made VPP system operating under intermittent exposure conditions. We developed a mathematical model describing the exposure profile outputted by this custom-made VPP setup, since its operating principle greatly differs from commercial platforms. Then, these new materials were 3D printed after characterizing their VPP parameters and photopolymerization kinetics. Lastly, we examined the optical homogeneity and anisotropy of additive manufactured elements from these materials.

Initially, we explored a series of reactants and synthesis protocols to achieve photopolymerizable aluminum-phosphate sols suitable for VPP. The first series of materials obtained were reported in **Chapter 1**, comprehending organic-inorganic hybrid (OIH) materials composed by poly (2-hydroxyethyl methacrylate) chains with aluminum-phosphate groups covalently bonded to the polymeric backbone, as revealed by solid-state NMR, and infrared spectroscopy. The connectivity between aluminum and phosphate groups was investigated in-depth by solid-state NMR, showing strong dependency to the aluminum to phosphorus ratio. Ultimately, these inorganic units provide numerous crosslinkers, resulting in a highly interconnected and interlocked inorganic/organic structure. The obtained materials are stable solutions that can be photopolymerized to yield OIH materials optically transparent between the 420 nm - 1100 nm range with low volumetric retraction compared to methacrylate polymers, making them ideal candidates for additive manufacturing via VPP. However, these materials suffer from poor transmittance in the near-infrared region (NIR) due to the high organic content of these matrices.

We addressed these issues by developing the materials presented in **Chapter 2**, where we substituted the 2-hydroxyethyl methacrylate by a common alkoxysilane precursor, resulting in aluminum-phosphate-silicate OIH materials. Similarly, we obtained photopolymerizable and stable solutions compatible with VPP technologies, resulting in transparent hybrid materials with high inorganic mass content and improved transmittance in the NIR. We investigated the structural evolution with Si concentration for polymerized samples with different Al:P ratios by means of solid-state NMR,

SEM and phase contrast AFM imaging. An extensive solid-state NMR analysis showed that these materials follow the build-up principle with aluminum-phosphate species and alkoxysilane chains acting as fundamental building blocks. The Al:P ratio dictates the hetero-condensation of aluminum and phosphate precursors, resulting in linear aluminum-phosphate units with monomeric or dimeric nature depending on the Al:P ratio. The dimeric structure favors alkoxysilane homo-condensation, resulting in separate silicate and aluminum-phosphate inorganic networks, while the monomeric structure allows Al-O-Si hetero-condensation, resulting in an inorganic network composed by aluminum-phosphate units interconnected by silicate chains. These structural features present these materials as potential candidates to immobilize lanthanide ions for developing active optical components.

In **Chapter 3**, we tested a mathematical model describing the exposure profile outputted by the custom-built printer employed in this work, allowing us to model the laser-resin interaction in this equipment, and to correlate the printing parameters measured for our materials with those of commercial AM setups. We observed that our proposed model has the same logarithmic dependence of Jacobs work curve (laser-resin interaction model widely employed), with the addition of a factor describing the overlap from adjacent pulses. This study led to two important observations: first, it is possible to correlate the printing parameters measured for our resin in this equipment and recalculate the values to other commercial setups; second, there are limits concerning the applicability of the Jacobs work curve model in the new generation of VPP platforms. Furthermore, we identified that this printing system can, theoretically, print faster compared to commercial platforms under specific conditions of beam diameter and overlap between pulses.

In **Chapter 4**, we explored the additive manufacturing of the aluminum-phosphate-silicate resins studied in **Chapter 2**. We studied the evolution of the 3D printing parameters of these materials (critical energy and penetration depth), and of the photopolymerization kinetics with light intensity and silicate concentration. Furthermore, we used our experimental data to validate a photochemical model published in the literature describing the VPP process. The model predicts that $E_c \propto (k_t{}^{1/2}/k_p) \ln p_c$ and $D_p \propto \epsilon$, where k_t k_p, p_c, and ϵ are the kinetic constant of bimolecular termination, kinetic constant of propagation, critical conversion, and absorption coefficient at the laser wavelength, respectively. Our study reveals that both $E_c \propto (k_t{}^{1/2}/k_p)$ and $D_p \propto \epsilon$ relationships hold true and there is a link between the critical energy and the kinetic constants describing the polymerization process of a given material.

Lastly, in **Chapter 5**, we studied the refractive index distribution and the presence of optical anisotropies in 3D printed lines (the fundamental structure fabricated by VPP) fabricated using one of the aluminum-phosphate-silicate resins studied in **Chapter 2**. Micro-Raman mapping showed a gradient of polymerization degree present in the lines, where smaller C=C conversions were achieved as the light intensity decreased (deeper light penetration and farther from the beam center), however, this gradient did not lead to significant variation of refractive index ($<10^{-4}$). Further studies by polarimetry, revealed the presence of optical anisotropies in these lines; however, these anisotropies did not arise due to molecular alignment, as showed by polarized micro-Raman mapping, indicating that the birefringence arises from the shear stress perpendicular to the scan direction due to the inflow of monomer towards the polymerization spot. To the best of our knowledge, this is the first study on the optical properties of 3D printed parts.

Overall, the results of this Ph.D. project present a myriad of prospects. For instance, we explored the synthesis and characterization of sol-gel hybrid materials with exotic compositions, whose synthesis is known to be challenging. Not surprisingly, we are the first to report these kinds of materials, that is, stable photopolymerizable resins that result in transparent aluminum-phosphate OIH materials. As prior mentioned, these materials could be interesting hosting matrices of lanthanide ions for the development of active optical devices, however further study must be done address its feasibility. Furthermore, these materials still have an organic nature, which has deleterious effects on transmission properties at NIR and could prevent the application of these materials in photonics. There is still room for improving the optical properties of these materials.

Concerning the additive manufacturing, we observed that further effort would be required to better understand the relationship between photochemistry and VPP. The study of the 3D printing parameters of our materials and their kinetics of photopolymerization provided insight into the link between process modelling and the chemical reactions involved. This relationship is a fundamental gap in the additive manufacturing area, which would ultimately lead to more precise models, simulations and understanding of the relationship between properties and processing conditions in VPP. Similarly, our mathematical model describing the exposure profile of our custom-made intermittent exposure VPP setup addressed another major gap in the literature, since the Jacobs work curve is still employed to model the laser-resin interaction, even thou its development assumed the use of continuous laser sources that became totally obsolete in the last 30 years. The model that we developed is very simplistic, and ignores a series of different dynamic effects associated to the

photopolymerization that can deeply affect the additive manufacturing, requiring additional investigations to include these factors.

Finally, we stablished a protocol to measure optical anisotropies and inhomogeneities in 3D printed materials. So far, all published works concerning additive manufacturing for photonics did not address the anisotropic nature of the additive manufacturing process, and our results demonstrate that further application of VPP techniques for additive manufacturing of photonic materials requires additional effort into elucidating the optical properties at microscale in these materials. Our work provided insight into the nature of these optical heterogeneities and anisotropies. Nonetheless, further understanding of its origins, improvements in the methods for quantification and mitigation strategies must be studied.

RESUMO EXPANDIDO

A MA é uma tecnologia promissora para a área de fotônica, e tem recebido ampla atenção na última década como um método para contornar as limitações geométricas e de integração presentes em métodos tradicionais de fabricação, o que poderia permitir uma nova geração de dispositivos ópticos integrados. As tecnologias MA para fotônica devem ser capazes de fabricar objetos com alta resolução (<10 um) e elevada qualidade de acabamento de superfície, que são condições atendidas por poucas tecnologias de MA. Neste quesito, a família de técnicas de fotopolimerização em cuba (*"vat photopolymerization"* VPP) é uma das poucas que atendem a tais requisitos e, embora existam inúmeros exemplos na literatura sobre o uso da VPP em fotônica, existem poucas investigações fundamentais sobre a qualidade óptica das peças produzidas, especialmente no que tange a homogeneidade e anisotropia óptica, visto que a MA é um processo fundamentalmente anisotrópico.

A disponibilidade de materiais compatíveis com a VPP é um dos principais problemas limitando ampla aplicação dessa família de técnicas no domínio da fotônica. A VPP constrói objetos por meio da fotopolimerização seletiva de uma resina, formando cada secção transversal do objeto. Entretanto, o mecanismo de fotopolimerização é restrito a polímeros, o que limita a aplicação em óptica de objetos fabricados por VPP as regiões do visível e de terahertz do espectro eletromagnético, uma vez que os grupos orgânicos apresentam elevada absorção na região do infravermelho próximo. Dessa maneira, o desenvolvimento de novos materiais compatíveis com a VPP para aplicação fotônica se transformou em um campo emergente e de grande relevância. Nos últimos anos, tem havido intensa pesquisa para permitir a MA de vidros inorgânicos via VPP, que é um material clássico no desenvolvimento de dispositivos ópticos ativos e passivos. A principal desvantagem, no entanto, é que todas as abordagens disponíveis requerem tratamento térmico a alta temperatura, dificultando a construção de dispositivos eletro-ópticos integrados. Nesse contexto, o uso de materiais híbridos orgânico-inorgânicos (HOI) com VPP surgiu como uma alternativa aos materiais poliméricos e vidros inorgânicos, uma vez que suas propriedades ópticas podem ser ajustadas para atender aos requisitos de transmissão para dispositivos ópticos ativos e passivos que operam nas regiões do espectro UV (ultravioleta) ao NIR (infravermelho próximo) e ideais para estruturas fotônicas ativas e passivas integradas, uma vez que não requerem tratamentos térmicos.

A rota híbrida sol-gel surgiu nos últimos 3 anos como uma rota química conveniente para obter materiais transparentes de HOI processáveis através de VPP. Rotas de síntese alternativas para materiais HOI não são inatamente compatíveis para VPP como a rota híbrida sol-gel, e muitas vezes sofrem de segregação de fase, produzindo materiais opacos. Essa rota de síntese permitiu a impressão de HOIs à base de silicato com boa qualidade óptica, que foram explorados na fabricação de estruturas ópticas passivas, como guias de onda. No entanto, essas matrizes não são boas candidatas para o desenvolvimento de dispositivos ópticos ativos, devido à sua baixa solubilidade de íons lantanídeos. Dessa maneira, há a necessidade de materiais HOI que sejam inerentemente compatíveis com a química dos lantanídeos para a fabricação de dispositivos ópticos ativos via VPP.

A este respeito, os materiais HOI a base de alumínio-fosfato (AlP) são candidatos promissores para a fabricação de dispositivos ópticos ativos. Compostos baseados em alumínio-fosfato possuem excelente solubilidade para os íons lantanídeos, impedindo a formação de *clusters* agrupamento e redução da fotoluminescência. A química do sol-gel AlP é desafiadora em comparação com a química bem estabelecida do sol-gel de silicato, uma vez que os precursores de fosfato e de alumínio para a rota sol-gel são muito reativos ou inertes. Até o momento, há pouca informação sobre a síntese de materiais transparentes e fotopolimerizáveis de AlP OIH.

O objetivo deste projeto de doutorado foi o desenvolvimento e caracterização estrutural de materiais híbridos à base de fosfato de alumínio obtidos a partir da rota sol-gel para a manufatura aditiva via VPP, com potencial aplicação na fabricação de novos dispositivos fotônicos ativos e passivos. Para tal, foi utilizado um sistema de VPP customizado operando sob condições de exposição intermitente, cujo princípio de funcionamento difere de plataformas comerciais. Foi desenvolvido um modelo matemático que descreve o perfil de exposição produzido pelo equipamento de VPP e os parâmetros operacionais para impressão dos materiais sintetizados, bem como suas cinéticas de fotopolimerização, foram estudados. Por fim, examinamos a homogeneidade óptica e a anisotropia de elementos manufaturados aditivamente a partir desses materiais.

Inicialmente, exploramos uma série de reagentes e protocolos de síntese para obter sóis fotopolimerizáveis à base de fosfato de alumínio adequados para VPP. A primeira série de materiais obtidos foi relatada no **Capítulo 1**, compreendendo materiais HOI formado por cadeias poliméricas de 2-hidroxietil metacrilato ligadas covalentemente a espécies de fosfato de alumínio, conforme revelado por RMN de estado sólido e espectroscopia de infravermelho. A conectividade entre os grupos

alumínio e fosfato foi investigada em profundidade por RMN de estado sólido, e os resultados demonstraram forte dependência com a relação alumínio/fósforo. Estruturalmente, essas unidades inorgânicas atuam como ligações cruzadas, resultando em uma estrutura inorgânica/orgânica altamente interconectada e interligada. Os materiais obtidos começam como soluções altamente estáveis que podem ser fotopolimerizadas para produzir materiais híbridos opticamente transparentes na faixa de 420 nm - 1100 nm, e com baixa retração volumétrica comparado a materiais do tipo metacrilato, tornando-os candidatos ideais para manufatura aditiva via VPP. No entanto, esses materiais apresentaram baixa transmitância na região do infravermelho próximo (NIR) devido ao alto teor orgânico dessas matrizes.

Esses materiais tiverem suas propriedades de transmissão melhoras através da substituição do 2-hidroxietil metacrilato por um precursor de alcoxissilano, resultando em materiais híbridos de alumínio-fosfato-silicato, conforme reportado no **Capítulo 2**. De maneira similar, obtivemos soluções fotopolimerizáveis e estáveis, compatíveis com as tecnologias de VPP, resultando em materiais híbridos transparentes com alto teor de massa inorgânica (até 40% em massa) e melhor transmitância no NIR, conforme ilustrado na **Figure 70**.

Figure 70. Monolitos polidos obtidos a partir da termopolimerização dos materiais de composição 30% TMSPM com razão Al:P de (a) 1:1, (b) 3:1, e (c) 1:3. Espessura entre 2 e 4 mm, com largura de 10 mm e comprimento de 15 a 30 mm. (d) Torre de Voroni impressa 3D (5 cm de altura) com o material 0% TMSPM Al:P = 1:1 (1% em massa de TPO).

A evolução estrutural com a concentração de Si para amostras com diferentes razões Al:P foi investigada por meio de RMN de estado sólido, microscopia eletrônica de varredura (MEV), e microscopia de força atômica com contraste de fase. Uma análise detalhada por meio de RMN de

estado sólido mostrou que esses materiais seguem o princípio de construção *build-up*, com espécies de fosfato de alumínio e cadeias de alcoxissilano atuando como blocos fundamentais. A razão Al:P determina a heterocondensação dos precursores de alumínio e fosfato e a estrutura das unidades de fosfato de alumínio resultantes. Essas estruturas se apresentaram como compostos lineares de fosfato de alumínio com natureza monomérica ou dimérica, dependendo da razão Al:P, conforme ilustrado na **Figure 71**. A estrutura dimérica favorece a homocondensação do alcoxissilano, resultando em redes inorgânicas separadas de silicato e fosfato de alumínio, enquanto as estruturas monoméricas permitem a heterocondensação Al-O-Si, resultando em uma rede inorgânica composta por unidades de fosfato de alumínio interligadas por cadeias de silicato. Estas características estruturais apresentam estes materiais como candidatos potenciais para imobilizar íons lantanídeos para o desenvolvimento de componentes ópticos ativos.

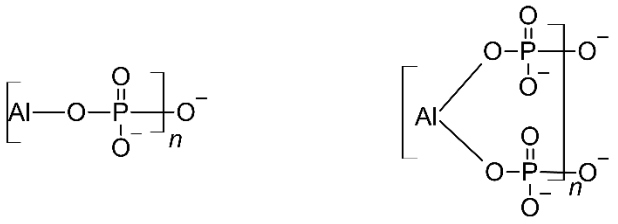

Figure 71. Estruturas lineares de alumino-fosfato do tipo monomérica e dimérica identificadas como bloco fundamentais compondo os materiais descritos no **Capítulo 2**.

No **Capítulo 3**, testamos um modelo matemático que descreve o perfil de exposição produzido pela impressora empregada neste trabalho, de maneira a permitir a correlação dos parâmetros de impressão medidos para nossos materiais com os de plataformas MA comerciais, conforme ilustrado na **Figure 72**. Observamos que o modelo possui a mesma dependência logarítmica da curva de trabalho de Jacobs (empregada em sistemas comerciais), com a adição de um fator que descreve a sobreposição de pulsos adjacentes, permitindo que os parâmetros de impressão medidos para nossas resinas em nossa plataforma customizada sejam extrapolados para outros equipamentos comerciais.

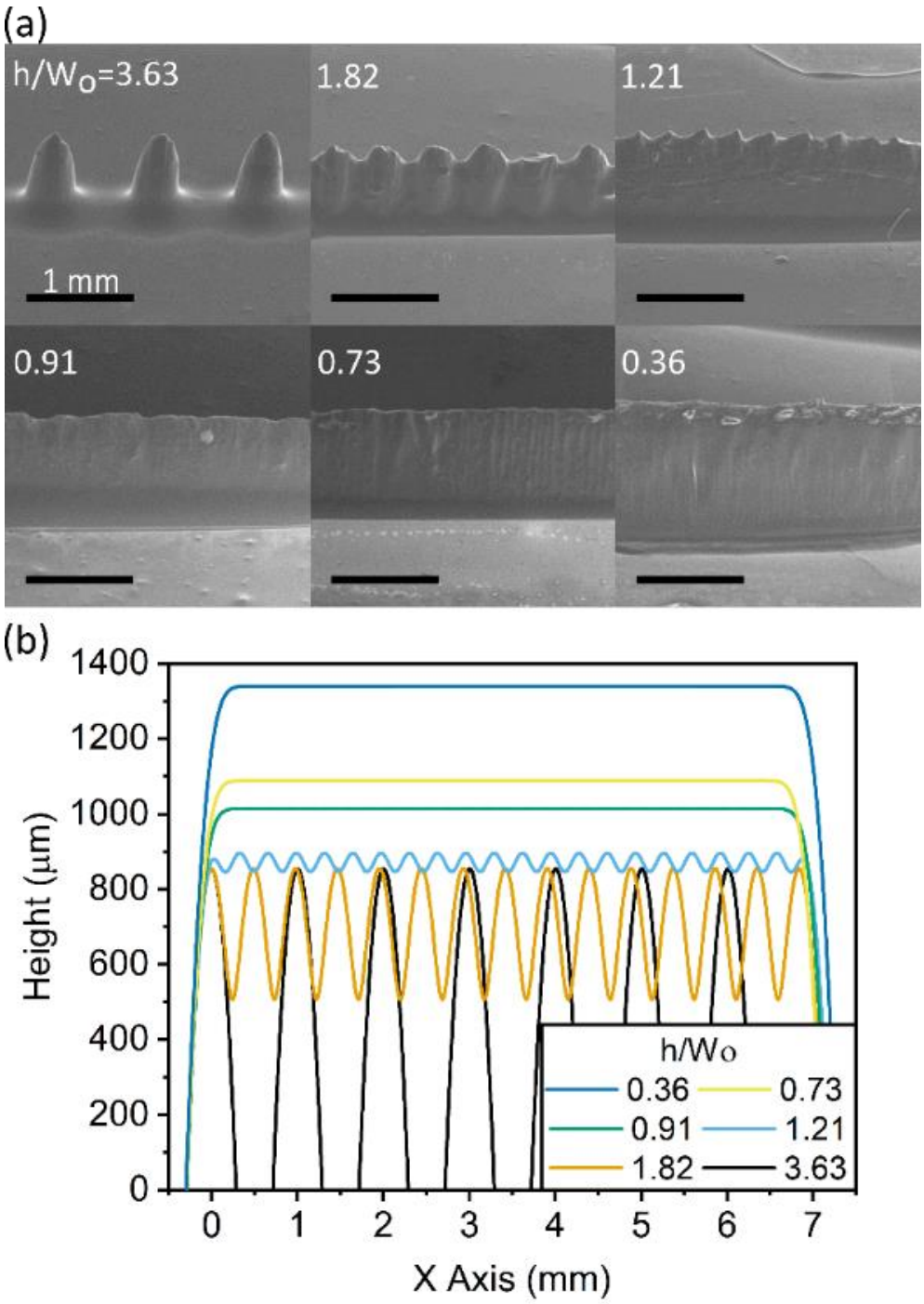

Figure 72. (a) Imagem de MEV de uma linha impressa 3D utilizando diferente distancias interpulso com um material de composição 0.73 % em massa de fotoiniciador e [PETA/BAPO]-[MPTMS-HAD] utilizando um laser de emissão em 360 nm (Ø=550±10 µm), potência de 800 µW (336.7 mW.cm^{-2}), e 100 ms de tempo de exposição. Escala de 1 mm; (b) Perfil topográfico de acordo com o modelo VPP-UVL-IE calculado a partir dos mesmos parâmetros experimentais.

No **Capítulo 4**, exploramos a manufatura aditiva das resinas de alumínio-fosfato-silicato estudadas no **Capítulo 2**. A evolução dos parâmetros de impressão 3D desses materiais (energia crítica e profundidade de penetração) e da cinética de fotopolimerização com intensidade de luz e silicato concentração foram estudados, conforme ilustrado na **Figure 73**. Além disso, usamos nossos dados experimentais para validar um modelo fotoquímico publicado na literatura descrevendo o processo VPP. O modelo prevê que $E_c \propto ({k_t}^{1/2}/k_p) \ln p_c$ and $D_p \propto \epsilon$, where k_t k_p, p_c, and ϵ são a constante cinética de terminação bimolecular, constante cinética de propagação, conversão crítica e coeficiente de absorção no comprimento de onda do laser, respectivamente. Nosso estudo revela que tanto $E_c \propto ({k_t}^{1/2}/k_p)$ and $D_p \propto \epsilon$ as relações são verdadeiras e existe uma ligação entre a energia crítica e as constantes cinéticas que descrevem o processo de polimerização de um determinado material.

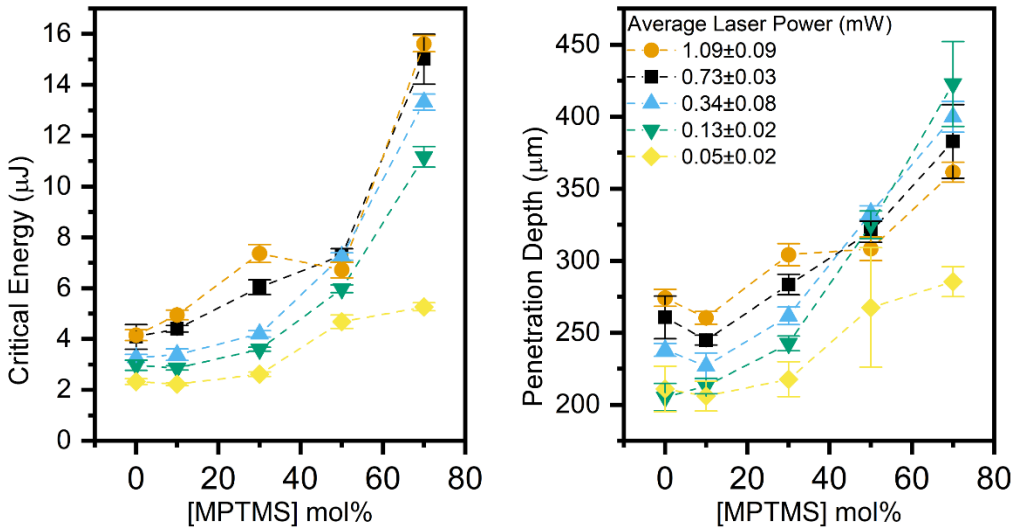

Figure 73. Energia crítica (a direita) e profundidade de penetração (a esquerda) em função da concentração de MPTMS medidas com potencias de laser médio de 1.09, 0.73, 0.34, 0.13, e 0.05 mW.

Por fim, no **Capítulo 5**, estudamos a distribuição do índice de refração e a presença de anisotropias ópticas em linhas impressas em 3D fabricadas com uma das resinas de alumínio-fosfato-silicato estudadas no Capítulo 2. O mapeamento micro-Raman mostrou um gradiente de grau de polimerização presente nas linhas, onde menores conversões C=C foram alcançadas à medida que a intensidade da luz diminuiu (penetração mais profunda da luz e mais distante do centro do feixe), no entanto, esse gradiente não resultou em variações de índice de refração superiores ao limite de detecção do nosso procedimento de medição ($<10^{-4}$). Imagens de polarimetria revelaram a presença

de anisotropias ópticas nessas linhas, conforme ilustrado na **Figure 74**; no entanto, essas anisotropias não surgem devido ao alinhamento molecular, como mostrado pelo mapeamento micro-Raman polarizado, indicando que a birrefringência surge da tensão de cisalhamento perpendicular à direção da varredura do laser durante a impressão 3D, resultando em influxo de monômero em direção ao ponto de polimerização.

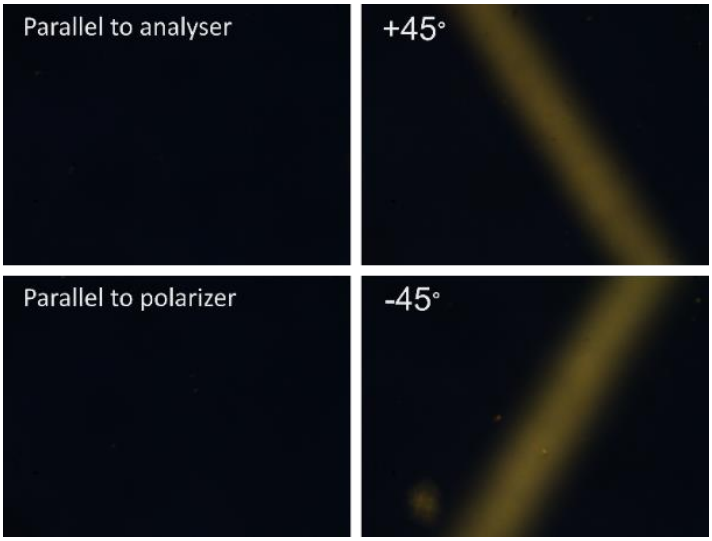

Figure 74. Imagens de polarimetria de uma linha impressa 3D e imersa óleo de mesmo índice de refração. Fotos adquiridas com a linha alinhada paralela, +45, -45, e perpendicular ao polarizador.

BIBLIOGRAPHIC REFERENCES

[1] S. Mellor, L. Hao, and D. Zhang, "Additive manufacturing: A framework for implementation," *International Journal of Production Economics*, vol. 149, pp. 194–201, 2014, doi: 10.1016/j.ijpe.2013.07.008.

[2] T. D. Ngo, A. Kashani, G. Imbalzano, K. T. Q. Nguyen, and D. Hui, "Additive manufacturing (3D printing): A review of materials, methods, applications and challenges," *Composites Part B: Engineering*, vol. 143, no. December 2017, pp. 172–196, Jun. 2018, doi: 10.1016/j.compositesb.2018.02.012.

[3] B. Bhushan and M. Caspers, "An overview of additive manufacturing (3D printing) for microfabrication," *Microsystem Technologies*, vol. 23, no. 4, pp. 1117–1124, 2017, doi: 10.1007/s00542-017-3342-8.

[4] C. L. Weber *et al.*, "The Role of the National Science Foundation in the Origin and Evolution of Additive Manufacturing in the United States," 2013. [Online]. Available: https://www.ida.org/idamedia/Corporate/Files/Publications/STPIPubs/ida-p-5091.ashx

[5] A. Camposeo, L. Persano, M. Farsari, and D. Pisignano, "Additive Manufacturing: Applications and Directions in Photonics and Optoelectronics," *Advanced Optical Materials*, vol. 7, no. 1, 2019, doi: 10.1002/adom.201800419.

[6] J. I. N. G. Y. Ang *et al.*, "3D printed low-loss THz waveguide based on Kagome photonic crystal structure," *Optic Express*, vol. 24, no. 20, pp. 22454–22460, 2016.

[7] K. Cook *et al.*, "Step-index optical fiber drawn from 3D printed preforms," *Optics Letters*, vol. 41, no. 19, pp. 4554–4557, 2016, doi: 10.1364/OL.41.004554.

[8] B. Lebeau and P. Innocenzi, "Hybrid materials for optics and photonics," *Chem. Soc. Rev.*, vol. 40, no. 2, p. 886, 2011, doi: 10.1039/c0cs00106f.

[9] B. Yan, "Recent progress in photofunctional lanthanide hybrid materials," *RSC Advances*, vol. 2, no. 25, pp. 9304–9304, 2012, doi: 10.1039/c2ra20976d.

[10] R. A. S. Ferreira, P. S. André, and L. D. Carlos, "Organic-inorganic hybrid materials towards passive and active architectures for the next generation of optical networks," *Optical Materials*, vol. 32, no. 11, pp. 1397–1409, 2010, doi: 10.1016/j.optmat.2010.06.019.

[11] L. D. Carlos, R. A. S. Ferreira, V. de Zea Bermudez, B. Julián-López, and P. Escribano, "Progress on lanthanide-based organic–inorganic hybrid phosphors," *Chem. Soc. Rev.*, vol. 40, no. 2, pp. 536–549, 2011, doi: 10.1039/C0CS00069H.

[12] I. Cooperstein *et al.*, "Hybrid Materials for Functional 3D Printing," *Advanced Materials Interfaces*, vol. 1800996, pp. 1–15, 2018, doi: 10.1002/admi.201800996.

[13] P. Judeinstein and C. Sanchez, "Hybrid organic–inorganic materials: a land of multidisciplinarity," *J. Mater. Chem.*, vol. 6, no. 4, pp. 511–525, 1996, doi: 10.1039/JM9960600511.

[14] L. Nicole, C. Laberty-Robert, L. Rozes, and C. Sanchez, "Hybrid materials science: a promised land for the integrative design of multifunctional materials," *Nanoscale*, vol. 6, no. 12, pp. 6267–6292, 2014, doi: 10.1039/C4NR01788A.

[15] C. Sanchez, G. J. de A. A. Soler-Illia, F. Ribot, T. Lalot, C. R. Mayer, and V. Cabuil, "Designed Hybrid Organic−Inorganic Nanocomposites from Functional Nanobuilding Blocks," *Chemistry of Materials*, vol. 13, no. 10, pp. 3061–3083, Oct. 2001, doi: 10.1021/cm011061e.

[16] F. Ribot and C. Sanchez, "Organically Functionalized Metallic Oxo-Clusters: Structurally Well-Defined Nanobuilding Blocks for the Design of Hybrid Organic-Inorganic Materials," *Comments*

on Inorganic Chemistry, vol. 20, no. 4–6, pp. 327–371, Jan. 1999, doi: 10.1080/02603599908021449.

[17] I. Cooperstein, E. Shukrun, O. Press, A. Kamyshny, and S. Magdassi, "Additive Manufacturing of Transparent Silica Glass from Solutions," *ACS Applied Materials and Interfaces*, vol. 10, no. 22, pp. 18879–18885, 2018, doi: 10.1021/acsami.8b03766.

[18] E. Shukrun, I. Cooperstein, and S. Magdassi, "3D-Printed Organic–Ceramic Complex Hybrid Structures with High Silica Content," *Advanced Science*, vol. 5, no. 8, pp. 1–7, 2018, doi: 10.1002/advs.201800061.

[19] K. Arai, H. Namikawa, K. Kumata, T. Honda, Y. Ishii, and T. Handa, "Aluminum or phosphorus co-doping effects on the fluorescence and structural properties of neodymium-doped silica glass," *Journal of Applied Physics*, vol. 59, no. 10, pp. 3430–3436, May 1986, doi: 10.1063/1.336810.

[20] N. O. Dantas, E. O. Serqueira, A. C. A. Silva, A. A. Andrade, and S. A. Lourenço, "High Quantum Efficiency of Nd3+ Ions in a Phosphate Glass System using the Judd–Ofelt Theory," *Braz J Phys*, vol. 43, no. 4, pp. 230–238, Aug. 2013, doi: 10.1007/s13538-013-0145-y.

[21] J. Livage, P. Barboux, M. T. Vandenborre, C. Schmutz, and F. Taulelle, "Sol-gel synthesis of phosphates," *Journal of Non-Crystalline Solids*, vol. 147–148, pp. 18–23, 1992.

[22] F. Babonneau, L. Coury, and J. Livage, "Aluminum sec-butoxide modified with ethylacetoacetate: An attractive precursor for the sol-gel synthesis of ceramics," *Journal of Non-Crystalline Solids*, vol. 121, no. 1–3, pp. 153–157, May 1990, doi: 10.1016/0022-3093(90)90122-3.

[23] R. Lichtenberger, M. Puchberger, S. O. Baumann, and U. Schubert, "Modification of aluminum alkoxides with β-ketoesters: new insights into formation, structure and stability," *Journal of Sol-Gel Science and Technology*, vol. 50, no. 2, pp. 130–140, May 2009, doi: 10.1007/s10971-008-1890-1.

[24] I. Gibson, D. Rosen, and B. Stucker, *Additive Manufacturing Technologies: 3D Printing, Rapid Prototyping, and Direct Digital Manufacturing*, Second edi. Springer US, 2015. doi: 10.1520/F2792-12A.2.

[25] B. Redwood, F. Schöffer, and B. Garret, "The 3D Printing Handbook," *3D Hubs*, p. 304, 2017.

[26] B. DeBoer, N. Nguyen, F. Diba, and A. Hosseini, "Additive, subtractive, and formative manufacturing of metal components: a life cycle assessment comparison," *Int J Adv Manuf Technol*, vol. 115, no. 1–2, pp. 413–432, Jul. 2021, doi: 10.1007/s00170-021-07173-5.

[27] B. Bhushan and M. Caspers, "An overview of additive manufacturing (3D printing) for microfabrication," *Microsystem Technologies*, vol. 23, no. 4, pp. 1117–1124, 2017, doi: 10.1007/s00542-017-3342-8.

[28] J. Butt, "Exploring the Interrelationship between Additive Manufacturing and Industry 4.0," *Designs*, vol. 4, no. 2, Art. no. 2, Jun. 2020, doi: 10.3390/designs4020013.

[29] M. E. Hernandez Korner, M. P. Lambán, J. A. Albajez, J. Santolaria, L. del C. Ng Corrales, and J. Royo, "Systematic Literature Review: Integration of Additive Manufacturing and Industry 4.0," *Metals*, vol. 10, no. 8, Art. no. 8, Aug. 2020, doi: 10.3390/met10081061.

[30] S. M. E. Sepasgozar, A. Shi, L. Yang, S. Shirowzhan, and D. J. Edwards, "Additive Manufacturing Applications for Industry 4.0: A Systematic Critical Review," *Buildings*, vol. 10, no. 12, Art. no. 12, Dec. 2020, doi: 10.3390/buildings10120231.

[31] S. Mellor, L. Hao, and D. Zhang, "Additive manufacturing: A framework for implementation," *International Journal of Production Economics*, vol. 149, pp. 194–201, 2014, doi: 10.1016/j.ijpe.2013.07.008.

[32] W. Gao *et al.*, “The status, challenges, and future of additive manufacturing in engineering,” *CAD Computer Aided Design*, vol. 69, pp. 65–89, 2015, doi: 10.1016/j.cad.2015.04.001.
[33] P. Tack, J. Victor, P. Gemmel, and L. Annemans, “3D-printing techniques in a medical setting: A systematic literature review,” *BioMedical Engineering Online*, vol. 15, no. 1, pp. 1–22, 2016, doi: 10.1186/s12938-016-0236-4.
[34] J. M. Nadal-Serrano, A. Nadal-Serrano, and M. Lopez-Vallejo, “Democratizing science with the aid of parametric design and additive manufacturing: Design and fabrication of a versatile and low-cost optical instrument for scattering measurement,” *PLoS ONE*, vol. 12, no. 11, pp. 1–18, 2017, doi: 10.1371/journal.pone.0187219.
[35] J. Goole and K. Amighi, “3D printing in pharmaceutics: A new tool for designing customized drug delivery systems,” *International Journal of Pharmaceutics*, vol. 499, no. 1–2, pp. 376–394, 2016, doi: 10.1016/j.ijpharm.2015.12.071.
[36] F. C. Godoi, S. Prakash, and B. R. Bhandari, “3d printing technologies applied for food design: Status and prospects,” *Journal of Food Engineering*, vol. 179, pp. 44–54, 2016, doi: 10.1016/j.jfoodeng.2016.01.025.
[37] M. LaMonica, “Additive Manufacturing: GE, the worlds’s largest manufacturer, is on the verge of using 3-D printing to make jet parts,” *MIT Technology Review*, vol. 116, no. 3, p. 59, 2014, doi: 10.1016/B978-0-08-096532-1.01000-1.
[38] ASTM International, “F2792-12a - Standard Terminology for Additive Manufacturing Technologies,” *Rapid Manufacturing Association*, pp. 10–12, 2013, doi: 10.1520/F2792-12A.2.
[39] “Additive manufacturing - General principles - Fundamentals and vocabulary,” ISO/ASTM, International standard ISO/ASTM 52900:2021(E), 2021. doi: 10.3403/30448424.
[40] M. Ziaee and N. B. Crane, “Binder jetting: A review of process, materials, and methods,” *Additive Manufacturing*, vol. 28, pp. 781–801, Aug. 2019, doi: 10.1016/j.addma.2019.05.031.
[41] D.-G. Ahn, “Directed Energy Deposition (DED) Process: State of the Art,” *Int. J. of Precis. Eng. and Manuf.-Green Tech.*, vol. 8, no. 2, pp. 703–742, Mar. 2021, doi: 10.1007/s40684-020-00302-7.
[42] A. Oleff, B. Küster, M. Stonis, and L. Overmeyer, “Process monitoring for material extrusion additive manufacturing: a state-of-the-art review,” *Prog Addit Manuf*, vol. 6, no. 4, pp. 705–730, Dec. 2021, doi: 10.1007/s40964-021-00192-4.
[43] J. Gonzalez-Gutierrez, S. Cano, S. Schuschnigg, C. Kukla, J. Sapkota, and C. Holzer, “Additive Manufacturing of Metallic and Ceramic Components by the Material Extrusion of Highly-Filled Polymers: A Review and Future Perspectives,” *Materials*, vol. 11, no. 5, Art. no. 5, May 2018, doi: 10.3390/ma11050840.
[44] R. Singh *et al.*, “Powder bed fusion process in additive manufacturing: An overview,” *Materials Today: Proceedings*, vol. 26, pp. 3058–3070, Jan. 2020, doi: 10.1016/j.matpr.2020.02.635.
[45] T. Özel, A. Altay, B. Kaftanoğlu, R. Leach, N. Senin, and A. Donmez, “Focus Variation Measurement and Prediction of Surface Texture Parameters Using Machine Learning in Laser Powder Bed Fusion,” *Journal of Manufacturing Science and Engineering*, vol. 142, no. 1, Nov. 2019, doi: 10.1115/1.4045415.
[46] O. Gülcan, K. Günaydın, and A. Tamer, “The State of the Art of Material Jetting—A Critical Review,” *Polymers*, vol. 13, no. 16, Art. no. 16, Jan. 2021, doi: 10.3390/polym13162829.
[47] B. Derby, “Inkjet Printing of Functional and Structural Materials: Fluid Property Requirements, Feature Stability, and Resolution,” *Annual Review of Materials Research*, vol. 40, no. 1, pp. 395–414, Jun. 2010, doi: 10.1146/annurev-matsci-070909-104502.
[48] J. Zhang and P. Xiao, “3D printing of photopolymers,” *Polymer Chemistry*, vol. 9, no. 13. Royal Society of Chemistry, pp. 1530–1540, 2018. doi: 10.1039/c8py00157j.

[49] R. Liska *et al.*, “Photopolymers for rapid prototyping,” *Journal of Coatings Technology and Research*, vol. 4, no. 4, pp. 505–510, Nov. 2007, doi: 10.1007/s11998-007-9059-3.
[50] M. Mao *et al.*, “The emerging frontiers and applications of high-resolution 3D printing,” *Micromachines*, vol. 8, no. 4, pp. 1–20, 2017, doi: 10.3390/mi8040113.
[51] M. Shah *et al.*, “Vat photopolymerization-based 3D printing of polymer nanocomposites: current trends and applications,” *RSC Advances*, vol. 13, no. 2, pp. 1456–1496, 2023, doi: 10.1039/D2RA06522C.
[52] Y. Zhu *et al.*, “Recent advancements and applications in 3D printing of functional optics,” *Additive Manufacturing*, vol. 52, p. 102682, Apr. 2022, doi: 10.1016/j.addma.2022.102682.
[53] Y. Cao *et al.*, “Polymer/glass hybrid DC-MZI thermal optical switch for 3D-integrated chips,” *RSC Advances*, vol. 9, no. 19, pp. 10651–10656, 2019, doi: 10.1039/c9ra00037b.
[54] R. Gvishi and I. Sokolov, “3D sol–gel printing and sol–gel bonding for fabrication of macro- and micro/nano-structured photonic devices,” *Journal of Sol-Gel Science and Technology*, 2020, doi: 10.1007/s10971-020-05270-7.
[55] T. Gissibl, S. Thiele, A. Herkommer, and H. Giessen, “Two-photon direct laser writing of ultracompact multi-lens objectives,” *Nature Photonics*, vol. 10, no. 8, pp. 554–560, 2016, doi: 10.1038/nphoton.2016.121.
[56] S. Juodkazis, “Manufacturing: 3D printed micro-optics,” *Nature Photonics*, vol. 10, no. 8, pp. 499–501, 2016, doi: 10.1038/nphoton.2016.150.
[57] N. Vaidya and O. Solgaard, “3D printed optics with nanometer scale surface roughness,” *Microsyst Nanoeng*, vol. 4, no. 1, p. 18, Dec. 2018, doi: 10.1038/s41378-018-0015-4.
[58] G. Berglund, A. Wisniowiecki, J. Gawedzinski, B. Applegate, and T. S. Tkaczyk, “Additive manufacturing for the development of optical/photonic systems and components,” *Optica*, vol. 9, no. 6, p. 623, Jun. 2022, doi: 10.1364/OPTICA.451642.
[59] A. L. S. Cruz *et al.*, “3D Printed Hollow Core Fiber with Negative Curvature for Terahertz Applications,” *Journal of Microwaves, Optoelectronics and Electromagnetic Applications*, vol. 14, no. SI-1, pp. 45–53, 2015.
[60] A. L. S. Cruz, C. M. B. Cordeiro, and M. A. R. Franco, “3D Printed Hollow-Core Terahertz Fibers,” *Fibers*, vol. 6, no. 43, pp. 1–11, 2018, doi: 10.3390/fib6030043.
[61] C. R. Tubío, J. A. Nóvoa, J. Martín, F. Guitián, J. R. Salgueiro, and A. Gil, “3D printing of Al 2 O 3 photonic crystals for terahertz frequencies,” *RSC Adv.*, vol. 6, no. 3, pp. 2450–2454, 2016, doi: 10.1039/C5RA22737B.
[62] Q. Zhao *et al.*, “Optical fibers with special shaped cores drawn from 3D printed preforms,” *Optik*, vol. 133, no. 19, pp. 60–65, Mar. 2017, doi: 10.1016/j.ijleo.2017.01.002.
[63] K. Cook *et al.*, “Air-structured optical fiber drawn from a 3D-printed preform,” *Optics Letters*, vol. 40, no. 17, pp. 3966–3969, 2015, doi: 10.1364/OL.40.003966.
[64] Y. Chu *et al.*, “Silica optical fiber drawn from 3D printed preforms,” *Opt. Lett., OL*, vol. 44, no. 21, pp. 5358–5361, Nov. 2019, doi: 10.1364/OL.44.005358.
[65] D. Zhu, J. Zhang, Q. Xu, and Y. Li, “3D Printing of Customized Aspheric Lenses for Imaging,” *Polymers*, vol. 13, no. 20, p. 3477, Oct. 2021, doi: 10.3390/polym13203477.
[66] U. Blessing and K. Blessing, “Device for directing light beams, illustration device, method for producing a device and an illustration device,” US20160341851A1, Nov. 24, 2016 Accessed: Jan. 31, 2023. [Online]. Available: https://patents.google.com/patent/US20160341851A1/en?q=Luxexcel&oq=Luxexcel+
[67] K. Blessing and R. van de Vrie, “Print head, upgrade kit for a conventional inkjet printer, printer and method for printing optical structures,” US9592690B2, Mar. 14, 2017 Accessed: Jan. 31,

2023. [Online]. Available: https://patents.google.com/patent/US9592690B2/en?q=Luxexcel&oq=Luxexcel+
[68] R. van de Vrie, J. Biskop, and R. Blomaard, "Device for printing a three-dimensional structure," US20160271869A1, Sep. 22, 2016 Accessed: Jan. 31, 2023. [Online]. Available: https://patents.google.com/patent/US20160271869A1/en?q=Luxexcel&oq=Luxexcel+
[69] R. van de Vrie and J. Biskop, "Method for printing a three-dimensional structure, method for controlling a print head and printed article," US9463597B2, Oct. 11, 2016 Accessed: Jan. 31, 2023. [Online]. Available: https://patents.google.com/patent/US9463597B2/en?q=Luxexcel&oq=Luxexcel+
[70] "Applications in Microoptics, Optoelectronics & Photonics Packaging, Mastering, Biomedical Engineering." https://multiphoton.de/technology/application-examples (accessed Mar. 13, 2023).
[71] "Wide range of applications in research, prototyping and production processes." https://www.nanoscribe.com/en/applications/ (accessed Mar. 13, 2023).
[72] M. Et, "Production of 3D Free-Form waveguide structures," US 10343332 B2, 2019
[73] M. Ali, F. Alam, Y. F. Fah, O. Shiryayev, N. Vahdati, and H. Butt, "4D printed thermochromic Fresnel lenses for sensing applications," *Composites Part B: Engineering*, vol. 230, p. 109514, Feb. 2022, doi: 10.1016/j.compositesb.2021.109514.
[74] M. Ali, F. Alam, and H. Butt, "Fabrication of 5D Fresnel Lenses via Additive Manufacturing," *ACS Mater. Au*, vol. 2, no. 5, pp. 602–613, Sep. 2022, doi: 10.1021/acsmaterialsau.2c00026.
[75] M. Ali, F. Alam, N. Vahdati, and H. Butt, "3D-Printed Holographic Fresnel Lenses," *Advanced Engineering Materials*, vol. 24, no. 9, p. 2101641, Sep. 2022, doi: 10.1002/adem.202101641.
[76] M. Hossain and M. Gu, "Fabrication methods of 3D periodic metallic nano / microstructures for photonics applications," *Laser and Photonics Reviews*, vol. 8, no. 2, pp. 233–249, 2013, doi: 10.1002/lpor.201300052.
[77] Y. L. Kong *et al.*, "3D Printed Quantum Dot Light-Emitting Diodes," *Nano Letters*, vol. 14, no. 12, pp. 7017–7023, 2014, doi: 10.1021/nl5033292.
[78] R. Dangel, B. Offrein, U. Troppenz, M. Moehrle, W. Freude, and C. Koos, "In situ 3D nanoprinting of free-form coupling elements for hybrid photonic integration," *Nature Photonics*, vol. 12, no. April, 2018, doi: 10.1038/s41566-018-0133-4.
[79] T. Pereira, S. Rusinkiewicz, W. Matusik, and M. Csail, "Computational Light Routing : 3D Printed Optical Fibers for Sensing and Display," *ACM Transactions on Graphics*, vol. 33, no. 3, p. 24:1-24:13, 2014, doi: 10.1145/2602140.
[80] S. Korobogatiy, "3D printed hollow core terahertz Bragg waveguides with defect layers for surface sensing applications," *Optic Express*, vol. 25, no. 4, pp. 309–322, 2017.
[81] R. Wang, W. Yang, P. Zhu, S. Gao, B. Li, and Q. Li, "Creation of 3D terahertz photonic crystals by the direct writing technique with a TiO2sol-gel ink," *Journal of the American Ceramic Society*, vol. 101, no. 5, pp. 1967–1973, 2018, doi: 10.1111/jace.15347.
[82] Y. Liu *et al.*, "Structural color three-dimensional printing by shrinking photonic crystals," *Nat Commun*, vol. 10, no. 1, p. 4340, Dec. 2019, doi: 10.1038/s41467-019-12360-w.
[83] F. Kotz *et al.*, "Liquid Glass: A Facile Soft Replication Method for Structuring Glass," *Advanced Materials*, vol. 28, pp. 4646–4650, 2016, doi: 10.1002/adma.201506089.
[84] C. Xin, Z. Li, L. Hao, and Y. Li, "A comprehensive review on additive manufacturing of glass: Recent progress and future outlook," *Materials & Design*, vol. 227, p. 111736, Mar. 2023, doi: 10.1016/j.matdes.2023.111736.
[85] J. Klein *et al.*, "Additive Manufacturing of Optically Transparent Glass," *3D Printing and Additive Manufacturing*, vol. 2, no. 3, pp. 92–105, 2015, doi: 10.1089/3dp.2015.0021.

[86] S. Klein *et al.*, “3D printing of transparent glass,” *International Conference on Digital Printing Technologies*, pp. 336–337, 2012.
[87] P.-T. Brun *et al.*, “The molten glass sewing machine,” *Philosophical Transactions of the Royal Society A: Mathematical, Physical and Engineering Sciences*, vol. 375, no. 2093, pp. 20160156–20160156, 2017, doi: 10.1098/rsta.2016.0156.
[88] J. Luo, H. Pan, and E. C. Kinzel, “Additive Manufacturing of Glass,” *Journal of Manufacturing Science and Engineering*, vol. 136, no. 6, pp. 061024–061024, 2014, doi: 10.1115/1.4028531.
[89] J. Luo *et al.*, “Additive manufacturing of glass for optical applications,” in *Proceedings of SPIE*, 2016, vol. Proc. SPIE, no. April 2016, p. 97380Y/1-97380Y/9. doi: 10.1117/12.2218137.
[90] R. F. Shepherd *et al.*, “Stop-flow lithography of colloidal, glass, and silicon microcomponents,” *Advanced Materials*, vol. 20, no. 24, pp. 4734–4739, 2008, doi: 10.1002/adma.200801090.
[91] G. Marchelli, R. Prabhakar, D. Storti, and M. Ganter, “The guide to glass 3D printing: developments, methods, diagnostics and results,” *Rapid Prototyping Journal*, vol. 17, no. 3, pp. 187–194, 2011, doi: 10.1108/13552541111124761.
[92] J. F. Destino *et al.*, “3D Printed Optical Quality Silica and Silica-Titania Glasses from Sol-Gel Feedstocks,” *Advanced Materials Technologies*, vol. 1700323, pp. 1–10, 2018, doi: 10.1002/admt.201700323.
[93] R. M. Zaki *et al.*, “Direct 3D-printing of phosphate glass by fused deposition modeling,” *Materials & Design*, vol. 194, p. 108957, Sep. 2020, doi: 10.1016/j.matdes.2020.108957.
[94] S. Parola, B. Julián-López, L. D. Carlos, and C. Sanchez, “Optical Properties of Hybrid Organic-Inorganic Materials and their Applications,” *Advanced Functional Materials*, vol. 26, no. 36, pp. 6506–6544, Sep. 2016, doi: 10.1002/adfm.201602730.
[95] M. Malinauskas *et al.*, “Femtosecond laser polymerization of hybrid/integrated micro-optical elements and their characterization,” *J. Opt.*, vol. 12, no. 12, p. 124010, Nov. 2010, doi: 10.1088/2040-8978/12/12/124010.
[96] P. Wachholz, J. Wolf, S. Marx, D. Weber, J. Klein, and H. Schröder, “Novel technology for dispensing liquid polymers of a wide viscosity range on a picoliter scale for photonic applications,” in *Optical Interconnects XX*, Feb. 2020, vol. 11286, pp. 131–140. doi: 10.1117/12.2550566.
[97] L. Jacot-Descombes *et al.*, “Organic-inorganic-hybrid-polymer microlens arrays with tailored optical characteristics and multi-focal properties,” *Opt. Express*, vol. 23, no. 19, p. 25365, Sep. 2015, doi: 10.1364/OE.23.025365.
[98] J. Y. Kim, C. Martin-Olmos, N. S. Baek, and J. Brugger, “Simple and easily controllable parabolic-shaped microlenses printed on polymeric mesas,” *J. Mater. Chem. C*, vol. 1, no. 11, pp. 2152–2157, Feb. 2013, doi: 10.1039/C3TC00632H.
[99] L. Jacot-Descombes, M. R. Gullo, V. J. Cadarso, and J. Brugger, “Fabrication of epoxy spherical microstructures by controlled drop-on-demand inkjet printing,” *J. Micromech. Microeng.*, vol. 22, no. 7, p. 074012, Jun. 2012, doi: 10.1088/0960-1317/22/7/074012.
[100] D. J. Hayes, “Method for producing micro-optical components,” US5498444A, Mar. 12, 1996 Accessed: Mar. 17, 2023. [Online]. Available: https://patents.google.com/patent/US5498444/en
[101] J. Y. Kim, K. Pfeiffer, A. Voigt, G. Gruetzner, and J. Brugger, “Directly fabricated multi-scale microlens arrays on a hydrophobic flat surface by a simple ink-jet printing technique,” *J. Mater. Chem.*, vol. 22, no. 7, pp. 3053–3058, Jan. 2012, doi: 10.1039/C2JM15576A.
[102] A. Voigt *et al.*, “New inks for the direct drop-on-demand fabrication of polymer lenses,” *Microelectronic Engineering*, vol. 88, no. 8, pp. 2174–2179, Aug. 2011, doi: 10.1016/j.mee.2010.12.004.

[103] J. Y. Kim *et al.*, “Hybrid polymer microlens arrays with high numerical apertures fabricated using simple ink-jet printing technique,” *Opt. Mater. Express, OME*, vol. 1, no. 2, pp. 259–269, Jun. 2011, doi: 10.1364/OME.1.000259.
[104] R. Magazine, B. van Bochove, S. Borandeh, and J. Seppälä, “3D inkjet-printing of photo-crosslinkable resins for microlens fabrication,” *Additive Manufacturing*, vol. 50, p. 102534, Feb. 2022, doi: 10.1016/j.addma.2021.102534.
[105] A. Žukauskas, M. Malinauskas, C. Reinhardt, B. N. Chichkov, and R. Gadonas, “Closely packed hexagonal conical microlens array fabricated by direct laser photopolymerization,” *Appl. Opt., AO*, vol. 51, no. 21, pp. 4995–5003, Jul. 2012, doi: 10.1364/AO.51.004995.
[106] B. Sanchez-Padilla *et al.*, “Wrinkled axicons: shaping light from cusps,” *Opt. Express*, vol. 24, no. 21, p. 24075, Oct. 2016, doi: 10.1364/OE.24.024075.
[107] T. Gissibl, S. Thiele, A. Herkommer, and H. Giessen, “Sub-micrometre accurate free-form optics by three-dimensional printing on single-mode fibres,” *Nat Commun*, vol. 7, no. 1, Art. no. 1, Jun. 2016, doi: 10.1038/ncomms11763.
[108] S. Steenhusen, F. Burmeister, H.-C. Eckstein, and R. Houbertz, “Two-photon polymerization of hybrid polymers for applications in micro-optics,” presented at the SPIE LASE, San Francisco, California, United States, Mar. 2015, p. 93530K. doi: 10.1117/12.2079277.
[109] S. Steenhusen, S. Hasselmann, and G. Domann, “Strategies for rapid and reliable fabrication of microoptical structures using two-photon polymerization,” in *Advanced Fabrication Technologies for Micro/Nano Optics and Photonics X*, Feb. 2017, vol. 10115, pp. 128–136. doi: 10.1117/12.2252913.
[110] A. K. Petrov *et al.*, “Polymer X-ray refractive nano-lenses fabricated by additive technology,” *Opt Express*, vol. 25, no. 13, pp. 14173–14181, Jun. 2017, doi: 10.1364/OE.25.014173.
[111] E. Johlin, S. A. Mann, S. Kasture, A. F. Koenderink, and E. C. Garnett, “Broadband highly directive 3D nanophotonic lenses,” *Nat Commun*, vol. 9, no. 1, Art. no. 1, Nov. 2018, doi: 10.1038/s41467-018-07104-1.
[112] B. Stender, F. Hilbert, Y. Dupuis, A. Krupp, W. Mantei, and R. Houbertz, “Manufacturing strategies for scalable high-precision 3D printing of structures from the micro to the macro range,” *Advanced Optical Technologies*, vol. 8, pp. 225–231, Jun. 2019, doi: 10.1515/aot-2019-0022.
[113] E. Brasselet, M. Malinauskas, A. Žukauskas, and S. Juodkazis, “Photopolymerized microscopic vortex beam generators: Precise delivery of optical orbital angular momentum,” *Appl. Phys. Lett.*, vol. 97, no. 21, p. 211108, Nov. 2010, doi: 10.1063/1.3517519.
[114] A. Žukauskas, M. Malinauskas, and E. Brasselet, “Monolithic generators of pseudo-nondiffracting optical vortex beams at the microscale,” *Appl. Phys. Lett.*, vol. 103, no. 18, p. 181122, Oct. 2013, doi: 10.1063/1.4828662.
[115] S. Krivec *et al.*, “Silica-Based, Organically Modified Host Material for Waveguide Structuring by Two-Photon-Induced Photopolymerization,” *Advanced Functional Materials*, vol. 20, no. 5, pp. 811–819, 2010, doi: 10.1002/adfm.200901790.
[116] H. Segawa, K. Yoshida, T. Kondo, S. Matsuo, and H. Misawa, “Fabrication of Photonic Crystal Structures by Femtosecond Laser-Induced Photopolymerization of Organic-Inorganic Film,” *Journal of Sol-Gel Science and Technology*, vol. 26, no. 1, pp. 1023–1027, Jan. 2003, doi: 10.1023/A:1020729917721.
[117] A. Ovsianikov *et al.*, “Ultra-Low Shrinkage Hybrid Photosensitive Material for Two-Photon Polymerization Microfabrication,” *ACS Nano*, vol. 2, no. 11, pp. 2257–2262, Nov. 2008, doi: 10.1021/nn800451w.

[118] J. Serbin *et al.*, “Femtosecond laser-induced two-photon polymerization of inorganic–organic hybrid materials for applications in photonics,” *Opt. Lett.*, vol. 28, no. 5, p. 301, Mar. 2003, doi: 10.1364/OL.28.000301.
[119] J. Li, B. Jia, and M. Gu, “Engineering stop gaps of inorganic-organic polymeric 3D woodpile photonic crystals with post-thermal treatment,” *Opt. Express, OE*, vol. 16, no. 24, pp. 20073–20080, Nov. 2008, doi: 10.1364/OE.16.020073.
[120] Q. Sun, S. Juodkazis, N. Murazawa, V. Mizeikis, and H. Misawa, “Femtosecond laser photopolymerization of photonic and free-movable microstructures in sol-gel hybrid resist,” presented at the MOEMS-MEMS, San Francisco, California, Feb. 2010, p. 75910K. doi: 10.1117/12.840657.
[121] C.-L. Tai *et al.*, “Ultrastable, Deformable, and Stretchable Luminescent Organic–Inorganic Perovskite Nanocrystal–Polymer Composites for 3D Printing and White Light-Emitting Diodes,” *ACS Applied Materials & Interfaces*, Jul. 2019, doi: 10.1021/acsami.9b06248.
[122] C. Zhou *et al.*, “3D Printed Smart Windows for Adaptive Solar Modulations,” *Adv. Optical Mater.*, vol. 8, no. 11, p. 2000013, Jun. 2020, doi: 10.1002/adom.202000013.
[123] M. Faustini, D. Grosso, C. Boissière, R. Backov, and C. Sanchez, “‘Integrative sol–gel chemistry’: a nanofoundry for materials science,” *Journal of Sol-Gel Science and Technology*, vol. 70, no. 2, pp. 216–226, May 2014, doi: 10.1007/s10971-014-3321-9.
[124] D. G. Moore, L. Barbera, K. Masania, and A. R. Studart, “Three-dimensional printing of multicomponent glasses using phase-separating resins,” *Nature Materials*, vol. 19, no. 2, Art. no. 2, Feb. 2020, doi: 10.1038/s41563-019-0525-y.
[125] Z. Li *et al.*, “Additive manufacturing of lightweight and high-strength polymer-derived SiOC ceramics,” *Virtual and Physical Prototyping*, vol. 15, no. 2, pp. 163–177, Apr. 2020, doi: 10.1080/17452759.2019.1710919.
[126] D. J. Lorang, D. Tanaka, C. M. Spadaccini, K. A. Rose, N. J. Cherepy, and J. A. Lewis, “Photocurable liquid core-fugitive shell printing of optical waveguides,” *Advanced Materials*, vol. 23, no. 43, pp. 5055–5058, 2011, doi: 10.1002/adma.201102411.
[127] A. Chiappone *et al.*, “3D Printed PEG-Based Hybrid Nanocomposites Obtained by Sol–Gel Technique,” *ACS Applied Materials & Interfaces*, vol. 8, no. 8, pp. 5627–5633, Mar. 2016, doi: 10.1021/acsami.5b12578.
[128] C. Echalier *et al.*, “Modular bioink for 3D printing of biocompatible hydrogels: sol–gel polymerization of hybrid peptides and polymers,” *RSC Adv.*, vol. 7, no. 20, pp. 12231–12235, 2017, doi: 10.1039/C6RA28540F.
[129] E. Stankevicius *et al.*, “Fabrication of micro-tube arrays in photopolymer SZ2080 by using three different methods of a direct laser polymerization technique,” *J. Micromech. Microeng.*, vol. 22, no. 6, p. 065022, May 2012, doi: 10.1088/0960-1317/22/6/065022.
[130] D. T. Pham and C. Ji, “A study of recoating in stereolithography,” *Proceedings of the Institution of Mechanical Engineers, Part C: Journal of Mechanical Engineering Science*, vol. 217, no. 1, pp. 105–118, 2003, doi: 10.1243/095440603762554659.
[131] K. Renap and J. P. Kruth, “Recoating issues in stereolithography,” *Rapid Prototyping Journal*, vol. 1, no. 3, pp. 4–16, 1995, doi: 10.1108/13552549510094223.
[132] D. T. Pham and C. Ji, “A study of recoating in stereolithography,” *Proceedings of the Institution of Mechanical Engineers, Part C: Journal of Mechanical Engineering Science*, vol. 217, no. 1, pp. 105–118, 2003, doi: 10.1243/095440603762554659.
[133] J. Bachmann *et al.*, “Cavity vat photopolymerisation for additive manufacturing of polymer-composite 3D objects,” *Commun Mater*, vol. 2, no. 1, Art. no. 1, Oct. 2021, doi: 10.1038/s43246-021-00211-5.

[134] P. F. Jacobs, *Rapid Prototyping & Manufacturing: Fundamentals of StereoLithography*. American Society of Mechanical Engineers, 1992, p. 369.
[135] Jacobs P.F., *Stereolithography and other RP&M Technologies: from Rapid Prototyping to Rapid Tooling*. American Society of Mechanical Engineers, 1995.
[136] J. Bennett, "Measuring UV curing parameters of commercial photopolymers used in additive manufacturing," *Additive Manufacturing*, vol. 18, pp. 203–212, 2017, doi: 10.1016/j.addma.2017.10.009.
[137] T. F. Irzhak and V. I. Irzhak, "Critical conversion in polymerization processes," *Russ. Chem. Rev.*, vol. 79, no. 10, pp. 921–944, Dec. 2010, doi: 10.1070/RC2010v079n10ABEH004155.
[138] V. Irzhak, "Methods of description of the polycondensation kinetics and the structures of the polymers formed," *Russian Chemical Reviews*, vol. 66, p. 541, Oct. 2007, doi: 10.1070/RC1997v066n06ABEH000346.
[139] A. C. Uzcategui, A. Muralidharan, V. L. Ferguson, S. J. Bryant, and R. R. McLeod, "Understanding and Improving Mechanical Properties in 3D printed Parts Using a Dual-Cure Acrylate-Based Resin for Stereolithography," *Advanced Engineering Materials*, vol. 20, no. 12, p. 1800876, 2018, doi: 10.1002/adem.201800876.
[140] Y. Abouliatim, T. Chartier, P. Abelard, C. Chaput, and C. Delage, "Optical characterization of stereolithography alumina suspensions using the Kubelka–Munk model," *Journal of the European Ceramic Society*, vol. 29, no. 5, pp. 919–924, Mar. 2009, doi: 10.1016/j.jeurceramsoc.2008.07.008.
[141] V. Tomeckova and J. W. Halloran, "Cure depth for photopolymerization of ceramic suspensions," *Journal of the European Ceramic Society*, vol. 30, no. 15, pp. 3023–3033, 2010, doi: 10.1016/j.jeurceramsoc.2010.06.004.
[142] V. Tomeckova and J. W. Halloran, "Predictive models for the photopolymerization of ceramic suspensions," *Journal of the European Ceramic Society*, vol. 30, no. 14, pp. 2833–2840, Oct. 2010, doi: 10.1016/j.jeurceramsoc.2010.01.027.
[143] J. Tarabeux, V. Pateloup, P. Michaud, and T. Chartier, "Development of a numerical simulation model for predicting the curing of ceramic systems in the stereolithography process," *Journal of the European Ceramic Society*, vol. 38, no. 11, pp. 4089–4098, Sep. 2018, doi: 10.1016/j.jeurceramsoc.2018.03.052.
[144] V. Tomeckova and J. W. Halloran, "Critical energy for photopolymerization of ceramic suspensions in acrylate monomers," *Journal of the European Ceramic Society*, vol. 30, no. 16, pp. 3273–3282, 2010, doi: 10.1016/j.jeurceramsoc.2010.08.003.
[145] H. Li, Y. Qi, and J. T. Sheridan, "Three-dimensional extended nonlocal photopolymerization driven diffusion model Part II Photopolymerization and model development," *J. Opt. Soc. Am. B*, vol. 31, no. 11, p. 2648, Nov. 2014, doi: 10.1364/JOSAB.31.002648.
[146] A. S. Jariwala *et al.*, "Modeling effects of oxygen inhibition in mask-based stereolithography," *Rapid Prototyping Journal*, vol. 17, no. 3, pp. 168–175, Apr. 2011, doi: 10.1108/13552541111124734.
[147] M. M. Emami and D. W. Rosen, "An Improved Vat Photopolymerization Cure Model Demonstrates Photobleaching Effects," in *Solid Freeform Fabrication 2018: Proceedings of the 29th Annual International*, pp. 1940–1952. doi: http://dx.doi.org/10.26153/tsw/17195.
[148] N. B. Cramer, C. P. O'Brien, and C. N. Bowman, "Mechanisms, polymerization rate scaling, and oxygen inhibition with an ultra-rapid monovinyl urethane acrylate," *Polymer*, vol. 49, no. 22, pp. 4756–4761, Oct. 2008, doi: 10.1016/j.polymer.2008.08.051.
[149] Y. Tang, C. Henderson, J. Muzzy, and D. W. Rosen, "Stereolithography cure modelling and simulation," *IJMPT*, vol. 21, no. 4, p. 255, 2004, doi: 10.1504/IJMPT.2004.004941.

[150] M. B. Belgacem, S. Kamoun, M. Gargouri, K. D. H. Dorkenoo, A. Barsella, and L. Mager, "Light induced self-written waveguides interactions in photopolymer media," *Opt. Express, OE*, vol. 23, no. 16, pp. 20841–20848, Aug. 2015, doi: 10.1364/OE.23.020841.
[151] J. E. Elliott and C. N. Bowman, "Kinetics of Primary Cyclization Reactions in Cross-Linked Polymers: An Analytical and Numerical Approach to Heterogeneity in Network Formation," *Macromolecules*, vol. 32, no. 25, pp. 8621–8628, Dec. 1999, doi: 10.1021/ma990797i.
[152] J. E. Elliott, L. G. Lovell, and C. N. Bowman, "Primary cyclization in the polymerization of bis-GMA and TEGDMA: a modeling approach to understanding the cure of dental resins," *Dental Materials*, vol. 17, no. 3, pp. 221–229, May 2001, doi: 10.1016/S0109-5641(00)00075-0.
[153] J. W. Stansbury, "Cyclopolymerizable Monomers for Use in Dental Resin Composites," *J Dent Res*, vol. 69, no. 3, pp. 844–848, Mar. 1990, doi: 10.1177/00220345900690030201.
[154] W. V. Camp, H. Gao, F. E. D. Prez, and K. Matyjaszewski, "Effect of crosslinker multiplicity on the gel point in ATRP," *Journal of Polymer Science Part A: Polymer Chemistry*, vol. 48, no. 9, pp. 2016–2023, 2010, doi: https://doi.org/10.1002/pola.23970.
[155] G. A. O'Neil, M. B. Wisnudel, and J. M. Torkelson, "A Critical Experimental Examination of the Gel Effect in Free Radical Polymerization: Do Entanglements Cause Autoacceleration?," *Macromolecules*, vol. 29, no. 23, pp. 7477–7490, Jan. 1996, doi: 10.1021/ma9606263.
[156] J. H. Lee, R. K. Prud'homme, and I. A. Aksay, "Cure depth in photopolymerization: Experiments and theory," *Journal of Materials Research*, vol. 16, no. 12, pp. 3536–3544, 2001, doi: 10.1557/JMR.2001.0485.
[157] N. B. Cramer, C. P. O'Brien, and C. N. Bowman, "Mechanisms, polymerization rate scaling, and oxygen inhibition with an ultra-rapid monovinyl urethane acrylate," *Polymer*, vol. 49, no. 22, pp. 4756–4761, Oct. 2008, doi: 10.1016/j.polymer.2008.08.051.
[158] J. W. Wydra, N. B. Cramer, J. W. Stansbury, and C. N. Bowman, "The reciprocity law concerning light dose relationships applied to BisGMA/TEGDMA photopolymers: Theoretical analysis and experimental characterization," *Dental Materials*, vol. 30, no. 6, pp. 605–612, Jun. 2014, doi: 10.1016/j.dental.2014.02.021.
[159] W. Schnabel, *Polymers and Light*. Wiley, 2007, p. 382. doi: 10.1002/9783527611027.
[160] J. P. Fouassier and J. Lalevée, *Photoinitiators for Polymer Synthesis*. Weinheim, Germany: Wiley-VCH Verlag GmbH & Co. KGaA, 2012, p. 490. doi: 10.1002/9783527648245.
[161] J. P. Fouassier, X. Allonas, J. Laleve, and C. Dietlin, "Photoinitiators for Free Radical Polymerization Reactions," in *Photochemistry and Photophysics of Polymer Materials*, Hoboken, NJ, USA: John Wiley & Sons, Inc., 2010, pp. 351–419. doi: 10.1002/9780470594179.ch10.
[162] E. Andrzejewska, "Photopolymerization kinetics of multifunctional monomers," *Progress in Polymer Science*, vol. 26, no. 4, pp. 605–665, May 2001, doi: 10.1016/S0079-6700(01)00004-1.
[163] J. V. Crivello and E. Reichmanis, "Photopolymer materials and processes for advanced technologies," *Chemistry of Materials*, vol. 26, no. 1, pp. 533–548, 2014, doi: 10.1021/cm402262g.
[164] C. Decker and A. D. Jenkins, "Kinetic approach of oxygen inhibition in ultraviolet- and laser-induced polymerizations," *Macromolecules*, vol. 18, no. 6, pp. 1241–1244, Nov. 1985, doi: 10.1021/ma00148a034.
[165] J. Lalevée, H. Mokbel, and J.-P. Fouassier, "Recent Developments of Versatile Photoinitiating Systems for Cationic Ring Opening Polymerization Operating at Any Wavelengths and under Low Light Intensity Sources," *Molecules*, vol. 20, no. 4, pp. 7201–7221, Apr. 2015, doi: 10.3390/molecules20047201.

[166] M. D. Goodner and C. N. Bowman, “Modeling Primary Radical Termination and Its Effects on Autoacceleration in Photopolymerization Kinetics,” *Macromolecules*, vol. 32, no. 20, pp. 6552–6559, Oct. 1999, doi: 10.1021/ma9901947.
[167] J. V. Crivello, S. Holdcroft, and A. S. Hay, “Synergistic Effects in Hybrid Free Radical/Cationic Photopolymerizations,” *American Chemical Society, Polymer Preprints, Division of Polymer Chemistry*, vol. 49, no. 1, pp. 511–512, 2008, doi: 10.1002/pola.
[168] C. Decker, T. Nguyen Thi Viet, D. Decker, and E. Weber-Koehl, “UV-radiation curing of acrylate/epoxide systems,” *Polymer*, vol. 42, no. 13, pp. 5531–5541, Jun. 2001, doi: 10.1016/S0032-3861(01)00065-9.
[169] C. Decker, H. Le Xuan, and T. Nguyen Thi Viet, “Photocrosslinking of functionalized rubber. III. Polymerization of multifunctional monomers in epoxidized liquid natural rubber,” *Journal of Polymer Science, Part A: Polymer Chemistry*, vol. 34, no. 9, pp. 1771–1781, 1996, doi: 10.1002/(SICI)1099-0518(19960715)34:9<1771::AID-POLA15>3.0.CO;2-3.
[170] D. E. Karalekas and A. Agelopoulos, “On the use of stereolithography built photoelastic models for stress analysis investigations,” *Materials & Design*, vol. 27, no. 2, pp. 100–106, Jan. 2006, doi: 10.1016/j.matdes.2004.09.028.
[171] J. D. Curtis, S. D. Hanna, E. A. Patterson, and M. Taroni, “On the use of stereolithography for the manufacture of photoelastic models,” p. 15, 2003.
[172] B. Steinmann and A. Schulthess, “Liquid, radiation-curable composition, especially for stereolithography,” USOO5972563A, 1999
[173] B. Steinmann, J. Wolf, A. Schulthess, and M. Hunziker, “Photosensitive compositions,” US005476748A, 1995
[174] T. H. Pang, A. P. Melisaris, W. Renyi, and J. W. Fong, “Liquid radiation-curable composition especially for producing cured articles by stereolithography having high heat deflection temperatures,” US006100007A, 2000
[175] W. Renyi and T. H. Pang, “Liquid, radiation-curable composition, especially for producing flexible cured articles by stereolithography,” US 2002/0177073 A1, 2002
[176] C. M. Roland, “Interpenetrating Polymer Networks (IPN): Structure and Mechanical Behavior,” in *Encyclopedia of Polymeric Nanomaterials*, S. Kobayashi and K. Müllen, Eds. Berlin, Heidelberg: Springer Berlin Heidelberg, 2013, pp. 1–9. doi: 10.1007/978-3-642-36199-9_91-1.
[177] R. ; A. Adhikari H. ;. Alghamdi, M. N. ;. et al., *Micro and Nano- structured Interpenetrating Polymer Networks: From Design to Applications*. John Wiley & Sons, 2016, p. 425.
[178] T. Watanabe, A. Matsumura, Y. Haruta, and T. Ukachi, “Photo-curable resin composition and process for preparing resin-basedmold,” US5932625A, Aug. 03, 1999 Accessed: Mar. 21, 2021. [Online]. Available: https://patents.google.com/patent/US5932625A/en
[179] Y. K. Jung, K. Kuk, and O. H. Beak, “Ink compositions for 3d printing, 3d printer and method for controlling of the same,” WO2016108519A1, Jul. 07, 2016 Accessed: Mar. 21, 2021. [Online]. Available: https://patents.google.com/patent/WO2016108519A1/en
[180] J. V. Crivello, “Radical-promoted visible light photoinitiated cationic polymerization of epoxides,” *Journal of Macromolecular Science, Part A: Pure and Applied Chemistry*, vol. 46, no. 5, pp. 474–483, 2009, doi: 10.1080/10601320902797707.
[181] M. Faustini, L. Nicole, E. Ruiz-Hitzky, and C. Sanchez, “History of Organic–Inorganic Hybrid Materials: Prehistory, Art, Science, and Advanced Applications,” *Advanced Functional Materials*, vol. 28, no. 27, pp. 1–30, 2018, doi: 10.1002/adfm.201704158.
[182] C. Brinker and G. Scherer, “Sol-Gel Science: The Physics and Chemistry of Sol-Gel Processing,” *Advanced Materials*, vol. 3, no. 10, pp. 912–912, 1990, doi: 10.1186/1471-2105-8-444.

[183] D. M. Pickup, R. J. Newport, and J. C. Knowles, “Sol-gel phosphate-based glass for drug delivery applications,” *Journal of Biomaterials Applications*, vol. 26, no. 5, pp. 613–622, 2012, doi: 10.1177/0885328210380761.
[184] G. J. Owens *et al.*, “Sol-gel based materials for biomedical applications,” *Progress in Materials Science*, vol. 77, pp. 1–79, 2016, doi: 10.1016/j.pmatsci.2015.12.001.
[185] F. Foroutan, “Sol-Gel Synthesis of Phosphate-Based Glasses for Biomedical Applications,” 2015.
[186] M. Dressler *et al.*, “Sol-gel preparation of calcium titanium phosphate: Viscosity, thermal properties and solubility,” *Journal of Sol-Gel Science and Technology*, vol. 62, no. 3, pp. 273–280, 2012, doi: 10.1007/s10971-011-2653-y.
[187] V. Farano *et al.*, “Dissolution behaviour of a novel sol–gel derived phosphate glass,” *Dental Materials*, vol. 33, no. October, pp. e29–e30, 2017, doi: 10.1016/j.dental.2017.08.058.
[188] F. Foroutan *et al.*, “Novel sol–gel preparation of (P2O5)0.4–(CaO)0.25–(Na2O)X–(TiO2)(0.35−X)bioresorbable glasses (X = 0.05, 0.1, and 0.15),” *Journal of Sol-Gel Science and Technology*, vol. 73, no. 2, pp. 434–442, 2014, doi: 10.1007/s10971-014-3555-6.
[189] D. Carta, D. M. Pickup, J. C. Knowles, M. E. Smith, and R. J. Newport, “Sol–gel synthesis of the P2O5–CaO–Na2O–SiO2 system as a novel bioresorbable glass,” *Journal of Materials Chemistry*, vol. 15, no. 21, p. 2134, 2005, doi: 10.1039/b414885a.
[190] P. Q. Franco, C. F. C. João, J. C. Silva, and J. P. Borges, “Electrospun hydroxyapatite fibers from a simple sol-gel system,” *Materials Letters*, vol. 67, no. 1, pp. 233–236, 2012, doi: 10.1016/j.matlet.2011.09.090.
[191] K. Vojisavljević, P. Chevreux, J. Jouin, and B. Malič, “Characterization of the alkoxide-based sol-gel derived La9.33Si6O26 powder and ceramic.,” *Acta chimica Slovenica*, vol. 61, no. 3, pp. 530–41, 2014, doi: 10.1016/S1002-0721(10)60326-2.
[192] O. F. Göbel, M. Nedelcu, and U. Steiner, “Soft lithography of ceramic patterns,” *Advanced Functional Materials*, vol. 17, no. 7, pp. 1131–1136, 2007, doi: 10.1002/adfm.200600783.
[193] S. J. Kwon, J. H. Park, and J. G. Park, “Selective growth of ZnO nanorods by patterning of sol-gel-derived thin film,” *Journal of Electroceramics*, vol. 17, no. 2–4, pp. 455–459, 2006, doi: 10.1007/s10832-006-5412-7.
[194] A. Ershad-Langroudi, H. Abdollahi, and A. Rahimi, “Mechanical properties of sol–gel prepared nanocomposite coatings in the presence of titania and alumina-derived nanoparticles,” *Plastics, Rubber and Composites*, vol. 46, no. 1, pp. 25–34, 2017, doi: 10.1080/14658011.2016.1245821.
[195] S. Saeed, R. M. Al Soubaihi, L. S. White, M. F. Bertino, and K. M. Saoud, “Rapid fabrication of cross-linked silica aerogel by laser induced gelation,” *Microporous and Mesoporous Materials*, vol. 221, pp. 245–252, 2016, doi: 10.1016/j.micromeso.2015.09.012.
[196] S. Messaddeq and S. Pulcinelli, “Microstructure and corrosion resistance of inorganic–organic (ZrO 2–PMMA) hybrid coating on stainless steel,” *Journal of non-crystalline solids*, vol. 247, no. 1–3, pp. 164–170, 1999, doi: 10.1016/S0022-3093(99)00058-7.
[197] S. A. Omar, J. Ballarre, and S. M. Ceré, “Electrochimica Acta Protection and functionalization of AISI 316 L stainless steel for orthopedic implants : hybrid coating and sol gel glasses by spray to promote bioactivity,” *Electrochimica Acta*, vol. 203, pp. 309–315, 2016, doi: 10.1016/j.electacta.2016.01.051.
[198] V. G. Kessler, *Handbook of Sol-Gel Science and Technology*. 2017. doi: 10.1007/978-3-319-19454-7.
[199] A. A. Issa and A. S. Luyt, “Kinetics of Alkoxysilanes and Organoalkoxysilanes Polymerization: A Review,” *Polymers*, vol. 11, no. 3, Art. no. 3, Mar. 2019, doi: 10.3390/polym11030537.

[200] V. G. Kessler, *Handbook of Sol-Gel Science and Technology*. 2017. doi: 10.1007/978-3-319-19454-7.
[201] P. Albert, G. Lohden, C. Gall, and B. Borup, “Ormocers, method for their production and their use,” 2009023471, 2001 doi: 10.1037/t24245-000.
[202] C. Sanchez, P. Belleville, M. Popall, and L. Nicole, “Applications of advanced hybrid organic–inorganic nanomaterials: from laboratory to market,” *Chemical Society Reviews*, vol. 40, no. 2, pp. 696–696, 2011, doi: 10.1039/c0cs00136h.
[203] J. Wang, T. J. Shi, and X. C. Jiang, “Synthesis and characterization of core-shell ZrO2/PAAEM/PS nanoparticles,” *Nanoscale Research Letters*, vol. 4, no. 3, pp. 240–246, 2009, doi: 10.1007/s11671-008-9232-3.
[204] U. Posset, F. Institut, and D. W, “Radiation curing of hybrid polymer coatings,” vol. 89, no. March, pp. 41–48, 2006.
[205] Y. Mencelog, “The novel use of organo alkoxy silane for the synthesis of organic – inorganic hybrid coatings,” vol. 352, pp. 2143–2151, 2006, doi: 10.1016/j.jnoncrysol.2006.02.029.
[206] C. Belon, M. Schmitt, S. Bistac, C. Croutxé-barghorn, and A. Chemtob, “Applied Surface Science Friction and wear properties of hybrid sol – gel nanocomposite coatings against steel : Influence of their intrinsic properties,” *Applied Surface Science*, vol. 257, no. 15, pp. 6618–6625, 2011, doi: 10.1016/j.apsusc.2011.02.088.
[207] M. Sangermano, E. Amerio, A. Priola, A. Di Gianni, and B. Voit, “Preparation and Characterization of Acrylic Resin / Titania Hybrid Nanocomposite Coatings by Photopolymerization and Sol – Gel Process,” 2006, doi: 10.1002/app.24707.
[208] R. Nagarjuna, S. Challagulla, P. Sahu, S. Roy, and R. Ganesan, “Polymerizable sol–gel synthesis of nano-crystalline WO3and its photocatalytic Cr(VI) reduction under visible light,” *Advanced Powder Technology*, vol. 28, no. 12, pp. 3265–3273, 2017, doi: 10.1016/j.apt.2017.09.030.
[209] S. Challagulla, R. Nagarjuna, S. Roy, and R. Ganesan, “Scalable Free-Radical Polymerization Based Sol-Gel Synthesis of $SrTiO_3$ and its Photocatalytic Activity,” *ChemistrySelect*, vol. 2, no. 17, pp. 4836–4842, 2017, doi: 10.1002/slct.201700570.
[210] D. P. Dworak and M. D. Soucek, “Protective space coatings : a ceramer approach for nanoscale materials,” vol. 47, pp. 448–457, 2003, doi: 10.1016/S0300-9440(03)00135-8.
[211] P. Coudray, P. Etienne, and Y. Moreau, “Integrated optics based on organo-mineral materials,” vol. 3, no. 2000, pp. 331–337, 2001.
[212] R. Ganesan *et al.*, “Direct nanoimprinting of metal oxides by in situ thermal co-polymerization of their methacrylates,” *Journal of Materials Chemistry*, vol. 21, no. 12, p. 4484, 2011, doi: 10.1039/c0jm04105j.
[213] S. S. Dinachali, M. S. M. Saifullah, R. Ganesan, E. S. Thian, and C. He, “A universal scheme for patterning of oxides via thermal nanoimprint lithography,” *Advanced Functional Materials*, vol. 23, no. 17, pp. 2201–2211, 2013, doi: 10.1002/adfm.201202577.
[214] R. Ganesan, J. Dumond, M. S. M. Saifullah, S. H. Lim, H. Hussain, and H. Y. Low, “Direct patterning of TiO \n 2 using step-and-flash imprint lithography,” *ACS Nano*, vol. 6, no. 2, pp. 1494–1502, 2012, doi: 10.1021/nn204405k.
[215] R. Ganesan *et al.*, “Direct nanoimprint lithography of Al 2O 3 using a chelated monomer-based precursor,” *Nanotechnology*, vol. 23, no. 31, 2012, doi: 10.1088/0957-4484/23/31/315304.
[216] R. Nagarjuna, M. S. M. Saifullah, and R. Ganesan, “Oxygen insensitive thiol–ene photo-click chemistry for direct imprint lithography of oxides,” *RSC Advances*, vol. 8, no. 21, pp. 11403–11411, 2018, doi: 10.1039/C8RA01688G.

[217] S. H. Mir, L. A. Nagahara, T. Thundat, P. Mokarian-Tabari, H. Furukawa, and A. Khosla, "Review—Organic-Inorganic Hybrid Functional Materials: An Integrated Platform for Applied Technologies," *Journal of The Electrochemical Society*, vol. 165, no. 8, pp. B3137–B3156, 2018, doi: 10.1149/2.0191808jes.

[218] M. Faustini, D. Grosso, C. Boissière, R. Backov, and C. Sanchez, "'integrative sol-gel chemistry': A nanofoundry for materials science," *Journal of Sol-Gel Science and Technology*, vol. 70, no. 2, pp. 216–226, 2014, doi: 10.1007/s10971-014-3321-9.

[219] L. Nicole, C. Laberty-Robert, L. Rozes, and C. Sanchez, "Hybrid materials science: A promised land for the integrative design of multifunctional materials," *Nanoscale*, vol. 6, no. 12, pp. 6267–6292, 2014, doi: 10.1039/c4nr01788a.

[220] L. Nicole, L. Rozes, and C. Sanchez, "Integrative approaches to hybrid multifunctional materials: from multidisciplinary research to applied technologies.," *Advanced materials (Deerfield Beach, Fla.)*, vol. 22, no. 29, pp. 3208–3214, 2010, doi: 10.1002/adma.201000231.

[221] A. Chiappone *et al.*, "3D Printed PEG-Based Hybrid Nanocomposites Obtained by Sol–Gel Technique," *ACS Applied Materials & Interfaces*, vol. 8, no. 8, pp. 5627–5633, 2016, doi: 10.1021/acsami.5b12578.

[222] P. Judeinstein and C. Sanchez, "Hybrid organic-inorganic materials : a land of multidisciplinarity Chemistry : Synthesis of Hybrid Materials," vol. 6, no. 4, pp. 511–525, 1996.

[223] R. Lichtenberger and U. Schubert, "Chemical modification of aluminium alkoxides for sol-gel processing," *Journal of Materials Chemistry*, vol. 20, no. 42, pp. 9287–9296, 2010, doi: 10.1039/c0jm00993h.

[224] F. Ribot and C. Sanchez, "Comments on Inorganic Chemistry : A Journal of Critical Discussion of the Current Literature Organically Functionalized Metallic Oxo-Clusters : Structurally Well-Defined Nanobuilding Blocks for the Design of Hybrid Organic- Inorganic Materials," no. January 2014, pp. 37–41, 1999, doi: 10.1080/02603599908021449.

[225] C. Sanchez, K. J. Shea, and S. Kitagawa, "Hybrid materials themed issue," *Chemical Society reviews*, vol. 40, no. 2, pp. 473–497, 2011, doi: 10.1039/c0cs00076k.

[226] K. Velez, J. F. Quinson, and B. Fenet, "Modification study of aluminum sec-butoxide by acrylic acid," *Journal of Sol-Gel Science and Technology*, vol. 16, no. 3, pp. 201–208, 1999, doi: 10.1023/A:1008767218134.

[227] J. Méndez-Vivar, P. Bosch, V. H. Lara, and R. Mendoza-Serna, "The role of 2-(methacryloyloxy) ethyl acetoacetate in the polymerization of hybrid multicomponent (Si, Ti, Zr) sols of hybrid multicomponent (Si, Ti, Zr) sols," *Journal of Sol-Gel Science and Technology*, vol. 25, no. 3, pp. 249–254, 2002, doi: 10.1023/A:1020216229397.

[228] R. Lichtenberger, M. Puchberger, S. O. Baumann, and U. Schubert, "Modification of aluminum alkoxides with β-ketoesters: New insights into formation, structure and stability," *Journal of Sol-Gel Science and Technology*, vol. 50, no. 2, pp. 130–140, 2009, doi: 10.1007/s10971-008-1890-1.

[229] Y. Gotoh, Y. Ohkoshi, and M. Nagura, "Preparation and Viscoelastic Behavior of (Meth)acrylate Ionomers Crosslinked by Titanium(IV), Zirconium(IV) and Niobium(V) Ions," *Polymer Journal*, vol. 36, no. 3, pp. 255–260, 2004, doi: 10.1295/polymj.36.255.

[230] S. H. Lim, M. S. M. Saifullah, H. Hussain, W. W. Loh, and H. Y. Low, "Direct imprinting of high resolution TiO2 nanostructures," *Nanotechnology*, vol. 21, no. 28, 2010, doi: 10.1088/0957-4484/21/28/285303.

[231] P. Stoch, P. Goj, A. Wajda, and A. Stoch, "Alternative insight into aluminium-phosphate glass network from ab initio molecular dynamics simulations," *Ceramics International*, vol. 47, no. 2, pp. 1891–1902, Jan. 2021, doi: 10.1016/j.ceramint.2020.09.018.

[232] Y. Li, H.-Y. Li, K.-C. Chang, H.-M. Lin, and C.-M. Wang, “Recent developments in organic–inorganic hybrid metal phosphates and phosphites,” *Dalton Trans.*, vol. 50, no. 29, pp. 10014–10019, 2021, doi: 10.1039/D1DT01016F.
[233] D. Carta, D. M. Pickup, J. C. Knowles, M. E. Smith, and R. J. Newport, “Sol–gel synthesis of the P2O5–CaO–Na2O–SiO2 system as a novel bioresorbable glass,” *Journal of Materials Chemistry*, vol. 15, no. 21, pp. 2134–2134, 2005, doi: 10.1039/b414885a.
[234] P. H. Mutin and G. Guerrero, “Hybrid materials from organophosphorus coupling molecules,” *Journal of Materials Chemistry*, vol. 15, pp. 3761–3768, 2005, doi: 10.1039/b505422b.
[235] P. H. Mutin and A. Vioux, “Nonhydrolytic Processing of Oxide-Based Materials: Simple Routes to Control Homogeneity, Morphology, and Nanostructure,” *Chemistry of Materials*, vol. 21, no. 4, pp. 582–596, Feb. 2009, doi: 10.1021/cm802348c.
[236] S. S. Dinachali, M. S. M. Saifullah, R. Ganesan, E. S. Thian, and C. He, “A Universal Scheme for Patterning of Oxides via Thermal Nanoimprint Lithography,” *Advanced Functional Materials*, vol. 23, no. 17, pp. 2201–2211, May 2013, doi: 10.1002/adfm.201202577.
[237] M. Guglielmi and G. Carturan, “Precursors for sol-gel preparations,” *Journal of Non-Crystalline Solids*, vol. 100, no. 1–3, pp. 16–30, 1988, doi: 10.1016/0022-3093(88)90004-X.
[238] K. Velez, J. F. Quinson, and B. Fenet, “Modification study of aluminum sec-butoxide by acrylic acid,” *Journal of Sol-Gel Science and Technology*, vol. 16, no. 3, pp. 201–208, 1999, doi: 10.1023/A:1008767218134.
[239] U. Schubert, E. Arpac, W. Glaubitt, A. Helmerich, and C. Chau, “Primary hydrolysis products of methacrylate-modified titanium and zirconium alkoxides,” *Chem. Mater.*, vol. 4, no. 2, pp. 291–295, Mar. 1992, doi: 10.1021/cm00020a014.

ANNEX A. SUPPORTING INFORMATION OF CHAPTER 1. PREPARATION AND STRUCTURAL CHARACTERIZATION OF NEW PHOTOPOLYMERIZABLE TRANSPARENT ALUMINUM-PHOSPHATE HYBRID MATERIALS AS RESINS FOR 3D PRINTING

Table S11: Mass of reactants weighted for a 10 g batch of each composition. 0.1 g of TPO was added afterwards.

Al/(Al+P) molar ratio (%)	HEMA (g)	HEMA-P (g)	Al(MAEAA)2 (g)
0	5	5	0
10	5	3.583	1.417
25	5	2.287	2.713
40	5	1.482	3.514
50	5	1.097	3.903

Table S12: Concentration of reactants and Ethyl Methacrylate (EtM) groups for 10 g of each composition.

Al/(Al+P) molar ratio (%)	HEMA (mol)	HEMA-P (mol)	Al(MAEAA)2 (mol)	EtM groups (mol)
0	0.049	0.026	0	0.070
10	0.049	0.019	0.002	0.068
25	0.049	0.012	0.004	0.066
40	0.049	0.008	0.005	0.065
50	0.049	0.006	0.006	0.065

Number of EtM groups is calculated from reactants using the following stoichiometry: 1/1 (EtM/HEMA), 0.8/1(EtM/HEMA-P) and 2/1(EtM/Al(MAEAA)$_2$). EtM Molar Concentration in the samples is calculated using the equation:

$$EtM(\%\, mol) = \frac{Total\ EtM}{Total\ EtM + n_{HEMA-P} + n_{Al(MAEAA)2}}$$

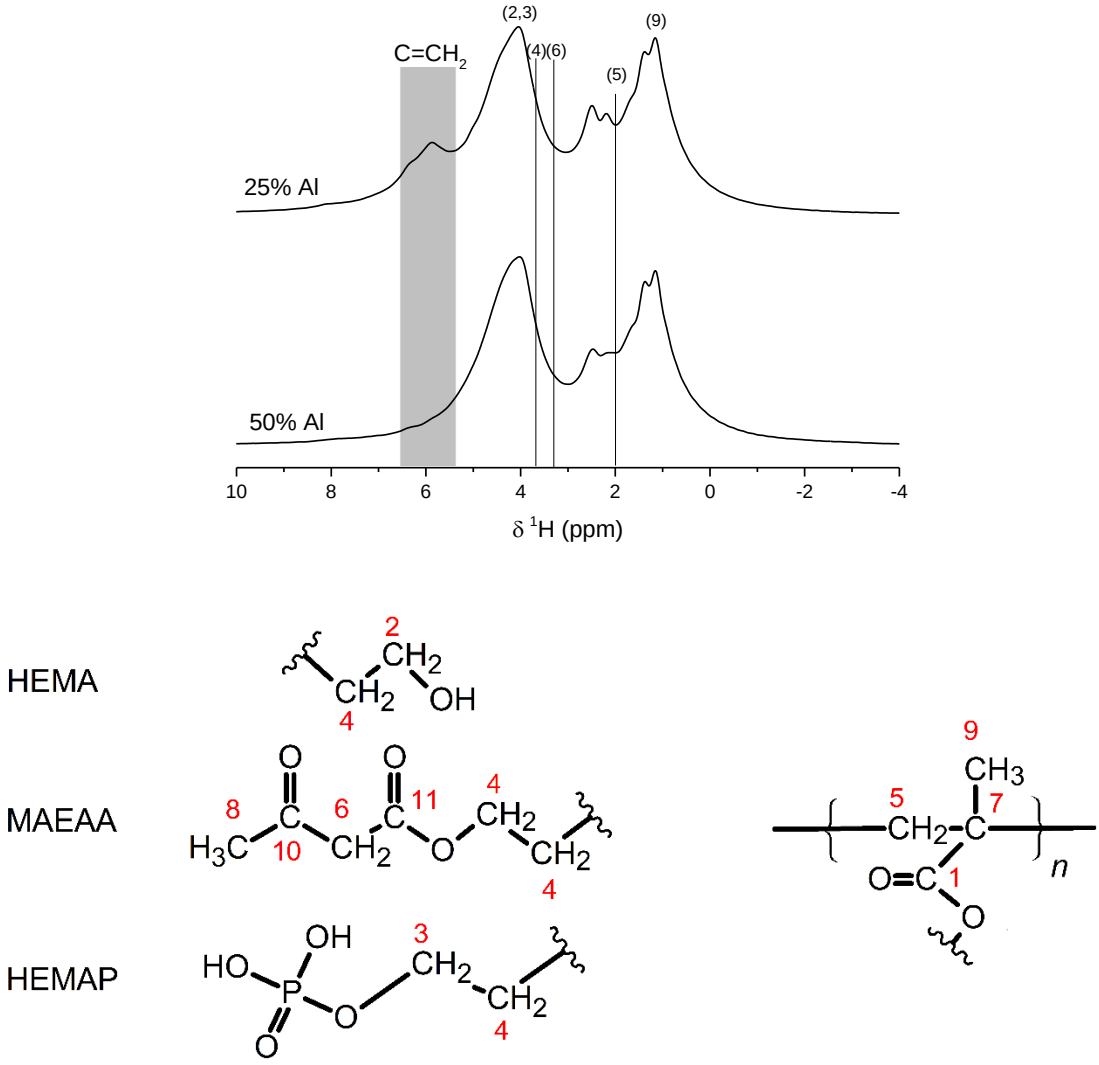

Figure S1. ^{1}H MAS NMR spectra and structural assignment for samples containing 25 and 50 % Al/(P+Al) at 60 kHz.

The ^{1}H MAS spectrum, on Figure , shows broad proton signals associated to unsaturated carbons. Signal identification was assisted by ^{13}C-^{1}H CP-HETCOR spectra measured(moles Al)× he on 25% Al/(Al+P) sample, shown in Figure S, with:150 µs and 500 µs contact times. Similar results were obtained for samples with x = Al/(Al+P) = 50%, therefore they are not presented here. Based on the cross-peaks, we can attribute the following proton signals: (I) 1 ppm: methyl groups from polymerized methacrylate substructure (**H9**); (II) 2 ppm: CH_2 within the polymeric chain (**H5**); (III) 3.7

and 4.0 ppm: CH_2 from ethyl ester group (**H2, H3**) and (**H4**), respectively; (IV) 3.3 ppm: (**H6**) from MAEAA. With small contact time (150 μs), the observed cross-peaks are associated with polarization transfer involving directly bonded H atoms only, and (I), (II) and (III) ^{1}H-^{13}C correlation are observable, although in cases (III) and (II) the ^{1}H-^{13}C dipolar interactions are weakened owing to CH_3 and CH_2 rotational motion. With longer contact time (500 μs), polarization transfer through space results in higher signal to noise ratios and in longer-range correlations. Appreciable changes occur for 500 μs contact time, with stronger ^{1}H-^{13}C correlation from (I) and (II) cross-peaks and observation of correlations involving IV. Quaternary carbon (45 ppm) cross-peak with 1.6 ppm proton signal results from cross-polarization with both methyl groups (1 ppm) (**C7-H9**) and polymeric chain CH_2(2 ppm) (**C7-H5**). In the ^{1}H MAS spectrum, $C=CH_2$ signals at 6 ppm are also observed from unpolymerized methacrylate.

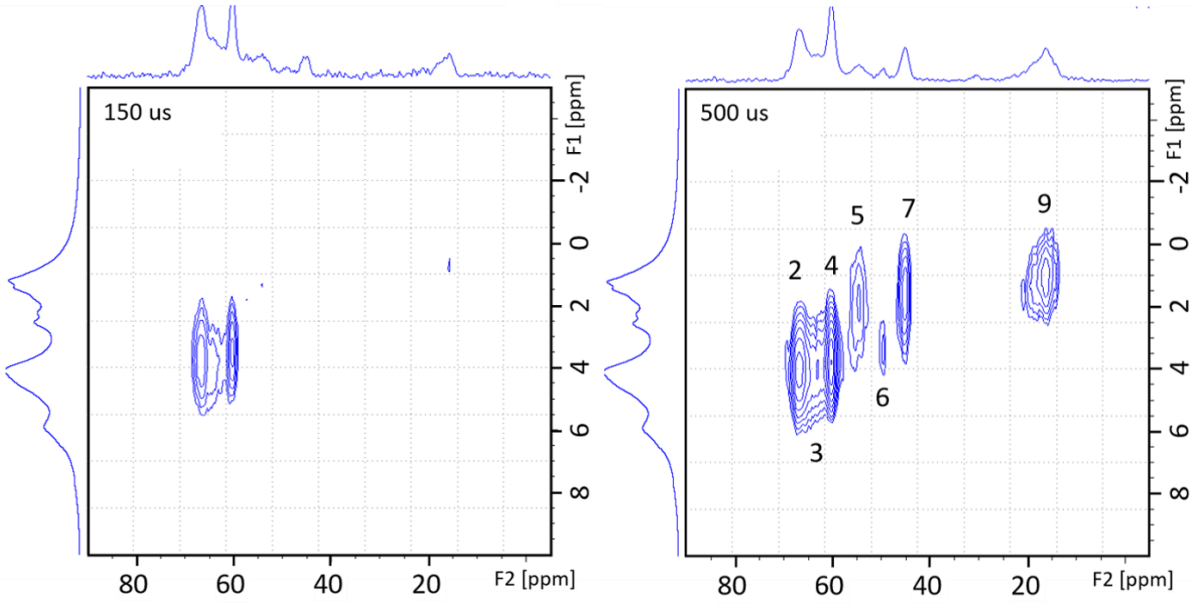

Figure S2. $^{13}C\{^{1}H\}$ HETCOR spectra for a sample with x = Al/(Al+P) = 25% with 150 μs and 500 μs contact time.

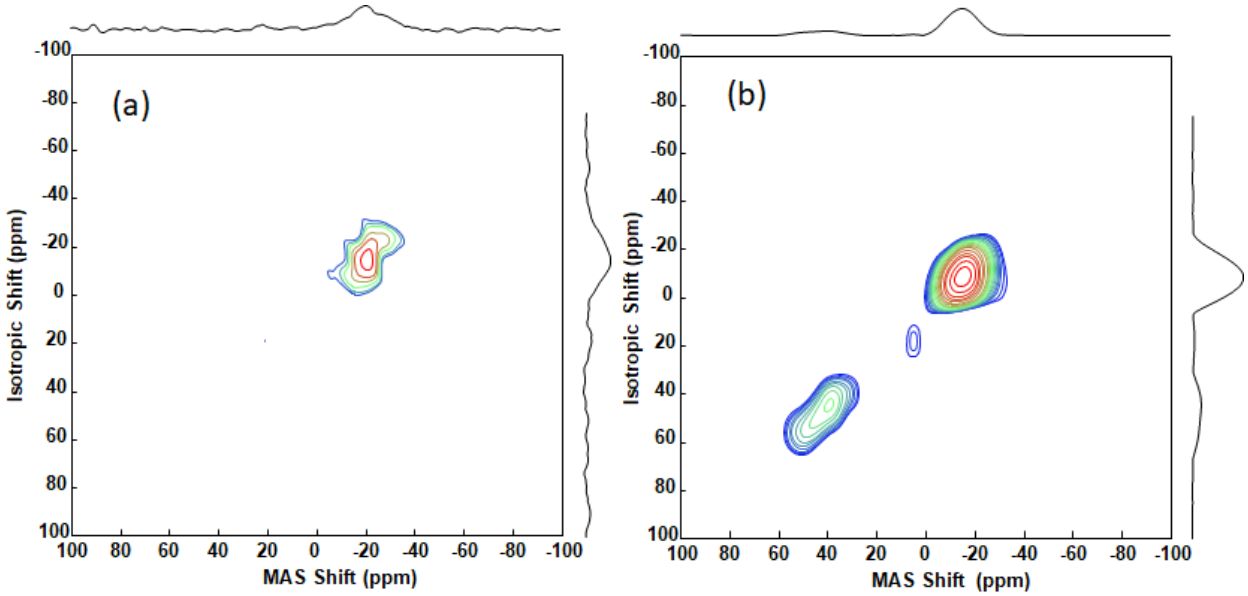

Figure S3. ^{27}Al TQMAS NMR spectra of the samples with x =Al/(Al+P) = 10% (a) and 40% (b).

ANNEX B. SUPPORTING INFORMATION OF CHAPTER 2. UNDERSTANDING THE MICROSTRUCTURE CONNECTIVITY IN PHOTOPOLYMERIZABLE ALUMINUM-PHOSPHATE-SILICATE SOL–GEL HYBRID MATERIALS FOR ADDITIVE MANUFACTURING

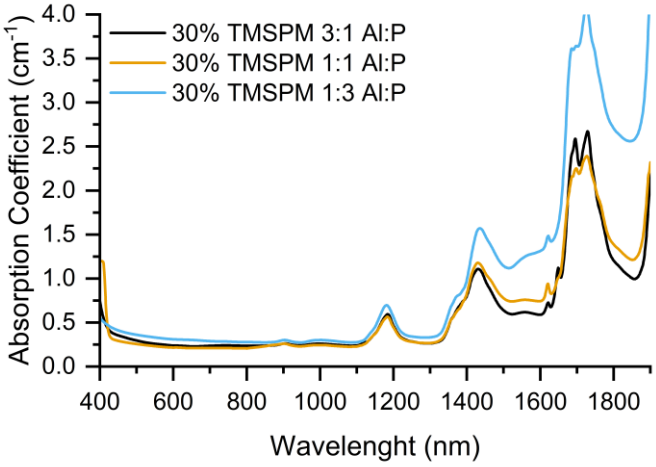

Figure S1. Absorption spectra from 400 to 1900 nm for hybrid samples containing 30% TMSPM 1:1, 1:3 and 3:1 Al:P ratio.

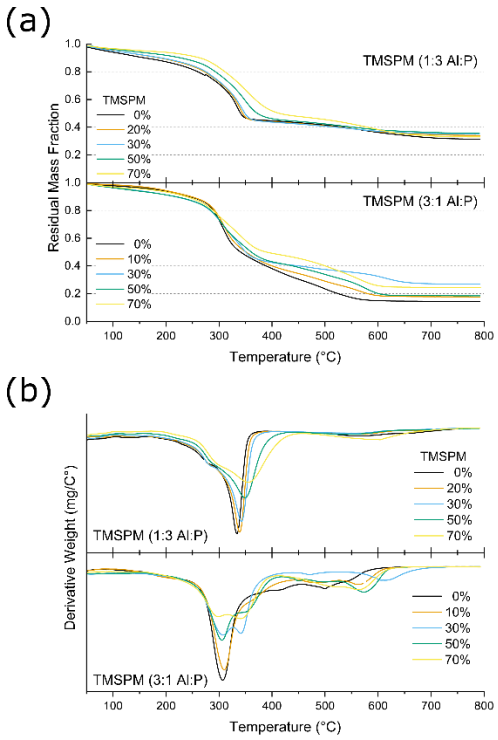

Figure S2. (a) Thermogravimetric (TGA) and (b) Differential Thermogravimetric Analysis (DTG) of TMSPM 3:1 and 1:3 Al:P hybrid materials with different concentration for TMSPM.

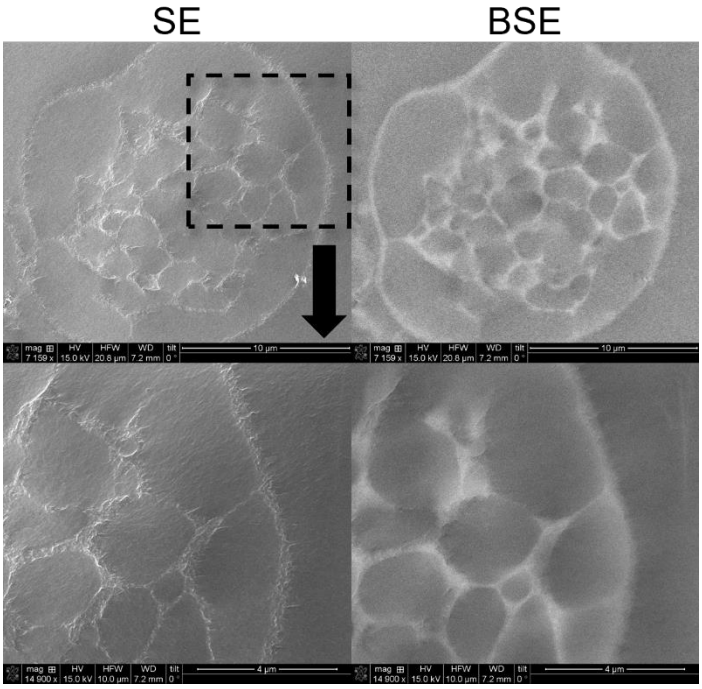

Figure S3. 70% TMSPM (1:3 Al:P) heterogeneities observed by SE and BSE imaging.

Table S1. Relative Si/(P+Al+Si) atomic composition and Al/(Al+P) atomic ratio according to Wavelength Dispersive Spectroscopy (WDS) analysis of 0, 30% and 70% TMSPM 1:3 and 3:1 Al:P hybrid materials.

Nominal Composition	Measured	
	at. Si (%)	Al/(P+Al) (%)
0% TMSPM + (1:3 Al:P)	0	27.1±1.1
30% TMSPM + (1:3 Al:P)	30.8±0.8	25.8±0.8
70% TMSPM + (1:3 Al:P)	78.7±5.0	24.0±2.0
0% TMSPM + (3:1 Al:P)	0	73.6±2.4
30% TMSPM + (3:1 Al:P)	31.4±0.6	73.0±2.4
70% TMSPM + (3:1 Al:P)	71.1±1.5	74.6±2.3

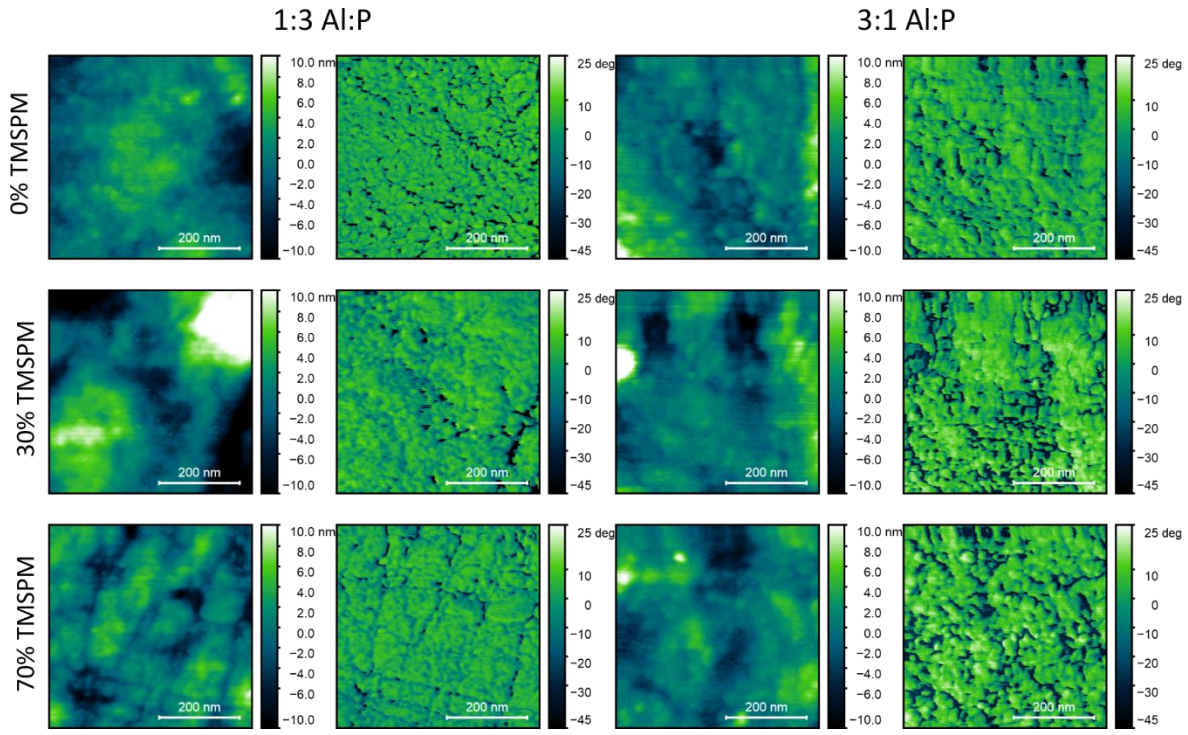

Figure S4. Phase-contrast and topography map of TMSPM 3:1 and 1:3 Al:P hybrid materials with 0%, 30% and 70% TMSPM.

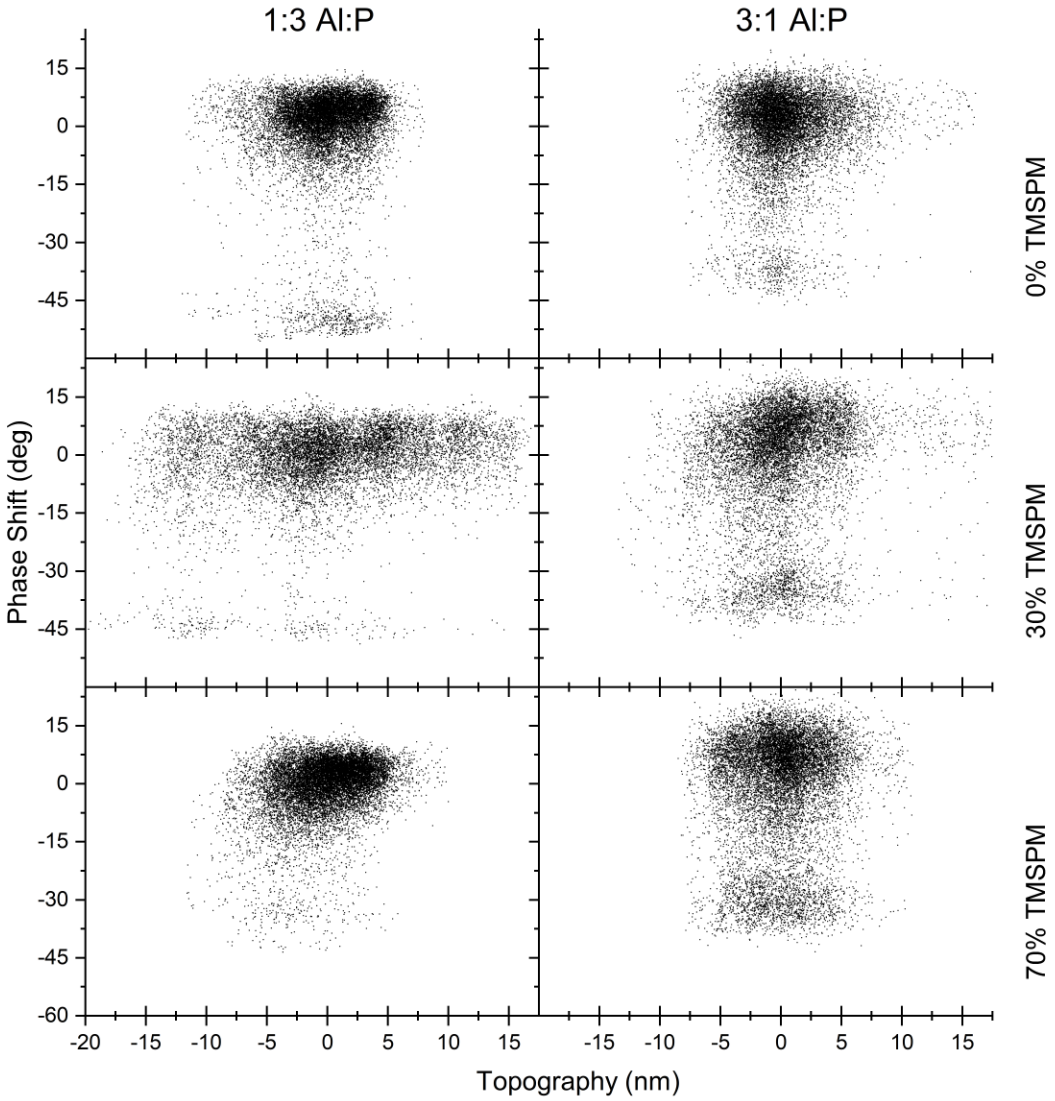

Figure S5. Phase-shift and topography relation plots of TMSPM 3:1 and 1:3 Al:P hybrid materials with 0%, 30% and 70% TMSPM.

Table S2. Deconvolution parameters for TMSPM (1:3 Al:P) compositions ^{31}P-MAS spectrum.

Al:P ratio	**1:3**		**3:1**	
% TMSPM	Position (ppm)	Relative Integrated Area (%)	Position (ppm)	Relative Integrated Area (%)
70	-0.2	5.4	-1.4	0.4
	-4.8	15.2	-5.7	6.8
	-12.6	56.2	-13.3	71.0
	-19.9	23.2	-21.7	21.8

60	-0.2	5.8	-1.4	0.5
	-4.8	15.2	-5.6	6.2
	-12.6	62.3	-12.9	68.2
	-20.0	16.7	-21.5	25.1
50	-0.2	5.6	-1.4	0.1
	-4.9	15.6	-5.5	7.7
	-12.6	64.6	-12.8	63.5
	-20.0	14.2	-21.0	28.7
40	-0.1	5.7	-1.4	0.1
	-4.9	16.9	-5.3	7.7
	-12.6	65.2	-12.2	59.5
	-20.0	12.3	-20.1	32.7
30	0.0	5.0	-1.2	0.5
	-4.8	17.0	-5.2	6.2
	-12.6	67.1	-11.9	57.4
	-20.0	10.8	-19.8	35.9
20	-0.1	5.4	-1.4	1.2
	-5.0	18.5	-5.2	6.7
	-12.7	65.4	-11.6	58.1
	-20.0	10.7	-19.3	34.0
10	-0.2	4.6	-1.7	2.0
	-5.0	17.1	-5.9	10.6
	-12.7	71.0	-11.8	55.2
	-20.1	7.4	-19.2	32.2
0			-1.6	2.3
			-5.3	8.4
			-11.1	55.1
			-18.3	34.3

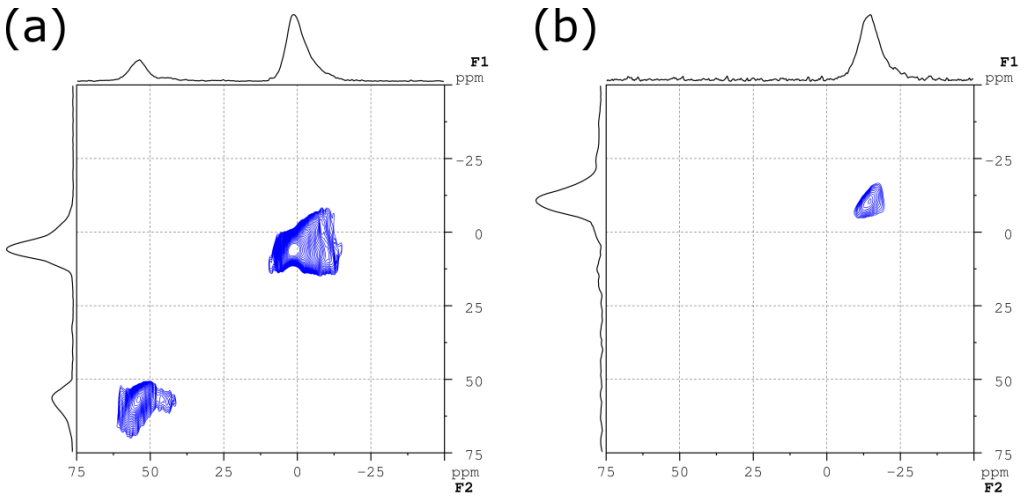

Figure S6. ^{27}Al TQMAS spectrum of 70% TMSPM 3:1 (a) and 1:3 (b) Al:P hybrid materials.

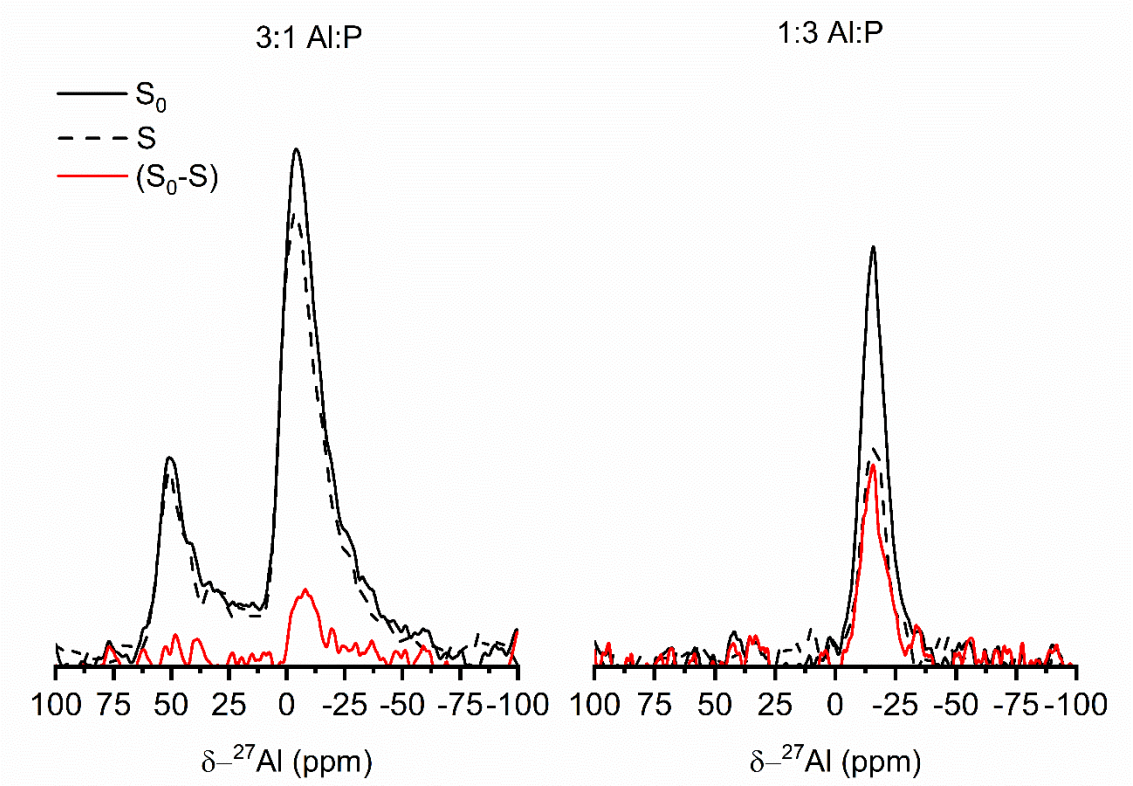

Figure S7. ^{27}Al{^{31}P} REDOR MAS curve of 70%TMSPM 1:3 and 3:1 Al:P compositions at 0.857 ms evolution time.

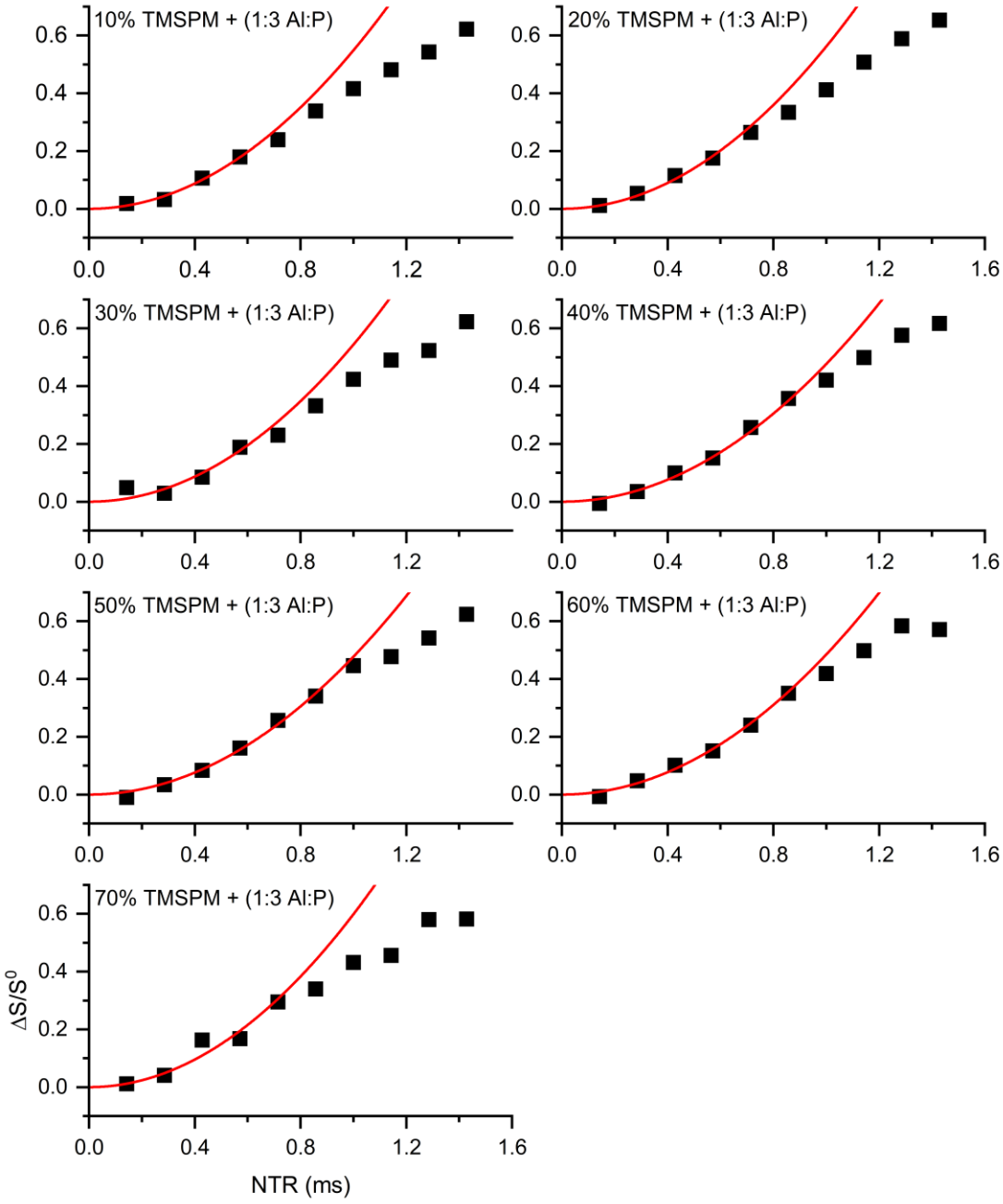

Figure S8. $^{27}Al\{^{31}P\}$ REDOR MAS curve and quadratic fitting for TMSPM 1:3 Al:P compositions with TMSPM concentration ranging from 10% to 70%.

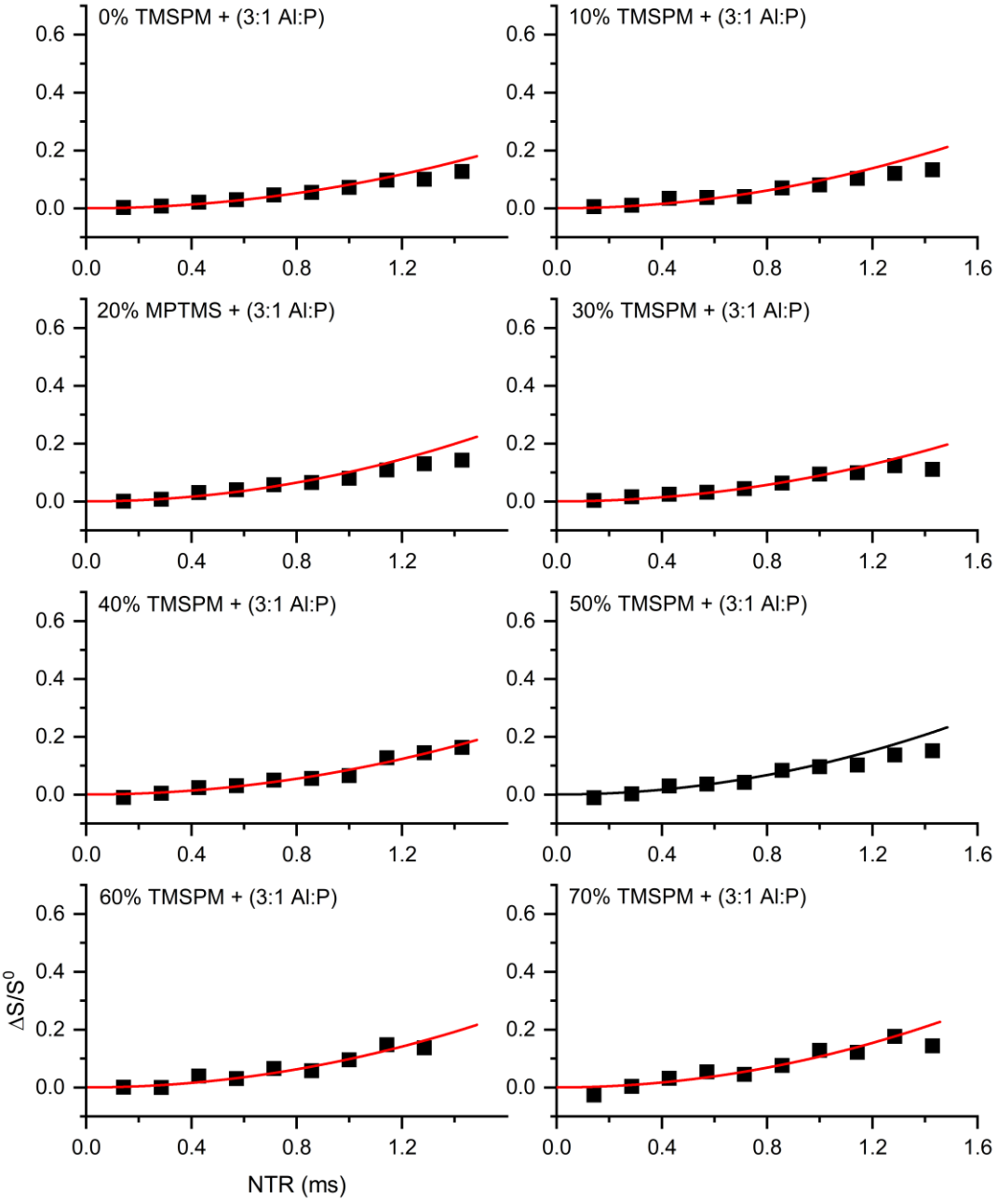

Figure S9. $^{27}Al\{^{31}P\}$ REDOR MAS curve and quadratic fitting for TMSPM 3:1 Al:P compositions with TMSPM concentration ranging from 0% to 70%.

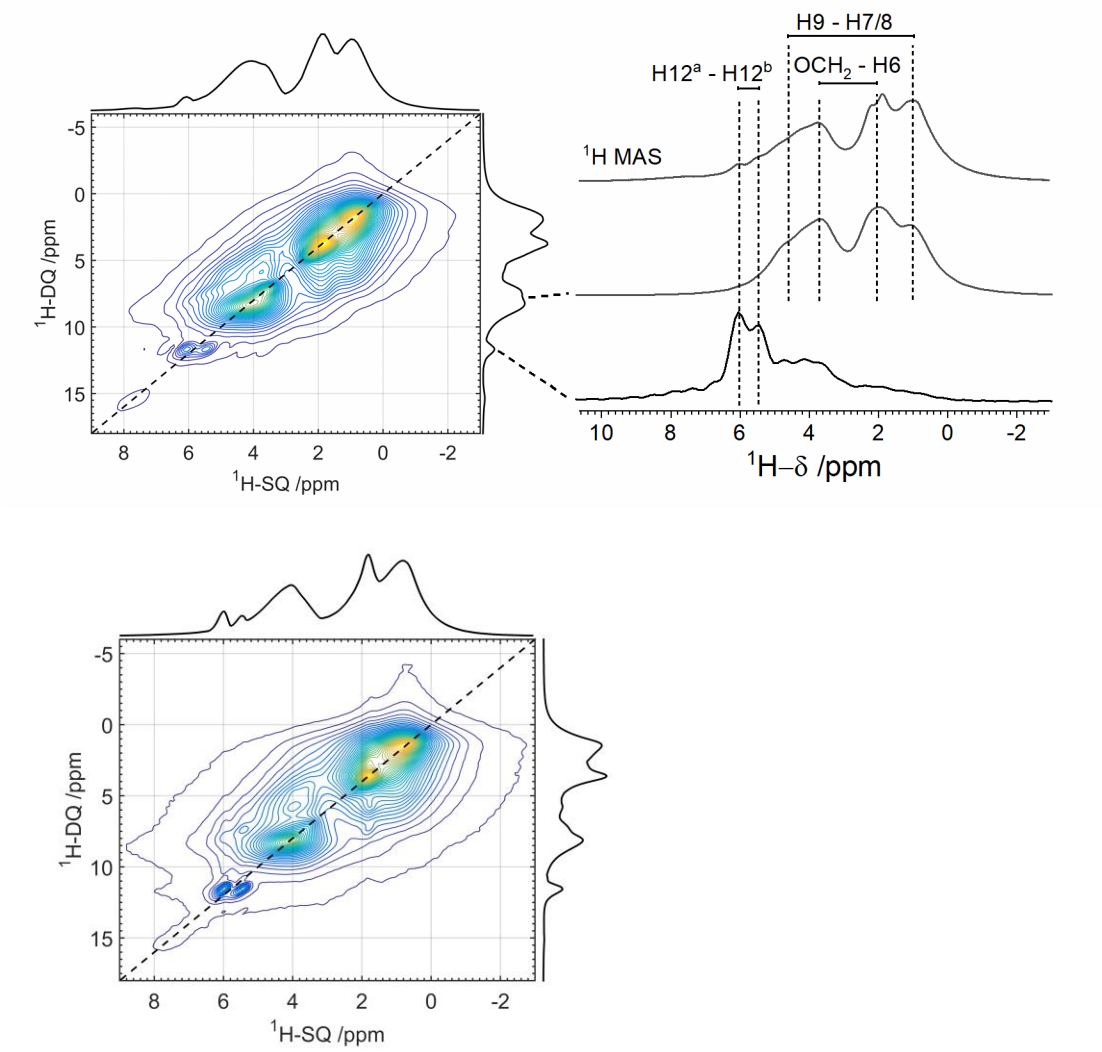

Figure S10. Left: 2D ^{1}H DQ-SQ correlation spectrum for of 50% TMSPM 3:1 Al:P (top) and 70% TMSPM 1:3 Al:P (bottom) hybrids, measured under 60 kHz MAS using $R14_4^5$ symmetry-based homonuclear recoupling and no homonuclear decoupling during DQ evolution. The dashed line indicates the 2δ-δ DQ-SQ diagonal. Right: Traces of the 2D spectrum on the left showing the observed DQ-SQ correlations for the 50% TMSPM 3:1 Al:P sample. The ^{1}H MAS spectrum acquired with direct excitation is also shown for the sake of comparison. The spectrum shows DQ-SQ correlation between the peaks at 5.5 and 6.1 ppm corresponding to the non-equivalent protons H12 from the C=CH_2 group. The DQ-SQ spectrum also shows correlations between H6, H13, H15 and H16 (CH_3 and CH_2) from the polymer backbone at 2.1 ppm with H1, H2, H7, H8, and H9 (ethyl and propyl groups) sites resonating around 3.5 ppm. There is correlation between protons H7 and H8 (propyl groups from TMSPM) with OCH_2 groups, most probably H9 from TMSPM.

ANNEX C. SUPPORTING INFORMATION OF CHAPTER 3. PROCESS MODELING OF LASER SCANNING VAT-PHOTOPOLYMERIZATION OPERATING UNDER INTERMITTENT EXPOSURE CONDITIONS

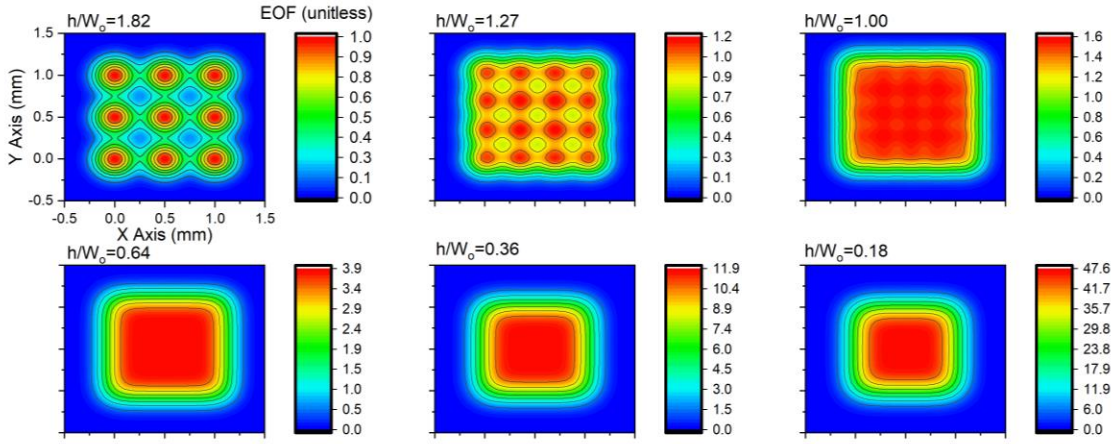

Figure S1. EOF values calculated for a 1 mm square for a W_o=275 µm beam at different hatch distances with h_1=h_2. Equation 3 was numerically solved using a 20 µm mesh for space discretization.

Topography Maps

Discrepancies in the width profile and the model are caused by the premature contact between the stylus (45° and 3µm curvature radius) and the structure due to the rapid increase in height, specially for long hatch distance sample (h/W_o<3.63).

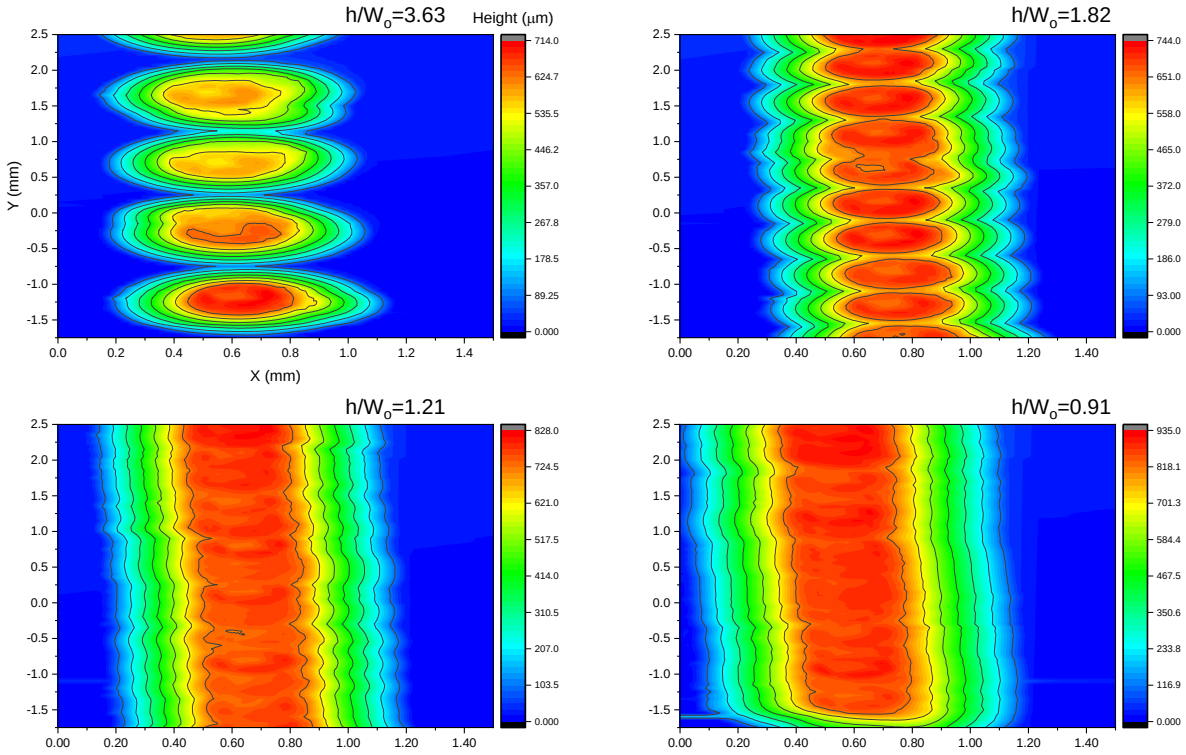

Figure S2. Topography map of line scan at different hatch distances using 0.73 wt% [PETA/BAPO]-[MPTS-HAD] resin with a 360 nm laser (Ø=550±10 μm) at 800μW and 100 ms of exposure time. Profilometer data for 0.73 and 0.36 h/W$_o$ are unavailable due to height exceeding 1 mm.

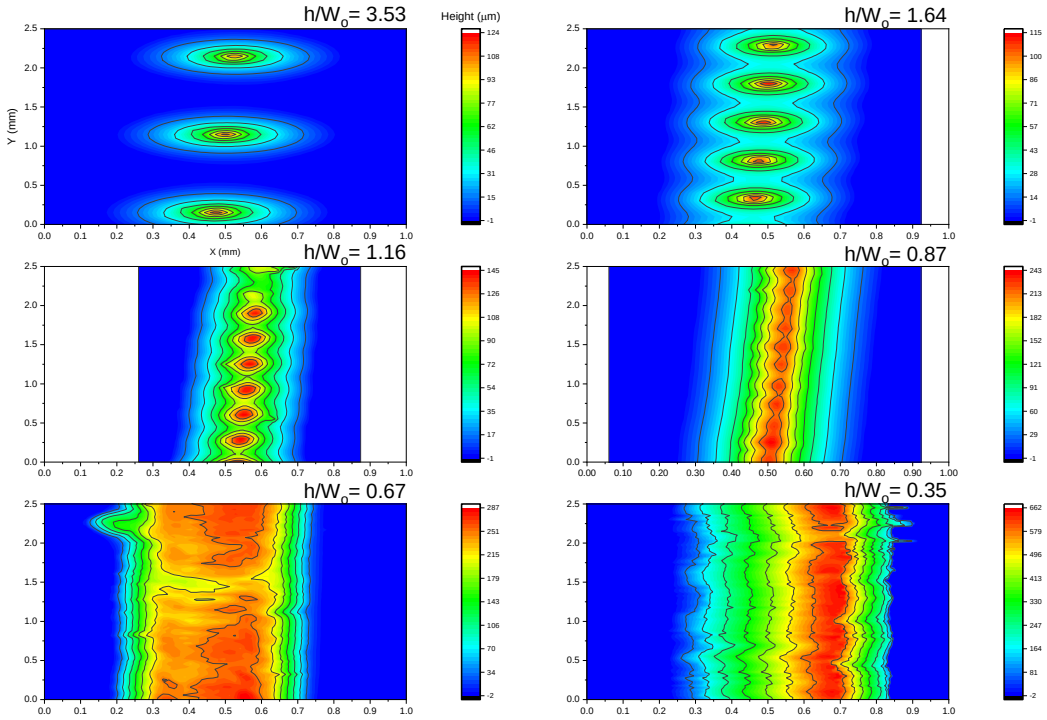

Figure S3. Topography map of line scans at different hatch distances using 0.73 wt% [PETA/BAPO]-[MPTS-HAD] resin with a 360 nm laser (Ø=550±10 μm) at 100μW and 100 ms of exposure time

ANNEX D. SUPPORTING INFORMATION OF CHAPTER 4. CORRELATION BETWEEN CRITICAL ENERGY, PENETRATION DEPTH, AND PHOTOPOLYMERIZATION KINETICS IN ALUMINUM-PHOSPHATE-SILICATE HYBRID MATERIALS FOR VAT-PHOTOPOLYMERIZATION

Table S1. Critical energy and penetration depth extracted from work curve fitting for resins with different MPTMS concentration under different laser powers. Coefficient of fitting adjustment is presented as well.

[MPTMS] (%)	Laser Power (mW)	Critical Energy (mJ)	Penetration Depth (μm)	R^2
0	0.700	4.1E-03	261	0.975
	1.110	4.2E-03	274	0.997
	0.430	3.3E-03	238	0.996
	0.160	3.0E-03	205	0.971
	0.033	2.3E-03	211	0.952
10	0.028	2.2E-03	206	0.983
	0.110	2.9E-03	213	0.994
	1.200	5.0E-03	260	0.998
	0.780	4.4E-03	245	0.999
	0.320	3.4E-03	227	0.985
30	0.700	6.0E-03	283	0.994
	1.060	7.4E-03	304	0.995
	0.210	4.2E-03	262	0.995
	0.038	2.6E-03	218	0.973
	0.110	3.6E-03	243	0.995
50	0.740	7.3E-03	320	0.996
	0.049	4.7E-03	268	0.891
	0.950	6.7E-03	308	0.996
	0.130	6.0E-03	325	0.992
	0.380	7.3E-03	333	0.998
70	0.160	1.1E-02	423	0.958
	0.740	1.5E-02	383	0.970
	0.355	1.3E-02	400	0.995

	0.097	5.3E-03	285	0.985
	1.155	1.6E-02	361	0.999

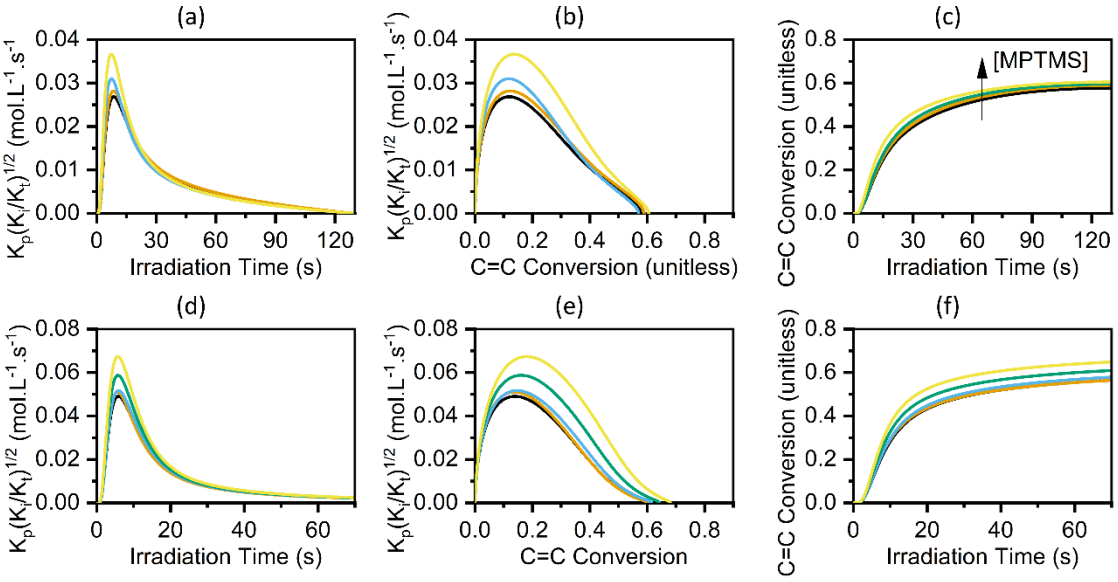

Figure S1. Lumped kinetic constant as function of exposure time with light intensity of 0.5 and 2.5 mW.cm^{-2} in (a) and (d), respectively. Lumped kinetic constant as function of C=C conversion with light intensity of 0.5 and 2.5 mW.cm^{-2} in (b) and (e), respectively. C=C conversion as function of exposure time with light intensity of 0.5 and 2.5 mW.cm^{-2} in (c) and (f), respectively.

Table S2. Fitting parameters for power law describing the peak lumped kinetic constant, ultimate conversion, and C=C conversion at peak polymerization rate dependence on light intensity for samples with different MPTMS concentration.

	Fitting Parameters					
[MPTMS]	**Max $K_p(K_i/K_t)^{1/2}$=a.I^b**		**Ultimate Conversion=a.I^b**		**C=C at Peak R_p =a.I^b**	
%	**a**	**b**	**a**	**b**	**a**	**b**
70	0.048	0.369	62.9	0.056	15.2	0.19
50	0.040	0.402	61.1	0.055	14.4	0.18
30	0.038	0.360	58.1	0.054	12.8	0.16
10	0.036	0.373	58.5	0.039	12.7	0.17
0	0.035	0.373	57.9	0.039	12.7	0.15

Table S3. Extrapolated critical energy values from experimental data (highlighted) using Lee`s photochemical model. Data was extrapolated from the highlighted values for same composition samples under different irradiation conditions (collum).

[MPTMS]	Laser Power	Critical Energy	Laser Power	Critical Energy	Laser Power	Critical Energy	Laser Power	Critical Energy	Laser Power	Critical Energy
%	mW	mJ	mW	mJ	mW	mJ	mW	mJ	mW	mJ
0	**0.03**	**2.3E-03**	0.16	4.2E-03	0.43	6.1E-03	0.70	7.3E-03	1.11	8.6E-03
10	**0.03**	**2.2E-03**	0.11	3.7E-03	0.32	5.5E-03	0.78	7.7E-03	1.20	9.1E-03
30	**0.04**	**2.6E-03**	0.11	3.8E-03	0.21	4.8E-03	0.70	7.5E-03	1.06	8.7E-03
50	**0.05**	**4.7E-03**	0.13	6.9E-03	0.38	1.1E-02	0.74	1.4E-02	0.95	1.5E-02
70	**0.10**	**5.3E-03**	0.16	6.3E-03	0.36	8.5E-03	0.74	1.1E-02	1.16	1.3E-02
0	0.03	1.6E-03	**0.16**	**3.0E-03**	0.43	4.3E-03	0.70	5.1E-03	1.11	6.1E-03
10	0.03	1.7E-03	**0.11**	**2.9E-03**	0.32	4.3E-03	0.78	5.9E-03	1.20	7.0E-03
30	0.04	2.5E-03	**0.11**	**3.6E-03**	0.21	4.5E-03	0.70	7.0E-03	1.06	8.1E-03
50	0.05	4.0E-03	**0.13**	**6.0E-03**	0.38	9.2E-03	0.74	1.2E-02	0.95	1.3E-02
70	0.10	9.3E-03	**0.16**	**1.1E-02**	0.36	1.5E-02	0.74	2.0E-02	1.16	2.3E-02
0	0.03	1.3E-03	0.16	2.3E-03	**0.43**	**3.3E-03**	0.70	3.9E-03	1.11	4.7E-03
10	0.03	1.4E-03	0.11	2.3E-03	**0.32**	**3.4E-03**	0.78	4.7E-03	1.20	5.6E-03
30	0.04	2.3E-03	0.11	3.3E-03	**0.21**	**4.2E-03**	0.70	6.5E-03	1.06	7.5E-03
50	0.05	3.2E-03	0.13	4.7E-03	**0.38**	**7.3E-03**	0.74	9.5E-03	0.95	1.0E-02
70	0.10	8.3E-03	0.16	9.9E-03	**0.36**	**1.3E-02**	0.74	1.7E-02	1.16	2.1E-02
0	0.03	1.3E-03	0.16	2.4E-03	0.43	3.4E-03	**0.70**	**4.1E-03**	1.11	4.9E-03
10	0.03	1.3E-03	0.11	2.1E-03	0.32	3.2E-03	**0.78**	**4.4E-03**	1.20	5.2E-03
30	0.04	2.1E-03	0.11	3.1E-03	0.21	3.9E-03	**0.70**	**6.0E-03**	1.06	7.0E-03
50	0.05	2.4E-03	0.13	3.6E-03	0.38	5.6E-03	**0.74**	**7.3E-03**	0.95	8.1E-03
70	0.10	7.1E-03	0.16	8.5E-03	0.36	1.1E-02	**0.74**	**1.5E-02**	1.16	1.8E-02
0	0.03	1.1E-03	0.16	2.0E-03	0.43	2.9E-03	0.70	3.5E-03	**1.11**	**4.2E-03**
10	0.03	1.2E-03	0.11	2.0E-03	0.32	3.0E-03	0.78	4.2E-03	**1.20**	**5.0E-03**
30	0.04	2.2E-03	0.11	3.3E-03	0.21	4.1E-03	0.70	6.3E-03	**1.06**	**7.4E-03**
50	0.05	2.0E-03	0.13	3.0E-03	0.38	4.7E-03	0.74	6.1E-03	**0.95**	**6.7E-03**
70	0.10	6.3E-03	0.16	7.5E-03	0.36	1.0E-02	0.74	1.3E-02	**1.16**	**1.6E-02**

Table S4. Extrapolated critical energy values from experimental data (highlighted) using Lee`s photochemical model. Data was extrapolated from the highlighted values for similar irradiation conditions to different compositions (row).

[MPTMS]	Laser Power	Critical Energy	Laser Power	Critical Energy	Laser Power	Critical Energy	Laser Power	Critical Energy	Laser Power	Critical Energy
%	mW	mJ	mW	mJ	mW	mJ	mW	mJ	mW	mJ
0	**0.03**	**2.3E-03**	**0.16**	**3.0E-03**	**0.43**	**3.3E-03**	**0.70**	**4.1E-03**	**1.11**	**4.2E-03**
10	0.03	2.3E-03	0.11	2.7E-03	0.32	3.1E-03	0.78	4.4E-03	1.20	4.5E-03
30	0.04	2.8E-03	0.11	2.9E-03	0.21	2.8E-03	0.70	4.5E-03	1.06	4.5E-03
50	0.05	2.9E-03	0.13	3.0E-03	0.38	3.5E-03	0.74	4.8E-03	0.95	4.5E-03
70	0.10	4.8E-03	0.16	4.1E-03	0.36	4.2E-03	0.74	5.7E-03	1.16	5.8E-03
0	0.03	2.3E-03	0.16	3.2E-03	0.43	3.6E-03	0.70	4.1E-03	1.11	4.6E-03
10	**0.03**	**2.2E-03**	**0.11**	**2.9E-03**	**0.32**	**3.4E-03**	**0.78**	**4.4E-03**	**1.20**	**5.0E-03**
30	0.04	2.7E-03	0.11	3.1E-03	0.21	3.1E-03	0.70	4.5E-03	1.06	4.9E-03
50	0.05	2.8E-03	0.13	3.2E-03	0.38	3.9E-03	0.74	4.8E-03	0.95	5.0E-03
70	0.10	4.7E-03	0.16	4.4E-03	0.36	4.7E-03	0.74	5.7E-03	1.16	6.4E-03
0	0.03	2.2E-03	0.16	3.7E-03	0.43	4.9E-03	0.70	5.5E-03	1.11	6.9E-03
10	0.03	2.1E-03	0.11	3.3E-03	0.32	4.6E-03	0.78	6.0E-03	1.20	7.4E-03
30	**0.04**	**2.6E-03**	**0.11**	**3.6E-03**	**0.21**	**4.2E-03**	**0.70**	**6.0E-03**	**1.06**	**7.4E-03**
50	0.05	2.7E-03	0.13	3.7E-03	0.38	5.3E-03	0.74	6.5E-03	0.95	7.5E-03
70	0.10	4.5E-03	0.16	5.1E-03	0.36	6.3E-03	0.74	7.7E-03	1.16	9.6E-03
0	0.03	3.8E-03	0.16	5.9E-03	0.43	6.7E-03	0.70	6.2E-03	1.11	6.2E-03
10	0.03	3.7E-03	0.11	5.4E-03	0.32	6.3E-03	0.78	6.7E-03	1.20	6.6E-03
30	0.04	4.6E-03	0.11	5.8E-03	0.21	5.7E-03	0.70	6.8E-03	1.06	6.6E-03
50	**0.05**	**4.7E-03**	**0.13**	**6.0E-03**	**0.38**	**7.3E-03**	**0.74**	**7.3E-03**	**0.95**	**6.7E-03**
70	0.10	7.9E-03	0.16	8.2E-03	0.36	8.6E-03	0.74	8.7E-03	1.16	8.6E-03
0	0.03	2.5E-03	0.16	8.1E-03	0.43	2.9E-03	0.70	3.5E-03	1.11	4.2E-03
10	0.03	2.5E-03	0.11	7.3E-03	0.32	3.0E-03	0.78	4.2E-03	1.20	5.0E-03
30	0.04	3.1E-03	0.11	7.9E-03	0.21	4.1E-03	0.70	6.3E-03	1.06	7.4E-03
50	0.05	3.1E-03	0.13	8.2E-03	0.38	4.7E-03	0.74	6.1E-03	0.95	6.7E-03
70	**0.10**	**5.3E-03**	**0.16**	**1.1E-02**	**0.36**	**1.3E-02**	**0.74**	**1.5E-02**	**1.16**	**1.6E-02**

ANNEX E. SUPPORTING INFORMATION OF CHAPTER 5. REFRACTIVE INDEX DISTRIBUTION AND OPTICAL ANISOTROPIES IN ADDITIVE MANUFACTURED MATERIALS

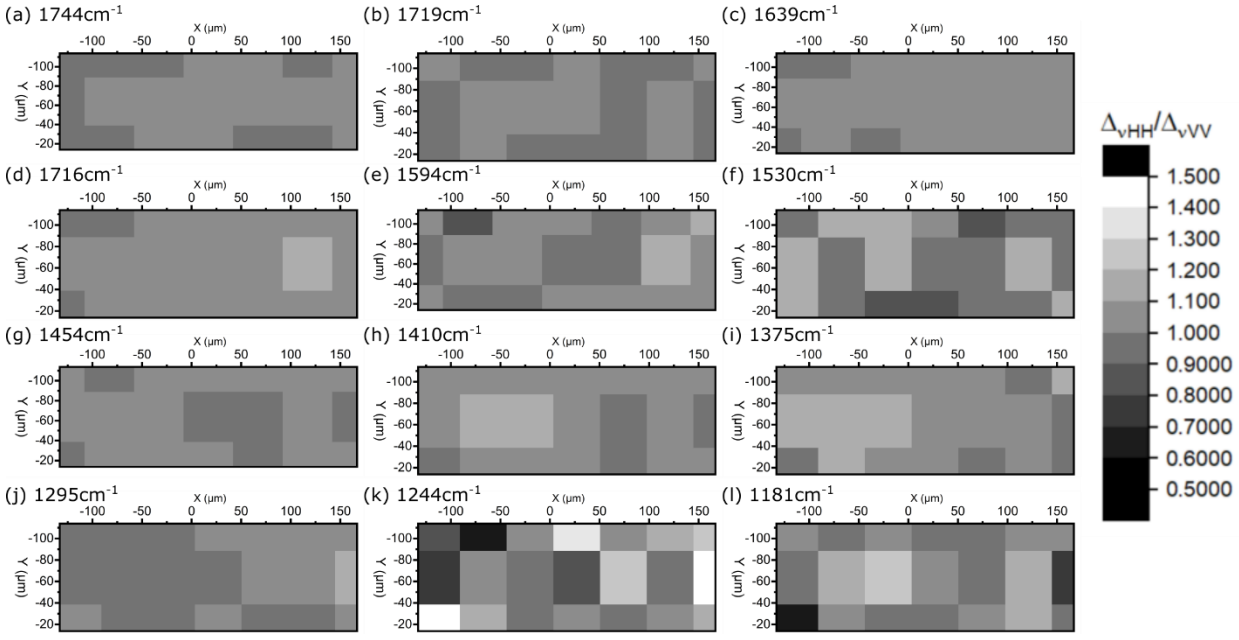

Figure S1. Mapping of Δ vXX/ Δ vYY ratio for the same vibrational band measured with XX and YY polarizer/analyzer micro-Raman setup.